O. Deppe
D* Electroproduction

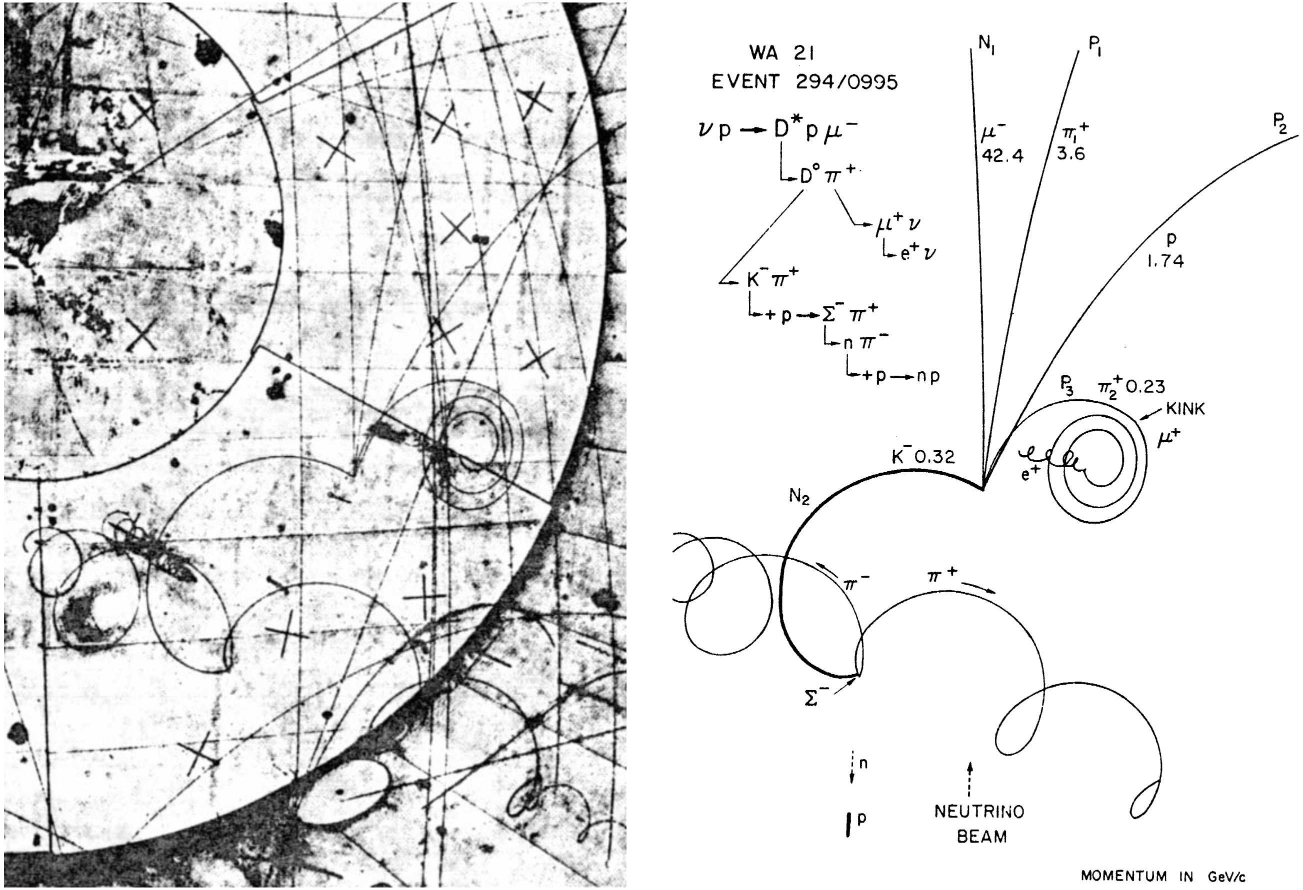

Bubble chamber photograph and drawing of a charged-current D^* production event at BEBC [33]. It is the first example of a $D^{*+} \rightarrow (D^0 \rightarrow K^- \pi^+)\pi^+$ decay where the evidence is based on the complete identification of the final state. One important factor in the identification is the ionisation energy loss, which gives kaon tracks at low momenta a larger thickness than pion tracks and, for instance, directly hints at the nature of the negative track labelled N_2.

DESY-THESIS 2000-006
ISSN 1435-8085

Measurement of $D^{*\pm}$ Electroproduction at HERA

Dissertation
zur Erlangung des Doktorgrades
des Fachbereichs Physik
der Universität Hamburg

vorgelegt von

Olaf Deppe

aus Hamburg

Hamburg
1999

Current address

Olaf Deppe
DESY – ZEUS/ISRL
Notkestr. 85
22603 Hamburg
Germany

Olaf.Deppe@desy.de

Cataloguing data

Measurement of D* electroproduction at HERA / by Olaf Deppe (*1968-04-24, Hamburg). – Hamburg, University (Physics Dept), Doctoral thesis, 1999. – 147 pp. : 89 ill.
Zsfassung in dt. Sprache. – 206 references. – DNB-SG: 29.

PACS: 13.60.Le, 14.65.Dw, 29.40.Gx, 34.50.Bw

HEP-index: D*(2010), electroproduction; positron p, deep inelastic scattering; experimental results; channel cross section; structure function, charm; magnetic detector, ZEUS; track data analysis; energy loss, ionization; particle identification; programming, off-line

Typeset with LyX ⟨http://www.lyx.org⟩
Printed in Germany by DESY

Gutachter der Dissertation	Prof. Dr. V. Blobel Prof. Dr. K. Meier Prof. Dr. G. Wolf
Gutachter der Disputation	Prof. Dr. G. Heinzelmann Prof. Dr. G. Wolf
Datum der Disputation	18. Februar 2000
Dekan des Fachbereichs Physik und Vorsitzender des Promotionsausschusses	Prof. Dr. Fr.-W. Büßer

---

Abstract

Open charm production in deep-inelastic scattering has been studied with the ZEUS detector in collisions between 27.5 GeV positrons and 820 GeV protons at the HERA storage ring. The decay of $\mathrm{D}^*(2010)^\pm$ mesons has been observed in the 1995 data set by reconstructing the daughter particles of the decay mode $\mathrm{D}^{*+} \rightarrow (\mathrm{D}^0 \rightarrow \mathrm{K}^- \pi^+)\pi_\mathrm{s}^+$ (and the charge-conjugated channel) in the central tracking detector (CTD). In the course of this work, a new analysis program shell ($\mathcal{EZ}$) has been developed, which simplifies especially the study of individual particles and their decays. Furthermore, the potential of the ionisation energy loss ($\mathrm{d}E/\mathrm{d}x$) in the CTD for particle identification has been studied in detail.

In the restricted region of the D^* phase space, $1.5 < p_{\perp\mathrm{D}^*} < 10\,\mathrm{GeV}$ and $|\eta_{\mathrm{D}^*}| < 1.5$, the integrated cross-section for D^* production has been measured to be $9.11 \pm 0.63\,^{+0.55}_{-0.50}$ nb for the kinematic range $y < 0.7$ and $1 < Q^2 < 600\,\mathrm{GeV}^2$, and $5.24 \pm 0.42\,^{+0.45}_{-0.40}$ nb for $5 < Q^2 < 100\,\mathrm{GeV}$. Differential cross-sections have been measured as functions of Q^2, W, $p_{\perp\mathrm{D}^*}$ and η_{D^*}, and are compared to NLO predictions of perturbative QCD. The good agreement observed permits use of the NLO calculation for the extrapolation of the measured cross-sections to the full phase space, allowing the determination of the charm contribution $F_2^\mathrm{c}(x, Q^2)$ to the proton structure function F_2, where x is the Bjorken scaling variable. For fixed Q^2, F_2^c has been found to rise rapidly as $x \rightarrow 0$. NLO predictions for F_2^c, based on the gluon density $g(x, Q^2)$ in the proton as determined from the scaling violations of F_2, agree with the data; this presents an important test of the DGLAP evolution mechanism of perturbative QCD.

Messung der $D^{*\pm}$-Elektroproduktion bei HERA

Die Erzeugung charmanter Teilchen in tiefunelastischer Streuung wurde mit dem ZEUS-Detektor beim HERA-Speicherring untersucht. Im Datennahmejahr 1995 stießen hier Positronen mit einer Strahl-Energie von 27.5 GeV auf Protonen mit einer Energie von 820 GeV. $D^*(2010)^\pm$ Mesonen wurden nachgewiesen durch Rekonstruktion der Tochterteilchen aus dem Zerfall $D^{*+} \rightarrow (D^0 \rightarrow K^- \pi^+)\pi_s^+$ (und dem ladungskonjugierten Kanal) mittels des zentralen Spurdetektors (CTD). Zu diesem Zweck wurde für die Ereignisanalyse eine neue Programmumgebung ($\mathcal{EZ}$) geschaffen, welche die Untersuchung von Einzelteilchen und ihrer Zerfälle erleichtert. Besonderes Augenmerk galt der Nutzbarmachung des spezifischen Ionisationsverlustes $\mathrm{d}E/\mathrm{d}x$ zur Hadron-Identifikation.

In einem begrenzten Bereich des D^* Phasenraums, $1.5 < p_{\perp D^*} < 10\,\mathrm{GeV}$ und $|\eta_{D^*}| < 1.5$, wurde der Wirkungsquerschnitt für D^* Produktion gemessen. Er beträgt $9.11 \pm 0.63\,^{+0.55}_{-0.50}\,\mathrm{nb}$ für $y < 0.7$ und $1 < Q^2 < 600\,\mathrm{GeV}^2$, bzw. $5.24 \pm 0.42\,^{+0.45}_{-0.40}\,\mathrm{nb}$ für $5 < Q^2 < 100\,\mathrm{GeV}$. Differentielle Wirkungsquerschnitte wurden als Funktion von Q^2, W, $p_{\perp D^*}$ und η_{D^*} gemessen und werden mit Vorhersagen der perturbativen QCD in nächstführender Ordnung (NLO) verglichen. Die gute Übereinstimmung zwischen Messung und Vorhersage gestattet, diese zur Extrapolation der gemessenen Wirkungsquerschnitte auf den gesamten D^* Phasenraum heranzuziehen. Auf diese Weise konnte der charmante Beitrag F_2^c zur Proton-Strukturfunktion F_2 als Funktion von Q^2 und Bjorken-x bestimmt werden. Bei festem Q^2 zeigt F_2^c einen steilen Anstieg für $x \rightarrow 0$. Die auf der Bestimmung der Gluondichte $g(x)$ aus des Skalenverletzung von F_2 beruhenden NLO-Vorhersagen sind in Übereinstimmung mit den Daten, womit der DGLAP-Formalismus der QCD einen wichtigen Test bestanden hat.

Contents

List of Figures

List of Tables

Abbreviations and Acronyms

ADAMO	ALEPH Data Model, a relational database
ALEPH	Experiment at the LEP collider
ALPHA	ALEPH Physics Analysis package
AMADEUS	Event generator shell, produces input for MOZART
ARGUS	A detector at DORIS (until Oct. 1992)
ARIADNE	Program for the simulation of QCD cascades implementing the colour dipole model
BAC	Backing Calorimeter
BCAL	Barrel Calorimeter
BCN	Bunch Crossing Number
BEBC	Big European Bubble Chamber
BNL	Brookhaven National Laboratories
C5	Beam monitor, installed in a collimator
CAL	Uranium–scintillator Calorimeter
CC	Charged Current
CERN	*Conseil* (or *Centre*) *Européenne pour la Recherche Nucléaire*
CP	Combined Charge and Parity conjugation
CTD	Central Tracking Detector
CTEQ	Coordinated Theoretical-Experimental project on QCD
CZAR	Integrated ZEUS trigger simulation program
DA	Double Angle method
DNB	*Deutsche Nationalbibliographie*
DORIS	Storage ring at DESY
DESY	*Deutsches Elektronen-Synchrotron*
DGLAP	Dokshitser, Gribov, Lipatov, Altarelli and Parisi QCD evolution scheme
DIS	Deep Inelastic Scattering
DJANGO	MC generator that combines HERACLES with LEPTO
DQM	Data Quality Monitoring
DSP	Digital Signal Processor
DST	Data Summary Tape
DU	Depleted Uranium
EAZE	‘Easy Analysis of ZEUS Events’, an analysis shell
EEXOTIC	Electron finder by A. Caldwell and N. Pavel
ELEC 5	Electron finder by J. Repond
EMC	Electromagnetic Calorimeter
EVB	Event Builder
$\mathcal{EZ}$	New ZEUS analysis shell
FADC	Flash Analogue to Digital Converter
FCAL	Forward Calorimeter
FDET	Forward tracking Detector
FFN	Fixed Flavour Number scheme
FLT	First Level Trigger
FermiLab	Fermi National Acceleratory Laboratory (FNAL)
FMUON	Forward Muon Detector
FSAM	Forward presampler
GEANT	Detector description and simulation tool
GFLT	Global First Level Trigger
GHEISHA	Program that describes hadronic showers in matter
GIM	Glashow, Iliopoulos and Maiani
GRV	Glück, Reya and Vogt
GSLT	Global Second Level Trigger
H1	A detector at HERA
HAC	Hadron Calorimeter
HEP	High Energy Physics
HERA	*Hadron-Electron-Ring-Anlage*
HERA-B	HERA experiment for B studies
HERACLES	Event generator for ep interactions at HERA including radiative processes
HERMES	HERA experiment using polarised targets

HERWIG	Hadron Emission Reactions With Interfering Gluons, an MC generator
HES	Hadron–Electron Separator
HRS	High Resolution Spectrometer, former experiment at SLAC
HVQDIS	Heavy Quarks in DIS, cross-section calculation program by Harris and Smith
ISSN	International Standard Serial Number
IUPAP	International Union for Pure and Applied Physics
JB	Jacquet–Blondel method
JETSET	The Lund Monte Carlo for jet fragmentation
LAZE	'Look At Zeus Events', the ZEUS event display
LEP	Large Electron-Positron collider at CERN
LEPTO	The Lund Monte Carlo for deep inelastic lepton–nucleon scattering
LINAC	Linear Accelerator
LLA	Leading Log Approximation
LO	Leading Order
LOCAL	Electron finder by A. Caldwell, B. Straub, and N. Pavel
LUMI	Luminosity monitor
MC	Monte Carlo
mip	Minimum Ionising Particle
MOZART	Monte Carlo for ZEUS Analysis, Reconstruction and Trigger
MRS	Martin, Roberts and Stirling
MRRS	Martin, Roberts, Ryskin and Stirling
$\overline{\text{MS}}$	Modified Minimal Subtraction renormalisation scheme
NC	Neutral Current
NEG	Non-Evaporable Getter
NLO	Next-to-Leading Order
NMC	New Muon Collaboration, former experiment at CERN
OPAL	Omni-Purpose Apparatus at LEP
PACS	Physics and Astronomy Classification Scheme
PAI	Photon Absorption Ionisation
PDF	Parton Distribution Function
PDG	Particle Data Group
PETRA	Positron-Elektron-Tandem-Ring-Anlage
PGF	Photon–Gluon Fusion
PIA	Positron Intensity Accumulator
PMT	Photomultiplier Tube
QCD	Quantum Chromo-Dynamics
QED	Quantum Electro-Dynamics
QPM	Quark Parton Model
RAPGAP	'Rapidity Gap', Monte Carlo program for the simulation of ep scattering
RCAL	Rear Calorimeter
RF	Radio Frequency
RSAM	Rear presampler
RTD	Rear Tracking Detector
SCSN-38	A brand of polystyrene scintillator
SGI	Silicon Graphics Inc., a workstation maker
SINISTRA	Electron finder by R. Sinkus
SLAC	Stanford Linear Accelerator Center
SLT	Second Level Trigger
SRTD	Small angle Rear Tracking Detector
TASSO	Two Arm Spectrometer Solenoid, former PETRA experiment
TLT	Third Level Trigger
TPM	Triple Port Memory
VCTRAK	VXD & CTD Track reconstruction package
VFN	Variable Flavour Number scheme
VXD	Vertex Detector
ZARAH	*Zentrale* (or *ZEUS*) *Rechenanlage für HERA-Physik*
ZEBRA	Data management system
ZEPHYR	ZEUS Physics Reconstruction Program
ZEUS	A detector at HERA ('*Z*earch to Elucidate Underlying Symmetry')

1 Introduction

In 1964 Bjørken and Glashow [32] introduced on grounds of symmetry a new quantum number, which they called *charm,* and postulated the existence of a charmed meson doublet D and a charmed strange meson singlet S (later called F, then $\mathrm{D}_{\mathrm{s}}^{+}$). This hypothesis did not only extend the quark model [99, 103, 206] towards greater symmetry between quarks and leptons, it also provided a natural explanation (the GIM mechanism [106]) for the observed selection rules of the weak interaction, namely the nonobservation of flavour-changing neutral currents in kaon decays. When a narrow resonance at 3.1 GeV was found in 1974 at BNL [17] and at SLAC [18] (which lead to the discovery of further, closely related states), it soon became clear that the particle called 'J' or 'ψ' can be identified with the postulated orthocharmonium vector meson 'ϕ_{c}' (notation of Ref. 100). In the following years, most states of the pseudoscalar and vector SU(4) hexadecuplets were found and their masses and many of their decay fractions were measured. Charm spectroscopy is still an active field, with the main issues being the search for rare decay modes beyond the tree level, which could indicate new physics through *CP* violation or flavour-changing neutral currents, and the search for $\mathrm{D}\overline{\mathrm{D}}$ mixing, which in the standard model is expected to be much smaller than for kaons or B mesons [104].

The charm quark, having a (scheme-dependent) mass of $m_{\mathrm{c}} \sim 1.5\,\mathrm{GeV}$, is much heavier than u, d and s quarks. The large mass provides a hard scale for the scattering, equivalent to a spatial scale of $r = 1/m_{\mathrm{c}} \sim 0.1\,\mathrm{fm}$. This scale is small compared to the proton radius of 0.8 fm; therefore, charm production in deep inelastic scattering is characterised by *two* hard scales, Q^2 and m_{c}. Owing to their large mass, charmed particles are almost exclusively produced at the vertex of the hard interaction and not within the soft fragmentation. In deep inelastic scattering, the leading charm production mechanism is photon–gluon fusion (PGF) [4], which relates F_2^{c}, the contribution of charm production to the proton structure function F_2, directly with the gluon density in the proton; therefore the comparison of F_2^{c}, as determined in this analysis, with theoretical calculations based on the gluon density, which has been extracted through a QCD analysis of the F_2 scaling violations, provides an important consistency test of perturbative QCD.

The presence of charm photoproduction at HERA was established soon after the collider commenced operation in 1992 [82, 139]. Data collected in 1994 permitted for the first time the measurement of differential cross-sections for charm production in deep inelastic scattering at HERA and a determination of the charm contribution to F_2 [4]. The analysis of charm production in deep inelastic scattering presented in this report was performed using the data taken with the ZEUS detector in 1995. The data sample is about twice as large as that used before.

Charmed mesons (D^0, $\mathrm{D}^*(2010)^+$ and charge conjugates) are reconstructed from charged tracks recorded in the central tracking chamber. A concentrated effort has been made to incorporate in this analysis not only the spatial information but also the ionisation loss ($\mathrm{d}E/\mathrm{d}x$) measured in the chamber, so that the detection of charmed mesons can be improved by means of particle identification. Hence a major part of this thesis is devoted to the discussion of the performance of the tracking chamber.

2 Charm in Deep Inelastic Scattering

2.1 Deep Inelastic Electron–Proton Scattering

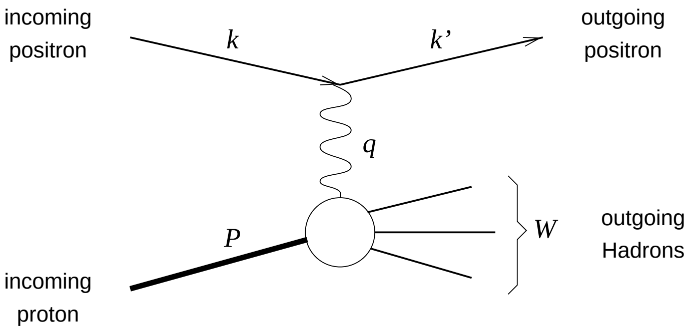

Fig. 2.1
Neutral current inelastic scattering

The scattering process between a lepton and a proton can be described by the exchange of an electroweak current.[†] The leading process is the exchange of a single boson, which may be a γ or Z (neutral current, NC) or a $\mathrm{W}^{\pm}$ (charged current, CC). In this analysis, inelastic neutral current collisions are studied, as illustrated in Fig. 2.1. P and k are the 4-momenta of the incident particles, k' is the 4-momentum of the outgoing electron[‡], and $q = k - k'$ the 4-momentum of the boson exchanged. Since q is spacelike, one defines by $Q^2 \equiv -q^2$ the negative value of the photon virtuality, which is a measure of the transverse spatial resolution[§] $\Delta \sim \sqrt{1/Q^2}$ with which the electron probes the proton. At $Q^2 \approx 0$ a quasi-real photon collinear with the incident electron strikes the proton—a regime hence called *photoproduction;* in that case, the electron escapes the central detector through the beampipe. For Q^2 values above 1–3 GeV^2, however, the scattered electron is observed in the main calorimeter. This type of collision is denoted as *electroproduction* or *deep inelastic scattering* (DIS).

Let the initial electron energy in the proton rest frame be E_e, and E'_e after the scattering; then the energy transferred to the proton of mass m_p is $\nu \equiv E_\mathrm{e} - E'_\mathrm{e} = (P \cdot q)/m_\mathrm{p}$. The proton mass is the minimum value for the mass W of the outgoing hadronic system,

---

[†] For a general introduction and an overview over various aspects of HERA physics see, for instance, Wolf [201].

[‡] Here and in the following, the word ‘electron’ is used as a generic term for both, electrons and positrons.

[§] Whenever appropriate, units have been chosen so that $\hbar = c = 1$ and $\varepsilon_0 = \mu_0 = 1$. Otherwise the notation generally follows the IUPAP recommendations [71].

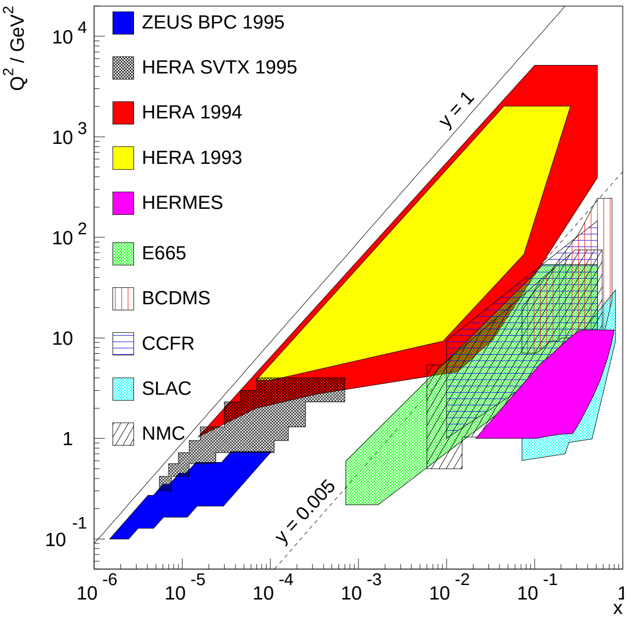

Fig. 2.2
Kinematic range covered by the HERA experiments and various fixed target experiments [163]

$$W^2 \equiv (P+q)^2 = m_\mathrm{p}^2 + 2m_\mathrm{p}\nu - Q^2 \geqslant m_\mathrm{p}^2 \ ,$$

and therefore

$$x \equiv \frac{Q^2}{2P\cdot q} = \frac{Q^2}{2m_\mathrm{p}\nu} \leqslant 1 \ .$$

The scaling variable x has been introduced by Bjorken [31]. In the naïve quark parton model (QPM), the electron scatters elastically off one of the independent constituent *partons* (quarks) of the proton and x is the momentum fraction of the proton carried by the struck quark in a reference frame where the proton is very fast (‘infinite momentum frame’). In this picture, the struck quark emerges from the proton forming a so-called *current jet,* which balances the transverse momentum of the scattered electron, whereas the *proton remnant,* consisting of partons not involved in this interaction, emerges in the direction of the proton beam. In the proton rest frame, the quantity

$$y \equiv \frac{P\cdot q}{P\cdot k} \approx \frac{E_\mathrm{e}-E'_\mathrm{e}}{s/(2M)} = \frac{\nu}{\nu_\mathrm{max}} \ , \qquad \nu_\mathrm{max} \approx 48\,\mathrm{TeV} \ ,$$

approximates the momentum fraction of the electron transferred to the proton, where $s = (P+k)^2$ is the square of the ep centre of mass energy. For fixed s, the values of any two of the invariant variables Q^2, W^2, x and y are sufficient for determining the kinematics of the scattering process.

Figure 2.2 shows the kinematic range covered by deep inelastic scattering at HERA in comparison with fixed target experiments: values of x (and Q^2)

have been reached that are by a factor of hundred lower (more than a factor of ten higher) than attained previously.

2.2 Proton Structure

The differential Born cross-section for neutral current deep inelastic ep scattering ($\mathrm{ep} \rightarrow \mathrm{e}'X$) can be expressed in leading order standard electroweak theory in terms of three independent functions $\mathscr{F}_{1,2,3}$ of x and Q^2 [78, 138],

$$\frac{\mathrm{d}^2\sigma^{\mathrm{NC}}_{\mathrm{e^{\pm}p}}}{\mathrm{d}x\,\mathrm{d}Q^2} = \frac{4\pi\alpha^2}{xQ^4}\left[xy^2\mathscr{F}_1 + (1-y)\mathscr{F}_2 \mp (y - \tfrac{y^2}{2})x\mathscr{F}_3\right], \tag{2.1}$$

where α is the electromagnetic coupling constant and the $+(-)$ sign applies to $\mathrm{e^-p}$ ($\mathrm{e^+p}$) scattering. The functions $\mathscr{F}_i$ are superpositions of the 8 structure functions $F_{1,2}$ (purely electromagnetic), $G_{1,2,3}$ (γZ interference) and $H_{1,2,3}$ (purely weak), where the magnitudes of the relative contributions of (F_i, G_i, H_i) are governed by $(1, \chi_\mathrm{Z}, \chi_\mathrm{Z}^2)$, respectively. The quantity χ_Z is given by a function of the weak mixing angle θ_W and the ratio of the photon and Z propagators,

$$\chi_\mathrm{Z} \equiv \chi_\mathrm{Z}(Q^2) = \frac{1}{4\sin^2\theta_\mathrm{W}\cos^2\theta_\mathrm{W}}\,\frac{Q^2}{Q^2 + M_\mathrm{Z}^2}\,. \tag{2.2}$$

Inverting (2.2) one finds that at $Q^2 \sim 21\,000\,\mathrm{GeV}^2$ the electromagnetic, weak and interference terms have the same weight [35], while at $Q^2 \sim 1000\,\mathrm{GeV}^2$ weak interactions contribute to only $\sim 1\%$ of the cross-section.

This analysis is restricted to a kinematic region where $\chi_\mathrm{Z} \ll 1$, so that the parity violating $\mathscr{F}_3$ contribution and the remaining contributions from Z exchange and γZ interference are small corrections $(\delta_3, \delta_\mathrm{Z})$ to the electromagnetic cross-section. QED radiative corrections can be factorised in the leading log approximation (LLA) and are accounted for by another correction δ_R; they are mostly related to radiation from the electron line of Fig. 2.1 owing to the small electron mass. Their effect on measured cross-sections depends on the sensitivity to radiation of the method used to reconstruct the event kinematics.

The cross-section contribution from the exchange of longitudinally polarised photons is described by the structure function $F_\mathrm{L} \equiv F_2 - 2xF_1$. In the kinematic range studied, the contribution from the F_L term is small according to QCD. It will be represented by the correction δ_L. The corrections $\delta_{3,\mathrm{L,Z,R}}$ are assumed to be (approximately) independent of F_2 and of each other, so that (2.1) can be written as

$$\frac{\mathrm{d}^2\sigma}{\mathrm{d}x\,\mathrm{d}Q^2} = \frac{2\pi\alpha^2}{xQ^4}[1 + (1-y)^2]F_2(x, Q^2)\,(1 \mp \delta_3 - \delta_\mathrm{L})(1 - \delta_\mathrm{Z})(1 + \delta_\mathrm{R})\,. \tag{2.3}$$

If all constituents of the proton had spin $1/2$, as is the case in the quark–parton model (QPM), only transverse photons would couple to the proton and F_L would vanish, so that the Callan–Gross relation [59], $F_2 = 2xF_1$, holds. In the QPM, the electron scatters elastically off one of the pointlike quarks, so that the scattering process and the structure functions depend only on a single parameter, x. This *scaling* hypothesis was shown to approximately hold in fixed-target ep scattering experiments for $x \gtrsim 0.1$ (first seen at SLAC [46]). These experimental observations strongly suggested that nucleons are made of charged pointlike constituents, called *quarks*, which had been postulated by models describing elementary particle phenomenology [103, 206]. Logarithmic scaling violations observed at fixed-target deep inelastic scattering experiments [65, 97] and the observation that charged partons carried only half of the nucleon momentum [88] suggested the radiation of a strongly interacting field quantum, the *gluon*, and led to the formulation of quantum chromodynamics (QCD), the gauge theory of the strong interaction [99, 155]. Direct evidence for gluon radiation was provided by the observation of three-jet events in $\mathrm{e^+e^-}$ annihilation at PETRA [45].

In QCD, the interaction between quarks is mediated by the exchange of gluons, which couple to the colour charges of quarks and gluons. The quarks in the proton may radiate and absorb gluons, which in turn can split into quark–antiquark or gluon pairs. With decreasing wavelength of the probing photon, i.e., with increasing Q^2, more and more of these fluctuations can be resolved. The observed scaling violations are closely related to the gluon dynamics inside the proton: for large x there is a depletion of quarks at high Q^2 due to gluon bremsstrahlung, whereas at small x the number of quarks and antiquarks increases as a result of gluon splitting (cf. Fig. 2.3).

To the probing electron the monochromatic proton beam looks like a beam of partons with a broad momentum spectrum, which is described by the parton distribution functions (PDFs) $f_{i/\mathrm{p}}(x, \mu^2)$ of the proton, where $1/\mu$ is the spatial resolution with which the proton is viewed. The ep scattering cross-section σ_ep can be expressed as the incoherent sum of electron–parton cross-sections $\sigma_{\mathrm{e}i}$ folded with the respective parton distribution functions $f_{i/\mathrm{p}}$,

$$\sigma_\mathrm{ep}(x, Q^2) = \sum_{i \,\in\, \mathrm{partons}} \left[f_{i/\mathrm{p}}(x, \mu_\mathrm{F}^2) \otimes \sigma_{\mathrm{e}i}(x, Q^2, \mu_\mathrm{F}^2) \right] . \tag{2.4}$$

This is known as the factorisation theorem of perturbative QCD. The factorisation (or mass) scale μ_F^2 provides the dividing line between what is considered as the long-range inner dynamics of the proton ($f_{i/\mathrm{p}}$) and the short-range dynamics of the lepton–parton interaction ($\sigma_{\mathrm{e}i}$); it can in principle be chosen arbitrarily without changing the physical cross-section. Choosing $\mu_\mathrm{F}^2 \equiv Q^2$ puts all fluctuations into the parton distribution, so that $\sigma_{\mathrm{e}i}$ reduces to the Born graph (eq→eq in zeroth order of the strong coupling constant α_s); in

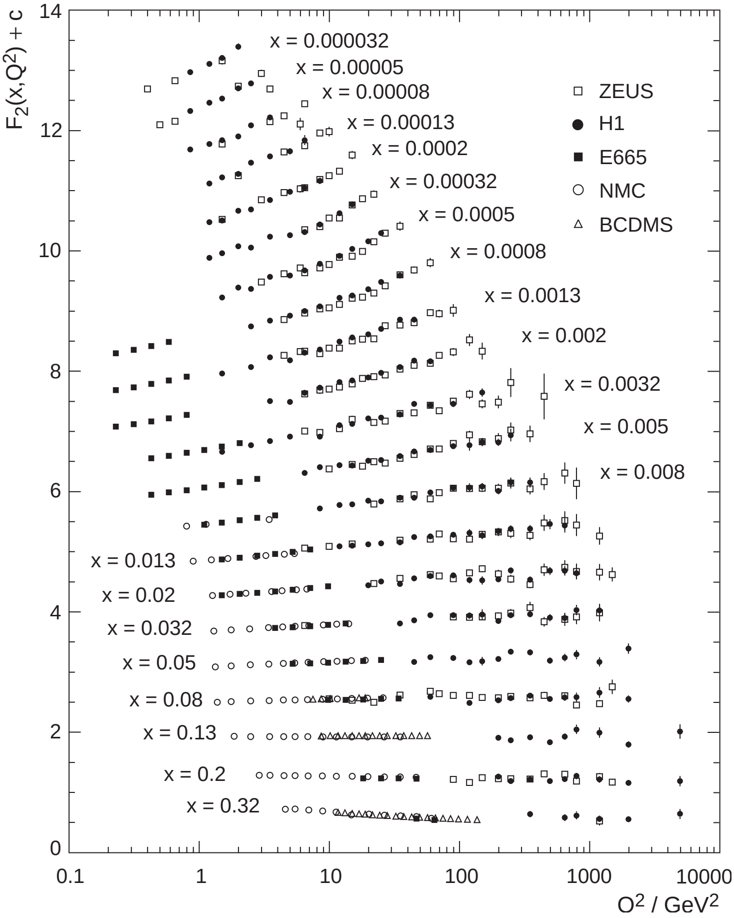

Fig. 2.3
The structure function $F_2(x, Q^2)$ for fixed values of x as measured at fixed target experiments and at HERA. For each x bin i a constant $c_i \equiv 0.6\,(i - 0.4)$ has been added for better visibility. Adapted from Ref. 62.

that case, F_2 is a simple function of the densities of quarks and antiquarks and their couplings e_i to the photon (i.e., their electric charges),

$$F_2(x, Q^2) = x \sum_i e_i^2 q_i(x, Q^2) \, .$$

The initial parton distributions cannot be derived from first principles and must be obtained from experiment. The electron–parton cross-sections, on the other hand, can in principle be calculated perturbatively as an expansion in the coupling constant α_s, which itself depends on the renormalisation scale μ_R^2, i.e., the characteristic energy scale (e.g. Q^2 in DIS, $p_\perp$ of partons). In first order LLA, α_s is given by

$$\alpha_\mathrm{s}(\mu_\mathrm{R}^2) = \frac{12\pi}{(33 - 2n_\mathrm{f}) \ln(\mu_\mathrm{R}^2/\Lambda_\mathrm{QCD}^2)} \, ,$$

where n_f is the number of active quark flavours with a mass less than the energy scale. One sees that for $\mu_\mathrm{R}^2 \to \infty$ (short distances) the coupling strength vanishes, so that the partons behave as free particles (*asymptotic freedom*), whereas for $\mu_{\mathrm{R}}^2 \to 0$ (long distances) the coupling grows beyond all bounds (*confinement*). The parameter Λ_{QCD} determines the scale at which coupling becomes so large that confinement sets in. From the size of the proton its order of magnitude can be estimated to be $\Lambda_{\mathrm{QCD}} \sim 1/0.8\,\mathrm{fm} = 0.25\,\mathrm{GeV}$; its actual value depends on n_{f} and on the renormalisation scheme used, and varies within 0.1–0.5 GeV.

One can ascribe all parton dynamics to the parton distributions entering (2.4) by setting $\mu_{\mathrm{F}}^2 \equiv Q^2$; however, it is not possible to describe the dynamics perturbatively down to an arbitrarily small scale μ_{F}^2. The calculation of the matrix element in $\mathscr{O}(\alpha_{\mathrm{s}})$ for eq scattering, for instance, allows for the emission of a hard gluon, but must exclude the phase space below a certain minimum $p_\perp$ of the radiated gluon; the collinear divergences below the minimum $p_\perp$ have to be factorised into the PDFs. There is no unique way of handling the absorption of divergences of the matrix elements into the PDFs for all processes to all orders and therefore the PDFs depend on the choice of the renormalisation scheme. Conceptually, the structure function F_2 results from a summation to all orders and does not depend on the choice of the renormalisation scheme; the actual calculations however are of finite order and thereby a renormalisation scheme dependence of the calculated F_2 is introduced.

The parton distributions for a fixed, low value of $\mu_{\mathrm{F}}^2 = Q_0^2$, give a picture of how the proton looks like when probing it with poor spatial resolution; in this regime one sees predominantly the scattering on the valence quarks. The parton distribution can be evolved to $\mu_{\mathrm{F}}^2 = Q^2 > Q_0^2$ by allowing for the possibility of partons to radiate or split. The probability of finding a parton i emerging with a momentum fraction z from a parton j when the scale changes by $\mathrm{d}\ln Q^2$ are described by splitting functions $P_{ij}(z)$, given in leading order (LO) by

$$\begin{aligned} P_{\mathrm{qq}}(z) &= \tfrac{4}{3}\tfrac{1+z^2}{1-z}\ , & P_{\mathrm{gq}}(z) &= P_{\mathrm{qq}}(1-z)\ , \\ P_{\mathrm{qg}}(z) &= \tfrac{1}{2}[z^2+(1-z)^2]\ , & P_{\mathrm{gg}}(z) &= 6[\tfrac{z}{1-z}+\tfrac{1-z}{z}+z(1-z)]\ . \end{aligned}$$

Then the evolution of the (anti-) quark (q_i) and gluon (g) densities can be expressed by a system of integro-differential equations,

$$\frac{\mathrm{d}q_i(x,Q^2)}{\mathrm{d}\ln Q^2} = \frac{\alpha_{\mathrm{s}}(Q^2)}{2\pi}\int_x^1 \frac{\mathrm{d}x'}{x'}\left[q_i(x',Q^2)P_{\mathrm{qq}}(\tfrac{x}{x'}) + g(x',Q^2)P_{\mathrm{qg}}(\tfrac{x}{x'})\right]\ ,$$

$$\frac{\mathrm{d}g(x,Q^2)}{\mathrm{d}\ln Q^2} = \frac{\alpha_{\mathrm{s}}(Q^2)}{2\pi}\int_x^1 \frac{\mathrm{d}x'}{x'}\left[\textstyle\sum_i q_i(x',Q^2)P_{\mathrm{gq}}(\tfrac{x}{x'}) + g(x',Q^2)P_{\mathrm{gg}}(\tfrac{x}{x'})\right]\ .$$

This formalism is known as DGLAP evolution [11, 86, 109, 110]. The coupled equations can be solved numerically for any value of $(Q^2, x > x_0)$, if input

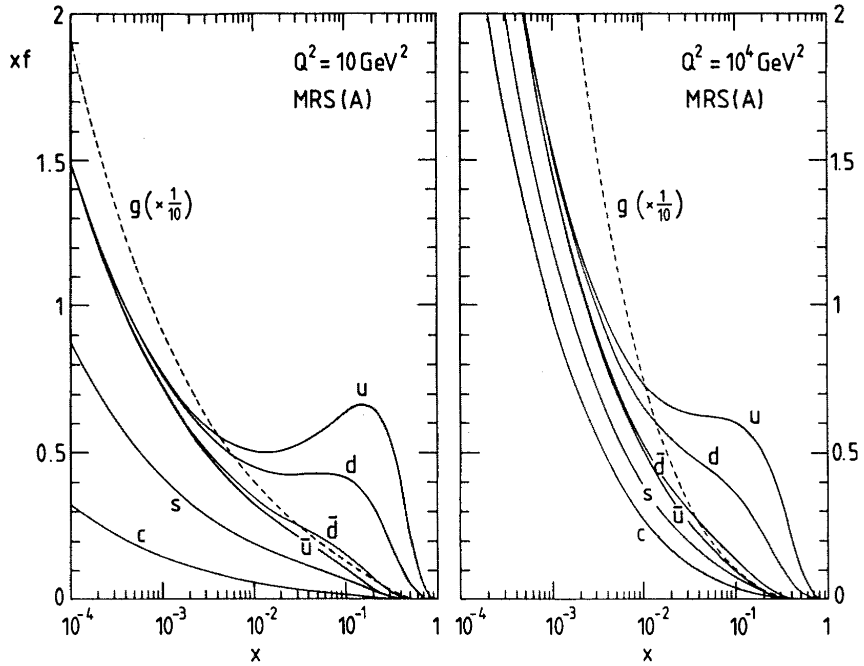

Fig. 2.4 Parton momentum densities of the MRS A set as a function of x at low and at high values of Q^2 [151]. Note that the gluon density has been scaled down by a factor of ten for this diagram.

distributions are provided for a fixed value $Q = Q_0^2$ for all x larger than a starting value x_0.

There are, in general, two different approaches for the determination of the PDFs: global fits of rational functions to the data, which are the parton density functions defined at a starting scale Q_0^2 and evolved to higher Q^2 using the DGLAP formalism. This procedure was chosen by Martin–Roberts–Stirling (MRS) and by the CTEQ collaboration. The other approach is based on a model that starts from a valencelike input distribution at very low Q^2 and predicts F_2 at larger values of Q^2 via QCD evolution, as adopted by Glück–Reya–Vogt (GRV).

The MRS parametrisations of the parton momentum density functions xf_i are of the form

$$xf_i(x) = A_i\, x^{\lambda_i}(1-x)^{\eta_i}(1+\varepsilon_i\sqrt{x}+\gamma_i x)\ ,$$

where A_i, λ_i, η_i, ε_i, and γ_i are free parameters, except for restrictions given by flavour and momentum sum rules. Figure 2.4 shows as an example the parton momentum densities of the MRS A parametrisation [151], which has been obtained using the next-to-leading order (NLO) DGLAP equations in the $\overline{\mathrm{MS}}$ renormalisation scheme at a starting scale of $Q_0^2 = 4\,\mathrm{GeV}^2$. Similar results were obtained by the CTEQ collaboration, who used essentially the same form for the parton distributions and chose $Q_0^2 = 2.56\,\mathrm{GeV}^2$ as a starting scale for their CTEQ 4 parametrisation [142]. The input data include, besides fixed-target data, the 1993 F_2 measurements from HERA. The most striking feature is the steep rise of F_2 observed at HERA, leading to rapidly rising parton momentum densities for $x \to 0$.

Glück–Reya–Vogt [107] started from a very low scale of $Q_0^2 = 0.34\,\mathrm{GeV}^2$. In the regime of the starting scale, the sea quarks and gluons follow the valence quarks and are parametrised as

$$\begin{aligned} xg(x,Q_0^2) &= A\,x^{\alpha}(1-x)^{\beta}\;, \\ x\bar{u},\bar{d}(x,Q_0^2) &= A'\,x^{\alpha'}(1-x)^{\beta'}\;, \\ xs(x,Q_0^2) &= 0\;. \end{aligned}$$

With increasing Q^2, non-valencelike sea quarks and gluons are produced dynamically through DGLAP evolution.

The ZEUS collaboration chose an input scale of $Q_0^2 = 7\,\mathrm{GeV}^2$ for their NLO fits to the ZEUS data [43, 81] and used a functional form similar to that of Martin–Roberts–Stirling for parametrising the gluon momentum density, the singlet quark momentum density and the density difference between up and down quarks,

$$\begin{aligned} xg(x,Q_0^2) &= A_g x^{\delta_g}(1-x)^{\eta_g}(1+\gamma_g x)\;, \\ xS(x,Q_0^2) &= A_s x^{\delta_s}(1-x)^{\eta_s}(1+\gamma_s x+\varepsilon_s\sqrt{x}) = 2x(\bar{u}+\bar{d}+\bar{s})\;, \\ x\Delta(x,Q_0^2) &= A_\Delta x^{\delta_\Delta}(1-x)^{\eta_\Delta} = x(u+\bar{u}) - x(d+\bar{d})\;. \end{aligned}$$

The input distributions for the valence quarks were taken from the MRS D'_{-} set [150], which is based on fits to pre-HERA data. Strange quarks were assumed to contribute 20% at $Q^2 = 4\,\mathrm{GeV}^2$. The evolution was done with three active quark flavours, whereas the charm contribution was calculated in NLO from photon gluon fusion (PGF); beauty quarks were neglected. Fixed target measurements from NMC were used for constraining the fit at large x. Figure 2.5 shows the fit result for the gluon momentum density $xg(x)$ at a fixed $Q^2 = 20\,\mathrm{GeV}^2$ in comparison with fits performed by the H1 and NMC experiments and with the results from global QCD analyses of MRS, CTEQ and GRV [108, 142, 149]. The error band shows the combined statistical and systematic uncertainty, which includes variations of the charm quark mass m_c and the strong coupling constant α_s. A strong rise is seen with decreasing x. All parametrisations are in good agreement within the uncertainties ($\sim 15\%$ at $x = 5 \times 10^{-4}$), except for GRV 94 HO, which for $x < 10^{-3}$ is steeper than the other distributions.

2.3 Identification of Charm

The aim of this analysis is the determination of the contribution from charm production in deep inelastic scattering. When looking for charm in the hadronic final state, one distinguishes between the production of *open* or *naked* charm, where the charm quarks fragment into charmed hadrons, and *hidden* charm, where the charm quarks form a bound $c\bar{c}$ state (e.g. J/ψ), which is flavour-neutral. J/ψ mesons can cleanly be detected through their leptonic decays into $\mu^+\mu^-$ or e^+e^-, with a branching ratio of 6.0% for each channel [62]. They are copiously produced in elastic and diffractive processes, since they carry the same quantum numbers as the photon. Their production cross-section in PGF, however, is 20 times smaller than for open charm—not only because the phase space is restricted by requiring the charm quarks to be produced in a bound state, but also because the charm quarks have to radiate away the colour charge of the initial gluon in order to form a meson, whereas open charm quarks may carry any colour. D mesons have a comparatively large production cross-section, but their branching ratios for all-charged-particles decays are small.

Figure 2.6 shows the family of known D mesons. Mediated through strong interactions, the heavier states immediately decay (widths of $\Gamma \sim 0.1$–$25\,\mathrm{MeV}$) into the lighter D mesons plus another hadron or photon. The ground state D mesons decay weakly into light particles with a lifetime of $\tau \sim 10^{-12}\,\mathrm{s}$. If the D mesons are not produced at rest, their decay vertex is displaced from

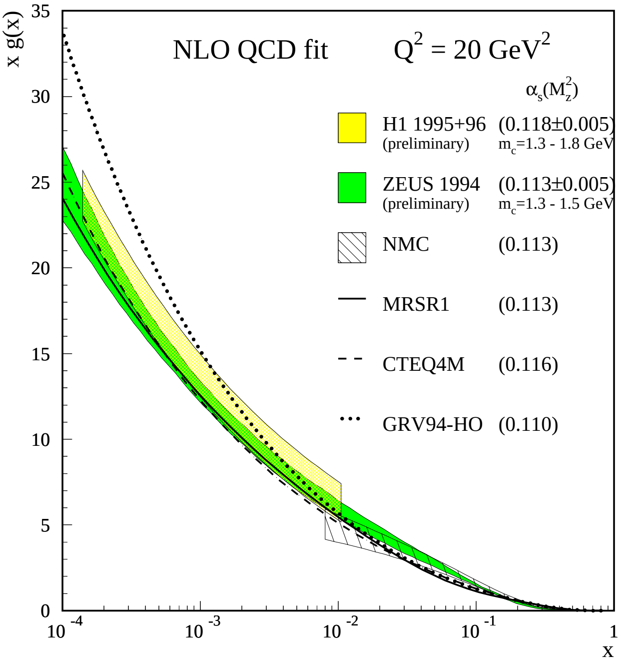

Fig. 2.5
The gluon momentum density $xg(x)$ at $Q^2 = 20\,\mathrm{GeV}$ as extracted from scaling violations of F_2 through QCD fits (taken from Ref. 52)

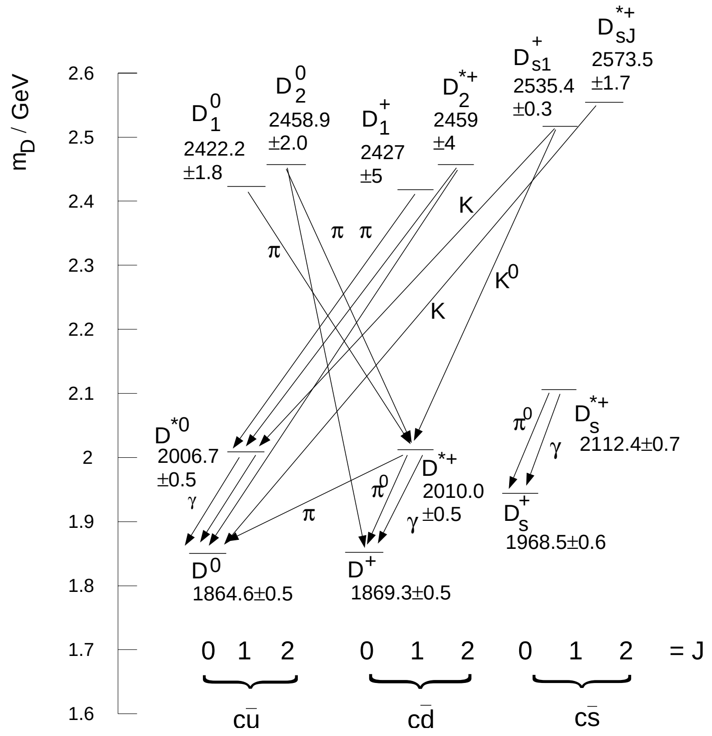

Fig. 2.6
D mesons and their transitions. Given are the meson masses, their quark contents and the total angular momentum J of the $\mathrm{q\bar{q}}$ system. Adapted from Ref. 24, values from Ref. 62.

their production vertex (typically by $c\tau \sim 200\,\mu\mathrm{m}$ for $p_\mathrm{D} = 3\,\mathrm{GeV}$). Currently a micro-vertex detector is being constructed for ZEUS, which will help recognising secondary vertices, providing a powerful tool for tagging charm decays [168, 203].

Shortly after the discovery of the J/ψ and the η_c, Nussinov [156]—studying their small mass difference—concluded that the mass difference between the D^* vector meson and the pseudoscalar D should be of the order of the pion mass. If it was slightly larger, so he suggested, the presence of a slow pion in the final state could serve as a distinctive signature for a D^* decay and thus for the presence of open charm. The first observation of the decay[†] $\mathrm{D}^{*+} \rightarrow \mathrm{D}^0\pi^+$ was reported by Feldman *et al.* [91], who found the mass difference between the D^{*+} and the D^0 to be, indeed, only slightly above the threshold of the pion mass. The $\mathrm{D}^{*\pm}$ and D^0 masses are [62]

$$m_{\mathrm{D}^{*\pm}} = 2010.0 \pm 0.5\,\mathrm{MeV} \qquad \text{and} \qquad m_{\mathrm{D}^0} = 1864.6 \pm 0.5\,\mathrm{MeV}\ , \qquad (2.5)$$

which implies that the kinetic energy of this decay is $Q = 5.8\,\mathrm{MeV}$. The pion carries in the D^* rest frame a momentum of only $p^*_{\pi_\mathrm{s}} = 39.6\,\mathrm{MeV}$ and is justly referred to as the 'slow pion'. In order for the D^* to be reliably detected in

---

[†] Due to the charge conjugation symmetry of the strong interaction, charge conjugation is implied in the following and everything stated for the D^{*+} meson applies to the D^{*-} analogously.

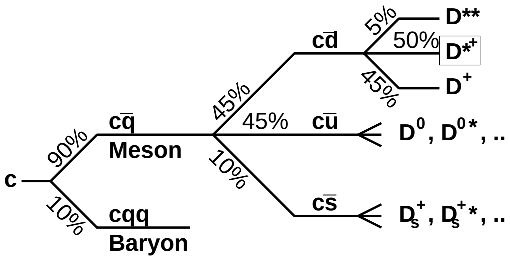

Fig. 2.7
Approximate branching ratios for the fragmentation of charm quarks into charmed baryons and mesons

the ZEUS detector, the momentum of the slow pion transverse to the beam needs to be $p_{\perp\pi_\mathrm{s}} \gtrsim 0.1\,\mathrm{GeV}$, corresponding to a D^* transverse momentum of $p_{\perp\mathrm{D}^*} \gtrsim 1.3\,\mathrm{GeV}$.† The slow pion hence not only carries the charge of the decayed D^*—also their directions of flight are strongly correlated with each other and with that of the fragmented quark.

Since the low-momentum track of the π_s can be reconstructed with better accuracy than the tracks from the D^0 decay, the $\mathrm{D}^{*\pm}$–D^0 mass difference is more precisely known than the absolute $\mathrm{D}^{*\pm}$ and D^0 mass values,

$$\Delta m \equiv m_{\mathrm{D}^{*\pm}} - m_{\mathrm{D}^0} = 145.397 \pm 0.030\,\mathrm{MeV}\,. \tag{2.6}$$

The branching fraction for this decay mode is [62]

$$\mathscr{B}(\mathrm{D}^{*+} \to \mathrm{D}^0\pi_\mathrm{s}^+) = 68.3 \pm 1.4\%\,.$$

Figure 2.7 shows the branching fractions for charm fragmentation as expected from basic symmetry arguments. About 20% of the charm quarks are expected to fragment into D^{*+} mesons; this has been confirmed by OPAL [3], measuring a value of

$$f(\mathrm{c} \to \mathrm{D}^{*+}X) = 22.2 \pm 1.4 \pm 1.4\%$$

for charm fragmentation into D^{*+} mesons. Although the expected D^{*+} production rate is about half of that for D^0 mesons (and D^0's emerge also from D^{*+} decays), the detection of D^{*+} is favoured due to the clear experimental signature provided by the presence of the characteristic slow pion.

At HERA, charmed particles are produced predominantly in jets; therefore, the particles arising from charm decays have to be recognised within a narrow

---

† This number has been estimated as follows: the D^* transverse momentum will be considered large enough if the probability for the outgoing slow pion to have $p_{\perp\pi_\mathrm{s}} \gtrsim 0.1\,\mathrm{GeV}$ is larger than 50%. This holds if $p_{\perp\mathrm{D}^*}$ is large enough to allow a slow pion to be reconstructed that emerges at a decay angle $\theta^*_{\pi_\mathrm{s}} = 90^\circ$, where $\theta^*_{\pi_\mathrm{s}}$ is the angle between the D^* direction of flight and the slow pion trajectory in the rest frame of the D^*. In this case $E_{\mathrm{D}^*}/m_{\mathrm{D}^*} = E_{\pi_\mathrm{s}}/E^*_{\pi_\mathrm{s}} = (m_{\pi_\mathrm{s}} \oplus 100\,\mathrm{MeV})/(m_{\pi_\mathrm{s}} \oplus 39.6\,\mathrm{MeV}) \approx 1.18$, yielding $p_{\mathrm{D}^*} \approx 1.27\,\mathrm{GeV}$. In the worst case of $\theta^*_{\pi_\mathrm{s}} = 180^\circ$, a D^* momentum $p_{\mathrm{D}^*} > 2.2\,\mathrm{GeV}$ is required to obtain $p_{\pi_\mathrm{s}} > 0.1\,\mathrm{GeV}$.

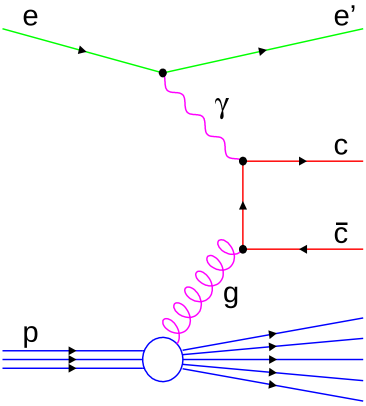

Fig. 2.8
The photon–gluon fusion process in lowest order

group of several other particles. For this reason, the lowest multiplicity decay of the D^0 into charged particles, $\mathrm{D}^0 \to \mathrm{K}^-\pi^+$,[†] has been chosen for this study. Its branching ratio [62],

$$\mathscr{B}(\mathrm{D}^0 \to \mathrm{K}^-\pi^+) = 3.85 \pm 0.09\% \ ,$$

is about half of that of the 4-prong decay $\mathrm{D}^0 \to \mathrm{K}^-\pi^+\pi^+\pi^-$, but the background from misidentification and wrong combinations is substantially lower. The total fraction of charm quarks that follow the described decay chain is

$$f(\mathrm{c} \to \mathrm{D}^{*+} \to [\mathrm{D}^0{\to}\mathrm{K}^-\pi^+]\,\pi_\mathrm{s}) = 0.584 \pm 0.055\% \ . \tag{2.7}$$

2.4 The Charm Content of the Proton

The observation of charm in the final state of neutral-current DIS raises the question of its origin. Possible sources are:

- *Flavour excitation.* One of the charm quarks of a $\mathrm{g}{\to}\mathrm{c\bar{c}}$ fluctuation (charm sea) receives a large momentum transfer, so that the pair cannot recombine; the other charm quark remains roughly collinear with the proton remnant.
- *Photon–gluon fusion (PGF)* [135]. The photon couples with a gluon of the proton via a virtual charm quark (see Fig. 2.8). This situation is kinematically much different from the flavour excitation, because the outgoing c and $\bar{\mathrm{c}}$ quarks are back-to-back in the photon–gluon rest-frame. At small x,

---

[†] Also for the D^0 charge conjugation is implied. It should be noted that electroweak *CP* violation is expected to be small in the $\mathrm{D\overline{D}}$ system. The rate of 'wrong sign' decays $\mathrm{D}^0 \to \mathrm{K}^+\pi^-$ has been measured to be $\mathscr{B}(\mathrm{D}^0 \to \mathrm{K}^+\pi^-)/\mathscr{B}(\mathrm{D}^0 \to \mathrm{K}^-\pi^+) = 0.31 \pm 0.11\%$ [112], originating predominantly from doubly Cabibbo suppressed decay modes.

PGF is expected to dominate the charm production due to the large gluon content in the proton.

- *Diffractive charm production* [55]. The photon fluctuates into a $c\bar{c}$ pair. One of the charm quarks scatters diffractively off the proton via multi-gluon exchange.
- *Fragmentation* [173]. Here charm quarks are not directly involved in the hard scattering process, but emerge from gluon splitting in the parton shower. At LEP the average number of gluons per hadronic Z^0 decay that split to $c\bar{c}$ was found to be about 2.3% [8]. Since the typical jet energies are much lower at HERA than at LEP (except for the proton remnant), the suppression of charm production in fragmentation by the large mass of the charm quark can be expected to be even stronger.
- *Intrinsic charm* [51]. It has been suggested [50] that at very large values of x ($x \gtrsim 0.1$) charm production at HERA is dominated by an intrinsic component, that is, by a certain probability of the proton to be in a Fock state that contains a $c\bar{c}$ pair, $|\mathrm{p}\rangle = \alpha\,|\mathrm{uud}\rangle + \beta\,|\mathrm{uudc\bar{c}}\rangle + \cdots$. Intrinsic charm would be emitted in DIS in the very forward, proton-beam direction and may be observable in the ZEUS forward plug calorimeter [204], which has been installed recently.
- *Beauty decays.* Charm quarks can also result from the decay of b quarks. At the Q^2 values of this analysis, beauty production is estimated to be suppressed due to the large b mass by a factor of ~ 50 relative to the cross-section for charm production [76]. Observation of open beauty production at HERA was recently reported [113, 200].

Since the charm quark mass[†] is larger than the proton mass, the treatment of c quarks as partons inside the proton is not straightforward.[‡] Considering that the spatial resolution of the virtual photon is given by $\sqrt{1/Q^2}$, the scale at which charm production should become visible is $Q^2 \gtrsim 4m_c^2$. Their production is kinematically allowed as soon as the centre-of-mass energy $\hat{s}$ of the photon–gluon system in the PGF process reaches $2m_c$. In the *fixed flavour number* (FFN) scheme charm is treated like the production of other massive particles, that is, it appears only as a part of the final state and is not part of the DGLAP evolution ($n_f = 3$). For $Q^2 \gg m_c^2$ however, terms $\mathcal{O}(m_c^2/Q^2)$ become small and charm could be treated as any other flavour in the DGLAP

[†] The charm quark mass m_c is not exactly known—not even unambiguously defined. Its value depends on the scheme used for extracting it from the observed charmonium and D meson masses. In the $\overline{\mathrm{MS}}$ scheme, m_c is a scale-dependent 'running' mass with a value of $\bar{m}_c(m_c) \approx 1.1$–$1.4\,\mathrm{GeV}$ [62]. This corresponds to a mass value of $m_{\mathrm{Pc}} \approx 1.2$–$1.9\,\mathrm{GeV}$ at the pole of the charm quark propagator. For free particles, the pole mass equals the observable mass.

[‡] Conventionally, partons are assumed to have *zero* mass.

formalism. In the *variable flavour number* (VFN) scheme the number of active quark flavours is $n_\mathrm{f} = 3$ below a threshold of $Q^2 < \mu_0^2$; for larger Q^2, charm is included as an active flavour (usually as a massless parton). If the perturbation series were calculable to all orders, both schemes would be equivalent. In practice the calculation can only be carried out for a few leading terms (LO or NLO), imposing scale dependencies on the results.

While the hard scattering process is described in terms of quasi-free partons, the final state particles observed in the detector are hadrons (or leptons from hadron decays). The formation of hadrons from partons cannot be calculated perturbatively, but must be described by phenomenological models. The process is called *fragmentation,* since an outgoing hadron h carries only a fraction of the parton momentum k.† The probability density for h to have a share $z \equiv p_h/k$ of the initial parton momentum can be described by fragmentation distribution functions $D_h(z)$, which are constrained by the momentum sum rule

$$\sum_h \int_0^1 \mathrm{d}z \; z D_h(z) = 1 \; .$$

An outgoing quark is likely to form a meson if there is an antiquark with a similar velocity. Pulling a light quark with similar velocity from the vacuum costs only a small fraction of the heavy quark's energy; accordingly for low momenta ($p_\perp^2 \sim m_\mathrm{c}^2$), the fragmentation of the heavy quark is expected to be hard, meaning that the momentum of the final state charm meson is close to that of the initially outgoing heavy quark. This feature is expressed by the function of Peterson *et al.* [159],

$$D(z) = \frac{N}{z\,\left[1 - 1/z - \varepsilon_\mathrm{P}/(1-z)\right]^2} \; ,$$

where N serves for the normalisation and ε_P is the momentum hardness parameter, whose value depends on the heavy quark mass, the meson species (esp. its spin), the production process and the energy range (owing to radiative corrections). Leaving ε_P and the normalisation as free parameters, the measured scaled momentum distributions at low energies can be well described by this functional form (see Figure 2.9). At larger momentum ($p_\perp^2 \gg m_\mathrm{c}^2$), the heavy quark can radiate a substantial amount of its energy before dressing up as a meson; here the fragmentation is described more adequately by a convolution of the nonperturbative function with a perturbative evolution. It depends on the factorisation scheme, to what extent the gluon radiation is accounted for by perturbative calculations or assigned to the nonperturbative

---

† The last, highly nonperturbative phase of the fragmentation process, in which a parton transforms into a hadron, is called *hadronisation.* Sometimes this term also is used as a synonym for *fragmentation*, which includes the parton cascade evolving between the hard process and the hadronisation.

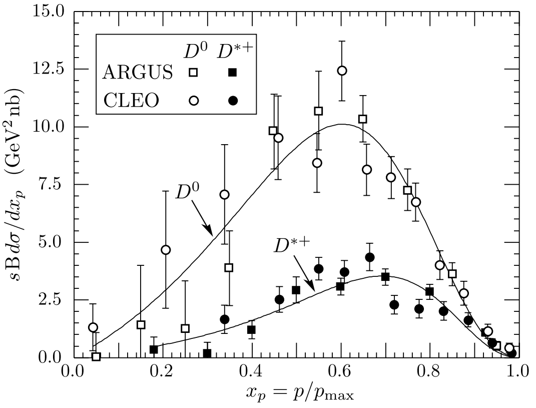

Fig. 2.9
Charm fragmentation in e^+e^- scattering [62]. The cross-sections for the production of D^0 and D^{*+} mesons at $\sqrt{s} \approx 10\,\mathrm{GeV}$ are shown as functions of the scaled momentum. Fits of the Peterson functional form to these distributions (overlayed curves) yield hardness parameter values of $\varepsilon_\mathrm{P}(D^0) = 0.135 \pm 0.01$ and $\varepsilon_\mathrm{P}(D^{*+}) = 0.078 \pm 0.008$.

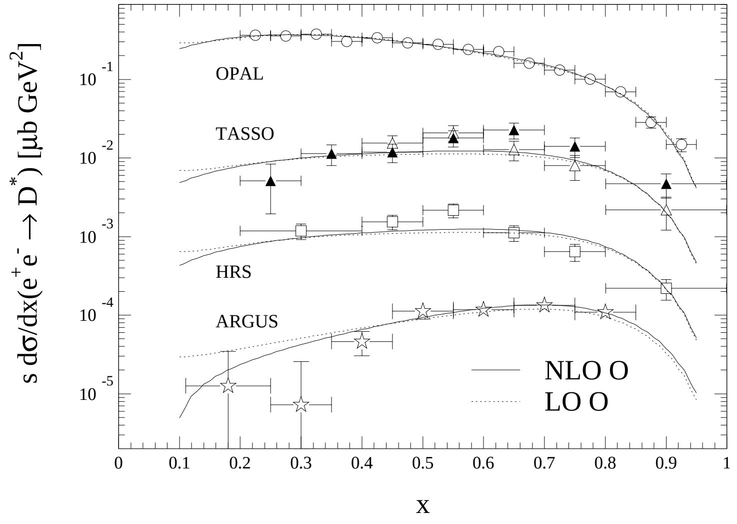

Fig. 2.10 Measured distributions of the $D^{*\pm}$ scaled momentum in e^+e^- annihilation at centre-of-mass energies $\sqrt{s} = 91.2\,\mathrm{GeV}$ (OPAL), $34.2\,\mathrm{GeV}$ (TASSO), $29\,\mathrm{GeV}$ (HRS) and $10.5\,\mathrm{GeV}$ (ARGUS), compared with LO and NLO calculations based on fits to the OPAL data [30]. For separation, the data have been scaled by powers of 10.

contribution of the Peterson function; therefore also ε_P is scheme dependent and must be determined from fits to the experimental data. Figure 2.10 shows a comparison of LO and NLO calculations by Binnewies *et al.* [30] with data from e^+e^- annihilation at various centre-of-mass energies. For all energies the nonperturbative part is determined by the same set of $(N, \varepsilon_\mathrm{P})$. The fragmentation becomes softer as one goes to higher energies; the change in shape is reproduced by the perturbative evolution.

The correct choice of the ε_P value to be used for theoretical calculations of cross-sections at HERA is not obvious. Fits of the type performed for e^+e^- data have not been done for HERA yet. It is difficult to compare HERA data with e^+e^- annihilation, because at HERA the energy scale $\sqrt{s_{c\bar{c}}}$

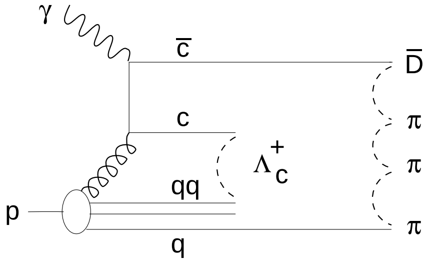

Fig. 2.11
Example for the hadronisation through string fragmentation near the charm production threshold

(i.e., the effective mass of the $c\bar{c}$ system) is not fixed and the momentum scale z cannot be defined in the same way as at LEP.† For the calculations done in the framework of this analysis, a value of $\varepsilon_{\mathrm{P}} = 0.035$ was used. This value was obtained by the OPAL collaboration from fits of their experimental data [7] to a convolution of JETSET parton showers [177] with the Peterson formalism. Recently Nason and Oleari [154] fitted a convolution of an NLO calculation with the Peterson fragmentation function (a convolution quite similar to the one used in this analysis [118]) and obtained for OPAL data a slightly softer value of $\varepsilon_{\mathrm{P}} = 0.041$, whereas for the ARGUS data, which lie at a value of $\sqrt{s_{c\bar{c}}}$ closer to the range at HERA, the fit resulted in $\varepsilon_{\mathrm{P}} = 0.036$.‡

It is still unclear to what extent colour drag effects towards the proton remnant affect charm fragmentation at HERA. The $c\bar{c}$ pair produced in PGF carries the colour of the incoming gluon, so that the charm quarks cannot fragment in isolation, but must have some colour exchange with other partons of the proton. In the extreme case of production near threshold ($W \sim 4\,\mathrm{GeV}$), the only possibility to produce open charm is to combine the charm quarks with the valence quarks of the proton, leading to $\gamma^* p \rightarrow \Lambda_c^+ \overline{D}^0$. The Lund string fragmentation model [177] allows for this situation by spanning colour singlet *strings* (colour flux tubes) between the c and the c̄ quarks and the partons (or diquarks) in the proton, and letting the strings independently form (decay into) hadrons, as illustrated in Fig. 2.11. The preference for c versus c̄ quarks in the formation of charmed baryons is strongly reduced as soon as the quark sea of the proton becomes kinematically accessible; however, it still could lead to an observable D^{*+}–D^{*-} asymmetry (anticorrelated to the Λ_c^+–Λ_c^- asymmetry). Such an asymmetry was measured in fixed-target photoproduction at FermiLab [16, 98], where the ratios $R \equiv N_{D^{*-}}/N_{D^{*+}} = 1.15 \pm 0.07$ at $\langle W \rangle \approx 15\,\mathrm{GeV}$ and $R = 1.13 \pm 0.03$ at $\langle W \rangle \approx 20\,\mathrm{GeV}$ were obtained in the channel $D^{*+} \rightarrow (D^0 \rightarrow K^0 \pi^+)\,\pi^+$. The Lund model describes the asymmetry only qualitatively, not quantitatively [98], so that currently no conclusion can be drawn as to how large an asymmetry should be expected at HERA.

---

† For a thorough discussion of these issues see Ref. 187.

‡ This value of ε_{P} does not conflict with the value given in Fig. 2.9, which resulted from the fit of plain Peterson fragmentation, which has not been convoluted with perturbative calculations.

3 HERA and ZEUS

3.1 The Hadron-Electron Ring Accelerator

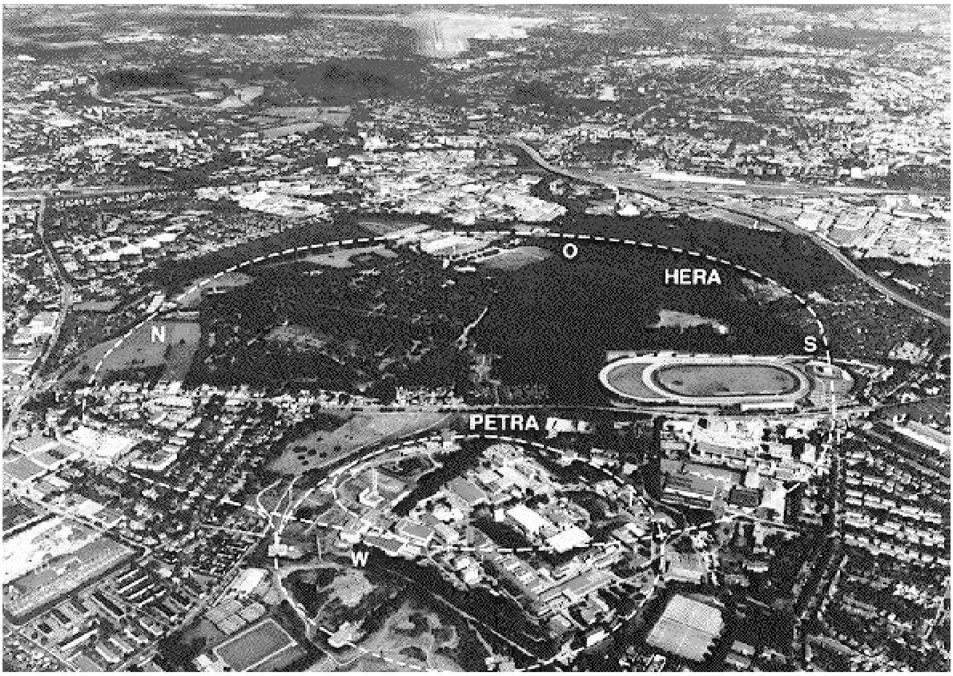

Fig. 3.1 View of DESY from an aeroplane approaching Hamburg airport from the west [85]. The location of the HERA and PETRA storage rings is indicated by the dashed outlines. While most of the other DESY buildings are encircled by the PETRA ring, the HERA south hall with the ZEUS detector is situated off the DESY main ground at the place marked with S, right beside the trotting course.

The HERA facility [60] is the world's first electron–proton storage ring. It was built at the Deutsches Elektronen-Synchrotron (DESY, see Fig. 3.1) in Hamburg during the years 1984–91. In May 1992 data taking was started.

Figure 3.2 shows the layout of HERA and its pre-accelerator system. Protons and electrons are stored in separate rings of 6.3 km circumference located twenty to forty metres under ground level. The proton and electron (or positron) bunches are accelerated to 820 GeV and 27.5 GeV, respectively, and circulate in opposite directions. Since a magnetic field of 4.68 T is needed to keep the protons on their orbit, the proton ring is equipped with superconducting dipole magnets (see Fig. 3.3). Their development and fabrication

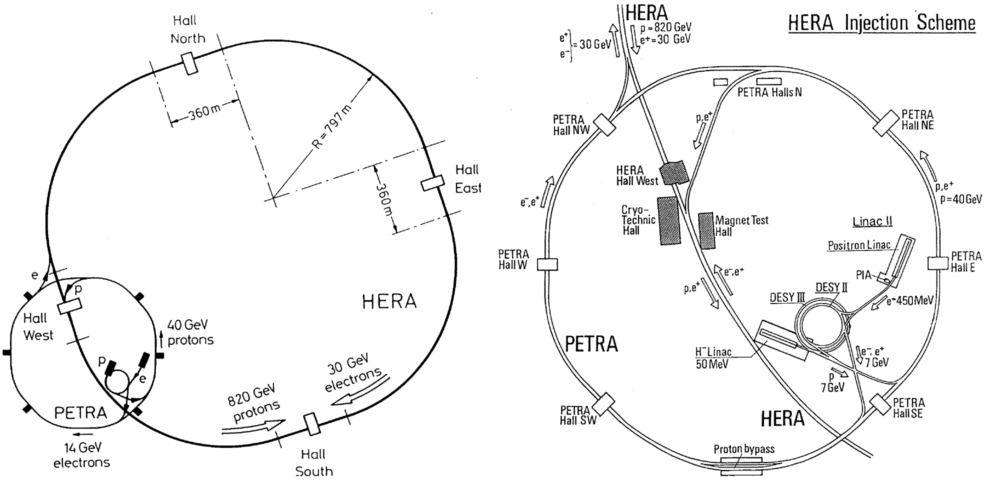

Fig. 3.2 HERA and its pre-accelerator system [195, 196]

posed one of the major technical challenges of the HERA project. For the electron ring conventional magnets producing a field of 0.15 T are used.

Electrons are produced directly by an electron gun, whereas positrons are obtained from interactions of electron bremsstrahlung in a tungsten target leading to e^+e^- pair production. After magnetic filtering and acceleration to 450 MeV in the linear accelerator LINAC II, the positrons (electrons) are stored in the positron intensity accumulator (PIA), which compresses the beam to bunches compatible with the time structure in HERA. When a current of $I \approx 60\,\mathrm{mA}$ (1995: 30 mA) is accumulated, a bunch is injected into the DESY II synchrotron and accelerated to 7.5 GeV. The bunches are transferred to the PETRA storage ring and from there injected at 12 GeV into HERA, where they are accelerated to their final energy of 27.5 GeV.

Protons are produced from H^- ions, which are accelerated to 50 MeV in a LINAC. The H^- ions strip off their electrons when they pass a thin foil after entering the DESY III storage ring. Eleven bunches with a spacing of 96 ns suited for HERA are accelerated to 7.5 GeV. In the PETRA storage ring 70 bunches are accumulated, accelerated to 40 GeV and transferred to HERA, where they are accelerated to their final energy of 820 GeV. HERA can be filled with up to 210 bunches each of electrons and protons; in normal running however, a fraction of the 210 positions are reserved for unpaired bunches, where either the electron or proton position is left empty in order to permit background studies. The clockwise circulating electrons are brought to collision with the anticlockwise revolving protons at zero crossing angle in the north and south halls of the ring, where the experiments H1 [2] and ZEUS are installed.

As the electrons revolve in the field of the bending magnets, the electron beam becomes transversally polarised by virtue of the Sokolov–Ternov effect [179], a small asymmetry in the electron spin flip amplitude between up

Fig. 3.3 View of the HERA tunnel [84]. The superconducting magnets of the proton storage ring are mounted above the conventional magnets of the electron ring.

and down polarisation. Near the interaction point of the HERMES experiment [123] located in the east hall, spin rotators are installed, which turn the transverse polarisation into longitudinal polarisation. Here the scattering of longitudinally polarised electrons off a polarised gas jet target is studied. Hydrogen, deuterium and helium-3 are used in turn as the target; in this way the spin-dependent structure functions of protons and neutrons, and thereby the origin of the nucleon spin, can be investigated. In the fourth experimental area, the HERA-B experiment [170] is being constructed, which will study *CP* violation in the $\mathrm{B}\overline{\mathrm{B}}$ system. The B mesons will be produced in interactions of protons with a tungsten wire target, which is put into the halo of the proton beam.

Since the summer of 1994 HERA is operated with positrons instead of electrons, because the electron beam lifetime was limited to typically 2–3 hours at a maximum current of 25 mA. This limit is presumably due to electron capture by positive ions escaping from the getter pumps which are integrated in the dipole magnets of the electron ring [83].† With positrons, higher currents and larger lifetimes of typically 8 hours can be achieved. While the neutral current cross section for not-too-large Q^2 is hardly affected by this change, the charged current cross section drops by a large factor (~ 10 at $Q^2 \sim 10^4\,\mathrm{GeV}^2$),

---

† In preparation for the 1998 data taking, where electrons instead of positrons were used, the titanium ion getter pumps were replaced by non-evaporable getter (NEG) pumps.

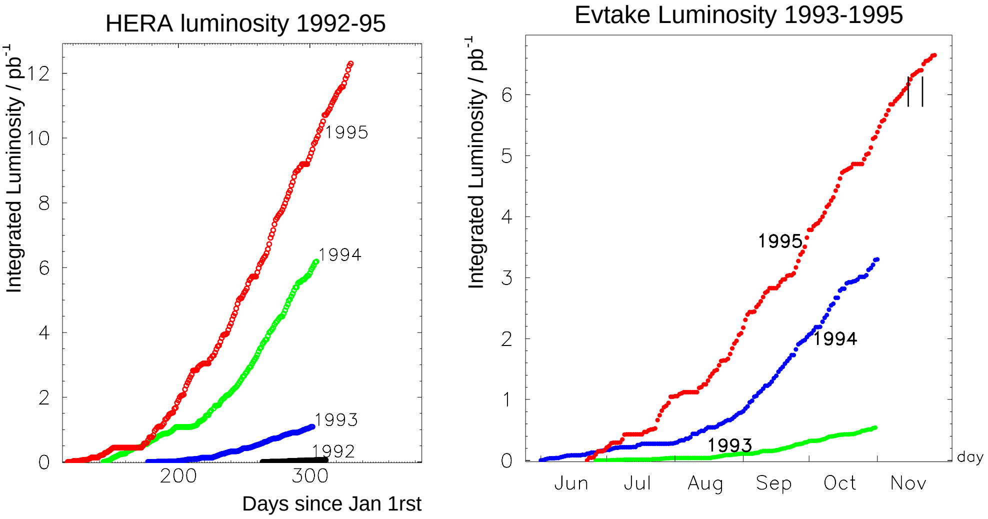

Fig. 3.4 Integrated luminosities of the HERA ring in 1992–95 and the luminosity accepted by the ZEUS detector after requiring good detector efficiency and off-line quality of the data [169]. The parallel vertical lines in the upper right corner of the right diagram mark the periods where the z position of the nominal vertex was shifted.

Table 3.1 HERA beam parameters of 1995 in comparison with the design values

HERA parameter	Unit	Design value		1995 value	
		e beam	p beam	e beam	p beam
Injection energy	GeV	14	40	12	40
Beam energy	GeV	30	820	27.5	820
Centre of mass energy	GeV	314		300	
Filling time	min	15	20	45	60
Maximum current	mA	58	160	30	55
Number of bunches		210	210	184	178
Horizontal beam size (rms)	mm	0.301	0.276	0.239	0.185
Vertical beam size (rms)	mm	0.067	0.087	0.055	0.058
Longitud. beam size (rms)	mm	8.0	110	8.0	110
Int. luminosity	$\mathrm{pb}^{-1}\,\mathrm{y}^{-1}$	35		12.5	

because the electroweak current couples to different quark flavours and the $x\mathscr{F}_3$ term in (2.1) changes its sign when using positrons instead of electrons. It is planned to run HERA in future alternatively with polarised electron and positron beams in order to achieve a precise measurement of the electroweak couplings of light quarks [61].

As shown in Fig. 3.4, the integrated luminosity of HERA has strongly increased since the start-up in 1992. Table 3.1 compares the values of the 1995 beam parameters with the design values. In 1997, integrated luminosities of up to $\int \mathrm{d}t\,\mathscr{L} \sim 1\,\mathrm{pb}^{-1}$ per week were achieved and the peak luminosity value was close to the design luminosity. An upgrade of the storage ring and the detectors is foreseen for the shutdown in 1999/2000 [171]. It is expected to increase the luminosity by a factor of 3–5. The consequences for the physics programme are discussed in Ref. 128.

3.2 The General Purpose Detector ZEUS

The ZEUS detector [126] has a size of 12 m × 11 m × 20 m and weighs 3600 t. It is built and operated by a collaboration of more than 450 physicists from 51 physics institutes in 12 different countries. The stage-one assembly, shown in Fig. 3.5, was completed in 1991. Since then the detector underwent several modifications and extensions. Figure 3.6 gives an overview of the main components of the ZEUS detector.† Those of the more than twenty components which are important for this analysis are discussed below in more detail.

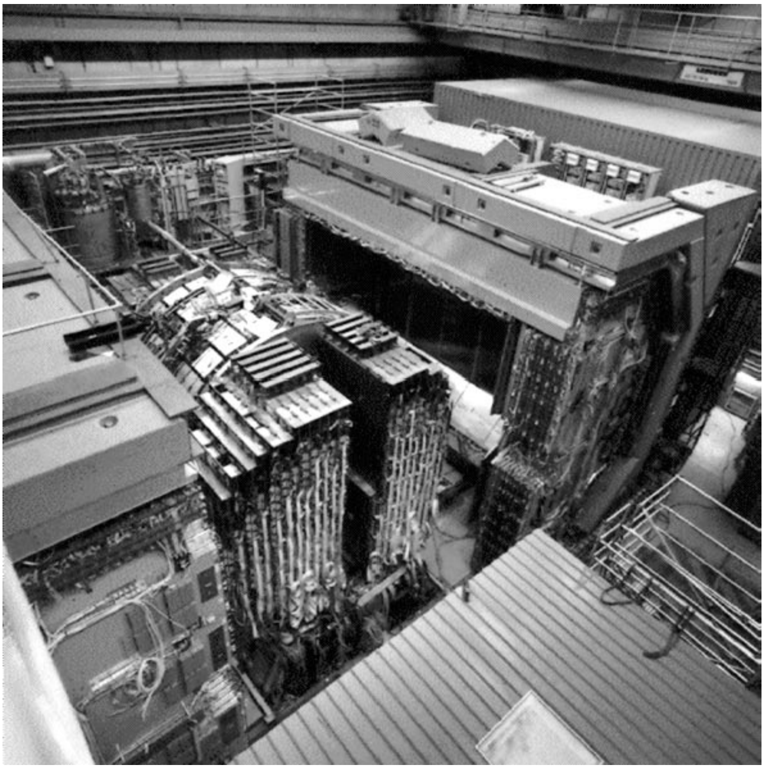

Fig. 3.5 Stage-one assembly of the ZEUS detector [126]. The open yoke permits a view on the modules of the uranium–scintillator calorimeter (CAL).

---

† Not shown in Fig. 3.6 is the *rucksack,* a three-storey container building parallel to the the detector (hidden behind it in the upper right corner of Fig. 3.5). Here the read-out and trigger electronics is accommodated in 126 water cooled racks, linked by a local area network with the control room and the data storage.

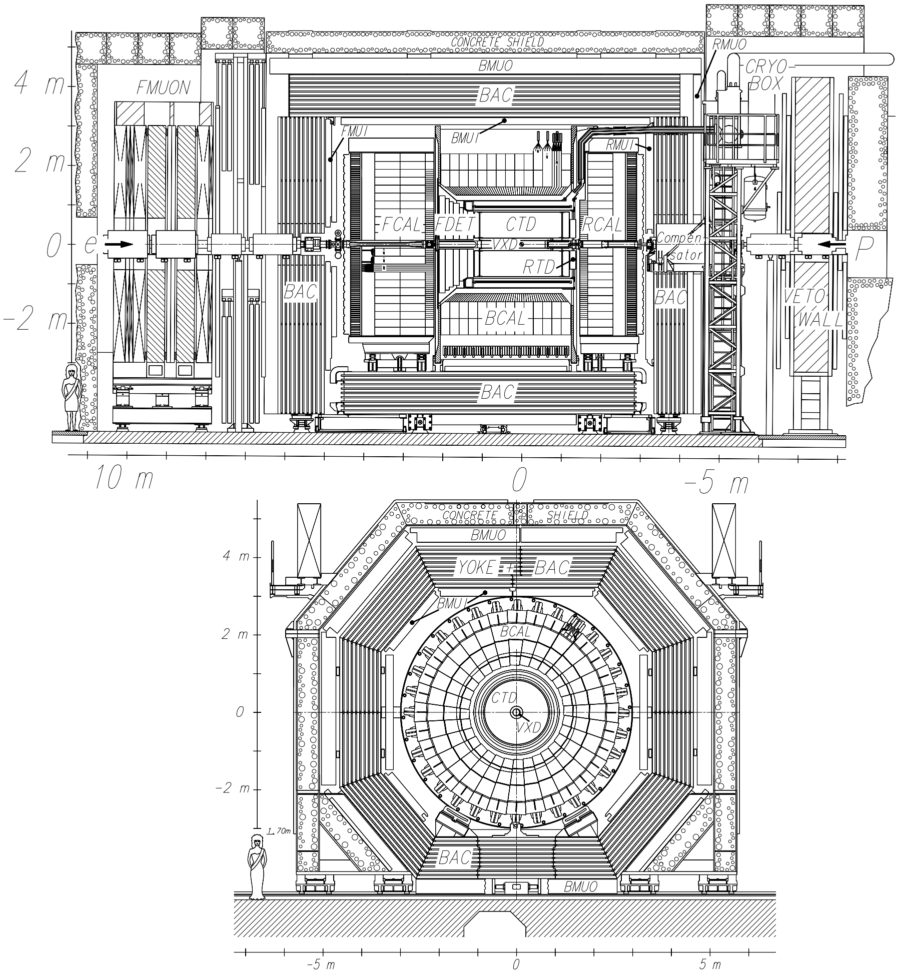

Fig. 3.6 Longitudinal (top) and transverse (bottom) cut through the ZEUS detector. The electron beam enters the detector from the left (top figure), the proton beam from the right, determining the positive-z or *forward* direction. The forward–backward asymmetry of the detector layout reflects the asymmetry of the electron and proton beam energies. The nominal interaction point is surrounded by the inner detector, which consists of the central tracking detector (*CTD*) and the forward and rear tracking devices (*FDET, RTD*). The inner detector is enclosed by a superconducting solenoid providing a magnetic field of 1.43 T. Outside the coil, the uranium–scintillator calorimeter is situated, which is divided into three segments (*F/B/RCAL*), enclosed by an iron yoke with an embedded backing calorimeter (*BAC*). Inner and outer muon detectors (*F/B/RMUI, B/RMUO*) are attached to the yoke and form the outermost layer of the active detector. In the forward direction a separate toroidal muon tracking system is installed (*FMUON*). The small angle rear tracking detector SRTD, the rear presampler RSAM, and the hadron-electron separator HES are not shown in this picture; they are mounted on the RCAL front face. The C5 beam monitor is installed in a collimator directly behind the RCAL. The *VETO WALL*, which consists of iron plated with scintillator, is placed 3 m behind the RCAL in electron beam direction.

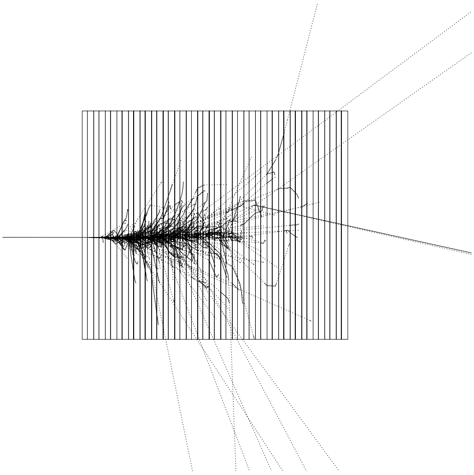

Fig. 3.7
GEANT simulation of the impact of an electron in the electromagnetic calorimeter. Dashed lines indicate the trajectories of all particles; the electron comes from the left with an energy of 26 GeV.

The ZEUS coordinate system [102, 124] is a right-handed orthogonal system. Its origin is situated in the nominal interaction point, with the z axis pointing in the direction of the proton beam; the y axis points vertically upward† and the x axis to the centre of the HERA ring.

3.2.1 The Uranium–Scintillator Calorimeter (CAL)

Calorimeters in particle physics measure the energy of particles by their absorption in a medium that becomes ionised or excited in shower processes. The ZEUS calorimeter [14, 58, 79] has been designed as a *sampling* calorimeter (Fig. 3.7), where absorber layers alternate with scintillator layers, which are optically read out. Such a device is especially suited for the measurement of high energetic particles: roughly speaking, every secondary process halves the energies of the particles in the shower; therefore the material depth needed to fully absorb the particle shower rises only logarithmically with the energy; furthermore, the fractional resolution of the measurement improves with rising energy as $\sigma_E/E \propto 1\big/\sqrt{E}$, owing to the statistical nature of the measurement.

Uranium is an advantageous absorber for hadron calorimetry, since it provides a high yield of spallation neutrons. These impart their energy to the hydrogen nuclei of the scintillator. Together with an additional contribution of photons from neutron capture in the uranium, this helps compensating the signal loss that hadrons suffer from the loss of binding energy, nuclear fission fragments and from undetected decay products (neutrinos and minimum ionising muons). Electrons and photons do not suffer such losses as they interact predominantly with the atomic electrons and not with the nuclei.

In the ZEUS calorimeter, depleted uranium‡ plates of 3.3 mm thickness,

---

† As HERA has been constructed with a slight tilt of the ring plane for easier tunneling, the proton beam is inclined by roughly 6 mrad; therefore the z and y axes are inclined by the same amount.

‡ DU, containing less than 0.2% ^{235}U.

Table 3.2 CAL segments and the angular ranges covered by them. The polar angle θ is given with respect to the proton beam direction and is related to the pseudorapidity by $\eta \equiv -\ln\tan(\theta/2)$.

Segment	Polar angle	Pseudorapidity
FCAL, forward calorimeter	$2.2^\circ < \theta < 39.9^\circ$	$4.0 > \eta > 1.0$
BCAL, barrel calorimeter	$36.7^\circ < \theta < 129.1^\circ$	$1.1 > \eta > -0.7$
RCAL, rear calorimeter	$128.1^\circ < \theta < 176.5^\circ$	$-0.7 > \eta > -3.5$

encased in a thin stainless steel sheet (0.2/0.4 mm), serve as the absorber, while SCSN-38 polystyrene scintillator layers of 2.6 mm thickness are used for particle detection. For a signal integration time of 100 ns this configuration provides equal signals for hadrons and electromagnetic particles (e, γ) of the same initial energy ('compensating calorimeter'). Indeed, test beam measurements have verified that the signal heights for hadrons and electrons agree within 3% for momenta greater than 2 GeV. The permanent irradiation of the calorimeter by particles from nuclear decays of the uranium plates is detected and used for keeping the detector calibration stable within 1%.

The energy resolution for electrons and hadrons was measured in the test beam to be

$$\frac{\sigma_{\mathrm{e}}(E)}{E} \approx \frac{18\%}{\sqrt{E}} \quad \text{and} \quad \frac{\sigma_{\mathrm{h}}(E)}{E} \approx \frac{35\%}{\sqrt{E}},$$

respectively, where E is measured in GeV. For energies between 15 GeV and 110 GeV the calorimeter response to electrons is linear within 1–2%. Very energetic hadrons do not deposit all their energy within the CAL volume; for this reason, the surrounding iron yoke is instrumented with a backing calorimeter in order to capture leaking particle showers.

The CAL is divided into three independent segments (see Table 3.2), which together cover 99.7% of 4π solid angle around the nominal interaction point. While the forward and rear calorimeters (FCAL and RCAL) have the shape of planar discs, the BCAL encloses the inner detector cylindrically. The three calorimeter segments are divided into 80 modules, the largest of which is shown in Fig. 3.8.

The FCAL modules consist of 185 absorber and 185 scintillator layers, which are transversely segmented to form calorimeter *towers*. The total depth of an FCAL tower is 7 nuclear absorption lengths (7λ). The towers are longitudinally divided into three sections, the electromagnetic and hadronic calorimeters (EMC, HAC 1 and HAC 2), which are read out independently. Electromagnetic particles deposit most or all of their energy in the front section (EMC), which has a thickness of 26 radiation lengths (X_0) and is transversally segmented into cells of 5 cm × 20 cm. For energetic hadrons the particle shower extends beyond the EMC into the HAC sections, which are 85 X_0 deep each.

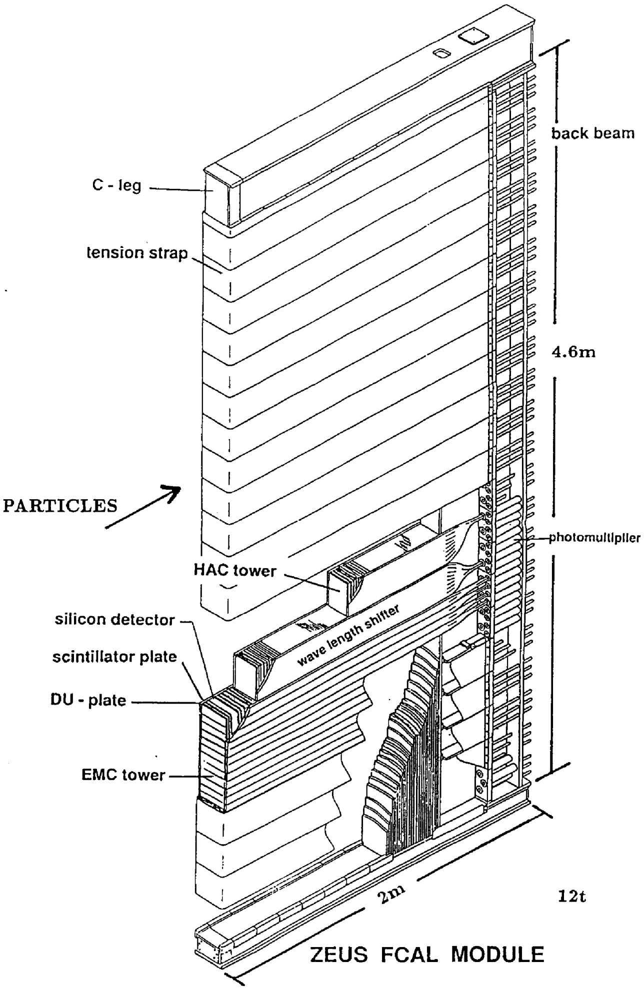

Fig. 3.8
Cut-away view of a large FCAL module [126]

The HAC cells are 20 cm × 20 cm wide. Wave length shifters guide the light generated in the scintillator plates to photomultiplier tubes (PMTs) on either side of the towers for measuring the pulse height and arrival time. For energy deposits of more than 4 GeV the resolution of the arrival time measurement is better than 1 ns.

The RCAL modules have no HAC 2 towers, because the hadron energies in the backward direction are kinematically limited to the value of the electron beam energy. The rear EMC is less fine segmented than in the FCAL and has a cell size of 10 cm × 20 cm; however there are additional tracking devices (RSAM, SRTD, HES) attached to the RCAL, which permit a substantial enhancement of the identification and location of the scattered electron in this calorimeter section.

The BCAL consists of 32 wedge-shaped modules, which are tilted by 2.5° in ϕ. Its EMC and HAC 1+2 sections are only $23\,X_0$ and $52\,X_0$ deep, respectively, amounting to a total of $5\,\lambda$. The front face dimensions of the EMC

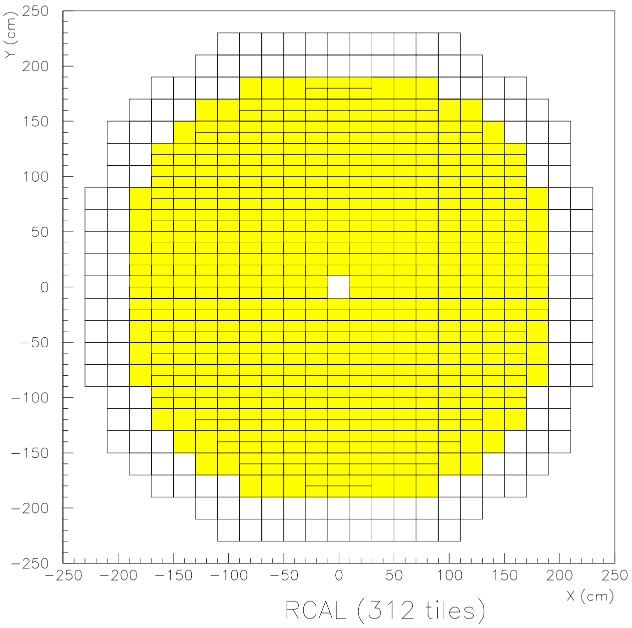

Fig. 3.9
Front view of the RCAL [20]. The shaded area marks the coverage of the presampler.

towers are 4.9 cm × 23.3 cm. One HAC tower covers four EMC towers, except for the front (rear) ring, where only two (three) EMC towers are covered by one HAC tower.

The Presamplers. Scintillator tiles mounted in front of the CAL modules serve as presamplers. They are read out with wavelength-shifting fibres. In 1995 FCAL and RCAL were equipped with presamplers, FSAM and RSAM [20]; the latter was used for this analysis. The scintillator tiles cover a large fraction of the RCAL surface and match its HAC segmentation of 20 cm × 20 cm (see Fig. 3.9). The purpose of this supplementary detector is to measure on an event-by-event basis the energy loss of particles reaching the calorimeter, which is primarily caused by preshowering in the material between the interaction point and the calorimeter front face. It can be regarded as an extra scintillator layer of the sampling calorimeter, made of the same polystyrene that was used for the CAL.

The Small Angle Rear Tracking Detector. A component for precise impact position measurement of the scattered electron and for energy correction in the rear direction is the SRTD [21], which was installed in 1994, covering the small angle region between the rear tracking detector (RTD) and the beampipe (see Fig. 3.10). It consists of polystyrene scintillator strips (5 mm × 9.8 mm × 240/440 mm), arranged in two planes of four 24 cm × 44 cm quadrants each, as shown in Fig. 3.11. The SRTD provides a measurement of the scattered lepton position with a resolution of 3 mm; furthermore, its timing information is used by the first level trigger for rejecting upstream proton beam–gas interactions.

3.2.2 The Central Tracking Detector (CTD)

The tracking system of the ZEUS detector consists of the forward, central and rear tracking devices.[†] They are placed within the magnetic field provided by a superconducting coil ($B = 1.43\,\mathrm{T}$), which is indirectly cooled by liquid helium and situated between CAL and CTD. The magnetic flux is returned through the iron structures of the calorimeter and through the iron yoke; a

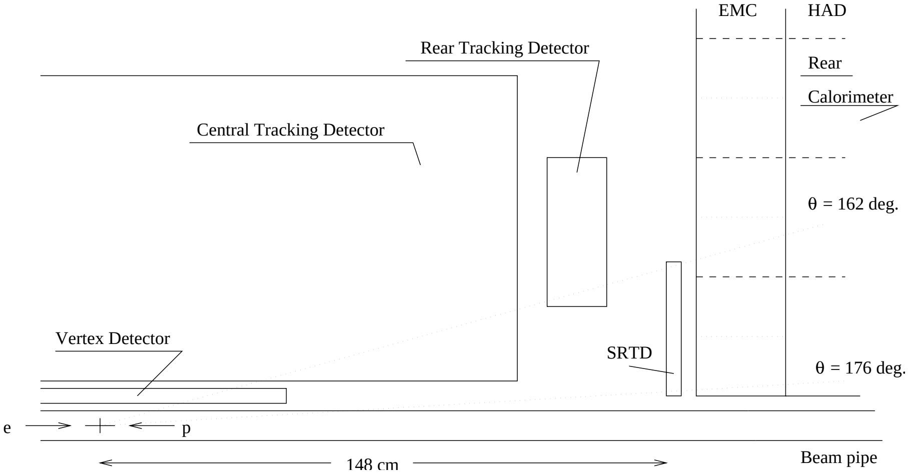

Fig. 3.10 View of the ZEUS detector near the rear beampipe [21] (not to scale!)

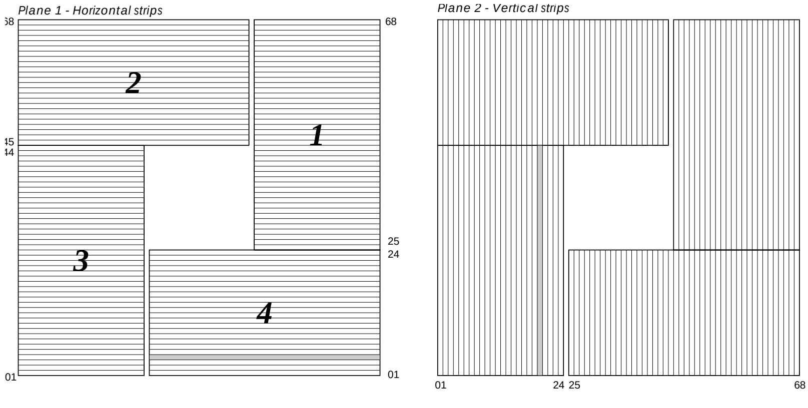

Fig. 3.11 Orientation and numbering scheme of the strips of the two SRTD planes [21]. The strip raster is 0.98 cm × 24/28 cm. In 1995 the RCAL modules above and below the beampipe hole have been moved closer together; the SRTD quadrants have been moved accordingly, so that quadrants 2 and 4 are only separated by 8 cm.

[†] The vertex detector (VXD), which was partly inoperational in 1995 due to radiation damage and high-voltage problems, was removed at the end of the 1995 run. It was not used in this analysis.

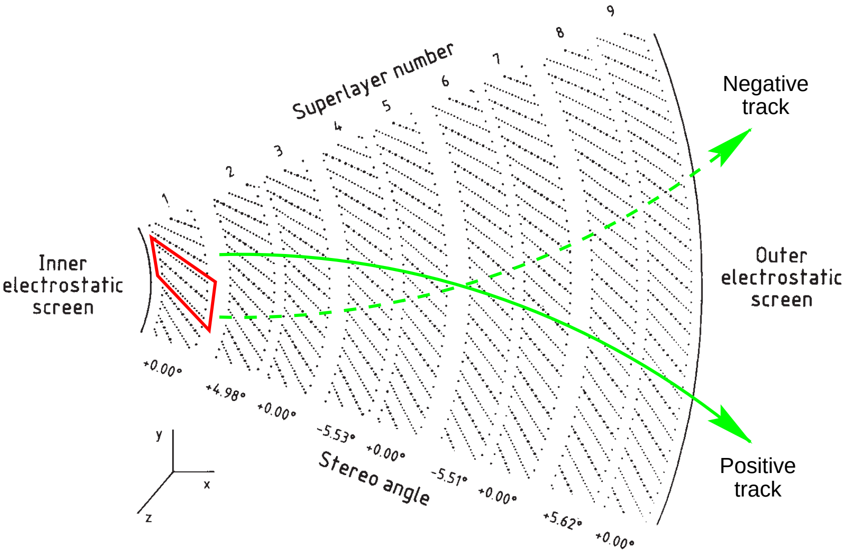

Fig. 3.12 Wire positions of an octant of the CTD at the forward endplate. The larger dots mark the sense wires. A group of 8 sense wires plus associated field-shaping wires and drift-region define a *cell,* as indicated in superlayer 1. At the opposite endplate, the even-numbered stereo layers are azimuthally displaced by approximately four cell widths (see also Fig. 4.4). The arrows indicate how the magnetic field bends the trajectories of positive and negative. Adapted from [96].

Table 3.3 Axial superlayers of the CTD. The angular ranges covered by each superlayer refer to the cell centres; since the active volume extends from $z = -99$ cm to $z = 102$ cm, the angular coverage is slightly asymmetric. The minimum transverse momentum needed to reach the centre of the superlayer in a magnetic field of 1.43 T is also given.

№	# cells	Polar angle	Pseudorapidity	$p_{\perp\text{min}}$/ MeV
1	32	$11.6° < \theta < 168.0°$	$2.31 > \eta >$ -2.26	40
3	48	$18.9° < \theta < 160.5°$	$1.79 > \eta >$ -1.76	75
5	64	$25.5° < \theta < 153.8°$	$1.48 > \eta >$ -1.46	105
7	80	$31.6° < \theta < 147.6°$	$1.26 > \eta >$ -1.24	135
9	96	$37.9° < \theta < 142.3°$	$1.10 > \eta >$ -1.07	165

high-field solenoid ($B = 5$ T) situated behind the RCAL compensates the effect of the main solenoid on the electron beam.

The principal component used for this analysis is the central tracking device (CTD) [53, 96], a cylindrical wire drift chamber with an overall length of 240 cm and an outer radius of 85 cm. The active volume has a length of 203 cm with inner and outer radii of 19 cm and 78.5 cm, respectively.

It contains 72 concentric sense wire layers, arranged in 9 *superlayers* (see Fig. 3.12 and Table 3.3). Each superlayer is divided azimuthally into *cells* of 8 sense wires. The number of cells increases from 32 in superlayer 1 to 96 in superlayer 9. The total number of sense wires is 4608. The sense wires are read out and digitised every 9.6 ns by flash analogue to digital converters (FADCs) with a resolution of 8 bits. The position resolution achieved in (r, ϕ) is 190 µm. The wires of the odd-numbered superlayers are stretched parallel to the beam axis, whereas the even-numbered superlayers are tilted by stereo angles of $\alpha \approx \pm 5°$. With this configuration the z-position of a track can be reconstructed with an accuracy of approx. 2 mm. All wires of superlayer 1 and half the wires of superlayers 3 and 5 are additionally instrumented with a z-by-timing system—used primarily for trigger purposes—in which both ends of the wires are read out and the z position is calculated from the difference in the arrival times of the pulses at the two ends. This system achieves a z resolution of 4.4 cm [19]. For vertex-refitted tracks, the resolution in transverse momentum is [115] ($p_\perp$ in GeV)

$$\frac{\sigma_{p_\perp}}{p_\perp} = 0.0058 p_\perp \oplus 0.0065 \oplus 0.0014/p_\perp \,, \tag{3.1}$$

where the first term corresponds to the resolution of the hit positions, the second term to smearing from multiple scattering *within* the CTD and the last term to multiple scattering *before* the CTD.

Figure 3.13 shows the layout of a CTD cell: eight sense wires, made of gold-plated tungsten, alternate with 9 wires at ground potential in order to make gain and drift field adjustment independent of each other; the boundaries between neighbouring cells are defined by the field planes of 19 wires, two of which at either end are at maximum negative potential; 4 shaper wires along the radial boundary, together with the guard wires at the ends of the sense wire chain, ensure the uniformity of the drift field, making the drift velocity of approximately 50 µm/ns constant throughout the cell volume. The magnetic

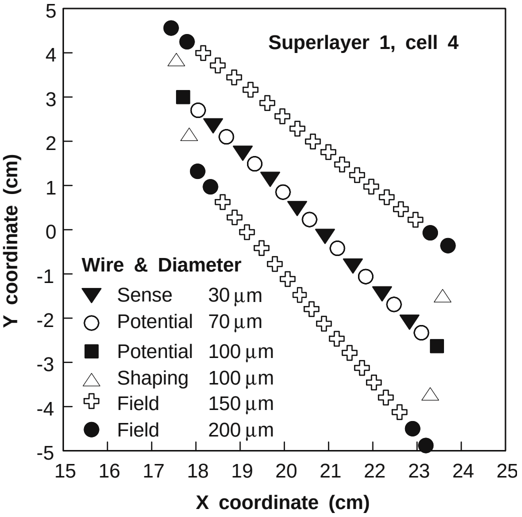

Fig. 3.13
Layout of the CTD cell marked in Fig. 3.12 [63]

field is perpendicular to the electric field. The cells are inclined by an angle of 45° with respect to the radial direction, so that a straight track emitted at the interaction point will cross the sense wire planes and almost always produce hits that are close to one or more sense wires. These hits have a drift time short enough ($t < 96\,\mathrm{ns}$) for the CTD first level trigger to assign the track to the correct beam crossing. The variable parameters (electric and magnetic fields, gas mixture) are tuned such that the Lorentz angle (see Sect. 4.3) also equals 45°. As a result, the electron drift paths are essentially azimuthal, i.e., perpendicular to high momentum tracks coming from the interaction point, which ensures optimal resolution.

The CTD is filled with a gas mixture of argon, carbon dioxide and ethane (in the ratio 83 : 5 : 12), which is bubbled through ethanol (see Sect. 4.7). This mixture has been chosen on the grounds of safety and detector lifetime [34], although a pure argon-ethane mixture (50 : 50) would provide a better resolution and less noise.

3.2.3 The Luminosity Detector

The luminosity, $\mathscr{L} \equiv \dot{N}/\sigma$, relates event rates $\dot{N}$ with the cross section σ for the process in question. The luminosity is determined from the rate of events for a process of which the cross section is theoretically well-known. At ZEUS the luminosity measurement is based on the Bethe–Heitler process, $\mathrm{ep} \rightarrow \mathrm{e}'\gamma\mathrm{p}$, where an electron scatters off a proton under emission of a bremsstrahlung photon. The total cross section of this QED process is about 326 mb for photon energies $0.1 < E_\gamma < 26.7\,\mathrm{GeV}$ [160].

The bremsstrahlung photons emitted in ep collisions at the interaction point leave the beampipe through a copper-beryllium window 82 m downstream in electron beam direction and are detected in a $22\,X_0$ deep lead-scintillator calorimeter [15] at a distance of 107 m from the interaction point (see Fig. 3.14).† A carbon filter with a thickness adjustable between $0.5\,X_0$ and $3.5\,X_0$ shields the photon calorimeter from synchrotron radiation. Layers of scintillator fingers are embedded in the photon calorimeter for reconstructing the photon impact point with a resolution of 2 mm. The energy resolution under experimental conditions is $\sigma(E)/E = 26\%/\sqrt{E}$, with E measured in GeV. The differential cross section as a function of the photon energy, and thus the luminosity, is calculable from the Bethe–Heitler formula [28]. The largest background arises from electron bremsstrahlung on the residual gas. This background shows almost the same experimental signature as the Bethe–Heitler process. Measuring the currents in the paired and unpaired electron bunches and the bremsstrahlung rate for the unpaired electron bunches, the beam–gas

---

† The information from a calorimeter located at a distance of 35 m from the interaction point for the detection of the scattered electron is not directly used for the luminosity measurement.

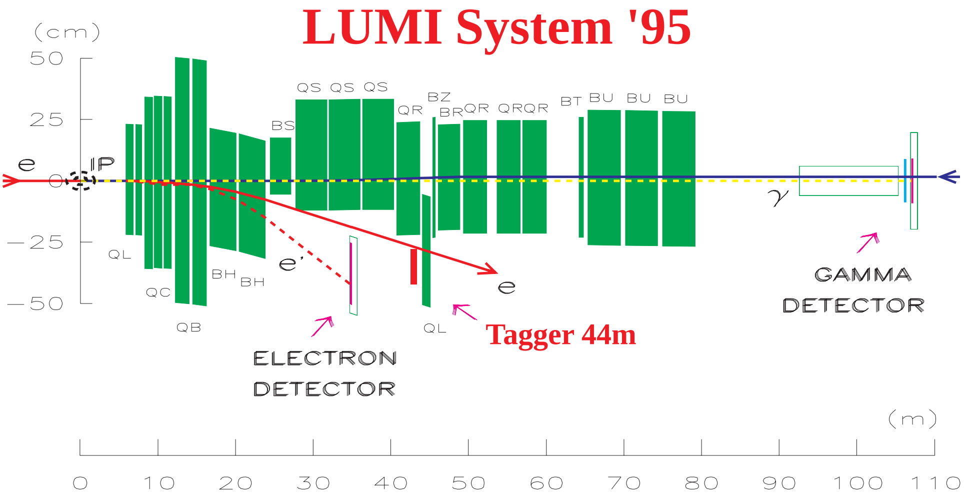

Fig. 3.14 Structure and location of the ZEUS LUMI system. The shaded parallelograms indicate size and position of the bending (B) and quadrupole (Q) magnets (note the scale ratio of the axes, 30 : 1). During the 1994/95 winter shutdown the 44 m tagger was installed at the quadrupole magnet QL. It measures electrons that are scattered under very small angles carrying energies in the range $23 < E'_e < 26$ GeV and is used for tagging photoproduction events with a corresponding centre of mass energy within the range $70 < W_{\gamma p} < 120$ GeV. Adapted from Ref. 186.

background can be subtracted statistically. A detailed description of the procedure and the modifications to the first setup can be found in Refs. 160, 161.

In 1995 an integrated luminosity of $6.73\,\mathrm{pb}^{-1}$, including shifted-vertex runs, was accumulated. The systematic error amounts to ±1.1% [87]. It is dominated by the uncertainties of the cross section calculation and the calorimeter energy scale.

3.3 Trigger and Data Acquisition

The rate of photoproduction and deep inelastic ep interactions is at the level of 1–100 Hz, which is several orders of magnitude smaller than the rate for background events (10–100 kHz), which mainly come from proton interactions with the residual gas molecules upstream of the detector. The raw data information from the roughly 250 000 detector channels has a size of about 0.5 MB. Since the writing speed is limited to 0.5 MB/s, it is essential to select the small fraction of interesting physics events and reduce redundancies in the data online at an early stage of the data acquisition. This reduction is accomplished by a three-level trigger system [202], as illustrated in Fig. 3.15.

Each detector component has its own custom built front-end and read-out

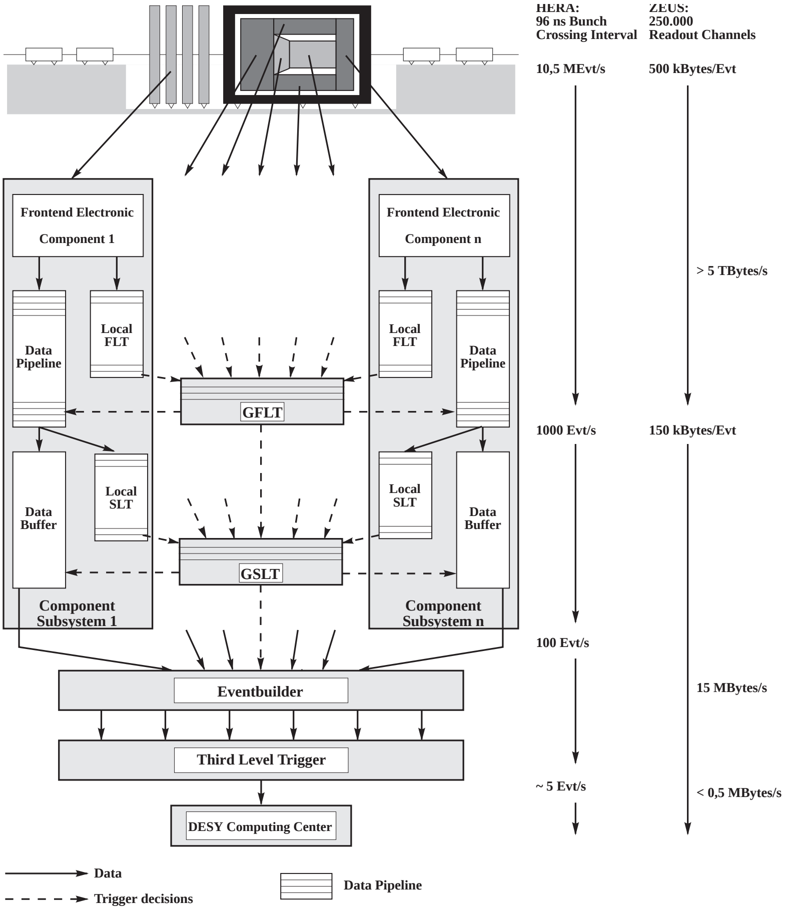

Fig. 3.15 The ZEUS trigger and data acquisition system. The event rates shown are the design values. Taken from Ref. 158.

electronics and a local first level trigger (FLT), which provides a first decision based on a subset of the data by means of very fast hardware as, e.g., programmable gate arrays, look-up tables, etc. The global first level trigger (GFLT) synchronises the component triggers with the HERA clock. Each bunch crossing is identified by a number (BCN), which is used for keeping the entire system in phase. The GFLT expects the FLT decisions from the subdetectors 31 clock cycles after the bunch crossing, and needs additional 15 clock cycles until an accept signal is generated from the logical OR of 64 logical trigger slots. Since it can take additional cycles until the accept signal has been propagated, components like the calorimeter keep their signals in data pipelines, which are 58 bunch crossings (5.5 µs) deep. The GFLT is supposed to reduce the rate below 1 kHz.

Accepted events are fully digitised and copied to the second level trigger (SLT), which again is local to most of the components. This step typically takes 30 µs and thus creates ∼ 3% dead-time (considering the average GFLT rate of ∼1 kHz). On the SLT level, objects like track momenta, the event vertex and calorimeter clusters are reconstructed, permitting a more restrictive trigger decision. The result is sent to the global SLT (GSLT) together with the reconstructed variables for an overall evaluation. Like many of the SLTs, the GSLT is based on a transputer network. Each transputer is devoted to a particular task such as general vetoing or the recognition of certain event signatures, leading to a further reduction down to the level of 50–100 Hz.

For each event that passes the GSLT, the data from the various components are handed over to the event builder (EVB), which is a network of custom-made transputer models with triple-ported memory (TPM). It combines all the data of an event into a single record of ADAMO [94] database tables. This is the data structure used at all subsequent levels up to the physics analysis programs, and distributes the assembled events over the processor nodes of the third level trigger (TLT).

The TLT is a computer farm of 36 Silicon Graphics (SGI) workstations. Each workstation individually analyses and classifies a single event with a custom version of the off-line reconstruction software, which uses the full event information. The accepted events pass the TLT at a rate of ∼5 Hz with a size of ∼150 KB each and are written onto a data summary tape (raw-DST), which is sent to the on-line cluster for monitoring and to the event repository, which is a tape robot in the DESY computing centre.

Later, a complete and final reconstruction of the events is performed off-line, with filter programs provided by the ZEUS physics groups serving as a fourth level trigger. A preselection bit-pattern is assigned to every event, where each bit is associated with a group of selection criteria. Based on the raw-DSTs, so-called mini-DSTs are written, which contain the event data in a condensed form and reconstructed objects, e.g., the tracks of scattered electrons found by the off-line software. In general, these mini-DSTs are the input files for physics analysis programs, whereas the raw-DSTs are used for background studies and data quality monitoring.

3.4 Off-Line Data Analysis

Figure 3.16 shows the dataflow of Monte Carlo simulation (MC) data and real data processing. MC events are produced by AMADEUS, which is a shell program for the actual physics event generator and serves as an interface between the generator output and the ZEUS data structures. At this stage, only the physics processes at the primary vertex are simulated, including the particle decays mediated by strong interactions. All other decays of the outgoing particles and interactions with the detector material are simulated by the MOZART program, which is based on GEANT [105] with GHEISHA [93]. The trigger decision is performed by the CZAR program, which incorporates a simulation of all three trigger levels. At this stage, the produced MC

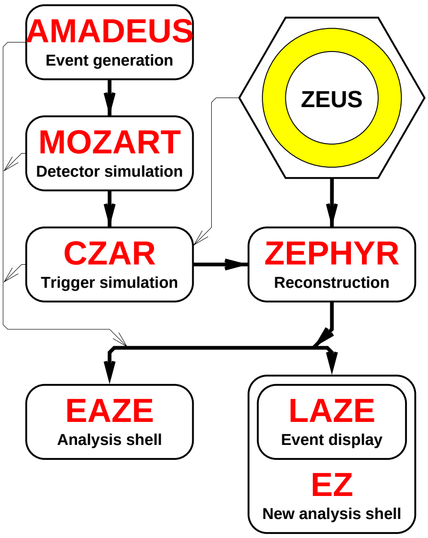

Fig. 3.16
The interplay of the ZEUS off-line programs

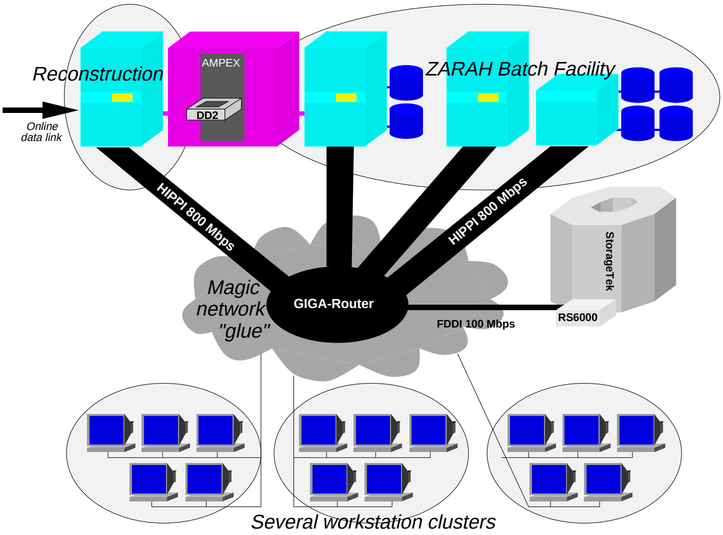

Fig. 3.17
ZEUS analysis environment (1995) [23]

data look like those coming from the real detector and can be handled by the ZEPHYR reconstruction program; the initial generator information, the so-called Monte Carlo *truth* is kept with the data sets.

It is worth noting that the same tools—like the analysis shells EAZE and $\mathcal{EZ}$, in which the event display LAZE, is embedded—can be used both on real data and MC data. The analysis shells provide the framework for user supplied analysis routines, which are called for each event after the data structures have been read from tape. These analysis jobs are run on a dedicated batch processing facility, the ZARAH [23] computer system (Fig. 3.17), a group of multiprocessor SGI machines in combination with two tape robots. The jobs are steered with control cards supplied by the user with his specific analysis code.

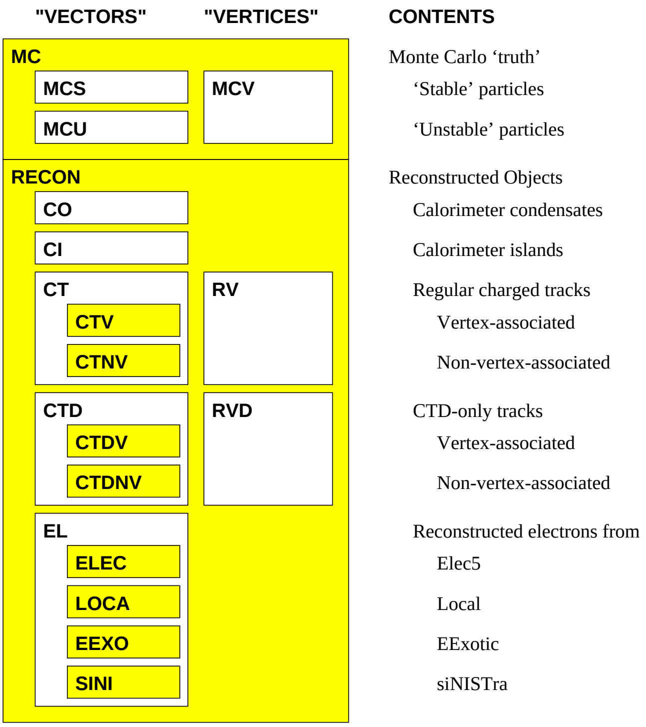

Fig. 3.18
$\mathcal{E}\mathcal{Z}$ list sections

3.5 The $\mathcal{E}\mathcal{Z}$ Analysis Shell

In the course of the analysis presented here, the new analysis shell $\mathcal{E}\mathcal{Z}$ has been developed, that provides a more advanced environment for physics analysis than EAZE. The $\mathcal{E}\mathcal{Z}$ program (see Ref. 77 for a detailed description) is much inspired by the ALPHA package [9] of the ALEPH experiment at LEP. The aim was to free the analysis job from the details of the data representation and to provide advanced analysis features. Since the organisation of the ZEUS data structures reflects the structure of the hardware, the event is described primarily by track parameters, numbers and energy values of photomultipliers that have fired, etc., and it was in the user's responsibility to obtain the physical variables from these data. However, the $\mathcal{E}\mathcal{Z}$ program fills its own data structures and gives easy access to physics variables, making a detailed knowledge about the ZEUS data structures no longer necessary.

Instead of keeping individual tables for each object type, $\mathcal{E}\mathcal{Z}$ copies all objects that basically can be described by 4-vectors (which $\mathcal{E}\mathcal{Z}$ calculates from the signal parameters) into a list of *vectors,* which is divided into sections for each object type. Each individual object can be identified by its unique number. Similarly, all vertices are gathered in a *vertices* list (see Fig. 3.18).

$\mathcal{E}\mathcal{Z}$ provides a uniform interface to all information through Fortran statement functions that take the object identifiers as their arguments. By circumventing the ADAMO table access package, these statement functions provide

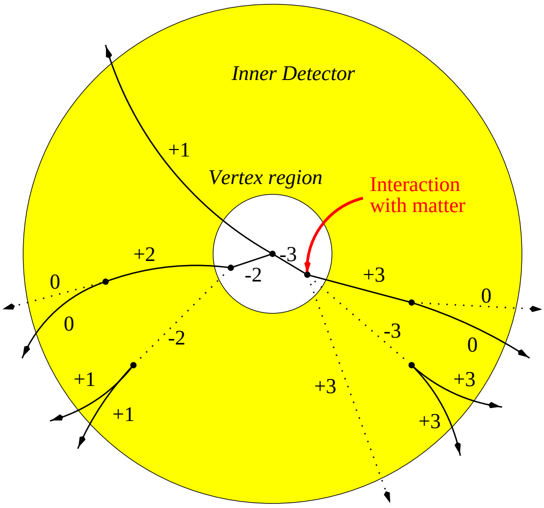

Fig. 3.19
Assignment of stability codes. Negative values denote particles that decay or interact with matter before they could be seen in the detector. Charged tracks are regarded being 'visible' (code > 0) as soon as they leave the cylindrical vertex region, whereas neutral particles must reach the calorimeter outside the inner detector volume. The daughters of these particles carry a zero code.

a fast access directly to the underlying common block of the ZEBRA [54] data management system. Through a list index, certain objects can quickly be found. For example, the true momenta of all MC generated D^{*+} mesons are histogrammed by the following Fortran code:

```
iVec = KOccur(KSMC, KPart('D*+'))   ! Find first D*+ occurrence in MC section
do while (iVec .ne. KNil)           ! Particle exists?
   call HFill(7, ZP(iVec), 0., 1.)  ! Fill momentum into histogram #7
   iVec = KFOccur(iVec)             ! Go to next occurrence
end do
```

Many kinds of interrelations between objects are supported. For example, there are statement functions that enable the user to navigate to the *mothers* or *daughters* of particles, from the 'true' MC particle to its reconstructed track and vice versa, to the same particle in another Lorentz frame, to other particles from the same production vertex, to and from the original data banks. Of course, vector operations like adding, scaling, mass assignment or Lorentz transformations are also easily done.

Other important and convenient features are macro-processing of the control cards, automatic histogram file administration and the assignment of stability codes to MC particles (see Fig. 3.19), which makes it easier to separate particles that leave the primary vertex from resonances and other short-lived particles, and from those produced in interactions with the detector material.

4 Particle Reconstruction and Identification

4.1 CTD Signal Pulses

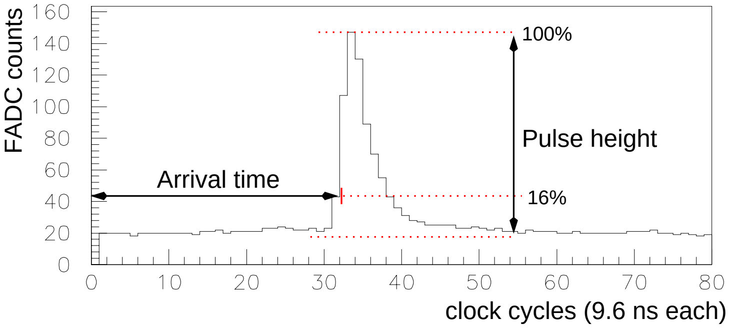

Fig. 4.1
Pulse train on a CTD signal wire

On its passage through the CTD, a charged particle interacts with the atomic electrons of the gas and ionises it. Electrons and ions are kept from recombination by their acceleration in opposite directions along a drift path, which results from the superposition of the electric and the magnetic field in the chamber. When the primary ionisation electrons—and those produced by secondary particles—have gained sufficient kinetic energy, they ionise other gas molecules, and an avalanche is formed in the immediate neighbourhood of the sense wire, where the electric field becomes very large. The high-voltage level and the gas mixture have been chosen such that the drift cells operate as proportional counters, i.e., the number of electrons in the avalanche remains proportional to the number of primary electron-ion pairs, with a constant multiplication factor known as the *gas gain,* which is of the order of 10^4 for the CTD [126].

The motion of the ions and electrons (which drift to the field wires and to the sense wires, respectively) induces a pulse signal on the sense wire.† The front-end (r, ϕ) read-out system acts like an RC differentiating circuit that shorts the sense wire; therefore the time-integrated voltage of the preamplifier output is expected to be proportional to the amount of primary ionisation. This signal is digitised every 9.6 ns by an 8-bit FADC and kept in a pipeline awaiting the FLT decision. For accepted events, the pipeline is read-out by

---

† The contributions of the electron and the ion motion to the induced voltage rises logarithmically with their respective path lengths. As most of the electron–ion pairs are produced in the avalanche near the sense wire, the average drift path is much longer for the ions than for the electrons and the induced signal is almost entirely due to the ion motion. The fast electron pulse is additionally damped by the bandpass filter characteristic of the read-out electronics.

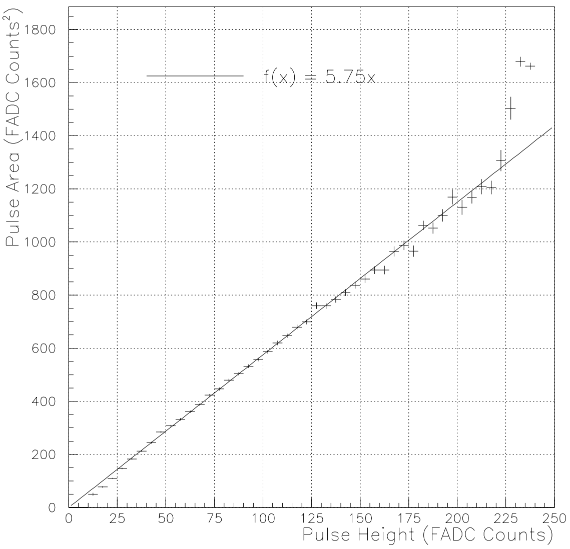

Fig. 4.2
CTD pulse area versus pulse height [64]. For a wide range, these are proportional to each other, with a scaling factor of 5.75

a Digital Signal Processor (DSP), which searches for a sequence of digitisations showing the expected characteristic, a so-called *pulse train,* one sample of which is shown in Fig. 4.1.

After subtracting the pedestal, the DSP determines the peak signal level, which is denoted as the *pulse height.* The pulse height is, after correcting for track angle effects (see Sect. 4.3), proportional to the integral over time of the pulse above the pedestal (cf. Fig. 4.2). The pulse height is registered instead of the area, because the latter suffers less from noise and—in case of a rapid succession of pulses—the signal from a first pulse can be disentangled more easily from the following pulses. However, the proportionality does not hold for very large pulses, which drive the FADC into saturation, and for small pulses, which are more affected by pulse shape variations depending on the hit position (esp. near cell boundaries) and the track angle. The DSP determines the arrival time as the moment when the pulse reaches 16% of its peak level above pedestal. For this purpose, the pulse train entries are interpolated with a granularity of 1/4 clock cycle (i.e. 2.4 ns). The pulse heights and arrival times are used for the spatial reconstruction of the particle trajectory and for the identification of particles by their ionisation energy loss, as described below.

4.2 Track Reconstruction

The arrival time of the signal pulse is converted into a spatial coordinate (*hit*) by the time-to-distance relationship given by the drift velocity. Since only the absolute value of the drift time is known, and not the drift direction, an ambiguity is introduced as to which side of the wire the hit originated from. Since the cell tilt of 45° with respect to the radial direction causes straight tracks from the interaction point to cross at least one cell boundary within a superlayer, this ambiguity can almost always be resolved when the pattern recognition looks for track segments at the superlayer level, as illustrated in Fig. 4.3. For the present analysis, the VC track reconstruction package (VCTRAK [120]) was used, which is capable of combining all hits and track segments of the inner detector (FDET, CTD, RTD), forming 'global' tracks. It was restricted to use CTD hits only, because the details of the combined use of CTD and the forward detectors, which requires a good knowledge of their relative alignments, multiple scattering at the component boundaries, etc., are currently not fully understood. The track finding algorithm first considers hits in the axial superlayers only, constructing a track candidate in the (r, ϕ) plane. Each track candidate begins as a track seed of 3 hits in an outer superlayer. After adding a virtual hit at $x = y = 0$, which is retained throughout the whole procedure, a circle arc is formed in the (r, ϕ) plane, which is followed inward from the seed hits, gathering more axial hits on the way and updating the trajectory parameters accordingly. Then a pattern recognition routine searches for stereo hits that match with the arc after being rotated. The z position is given by the amount of rotation needed to superimpose the stereo track segment on the existing track candidate (see Fig. 4.4). Since the match has to be constrained by hits on both sides of a superlayer, tracks may begin and end on the axial (odd-numbered) superlayers only; short tracks ending in

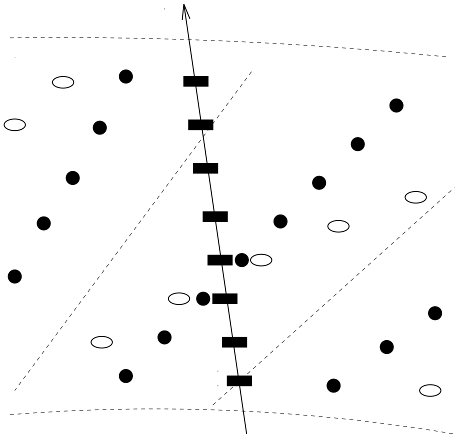

Fig. 4.3
Resolution of the left-right ambiguity by pattern recognition [64]: Those hits that line up to a track trajectory across cell boundaries must be genuine hits (solid rectangles); their mirrored counterparts are *ghost* hits (open ellipses).

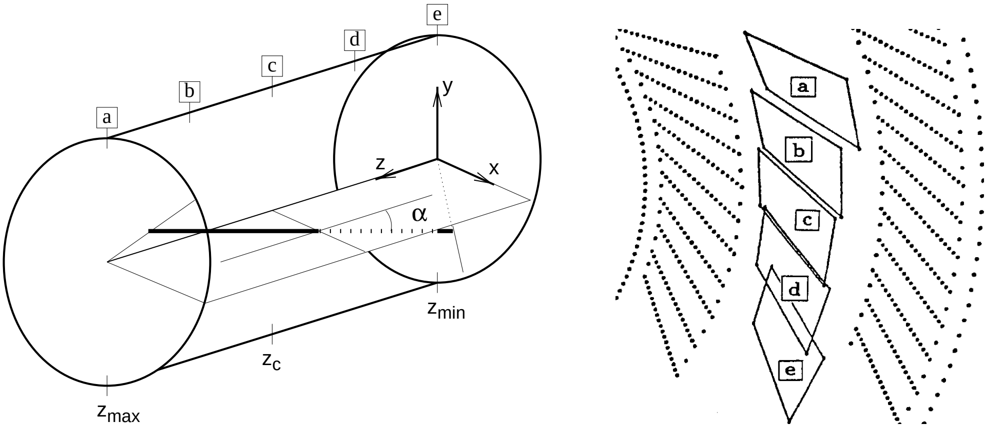

Fig. 4.4 Determination of the z-position from the stereo layers. For a sample cell of a stereo layer, its orientation in the CTD is shown. It is tilted by a stereo angle $\alpha \approx 5°$ with respect to the beam axis, which is exaggerated in the sketch. The right picture shows, as viewed from the forward endplate, for 5 discrete values of z (a–e, as indicated on the left) how the position of a cell changes with respect to the neighbouring axial layers. Thus from the displacement of the stereo hits with respect to the hits on the axial layers, the z-position can directly be inferred. Adapted from Ref. 166.

superlayer 1, however, are extrapolated into superlayer 2 in an attempt to collect more hits.† Those hits that have been assigned to a track are marked as 'taken' and cannot be used for other tracks.

The procedure is repeated until all track seeds in the outermost superlayer are used up, and then starts again with the next inner superlayer. In this manner, the longest tracks are found first, then the shorter ones, down to those which already end in superlayer 1. A second pass is done for picking up those tracks which do not reach the beampipe. These can arise from the decays of long-lived particles or from secondary interactions. It is also possible that two trajectories have common hits in inner superlayers. These hits are assigned to the longer track and are missing when reconstructing the shorter one. Finally, all track candidates are fitted to a 5-parameter ideal helix by 'swimming' the trajectory outward using a simplified model of the magnetic field and refining the parameters with every hit passed. The helix parameters are

$$(a_i) = (\,\phi_{\text{H}},\, Q/R,\, QD_{\text{H}},\, Z_H,\, \cot\theta\,)\,,$$

where ϕ_{H} is the angle between the helix tangent at the origin and the x-axis in the (x, y) plane, Q the charge, R the local radius, D_{H} the smallest distance

---

† Since the (s, z) plane pattern recognition fit provides a 'quantum leap in track purity and accuracy' [152], only such tracks are considered in this analysis which reach at least from superlayer 1 till superlayer 3 and thereby have full stereo information.

between the helix and the origin in the (x, y) plane, and Z_{H} the z-position of this point of closest approach. The coordinates of each point on the helix are a function of the azimuth only,

$$\begin{pmatrix} x \\ y \\ z \end{pmatrix} (\phi) = \begin{pmatrix} -(\sin\phi)/a_2 + (1/a_2 + a3)\sin a_1 \\ (\cos\phi)/a_2 - (1/a_2 + a3)\cos a_1 \\ a_4 + a_5(a_1 - \phi)/a_2 \end{pmatrix} ,$$

and with the momentum estimate p and $\theta = \pm\arctan(1/a_5)$, the 3-momentum is given by

$$(\, p_x,\, p_y,\, p_z\,) = (\, p\cos a_1 \sin\theta,\, p\sin a_1 \sin\theta,\, p\cos\theta\,) .$$

At the component boundaries, the helix is allowed to have a kink from multiple scattering, the angle of which is denoted by δ_{S} (see Fig. 4.5). For the present analysis this was switched off as only hits inside the CTD were used for the track fit.

Now the fit of the event vertex follows, which is done in three steps: first, tracks that do not pass close to the beam-line are discarded from the fit; then the weighted centre of gravity of the surviving tracks is calculated, where tracks that contribute too much to the overall χ^2 are dropped. The resulting (x, y, z) is the start value for the full fit, which not only determines the final value of the vertex position but also constrains the participating tracks to it and then recalculates their helix parameters, which provide the azimuth, polar angle and curvature (Q/R) at the vertex. The tracks that participated in the final vertex fit will in the following be denoted as *vertex-associated* tracks.

4.3 Positive and Negative Tracks

With zero magnetic field, the ionisation electrons drift at an almost constant velocity along the electric field lines towards the sense wires. In the presence of a magnetic field, the Lorentz force deflects the electrons from this direction by an angle λ, called *Lorentz angle* (see Fig. 4.6). In the planar drift approximation, where the electric and magnetic fields are assumed to be homogeneous, this angle has a constant value, which was designed for the CTD to be 45°. The angle ψ' is the angle between the normal to the drift direction and the tangent to the incident particle's direction. For positive tracks, ψ' is positive, for negative tracks it is negative and for straight tracks from the origin it is zero. In the planar drift approximation, the pulse height on the sense wire from particles of fixed velocity depends only on the absolute value of ψ', which directly enters the pulse height-to-area ratio (see Sect. 4.1).

Close to a sense wire the electric field becomes inhomogeneous and combining it with the magnetic field leads to a varying Lorentz angle. This causes

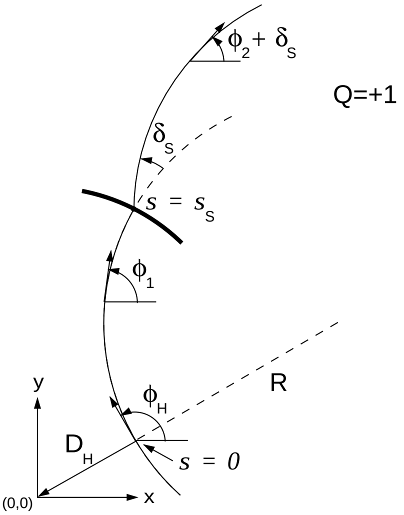

Fig. 4.5 Track helix in the (x, y) plane, without vertex constraint [120]

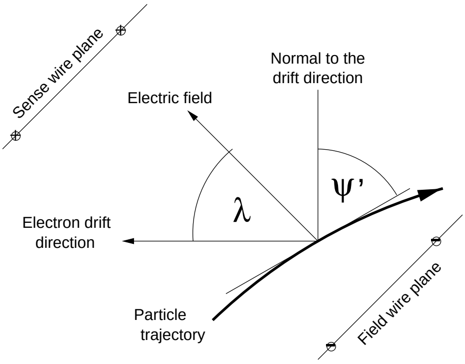

Fig. 4.6 Definition of the Lorentz angle (λ) and the ψ' angle

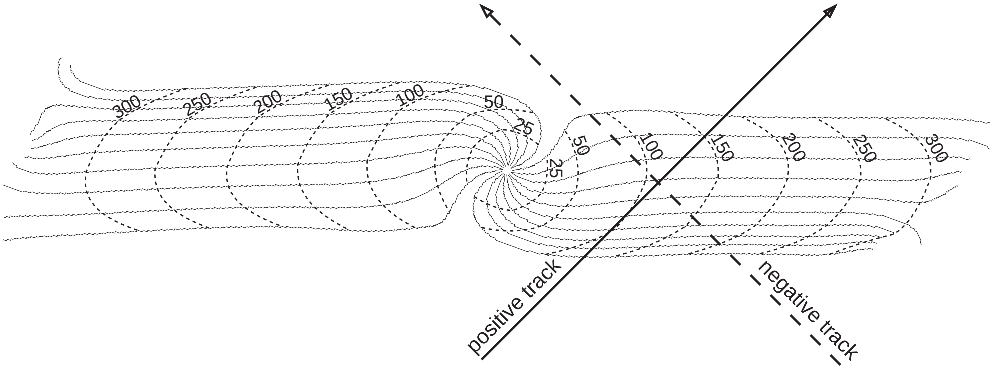

Fig. 4.7 Electron drift paths (solid lines) around a sense wire. The dashed lines indicate the drift isochrones, the numbers denote the drift time in nanoseconds. Positive and negative tracks turn to opposite directions in the magnetic field of the chamber (arrows, cf. Fig. 3.12). Adapted from Ref. 64.

the drift paths to twist (illustrated in Fig. 4.7), which leads to a more subtle dependence of the pulse height on ψ'. The more the drift paths of ionisation electrons produced along a trajectory differ, the lower the pulse height-to-area ratio is. The highest possible pulse is induced by a charged particle that moves along an isochrone (see Fig. 4.7), so that all ionisation electrons arrive simultaneously at the sense wire. The arrows in Fig. 4.7 indicate for two typical positively and negatively charged particles the direction they take in the presence of the magnetic field. Both trajectories are equally far apart from the sense wire and have the same absolute value of ψ'; however, the handedness of the drift path twist favours the drift electrons from the positive track, so that they arrive within a shorter time interval than those from the negative one. The consequences of this asymmetry are:

- Positive and negative tracks have different pulse shapes.
- A pulse from a negative track has a larger time spread, making it more likely to be *broken* by the DSP, i.e., to be misinterpreted as a series of pulses.
- The pulse heights of positive and negative particles of fixed velocity differ substantially.
- The single-hit efficiency, i.e., the probability that a track produces a reconstructed hit on a sense wire, is smaller for negative than for positive tracks.
- Hits of negative tracks at large ψ' angles are more likely to be lost.[†] Therefore the average number of hits for positive and negative tracks differs most at low $p_\perp$. As a consequence, the number of reconstructed positive tracks exceeds the number of negative tracks by $\sim 20\%$ at $p_\perp \approx 0.4\,\mathrm{GeV}$.
- The pulse peak of a negative track is less pronounced, leading to a larger spread of the arrival times and thereby to a worse spatial resolution for a single hit.

On the other hand, the cell tilt by 45° with respect to the radial direction is oriented such that it favours negative tracks[‡]:

- Negative tracks always cross the sense wire plane within a superlayer and hence produce more close hits than positive tracks.
- The z-resolution of positive tracks suffers from the cell tilt asymmetry. Since positive tracks cross cell boundaries less often within a superlayer than negative tracks, the resolution of the left-right ambiguity and the z-reconstruction by pattern recognition is more difficult for them. For negative tracks the efficiency of being assigned to the interaction vertex is at maximum (90%) if the track has the maximum number of hits, whereas this efficiency drops rapidly for positive tracks with more than 65 hits. This effect is caused by positive tracks with low momentum, which are bent so much that they are almost parallel to the sense wire plane by the time they reach superlayer 9; in that case, a displacement may be almost invisible in

---

[†] In addition, the gas gain is reduced for large-ψ' tracks, because the avalanches from early arriving electrons shield the sense wire charge.

[‡] The design decision to optimise the geometry for negative tracks was based on the assumption that HERA would predominantly be operated with electrons. The aim was to assist as much as possible the reconstruction of the scattered electron.

the residuals (the differences between the fitted track position and the hit measurements), but may have an impact on the track parameters.

Of course, the charge asymmetry caused by the cell tilt diminishes as the momenta increase.

4.4 Energy Loss Through Ionisation

As discussed in Sect. 4.1, a charged particle is detected in the CTD by the ionisation of the medium. The registered pulse height is proportional to the number of primary electron-ion pairs. The *average* energy transfer from the traversing particle needed for producing a single ion pair is higher than the ionisation potential of the medium, because part of the energy transfer leads only to an excitation of the gas atoms. For instance, the mean energy needed to produce a single e-Ar^+ pair is 26 eV, whereas the ionisation potential of Ar is 15.8 eV only [144].

Along a path Δx through the drift cell, the traversing particle undergoes multiple collisions, and the number of primary ions produced is connected to a certain energy loss in these collisions,

$$N_{\text{ions}} \propto \Delta E = \int_0^{\Delta x} \mathrm{d}x \left(\frac{\mathrm{d}E}{\mathrm{d}x}\right)_{\text{ionis}} .$$

Note that this integral measures the energy loss in *collisions,* and does not include the *radiative* energy loss, which in fact dominates [27] the slowing down of electrons that originate from the interaction point and have enough momentum to reach the CTD; however, in order to understand the pulse heights measured by the CTD and use them for particle identification, we have to study the ionisation energy loss.

4.4.1 The Bethe–Bloch Formula

Based on classical electrodynamics, Bohr has shown [39] that for fast particles heavier than electrons, the ionisation energy loss in a given medium is proportional to the square of the particle's charge and is a function of its velocity (up to small corrections).† This also holds for the results obtained from first-order quantum-mechanical perturbation theory by Bethe, Møller, Bloch and others. The average energy loss per unit pathlength is given by the Bethe–Bloch formula [26, 37]. As a function of the spatial component of the particle's 4-velocity, $u \equiv p/m = \beta\gamma$, where p and m are its momentum and mass, the formula reads for particles other than electrons ‡

---

† For a concise semiclassical discussion of the average ionisation energy loss consult Jackson [130].

‡ For convenience we give $\mathrm{d}E/\mathrm{d}x$ no negative sign, although an energy *loss* is calculated.

$$\left\langle \frac{\mathrm{d}E}{\mathrm{d}x} \right\rangle = D \frac{z^2}{m_\mathrm{e}\beta^2} \left[\ln \frac{2m_\mathrm{e}u^2 W_\mathrm{max}(u)}{I^2} - 2\beta^2 - 2\frac{C(u)}{Z} - \delta(u) \right] \tag{4.1}$$

$$\text{with} \quad D \equiv 2\pi n_\mathrm{e} e^4 / m_\mathrm{e} \ ,$$

where m_e denotes the electron mass, n_e the electron density of the medium, Z its atomic number, and ze the charge of the traversing particle. To the original formula, correction terms ($2C(u)/Z$, δ) have been added, which are explained below (Sect. 4.4.2). W_max is the maximum energy that can be transferred to a free electron in a head-on collision. Energy-momentum conservation leads to [29]:

$$W_\mathrm{max}(u) = \frac{2m_\mathrm{e}u^2}{1 + \gamma\frac{m_\mathrm{e}}{m} + \left(\frac{m_\mathrm{e}}{m}\right)^2} \tag{4.2a}$$

$$\approx 2m_\mathrm{e}u^2 \qquad \text{for} \quad m \gg m_\mathrm{e}, \quad u \ll \frac{m}{2m_\mathrm{e}} \ . \tag{4.2b}$$

For electrons, W_max is half as large, because in this case the incident particle and the struck atomic electron are indistinguishable after the scattering. At large energy transfers, which are related to small impact parameters $b \propto W^{-2}$ (so-called *close* or *hard* collisions), spin and mass effects become important, so that (4.2a) is exactly valid only for sufficiently fast, spinless particles much heavier than electrons. However, when averaging only over energy transfers up to a certain limit, $W_\mathrm{sep} \sim 10^4$–10^5 eV [188]—which is much larger than the binding energies, yet sufficiently small, so that the impact parameter is large compared to atomic dimensions and the particle thus can be treated as pointlike—the energy loss caused by these *distant* or *soft* collisions is the same for electrons and hadrons [26],

$$\left\langle \frac{\mathrm{d}E}{\mathrm{d}x} \right\rangle_{W < W_\mathrm{sep}} = D \frac{z^2}{m_\mathrm{e}\beta^2} \left[\ln \frac{2m_\mathrm{e}u^2 W_\mathrm{sep}}{I^2} - 2\beta^2 \right] \ , \tag{4.3}$$

where dielectric screening has been neglected.

The central parameter of the Bethe–Bloch formula is the *mean excitation potential I* per atomic electron, which is the logarithmic mean of the excitation energy levels E_i weighted by the optical dipole oscillator strengths f_i for the excitation to the level i,

$$\ln I = \sum_i f_i \ln E_i \ . \tag{4.4}$$

In the classical limit the oscillator strengths can be approximated by the relative number n_i/Z of atomic electrons at the same energy level E_i, which obviously satisfies the sum rule $\sum_i f_i{=}1$.† The use of a mean excitation potential is one of the weak points of the Bethe–Bloch theory, since the E_i are difficult

---

† The exact quantum mechanical formulation has thoroughly been discussed by Fano [90].

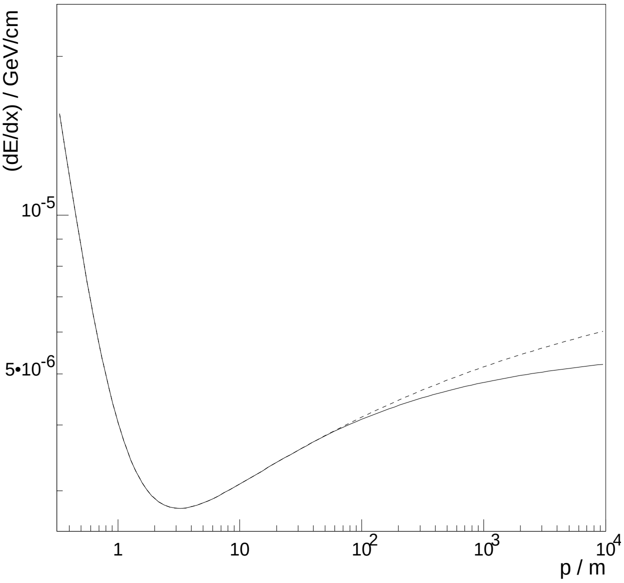

Fig. 4.8
The theoretical expectation for the mean ionisation energy loss of particles other than electrons in the CTD gas mixture as a function of $u = p/m$: solid line, with a correction for polarisation of the medium; dashed line, without correction. Note the double-logarithmic scale.

to calculate and are exactly known only for *atomic* hydrogen [6], whose $\mathrm{d}E/\mathrm{d}x$ cannot be studied experimentally; therefore I must be extracted from actual measurements; it is of the order of $I \sim 10\,\mathrm{eV} \times Z$ for elements heavier than oxygen.

Equation (4.1) indicates that particles of the same momentum but different mass, i.e., of different velocity, can be distinguished by the different amount of ionisation produced. Although some modifications are still necessary to make the Bethe–Bloch formula applicable for particle identification, (4.1) presents the gross features of the ionisation as a function of the particle's velocity.

As can be seen from Fig. 4.8, $\langle \mathrm{d}E/\mathrm{d}x \rangle$ falls, at low velocities, rapidly with increasing u. In the classical picture this can be explained by the fact that the collision time $\tau = b/u$, during which an atomic electron experiences the electric field of a charged particle passing by at impact parameter b, becomes shorter with increasing velocity. As a result, excitation processes become less likely. In this region the behaviour of (4.1) is dominated by the term $\propto \beta^{-2}$ in front of the square bracket; however, the actual slope is better approximated by $\langle \mathrm{d}E/\mathrm{d}x \rangle \propto \beta^{-5/3}$ [62].

For relativistic velocities ($\beta \approx 1$), the term $\propto \beta^{-2}$ becomes constant and the velocity dependence is determined by the behaviour of the square bracket of (4.1); hence $\langle \mathrm{d}E/\mathrm{d}x \rangle$ rises logarithmically after passing through a minimum at $u \sim 3.5$ ('relativistic rerise'). This rise occurs owing to two effects. First, the contribution from close collisions, which have a small impact parameter and therefore large W, rises with increasing $W_{\max}$ (see (4.2b)). Second, the contribution from distant collisions also rises, owing to the Lorentz boost of the particle's electric field, which contracts the longitudinal and inflates the radial extension of the field, enabling more distant atoms to take part in the process (cf. the factor u^2 in the logarithm). Under the simplifications made for (4.1) and (4.2b) and ignoring any corrections, the two contributions are approximately equal and grow beyond any bound with increasing velocity; on the other hand, the polarisation of the atoms near the trajectory of the particle reduces the electric field seen by the electrons of more distant atoms and diminishes the contribution from them, causing $\langle \mathrm{d}E/\mathrm{d}x \rangle$ to rise less dramatically, as indicated by the solid line in Fig. 4.8.

4.4.2 Correction Terms

The dielectric screening of the particle's charge, which limits the growth of $\langle \mathrm{d}E/\mathrm{d}x \rangle$ at highly relativistic velocities, obviously rises with the density of the medium; it is therefore referred to as the *density effect.* Fermi quantified this effect [92]; his calculations have been modified and extended by Sternheimer *et al.* [182, 185]. Although these calculations are based on classical electrodynamics, they describe the measured energy loss reasonably well [75]. The shortcomings in comparison with the results obtained from modelling ionisation through virtual photon absorption (photo absorption ionisation, PAI) and relating $\mathrm{d}E/\mathrm{d}x$ to the photon absorption cross-section [10] have been reduced in the latest review of Sternheimer's parameters [184].

The medium is represented by a dispersion oscillator model, like it was done for the definition of the mean excitation energy (4.4). The contributions from all oscillators, pertaining to isolated atoms or molecules, lead to a reduction of the energy loss by

$$-\Delta\left\langle \frac{\mathrm{d}E}{\mathrm{d}x} \right\rangle = D\frac{z^2}{\beta^2}\left[\sum_i f_i \ln\frac{E_i^2+E_u^2}{E_i^2} - \frac{(E_u/E_{\mathrm{plas}})^2}{1+u^2}\right] , \qquad (4.5)$$

with E_u being the solution of

$$\frac{1}{u^2} = E_{\mathrm{plas}}\sum_i \frac{f_i}{\tilde{E}_i^2+E_u^2} , \qquad E_i \equiv \sqrt{\tilde{E}_i^2 + \tfrac{2}{3}f_i E_{\mathrm{plas}}^2} . \qquad (4.6)$$

The $\tilde{E}_i$ are the absorption edges adjusted by a factor specific to the medium such that the energy levels E_i satisfy (4.4), and the f_i are the occupation numbers of the corresponding shells normalised by the atomic number. This adjustment of the absorption edges is motivated by the fact that also excitations to continuum states contribute, whose energy levels lie somewhat higher than the corresponding absorption edge. E_{plas} is the energy of the atomic electrons considered as a free electron gas, $E_{\mathrm{plas}} = \hbar\sqrt{4\pi n_{\mathrm{e}} e^2/m_{\mathrm{e}}}$. The lower velocity limit u_0 at which for an insulator the density effect sets in, can be obtained from (4.6) in the limit $E_u \to 0$,

$$\frac{1}{u_0^2} = E_{\mathrm{plas}}^2\sum_i f_i/\tilde{E}_i^2 = \varepsilon - 1 , \qquad (4.7)$$

where ε is the static dielectric constant. In the high energy limit ($\beta \approx 1$), the medium behaves like a free electron gas, so that $E_u^2 \to (1+u^2)E_{\mathrm{plas}}^2$ and the value of the square bracket in (4.5), denoted as $\delta(u)$, approaches

$$\delta(u) \to \ln u^2 - 2\sum_i f_i \ln \frac{E_i}{E_{\mathrm{plas}}} - 1 \,. \tag{4.8}$$

The same result for the asymptotic high energy behaviour of $\langle \mathrm{d}E/\mathrm{d}x\rangle$ can be obtained directly from (4.1) when considering the medium as a free electron gas (replacing I by E_{plas}) and assuming the relativistic broadening of the electric field to be completely screened, so that distant collisions do not contribute, viz. by subtracting (4.3) from (4.1), with $W_{\mathrm{sep}} = I$. For dense materials the asymptotic limit is reached shortly after the minimum, whereas for gases the relativistic rerise remains undamped until $u \sim 30$–100.

Another effect related to the dielectric properties of the medium is the energy loss due to Čerenkov radiation, which also is included in the relativistic rerise of the Bethe–Bloch formula. In principle, it is necessary to subtract the Čerenkov loss from (4.1) when calculating the energy deposited close to the particle trajectory. The contribution from Čerenkov radiation is considerable for H and He, but for the gases used in the CTD it accounts for only $\sim 1\%$ of the relativistic rise and can hence be neglected [183].

In the low-energy regime, when the particle's velocity is comparable with the orbital motion of the atomic electrons, additional correction terms are needed to take the tight binding of inner atomic shells into account. These inner shells gradually cease contributing to $\mathrm{d}E/\mathrm{d}x$ when the incident particle becomes slower. This effect is described by the term $-2C(u)/Z$ in the square bracket of (4.1), where Z is the atomic number and $C(u)$ is approximated by an empirical formula given by Barkas and Berger [22],

$$\begin{aligned} C(u) = &\left(\frac{0.422377}{u^2} + \frac{0.0304043}{u^4} - \frac{0.00038106}{u^6}\right) 10^{-6} I^2 \\ &+ \left(\frac{3.858019}{u^2} - \frac{0.1667989}{u^4} + \frac{0.00157955}{u^6}\right) 10^{-9} I^3 \,, \end{aligned}$$

which is valid for $u > 0.13$.

4.4.3 Restricted and Most Probable Energy Loss

The Bethe–Bloch formula describes the mean energy loss, averaged over all kinematically possible collisions. However, if the energy transfer to the struck atomic electron becomes sufficiently large, the electron escapes from the vicinity of the incident particle's trajectory and deposits its energy away from it (so-called *δ-rays*). Their contribution has to be removed when analysing the ionisation along a particle's trajectory. Equation (4.3) describes the energy loss restricted to energy transfers $W < W_{\mathrm{sep}}$ in the limit $W_{\mathrm{sep}} \ll W_{\mathrm{max}}$.

In order to obtain a more general formula, we will in the following explicitly subtract the contribution from δ-rays from (4.1).

For heavy particles traversing a free electron gas, the number n_δ of δ-rays produced at an energy transfer W is according to Bhabha [29] given by

$$\frac{\mathrm{d}^2 n_\delta}{\mathrm{d}W\,\mathrm{d}x} = \frac{Dz^2}{\beta^2 W^2}\left[1 - \beta^2 \frac{W}{W_{\max}} + \text{ spin terms } \mathscr{O}\left(\frac{W^2}{E^2}, \frac{W m_\mathrm{e}}{m^2}\right)\right] . \tag{4.9}$$

Neglecting the spin-dependent terms and integrating (4.9) yields the total energy transfer to all δ-rays with a kinetic energy larger than W_{lim},

$$\begin{aligned}\left\langle\frac{\mathrm{d}E}{\mathrm{d}x}\right\rangle_{W_{\text{lim}} < W < W_{\max}} &= \int_{W_{\text{lim}}}^{W_{\max}} \mathrm{d}W \, \frac{W\,\mathrm{d}^2 n_\delta}{\mathrm{d}W\,\mathrm{d}x} \\ &= D\frac{z^2}{\beta^2}\left[\ln\frac{W_{\max}}{W_{\text{lim}}} - \beta^2\left(1 - \frac{W_{\text{lim}}}{W_{\max}}\right)\right] .\end{aligned} \tag{4.10}$$

By subtracting (4.10) from (4.1) one obtains for fixed $W_0 \ll I$ the *restricted* energy loss,

$$\begin{aligned}\left\langle\frac{\mathrm{d}E}{\mathrm{d}x}\right\rangle_\mathrm{r} &\equiv \left\langle\frac{\mathrm{d}E}{\mathrm{d}x}\right\rangle_{W < W_0} \\ &= D\frac{z^2}{\beta^2}\left[\ln\frac{2 m_\mathrm{e} u^2 W_{\text{lim}}}{I^2} - \beta^2\left(1 + \frac{W_{\text{lim}}}{W_{\max}}\right) - 2\frac{C(u)}{Z} - \delta\right] ,\end{aligned} \tag{4.11}$$

with $W_{\text{lim}} \equiv \min\big(W_0, W_{\max}\big)$.

In case that $W_0 < W_{\max}$, the additional factor $(1 + W_{\text{lim}}/W_{\max})$ provides a smooth transition between the mean (4.1) and the restricted mean energy loss (4.3). It is worth noting that for $W_0 \ll m_\mathrm{e}$ this formula is valid for *any* particle—also for electrons. For particles other than electrons, the inclusion of the neglected spin-dependent terms changes the result for $W_0 < 1\,\mathrm{GeV}$ by less than 0.1% [131].

In the high energy limit the density effect removes the distant collision singularity $\propto \ln u^2$ of (4.1) and, by restricting the energy transfer range, the close collision singularity $\propto \ln W_{\max}(u)$. Hence $\langle \mathrm{d}E/\mathrm{d}x\rangle_\mathrm{r}$ has a finite limit, called the *Fermi plateau,*

$$\lim_{u\to\infty}\left\langle\frac{\mathrm{d}E}{\mathrm{d}x}\right\rangle_\mathrm{r} = Dz^2\frac{2m_\mathrm{e}^2 W_0}{E_{\text{plas}}} ,$$

which depends only on W_0 and the atomic electron density of the medium.

When considering fast particles traversing thin absorbers, the statistical character of the ionisation process becomes evident, and the energy loss is subject to considerable fluctuations from its mean value. With rising particle energy, the $\mathrm{d}E/\mathrm{d}x$ distribution becomes more and more asymmetric owing to the fact that collisions where energies comparable with $W_{\max}$ are transferred to the struck electron become rare. Since the number of collisions within a thin layer is rather small, the central limit theorem is no longer valid and the most probable value may differ from the mean. Bohr [40] already pointed out that in a layer of thickness Δx the limit which separates frequent from rare energy transfers is given by the energy ξ above which, on average, only one δ-ray is produced. Integration of (4.9) yields

$$\xi \approx D \frac{z^2}{\beta^2} \Delta x \, .$$

According to Landau [143], the most probable energy loss is given by (4.11) with the energy transfer limit chosen to be $W_0 = \xi$, if a numerical correction accounting for the tail of the distribution is added,

$$\left(\frac{\Delta E}{\Delta x} \right)_{\mathrm{mp}} = D \frac{z^2}{\beta^2} \left[\ln \frac{2 m_{\mathrm{e}} u^2 \xi}{I^2} - \beta^2 - \delta(u) + 0.198 \right] , \tag{4.12}$$

where for the correction the numerical value calculated by Maccabee and Papworth [146] is given. However, this formula is valid only for sufficiently thin layers or fast enough particles, such that $\varkappa \equiv \xi / W_{\max} \ll 1$ and $(\Delta E)_{\mathrm{mp}} \ll E_{\mathrm{kin}}$, where E_{kin} is the kinetic energy of the incident particle. Landaus calculation assumes $\varkappa = 0$ (i.e. $W_{\max} \to \infty$). The distribution function $f(\Delta x, \Delta E)$ for the probability that a particle will lose an amount ΔE of its initial energy when traversing a layer of thickness Δx is expressed by a universal function $\phi(\lambda) = \xi f(\Delta x, \Delta E)$ of the dimensionless variable λ,

$$\lambda = \frac{1}{\xi} \left[\Delta E - \xi \left(\ln \frac{2 m_{\mathrm{e}} u^2 \xi}{I^2} - \beta^2 + 1 - \mathrm{C} \right) \right] ,$$

$$\phi(\lambda) = \frac{1}{2\pi i} \int\limits_{\sigma - i\infty}^{\sigma + i\infty} \mathrm{d}v \exp(v \ln v + \lambda v) \, ,$$

for $v = \xi p$ and an arbitrary $\sigma > 0$.

Landau's distribution function (4.4.3) has been generalised by Vavilov [189] for any $\varkappa$, as shown for some sample values in Fig. 4.9. For larger values of $\varkappa$ (esp. towards lower velocities), the distribution becomes more and more symmetric and is almost Gaussian for $\varkappa \sim 1$.

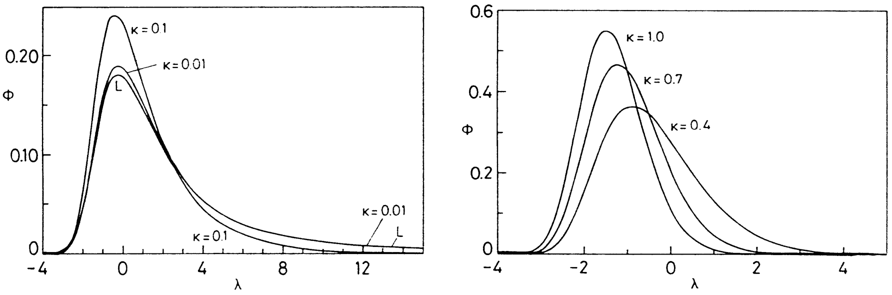

Fig. 4.9 Landau (L) and Vavilov distributions for various values of $\varkappa$ [144]

4.5 From Pulse Heights to dE/dx

In the following, the energy loss along the passage through the CTD will be assumed to be so small that the variation of $(\mathrm{d}E/\mathrm{d}x)_{\mathrm{ionis}}$ can be neglected; in that case, every hit provides—at an arbitrary scale—an independent estimate of the dE/dx of the track, because every sense wire is a separate proportional counter [67]. For every hit the pulse height needs to be corrected for the different path lengths Δx, which depend on the ψ' and λ angles, the superlayer and wire-to-wire differences. Those hits are excluded that are in drift cell regions where the drift velocity is not well understood or the electric field is non-uniform, for instance, close to the signal wires or the cell edges. Multiple hits on a single wire with time separation $\Delta t < 100\,\mathrm{ns}$ are discarded as are hits on *bad gain* wires, which suffer from noise or 'ringing', causing the same pulse to be recorded repeatedly.†

Figure 4.10 shows for an electron the distribution of the independent dE/dx measurements as obtained from the data. It resembles the asymmetric shape of a Landau or Vavilov distribution with a steep rise at the low flank ($\varkappa \sim 10^{-5}$). For a proton of similar momentum (but $\varkappa \sim 0.05$) the peak is shifted towards a substantially higher number of FADC counts and the distribution rises much less steeply and looks more symmetric (see Fig. 4.11). Although the Landau formalism describes the energy loss in liquids and solids very well, it has been shown that for very thin gas samples, as we find them in drift chambers under atmospheric pressure, the energy loss spectrum for low-relativistic particle velocities cannot be described by Landau or Vavilov distributions [68, 164, 167]; nevertheless, for highly relativistic particles such as electrons traversing the CTD, the *peak position,* i.e., the most probable value, coincides with the Landau maximum. For slow hadrons, on the other hand, the peak coincides with the value of the restricted mean energy loss. In principle, a more satisfactory description of the energy loss spectrum can be achieved by the PAI

---

† For a complete list of the single-hit correction dependencies and screening cuts see Ref. 119.

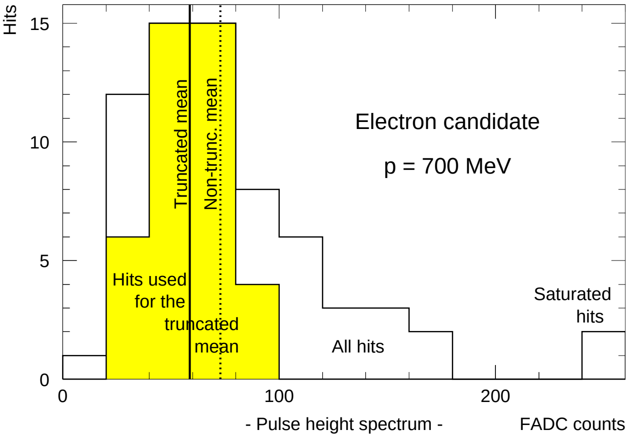

Fig. 4.10
Pulse height distribution of a 700 MeV electron track candidate. Two of the 67 hits are saturated. The shaded area corresponds to the 40 hits that have been used for calculating the truncated mean.

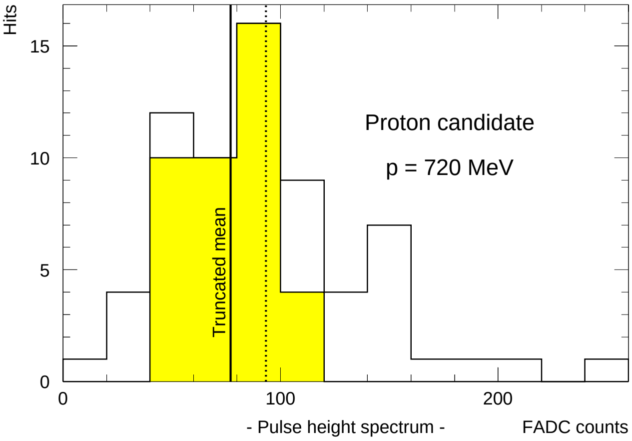

Fig. 4.11
Pulse height distribution of a sample 720 MeV proton track candidate.

model [10]; yet these difficult calculations were not tackled in the present analysis, since they consider an *ideal* detector and the gain in accuracy due to the better theoretical treatment will presumably be lost when proceeding from the primary ionisation to the measured quantities.† A significant improvement could be achieved if the full information from all pulses were taken into account—a procedure that does not seem feasible, as will be explained below.

A precise determination of the peak position of the $\mathrm{d}E/\mathrm{d}x$ distribution can be obtained by a maximum likelihood fit of a phenomenological distribution function to the measured distribution, but this consumes too much computer time if it has to be performed for all tracks of an event. In addition, with rising integrated luminosity one cannot afford any longer to store the single hit information of all tracks. However, almost the same accuracy can be achieved [133] by selectively averaging the pulse heights. For this purpose, certain fractions of the lowest pulses (which are subject to noise) and of the highest pulses are removed from the sample, so that the average is close to the most probable value. Discarding the lowest hits also removes noise and broken hits (see p. 57)

---

† See also remark on p. 61.

that happened to lie near the trajectory. Usually they have a much lower $\mathrm{d}E/\mathrm{d}x$ than genuine hits. The percentage of hits to be removed is optimised for best resolution. Note, if the fraction of selected hits is too low, the average fluctuates owing to low statistics; if it is too high, the hits from the tails of the distribution cause substantial fluctuations by their large weight. For the CTD a rejection of the 10% lowest and the 30% highest pulses was chosen. Other methods of averaging the data (e.g., calculating the median or the harmonic mean) have been proven not to be superior [197].

A modified treatment [191] is necessary if for more than 30% of the hits the pulse height is in the saturation[†] limit. This often happens to tracks at shallow polar angles, where the pulse heights can rise to very large values owing to the long path lengths and where at the same time the total number of hits is reduced, because these particles have traversed only a fraction of the wire layers when they leave the CTD through its endplate. The per-hit corrections cannot rectify it, because the pulse height must have a definite value in order to be correctable. In that case, the following procedure is applied: All saturated hits are removed before averaging; then the loss of their contribution is compensated by shifting the mean value towards a higher value. Since the decrease of the average by the additional hit removal follows a linear progression, the resulting shift can be taken into account by a correction factor $a = f(0.7)/f([n_{\mathrm{kept}} - n_{\mathrm{totsat}}]/n_{\mathrm{kept}})$, which is a function of the number of hits remaining after applying per-hit corrections,[‡] n_{kept}, and of the number of saturated hits, n_{totsat}. The function $f(x)$ is a polynomial fitted to the data,

$$f(x) \equiv 71.508x^4 - 100.4x^3 + 55.685x^2 + 30.92x + 26.95 \;.$$

The resulting average is the *variable truncated mean* of the pulse heights h_i, which is given by

$$\left\langle \frac{\mathrm{d}E}{\mathrm{d}x} \right\rangle_{\mathrm{VC}} = \frac{a(n_{\mathrm{kept}}, n_{\mathrm{totsat}})}{n_{\mathrm{trunc}}} \sum_{i=n_{\mathrm{low}}+1}^{n_{\mathrm{low}}+n_{\mathrm{trunc}}} h_i$$

$$\begin{aligned} \text{with}\quad n_{\mathrm{low}} &= \lfloor 0.1\, n_{\mathrm{kept}} + 0.5 \rfloor \;, \qquad & n_{\mathrm{used}} &= n_{\mathrm{kept}} - n_{\mathrm{low}} - n_{\mathrm{up}} \;, \\ n_{\mathrm{up}} &= \lfloor 0.3\, n_{\mathrm{kept}} + 0.5 \rfloor \;, & n_{\mathrm{sat}} &= \max\left(0, n_{\mathrm{totsat}} - n_{\mathrm{up}}\right) \;, \\ n_{\mathrm{trunc}} &= n_{\mathrm{used}} - n_{\mathrm{sat}} \;, \\ \text{and}\quad a(n_{\mathrm{kept}}, n_{\mathrm{totsat}}) &= 1 \qquad \text{for}\quad n_{\mathrm{totsat}} \leqslant n_{\mathrm{up}} \;, \end{aligned}$$

where $\lfloor \cdots \rfloor$ indicates the truncation of a number to its integer value (floor).

[†] The FADCs have a resolution of 8 bit. Pulses which have driven the FADC into saturation are marked by the DSP using 4 extra bits.

[‡] Remember, only hits from the (r, ϕ) read-out enter the $\mathrm{d}E/\mathrm{d}x$ calculation, while the track-fit also uses z-by-timing hits (and hits in neighbouring tracking devices).

A minimum of $n_{\text{trunc}} = 4$ hits is required; the maximum possible number is $n_{\text{trunc}} = \lfloor 0.6 \times 72 \rfloor = 43$.

The quantity $\langle \mathrm{d}E/\mathrm{d}x \rangle_{\text{VC}}$ is the '$\mathrm{d}E/\mathrm{d}x$' value that is determined by the VCTRAK program and stored together with n_{used}, n_{sat} and the reconstructed track parameters on the DST.[†] Note that $\langle \mathrm{d}E/\mathrm{d}x \rangle_{\text{VC}}$ is stored as an integer number, thus with a precision of ±1%, considering the typical value for a minimum ionising particle (mip) of $\langle \mathrm{d}E/\mathrm{d}x \rangle_{\text{VC}} \sim 50$ FADC counts.

By virtue of the central limit theorem, $\langle \mathrm{d}E/\mathrm{d}x \rangle_{\text{VC}}$ can be expected to follow a unique Gaussian distribution for particles of the same species and fixed momentum, provided that the operational conditions of the CTD remain unchanged and the number of hits used for calculating the mean is sufficiently large. Remember that $\langle \mathrm{d}E/\mathrm{d}x \rangle_{\text{VC}}$ is closely related to, but not to be confused with the actual ionisation energy loss. It is also *not* the mean ionisation. The exact term for it would be 'selectively averaged pulse height'. Although it is a coarse simplification to call this quantity $\mathrm{d}E/\mathrm{d}x$, this is done here as well, in order to be consistent with other publications.

4.6 Calibration of $\mathrm{d}E/\mathrm{d}x$

The measured $\langle \mathrm{d}E/\mathrm{d}x \rangle_{\text{VC}}$ values are affected by additional factors, for which the pulse heights have not yet been corrected. Variations of the gas mixture, the atmospheric pressure and the high voltage setup directly influence the drift velocity and the gas gain in the CTD. The major effect of this is a change of the pulse shapes so that the height–area relation is altered. The true energy loss does not vary as much with these parameters; it linearly follows the pressure variations, because the atomic electron density is proportional to the pressure and the $\mathrm{d}E/\mathrm{d}x$ slope is only affected logarithmically, which is negligible considering that the atmospheric pressure variation in Hamburg is $\Delta P \sim \pm 2\%$. Thus it is sufficient to correct for the overall scale variation caused by these factors. This correction can directly be applied to the truncated mean values as they are found on the DST.

Since the contributions from different particle species can be attributed to particular bands in the $(\mathrm{d}E/\mathrm{d}x, p)$ distribution, the $\mathrm{d}E/\mathrm{d}x$ scale of each run can be determined by measuring the average of $\langle \mathrm{d}E/\mathrm{d}x \rangle_{\text{VC}}$ for one of the bands in a momentum range, where the $\mathrm{d}E/\mathrm{d}x$ value for the chosen band is approximately constant; furthermore, the bands from the other particle species must be sufficiently apart and the number of particles in the band under study must be sufficiently large to permit a good fit of the mean. These requirements are in general fulfilled for the pion band within the momentum range of 300–400 MeV, which corresponds to the velocity range $u \sim 2$–3, where

---

[†] For 1995 data—except version 3 of the mini-DST—one must rerun the $\mathrm{d}E/\mathrm{d}x$ reconstruction of VCTRAK in order to obtain the *variable* truncated mean.

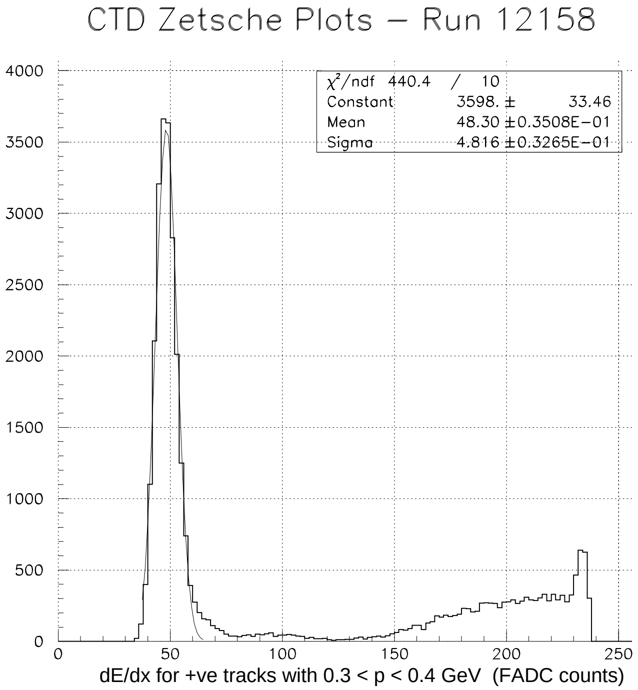

Fig. 4.12 $\langle \mathrm{d}E/\mathrm{d}x \rangle_{\mathrm{VC}}$ distribution and fit of the pion band in the momentum range $0.3 < p < 0.4\,\mathrm{GeV}$ for a single run from the 1995 data. A Gaussian is a good approximation for the main peak—as expected, since this is a distribution of pulse height *means.*

particles in the CTD are nearly minimum ionising (see Fig. 4.8). By fitting a Gaussian function to the pion peak, the number of FADC counts that correspond to a mip is found. Such a fit is done for every reconstructed run as part of the CTD data quality monitoring (DQM) and calibration procedure, as documented in the so-called Zetsche plots [181].

Figure 4.12 shows the fit result for a single run of the 1995 data. The peak at 50 FADC counts results from pions, which are copiously produced in jets. Muons in this momentum range have about the same $\mathrm{d}E/\mathrm{d}x$, so that their small contribution does not lead to a visible shift. The tail of the peak (at 60 to 80 counts) can be attributed to electrons and to the small number of pions that have large pulse height fluctuations. The flat peak at about 95 counts originates from kaons[†] and the smooth rise observed above 150 counts can be attributed to protons, for which $\mathrm{d}E/\mathrm{d}x$ falls steeply with rising momentum in this momentum range. The spike at the upper end of the distribution and the fact that the proton peak does not fade away at the upper end, reveal that in 1995 the strictly truncated and not the variable truncated mean was used on this level of event processing; hence saturated hits were not fully removed.

[†] The flat peak could also be taken for a ‘2 mip peak’ at 100 counts, but what is shown in Fig. 4.12 is a distribution of truncated means, not of single pulse heights. This means that two particles would not only have to meet in a single point, they must have almost parallel, very close trajectories (at a momentum of only $p \sim 0.4\,\mathrm{GeV}$), in order to produce such a double-hit peak. It should be noted in this context, that the DSP efficiency of resolving a double hit into two separate hits is 50% at a distance of 2.5 mm [64].

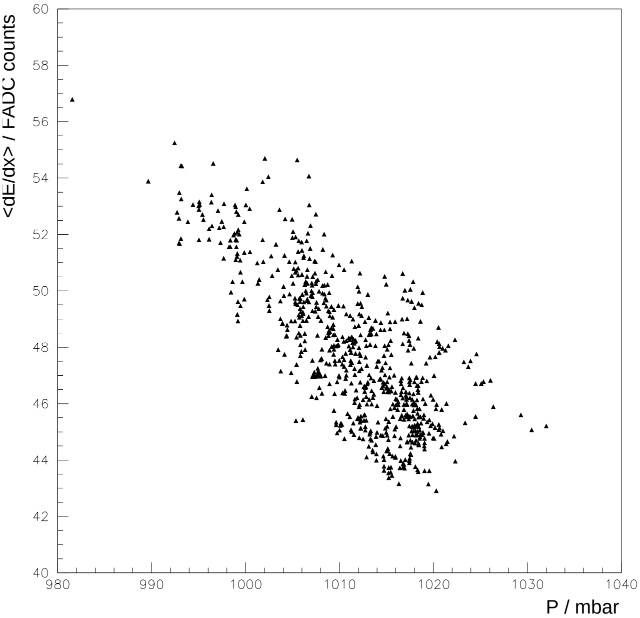

Fig. 4.13
The fitted $\langle \mathrm{d}E/\mathrm{d}x \rangle_{\mathrm{VC}}^{\mathrm{mip}}$ versus the atmospheric pressure

The fitted pion band position, which is misleadingly referred to as the *average* $\mathrm{d}E/\mathrm{d}x$ of a run, defines the CTD mip although the actual $\mathrm{d}E/\mathrm{d}x$ minimum lies at a pion momentum of $p \approx 550\,\mathrm{MeV}$. The CTD mip is used for normalising the $\mathrm{d}E/\mathrm{d}x$ measurement, making the results from different runs comparable. It corresponds to an energy loss of $\mathrm{d}E/\mathrm{d}x \sim 3\,\mathrm{keV/cm}$ under nominal operation conditions.

In 1995 a single high voltage and gas mixture setup was used for the CTD; therefore most of the $\mathrm{d}E/\mathrm{d}x$ variations can be attributed to pressure variations. In Fig. 4.13, the fitted mip $\langle \mathrm{d}E/\mathrm{d}x \rangle_{\mathrm{VC}}$ values of the 1995 runs are shown versus the atmospheric pressure. It is at first glance surprising to see $\langle \mathrm{d}E/\mathrm{d}x \rangle_{\mathrm{VC}}^{\mathrm{mip}}$ decrease with rising pressure. This phenomenon has been reproduced by a simulation of the ionisation avalanche in the vicinity of the sense wires [174] and can be attributed to two factors: first there is an atomic excitation edge of argon at 12 eV, which increasingly prohibits ionisation with rising pressure, leading to a reduction of the gas gain; second, the drift velocity becomes reduced with higher density of the medium, altering the height-to-area ratio of the pulses. Both effects together dominate over the rise of $\mathrm{d}E/\mathrm{d}x$ with increasing electron density.

By adjusting $\langle \mathrm{d}E/\mathrm{d}x \rangle_{\mathrm{VC}}^{\mathrm{mip}}$ to a nominal pressure of 1013 mbar, the pressure effects can be eliminated. It has been shown that the fluctuations which lead to the *spread* of the variation in Fig. 4.13, depend on the run number. They are anticorrelated with run-to-run variations of the drift velocity, the origin of which is not definitely known [197]. The peak values of the variations seem to occur predominantly after accesses to the detector, when the gas flow had to be switched back from the bypass. Still, even after correcting also for the drift

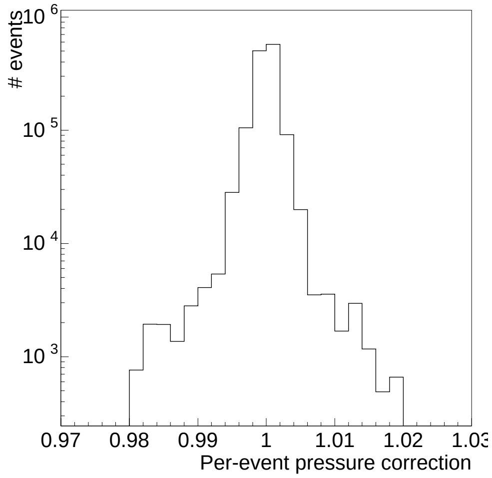

Fig. 4.14
Distribution of the per-event correction factor C_{evt} for the 1995 data (adapted from Ref. 198). Note the logarithmic scale.

velocity variations, a systematic decrease of $\langle \mathrm{d}E/\mathrm{d}x\rangle_{\mathrm{VC}}^{\mathrm{mip}}$ during the 1995 data taking period can be observed. The possibility of an ageing effect, for instance from deposits of polymerised ethane on the wires, is under study [114].

All effects discussed above affect only the overall scale of $\langle \mathrm{d}E/\mathrm{d}x\rangle_{\mathrm{VC}}$ and can be corrected for on a run-by-run basis by normalising to the mip value. An additional correction on a per-event basis can be applied that accounts for the pressure variation within long runs. For this purpose, the actual pressure reading was recorded every ten minutes and stored in end-of-run files.† By interpolation, the pressure at the time of a certain event can be obtained and the $\mathrm{d}E/\mathrm{d}x$ measurement can be corrected for by a factor [198, 199]

$$C_{\mathrm{evt}} = 1 + (P_{\mathrm{evt}} - \langle P\rangle_{\mathrm{run}})\frac{C_0}{1 + C_0(P_{\mathrm{evt}} - P_0)}\ ,$$
$$P_0 = 1013\,\mathrm{mbar} \qquad \text{and} \qquad C_0 = -0.006 \qquad (1995)\,.$$

This correction is small (see Fig. 4.14): only for a very small fraction of the events does it reach the percent level, but remains below 2%, which is about the typical granularity of $\langle \mathrm{d}E/\mathrm{d}x\rangle_{\mathrm{VC}}$ for minimum ionising particles.

Eventually an additional correction must be applied on a per-track basis in order to allow for the gas gain reduction by space charge effects [122], which give rise to further θ-dependence of $\langle \mathrm{d}E/\mathrm{d}x\rangle_{\mathrm{VC}}$ that is not covered by the per-hit path length correction.The problem is that the gas amplification may saturate if the crossing angle between track and signal wire is such that the length over which charges are collected is much shorter than the path length of the ionising particle within the detection volume.‡ During the 1995 data

---

† Since the beginning of the 1997 data taking, this information is stored with the data in the environmental records of the DST.

‡ The gas gain can also be reduced by space charges that are produced by other particles in the same event or from previous collisions (ep and background), by halo muons and by the synchrotron radiation from the positron beam—which largely is shielded. The resulting dependence of $\mathrm{d}E/\mathrm{d}x$ on the luminosity (or rather the electron beam current) is partly covered

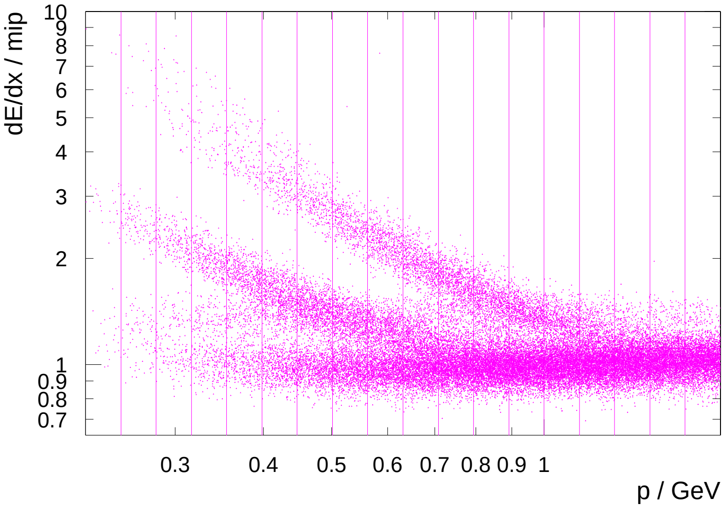

Fig. 4.15 $\langle \mathrm{d}E/\mathrm{d}x \rangle_{\mathrm{CTD}}$ versus momentum for negative vertex-associated tracks with $n_{\mathrm{used}} \geqslant 38$. The vertical lines indicate the momentum slices used for the fit procedure described in Sect. 4.8.

taking the CTD high voltage was 2% lower than in 1994, which greatly reduced the effect seen previously [194]. Part of the remaining effect is already accounted for by applying the variable instead of the strictly truncated mean and thereby removing saturated hits. The remaining correction can be parametrised by a phenomenological function that has been fitted to the measured $(\mathrm{d}E/\mathrm{d}x, \theta)$-dependence [193]. In a first step, all other corrections are applied and $\mathrm{d}E/\mathrm{d}x$ is normalised to the mip value,

$$\left\langle \frac{\mathrm{d}E}{\mathrm{d}x} \right\rangle_{\mathrm{norm}} = \frac{C_{\mathrm{evt}}}{\langle \mathrm{d}E/\mathrm{d}x \rangle_{\mathrm{VC}}^{\mathrm{mip}}} \left\langle \frac{\mathrm{d}E}{\mathrm{d}x} \right\rangle_{\mathrm{VC}} .$$

In a second step the correction for space-charge effects is performed,

$$\left\langle \frac{\mathrm{d}E}{\mathrm{d}x} \right\rangle_{\mathrm{CTD}} = \left\langle \frac{\mathrm{d}E}{\mathrm{d}x} \right\rangle_{\mathrm{norm}} + g \, \exp\left[-\frac{1}{2} \left(\frac{\theta - \frac{\pi}{2}}{0.23} \right)^2 \right] \tag{4.13}$$

$$\text{with} \quad g = \begin{cases} 0 & \text{if } \langle \mathrm{d}E/\mathrm{d}x \rangle_{\mathrm{norm}} < 1.05 \,, \\ 0.1 & \text{if } \langle \mathrm{d}E/\mathrm{d}x \rangle_{\mathrm{norm}} > 1.12 \,, \\ 1.44 \, \langle \mathrm{d}E/\mathrm{d}x \rangle_{\mathrm{norm}} - 1.5 & \text{otherwise.} \end{cases}$$

The $\langle \mathrm{d}E/\mathrm{d}x \rangle_{\mathrm{CTD}}$ value given by (4.13) is the quantity being taken as the *measured* $\mathrm{d}E/\mathrm{d}x$.

Figure 4.15 shows the distribution of tracks from a DIS $\mathrm{D}^{*\pm}$ preselection sample with a large number of hits in the $(\mathrm{d}E/\mathrm{d}x, p)$ plane. A clear band structure emerges, which can be associated with electrons, pions, kaons and protons, as will be described below.

---

by the per-run corrections. Since the electron beam current drops significantly during a run, there remains some variation within the run, which is not corrected for.

4.7 Ionisation of the CTD Filling Gas

In order to determine from the $\langle \mathrm{d}E/\mathrm{d}x \rangle_{\mathrm{CTD}}$ value observed for a single track its probability to be produced by a particle of a certain species, the value expected for such a particle and its variance must be known accurately. This information can be obtained from fits to the measured distributions. Since $\langle \mathrm{d}E/\mathrm{d}x \rangle_{\mathrm{CTD}}$ is closely related to the ionisation energy loss, its dependence on the particle's velocity can be expected to be similar to that of the restricted (4.11) and the most probable energy loss (4.12); in particular, the variation of this dependence with the gas mixture should be the same.

Table 4.1 lists the results from external chromatographic measurements of the CTD gas mixture in 1995. The long-term stability of the composition is excellent; short-term variations after restarting the gas system could be significant (see previous section), but they have to be measured by the on-line analysis system, which has a moderate accuracy.

Since $\mathrm{d}E/\mathrm{d}x$ scales with the atomic electron density, the $\mathrm{d}E/\mathrm{d}x$ of a mixture with no chemical binding between the components can be assumed to be the weighted sum of the contributions from each constituent (*Bragg's rule* [44]), where for the weights w_i the corresponding volume fractions are used,

$$\left(\frac{\mathrm{d}E}{\mathrm{d}x}\right)_{\mathrm{mix}} = \sum_i w_i \left(\frac{\mathrm{d}E}{\mathrm{d}x}\right)_{\mathrm{i}} .$$

This relation is certainly adequate for a low-density mixture, consisting predominantly of noble gases, like that used for the CTD. The $\mathrm{d}E/\mathrm{d}x$ properties are thus dominated by that of the Argon contribution. The admixtures play, however, an important rôle with respect to the ionisation yield: a fluctuation of the $\mathrm{CO_2}$content by ±1% changes the gas gain by ±7%; a similar fluctuation of the ethane content causes changes of ±10% [174]. The traces of alcohol vapour do not affect $\mathrm{d}E/\mathrm{d}x$, but the alcohol influences the gas gain indirectly

Table 4.1 CTD gas mixture in 1995. Results from gas chromatography analyses [172]. The measuring method is not very accurate for detecting the alcohol content; since the alcohol contribution to $\mathrm{d}E/\mathrm{d}x$ is negligible (cf. text), it has not been considered when calculating the volume percentages of the other components.

Date	Argon/%	$\mathrm{CO_2}$/%	Ethane/%	(Ethanol/%)
09.06.95	82.735	4.767	12.497	(0.355)
11.08.95	82.663	4.747	12.589	(0.544)
15.09.95	82.691	4.657	12.652	(0.527)
15.11.95	82.821	4.634	12.545	(0.507)
average	82.73	4.70	12.57	(0.48)

Table 4.2 Properties of the CTD gas components (taken mostly from Ref. 184). Z_{avg} is the average atomic number, Z/A the ratio of atomic number to atomic weight, ϱ the mass density, I the mean excitation potential, E_{plas} the plasma energy; X_0, X_1 and m_{S} are the Sternheimer parameters for the density correction, Δ_{max} the maximum error of the parametrisation.

Comp.	Z_{avg}	$\frac{Z/A}{\mathrm{mol/g}}$	$\frac{\varrho}{\mathrm{mg/cm^3}}$	$\frac{I}{\mathrm{eV}}$	$\frac{E_{\mathrm{plas}}}{\mathrm{eV}}$	X_0	X_1	m_{S}	$\frac{\Delta_{\mathrm{max}}}{\%}$
Argon	18.00	0.45059	1.6620	188.0	0.789	1.7635	4.4855	2.9618	3.7
CO_2	7.33	0.49989	1.8421	85.0	0.874	1.6294	4.1825	3.3227	9.1
Ethane	2.25	0.59861	1.2532	45.4	0.789	1.5107	3.8743	3.6095	9.7

by prohibiting the build-up of deposits (esp. the growth of *whiskers* from ethane polymerisation) on the wires [190]. Table 4.2 lists the material constants[†] used for the evaluation of $\langle \mathrm{d}E/\mathrm{d}x \rangle_{\mathrm{r}}$ (4.11) and $(\Delta E/\Delta x)_{\mathrm{mp}}$ (4.12).

For the calculation of the density correction, Sternheimer [185] has fitted an analytic function to the theoretical solutions of (4.5), which describes the density correction δ as a function of $X \equiv \log_{10} u$,

$$\delta(X) = \begin{cases} 0 & \text{if } X < X_0\,, \\ (2\ln 10)X + C_{\mathrm{S}} & \text{if } X > X_1\,, \\ (2\ln 10)X + C_{\mathrm{S}} + a(X_1 - X)^{m_{\mathrm{S}}} & \text{otherwise,} \end{cases}$$

with

$$C_{\mathrm{S}} \equiv -2\ln\frac{I}{E_{\mathrm{plas}}} - 1 \qquad \text{and} \qquad a \equiv \frac{-C_{\mathrm{S}} - (2\ln 10)X_0}{(X_1 - X_0)^{m_{\mathrm{S}}}}\,.$$

The values of X_0, X_1 and m_{S} are listed in Table 4.2. The lower limit X_0 is determined by (4.7). The free parameters of the fit, X_1 and m_{S}, have been chosen such that for $X > X_1$ the density correction differs by less than 1.5% from the asymptotic behaviour of (4.8), whereas in the intermediate region the deviation of the approximation function $a\,(X_1 - X)^{m_{\mathrm{S}}}$ from the precise theoretical value has been minimised; the maximum deviation Δ_{max} is given in Table 4.2.

[†] Throughout the calculations of this analysis the values of the fundamental physical constants have been taken from the 1986 adjustment [71].

4.8 Construction of a dE/ dx Parametrisation

Since positive and negative tracks produce different signals (see Sect. 4.3), all studies have been done separately for the two charges. For consistency, the illustration of the following will focus on negative tracks.

In Sect. 4.5 it was pointed out that in the low and high energy limits, the measured pulse height average $\langle \mathrm{d}E/\mathrm{d}x\rangle_{\mathrm{CTD}}$ should behave like the restricted (4.11) and the most probable energy loss (4.12), respectively. Fits to the $(\mathrm{d}E/\mathrm{d}x, p)$ distribution have been performed with the result that, indeed, the restricted energy loss formula (4.11) fits very well at low velocities, but overshoots the data after passing the minimum; conversely, the most probable energy loss describes the data at high velocities but lies above the data when passing the minimum towards lower momenta; consequently, the following ansatz was made for the parametrisation of the band centres as a function of p and m:

$$\left(\frac{\mathrm{d}E}{\mathrm{d}x}\right)_{\mathrm{fit}}(p,m) = \begin{cases} (a) \quad c_0\langle \mathrm{d}E/\mathrm{d}x\rangle_{\mathrm{r}}(p_0^{\pi}, p, m) & \text{if } p/m < u_0 \ , \\ (b) \quad c_1(\Delta E/\Delta x)_{\mathrm{mp}}(p_1^{\pi}, p, m) & \text{if } p/m > u_1 \ , \\ (c) \quad \hat{S}_3(p/m) & \text{in between.} \end{cases}$$

The mass enters only weakly through the maximum energy transfer W_{max} (4.2a); apart from this, $(\mathrm{d}E/\mathrm{d}x)_{\mathrm{fit}}$ is a function of $u = p/m$ alone. The function has 4 parameters to be adjusted: c_0 and c_1 normalise the function, whereas p_0^{π} and p_1^{π} determine the slope—they are the pion momenta at the minima of the respective functions. This set of parameters is convenient for estimating starting values for the fit. The transformations to the parameters of (4.11) and 4.12 are found by requiring the first derivatives to vanish at $p_{0,1}^{\pi}$. The parameters of the cubic spline, $\hat{S}_3(p/m)$, are fixed by demanding a smooth continuation of the other functions in u_0 and u_1. Since $\mathrm{d}E/\mathrm{d}x$ is supposed to be a convex function below values where the density correction sets in, the spline must be a convex function, too, so that $u_{0,1}$ are no longer free parameters. Each time one value of the 4-parameter set is modified during the fit, new $u_{0,1}$ positions are found by requiring the direct line between them to be a tangent to the two other functions, (a) and (b),

$$\left\langle\frac{\mathrm{d}E}{\mathrm{d}x}\right\rangle_{\mathrm{r}}'(\tilde{u}_0) = \left(\frac{\Delta E}{\Delta x}\right)_{\mathrm{mp}}'(\tilde{u}_1) = \frac{(\Delta E/\Delta x)_{\mathrm{mp}}(\tilde{u}_1) - \langle \mathrm{d}E/\mathrm{d}x\rangle_{\mathrm{r}}(\tilde{u}_0)}{\tilde{u}_1 - \tilde{u}_0} \ .$$

The solution $\tilde{u}_{0,1}$ of this equation is found by applying Newton's method. Since we seek an interpolation that is reasonably smooth also in the first derivative, both points are pulled a bit further apart:

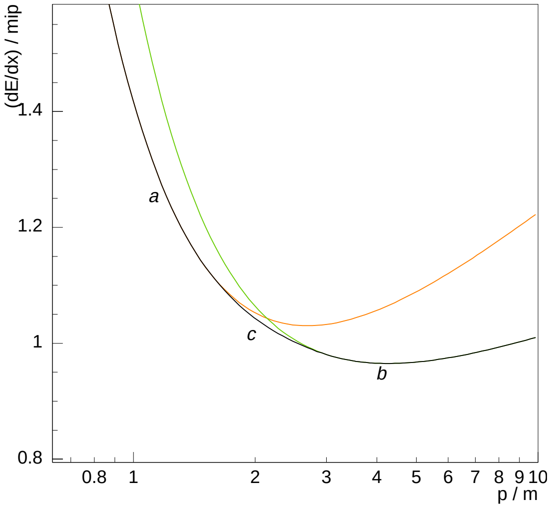

Fig. 4.16
Composition of the $\mathrm{d}E/\mathrm{d}x$ parametrisation: (a) $\langle \mathrm{d}E/\mathrm{d}x\rangle_\mathrm{r}$ (without density correction), (b) $(\Delta E/\Delta x)_\mathrm{mp}$, and ($c$) cubic spline. The light lines indicate how the components (a) and (b) continue outside the regions of their validity.

$$
\begin{aligned}
u_0 &= \tilde{u}_0 - \left\langle \frac{\mathrm{d}E}{\mathrm{d}x} \right\rangle_\mathrm{r}''(\tilde{u}_0)\frac{(\tilde{u}_1-\tilde{u}_0)^3}{(\Delta E/\Delta x)_\mathrm{mp}(\tilde{u}_1) - \langle \mathrm{d}E/\mathrm{d}x\rangle_\mathrm{r}(\tilde{u}_0)}\,, \\
u_1 &= \tilde{u}_1 + \left(\frac{\Delta E}{\Delta x}\right)_\mathrm{mp}''(\tilde{u}_1)\frac{(\tilde{u}_1-\tilde{u}_0)^3}{(\Delta E/\Delta x)_\mathrm{mp}(\tilde{u}_1) - \langle \mathrm{d}E/\mathrm{d}x\rangle_\mathrm{r}(\tilde{u}_0)}\,.
\end{aligned}
\tag{4.14}
$$

Figure 4.16 illustrates how the spline function closes the gap between the regions covered by the two energy loss functions.

It must be stressed that this is—although inspired by theory —a plain phenomenological function; any other function could have been used that fits the data equally well.

For the fit of $(\mathrm{d}E/\mathrm{d}x)_\mathrm{fit}$, the $(\mathrm{d}E/\mathrm{d}x, p)$ distribution of tracks from a 1995 DIS $\mathrm{D}^{*\pm}$ preselection sample with $n_\mathrm{used} \geqslant 38$ was divided into logarithmically spaced momentum slices, as shown in Fig. 4.15. The $\log_{10}(\mathrm{d}E/\mathrm{d}x)$ projections of each slice were fitted to a distribution function composed of 4 Gaussians—corresponding to the contributions from electrons, pions, kaons and protons. For each of the 4 Gaussians, the start value of its mean in each bin was taken from the $(\mathrm{d}E/\mathrm{d}x)_\mathrm{fit}$ of a previous iteration. Only one peak position at a time was allowed to vary, while the other parameters remained fixed. When the fit had become stable ($\Delta\chi^2 < 0.1\%$) and the positions of all 4 peaks had been iterated, the areas and widths of the peaks—of which the start values were obtained from an average of the values for the current and the neighbouring slices in the previous run—were allowed to vary, too. In Figure 4.17 the result of the 4-Gaussians fit for a sample momentum slice is displayed. Special care was taken to make the fit procedure follow each component across the band crossings. When starting with the final parametrisation, the procedure succeeded without any human intervention.

Figure 4.18 shows the resulting band positions, which served as input for the

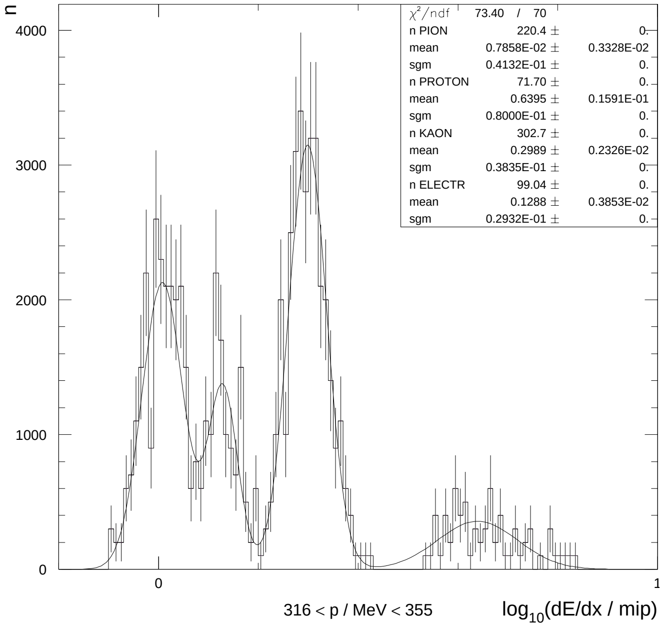

Fig. 4.17
Four-Gaussians fit to the $\log_{10}(\mathrm{d}E/\mathrm{d}x)$ distribution in one of the momentum slices

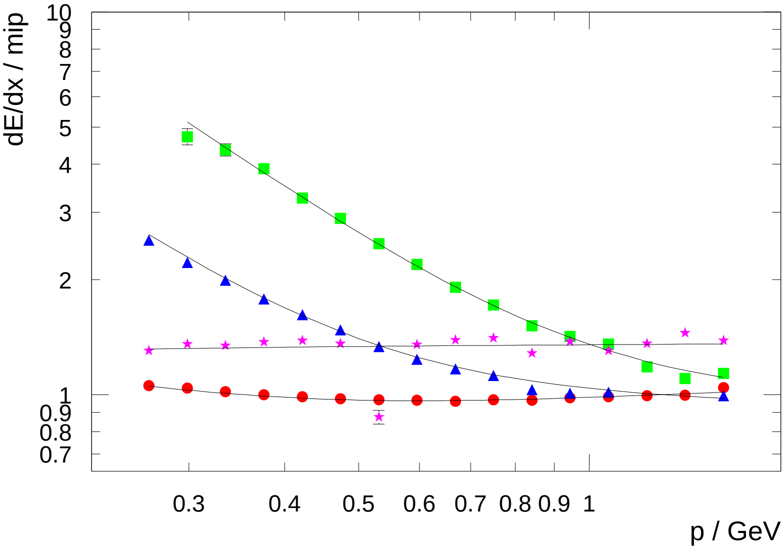

Fig. 4.18 Measured centres of the proton, ▲ kaon, ★ electron and ● pion bands and the fitted $\mathrm{d}E/\mathrm{d}x$ parametrisation. The error bars show the errors from the fits of the peak positions. At about 530 MeV, the kaon band crosses the electron band. Due to the abundance of kaons, the fit procedure could not disentangle the electron contribution to this peak; instead it attributed a fluctuation below the pion band to the electron band. The procedure ignored this erroneous data point when fitting the $\mathrm{d}E/\mathrm{d}x$ parametrisation, because it is too far apart from the value expected from interpolating the neighbouring bins.

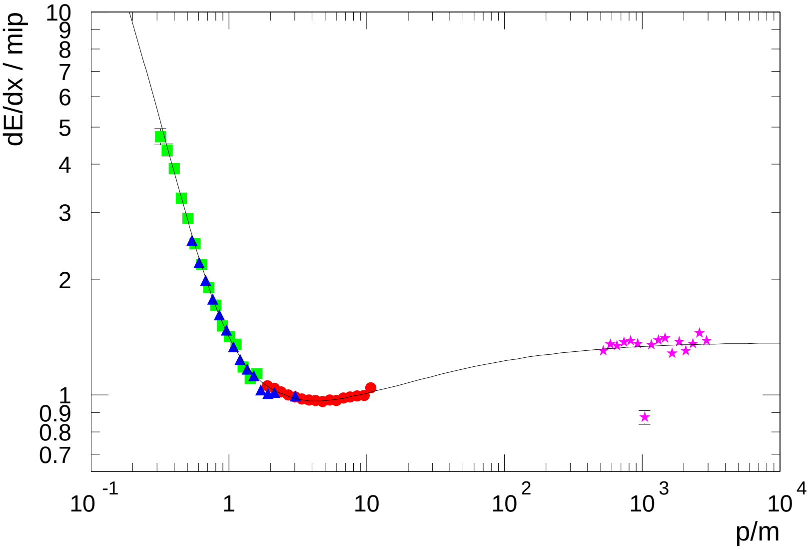

Fig. 4.19 Fitted $\mathrm{d}E/\mathrm{d}x$ parametrisation as a function of $u = p/m$. The weak mass dependence at low velocities has been neglected for this plot. The data points from Fig. 4.18 (protons, ▲ kaons, ★ electrons and ● pions) have been transformed accordingly. The low data point at $u \approx 10^3$ corresponds to that at $p = 530\,\mathrm{MeV}$ in Fig. 4.18.

least-squares fit of the $(\mathrm{d}E/\mathrm{d}x)_{\mathrm{fit}}$ parametrisation. In the region of the relativistic rerise of the hadron bands, $p \gtrsim 1.5\,\mathrm{GeV}$, this procedure was not applied, because it could not resolve the different hadron bands.† The fit resulted in the following parameter values:

$$c_{0,1} = 1.793, 1.031\ , \quad p^{\pi}_{0,1} = 432.8, 594.4\,\mathrm{MeV}\ , \quad \text{for positive tracks;}$$
$$c_{0,1} = 2.341, 1.018\ , \quad p^{\pi}_{0,1} = 376.4, 593.9\,\mathrm{MeV}\ , \quad \text{for negative tracks.}$$

After a transition from p to u and ignoring the weak mass dependence of the parametrisation, which enters only for slow heavy particles, all measurements lie on a single curve given by the parametrisation (see Fig. 4.19). Figure 4.20 demonstrates that the parametrisation reproduces the $(\mathrm{d}E/\mathrm{d}x, p)$ distribution. At the high $\mathrm{d}E/\mathrm{d}x$, low p end of the proton band, the spread of the distribution becomes larger towards higher $\mathrm{d}E/\mathrm{d}x$ values (see also Fig. 4.26). This effect is caused by tracks with very high pulses (height $\gtrsim 200$ counts), which have many saturated hits within the 60% hits considered for the truncated mean; in that case, the peak shift is overcorrected by the variable truncated mean method and too high values are obtained in comparison with tracks that suffer less from saturation.

---

† A possible way of exploring this region could be to tag certain particle species (e.g. cosmic muons) externally and fit them separately.

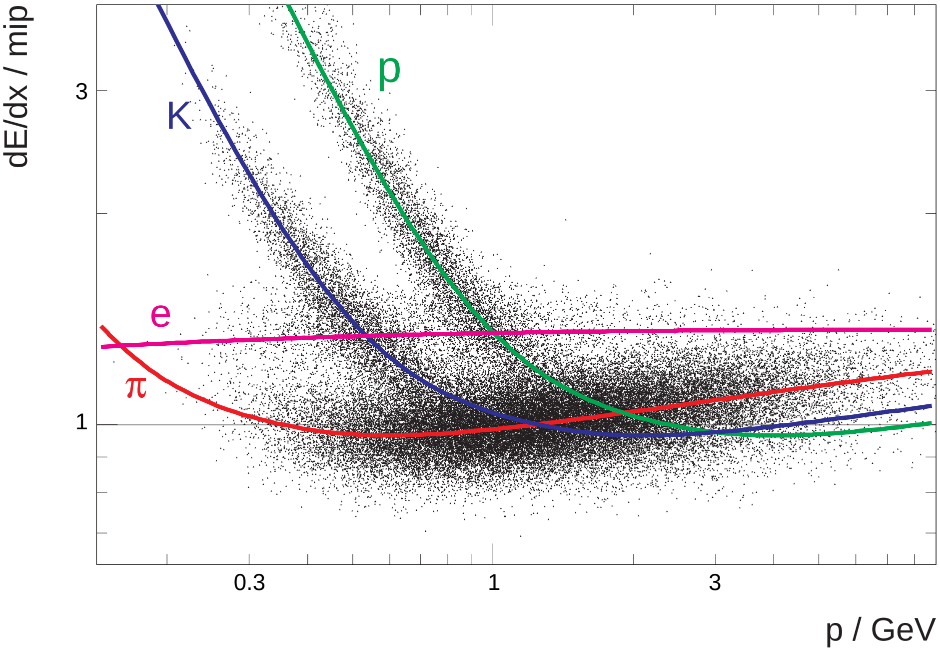

Fig. 4.20 The measured $(\mathrm{d}E/\mathrm{d}x, p)$ distribution and the fitted $\mathrm{d}E/\mathrm{d}x$ parametrisation

4.9 d*E*/ d*x* Resolution and Particle Separation

In order to use $\mathrm{d}E/\mathrm{d}x$ for particle identification not only the centres of the particle bands in the $(\mathrm{d}E/\mathrm{d}x, p)$ plane must be known but also their widths as a function of the track properties. The uncertainty of $\mathrm{d}E/\mathrm{d}x$ owing to the finite momentum resolution can be estimated from the derivative of $(\mathrm{d}E/\mathrm{d}x)_{\mathrm{fit}}$ and the momentum resolution of the CTD,

$$\sigma_{\mathrm{d}E/\mathrm{d}x}(p) = p \left| \frac{\partial(\mathrm{d}E/\mathrm{d}x)}{\partial p} \right| \frac{\sigma_p}{p} = \left| \frac{\partial(\mathrm{d}E/\mathrm{d}x)}{\partial \ln u} \right| \frac{\sigma_{p_\perp}}{p_\perp} \; .$$

Figure 4.21 shows the contribution of the momentum uncertainty to the relative uncertainty of $\mathrm{d}E/\mathrm{d}x$ as a function of p for tracks at a polar angle $\theta = 90°$ (i.e. $p_\perp = p$).[†] It stays well below the percent level (except for slow kaons and protons) and can be neglected. An explicit θ-dependence enters $\sigma_{\mathrm{d}E/\mathrm{d}x}$ through the uncertainty of the space-charge correction (neglected here) and, indirectly, through the dependence on n_{trunc}, because tracks that leave the CTD through the endplate have fewer hits.

[†] For this diagram an earlier $\sigma_{p_\perp}$ parametrisation, $\sigma_{p_\perp}/p_\perp = 0.0058 p_\perp \oplus 0.016$ ($p_\perp$ in GeV), was used instead of (3.1). This parametrisation was quoted in ZEUS publications up to very recently [49]. It overestimates the multiple scattering inside the CTD, but neglects the multiple scattering occurring before a particle reaches the CTD; therefore this parametrisation underestimates the $p_\perp$ uncertainty at low momenta.

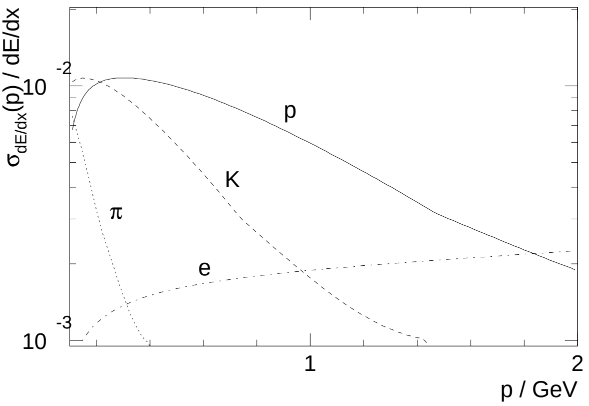

Fig. 4.21
The uncertainty of $\mathrm{d}E/\mathrm{d}x$ resulting from the momentum resolution

The dependence of $\sigma_{\mathrm{d}E/\mathrm{d}x}$ on n_{trunc} can be obtained by fitting the pion band near its minimum ($p = 0.4$–$0.5\,\mathrm{GeV}$), where it is almost flat in $\mathrm{d}E/\mathrm{d}x$ and still separated from the other hadrons. Figure 4.22 shows the distribution for about 10^6 tracks from this momentum range as a function of $\langle \mathrm{d}E/\mathrm{d}x\rangle_{\mathrm{CTD}}$ and n_{trunc}, which is the number of nonsaturated hits used for the truncated mean. The integer arithmetic used for the truncation favours certain values of n_{used}; therefore the even-numbered bins have been merged with the odd ones. Most of the tracks pass all 9 superlayers and thus produce the peak at the upper end of the distribution. The gaps around $n_{\mathrm{trunc}} = 15$ and $n_{\mathrm{trunc}} = 23$ are artefacts of the track reconstruction, which allows tracks only to end in odd-numbered superlayers. Tracks that lie within these gaps lost hits through inefficiencies of the chamber, or hits have been discarded at some stage of the reconstruction process.

In addition to the long band at $\mathrm{d}E/\mathrm{d}x \approx 1$, the distribution of the full track sample has an extra peak in the (low n_{trunc}, low $\mathrm{d}E/\mathrm{d}x$) corner—a feature that disappears when reducing the sample to those tracks which are associated with the primary vertex. The majority of the tracks in this peak are short tracks. Their low $\mathrm{d}E/\mathrm{d}x$ values are an indication that the fraction of noise hits or broken hits contributing to these tracks is rather large; such hits are known to have far lower $\mathrm{d}E/\mathrm{d}x$ values than regular hits [64, 152]. Noise hits also enter the tracks belonging to the long band in Fig. 4.22, but they usually are removed by the truncation of the 10% lowest pulse heights, except for small $n_{\mathrm{trunc}} \sim 5$, where they extend the spread of the band towards lower values and pull the average a bit down. Since the electron band contributes near $\mathrm{d}E/\mathrm{d}x \approx 1.4$ and kaons towards the upper end, there is for all values of n_{trunc} a tail towards higher $\mathrm{d}E/\mathrm{d}x$ values.

For each value of n_{trunc}, a Gaussian was fitted to the $\mathrm{d}E/\mathrm{d}x$ projection, for $\mathrm{d}E/\mathrm{d}x$ values from -3σ up to $+\frac{1}{2}\sigma$ in order to exclude the electron tail. The square of the σ value of the fitted Gaussians represents the $\mathrm{d}E/\mathrm{d}x$ variance for a fixed value of n_{trunc}; it is displayed in Fig. 4.23. That the resolution improves with the square root of the number of hits, except for very low n_{trunc}, where

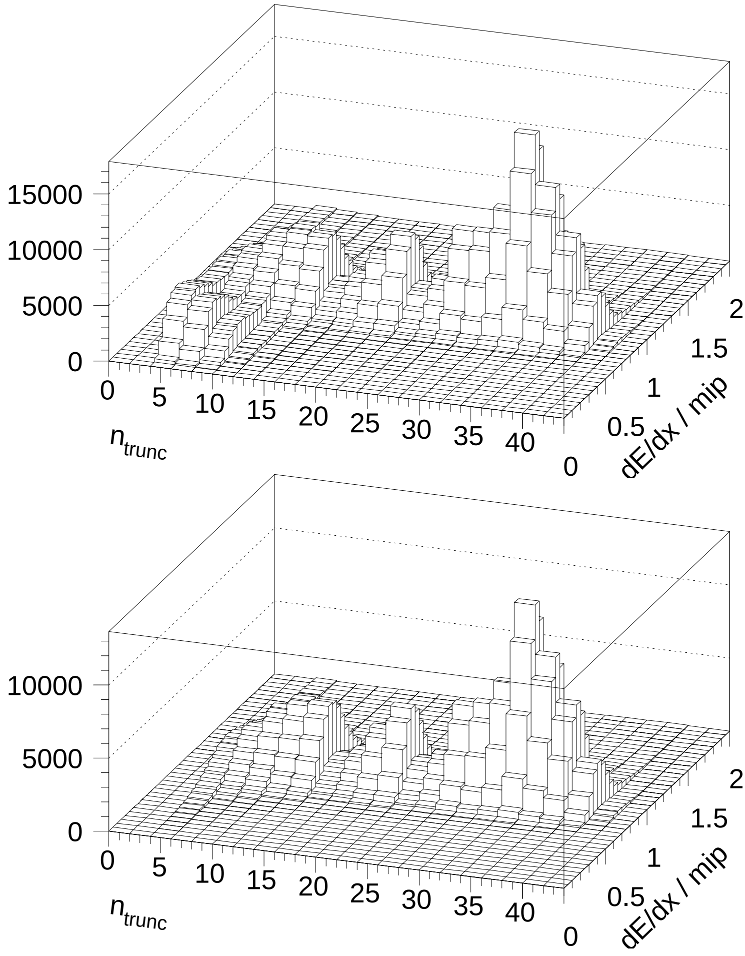

Fig. 4.22
(dE/dx n_{trunc}) distribution of tracks with dE/dx $<$ 2 mip in the momentum range p = 0.4–0.5 GeV. The upper plot shows the distribution for all tracks; for the lower plot, all tracks that are not associated with the primary vertex have been removed.

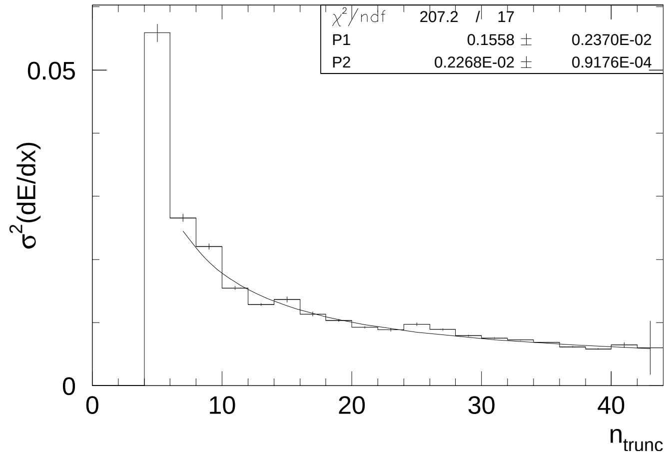

Fig. 4.23
Variance of dE/dx as a function of n_{trunc} for negative tracks in the momentum range p = 0.4–0.5 GeV

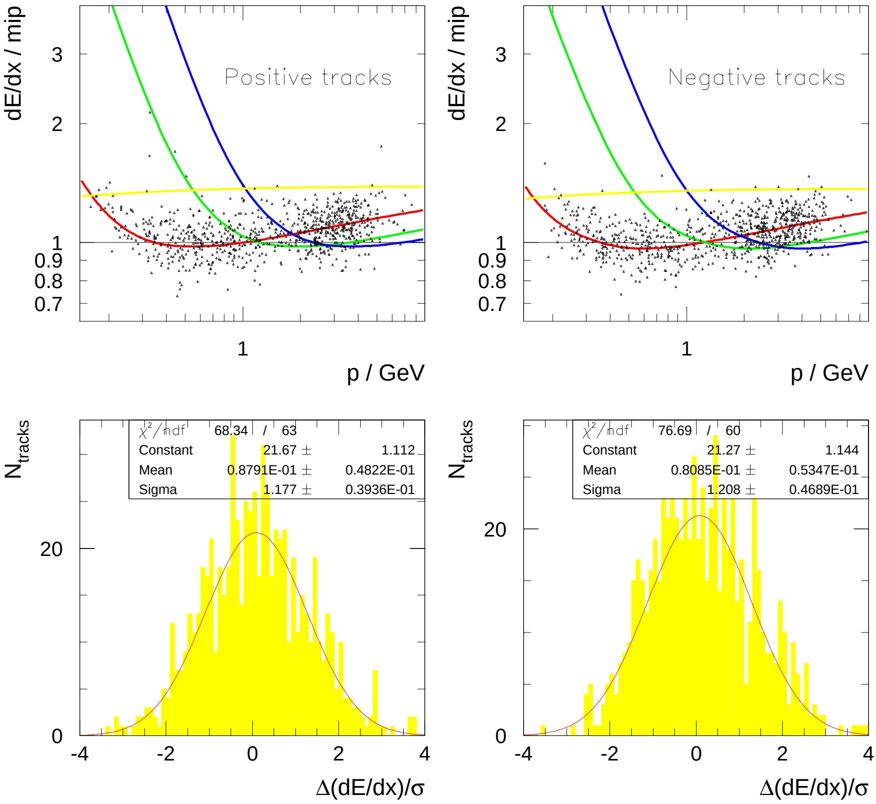

Fig. 4.24 Deviation of the measured $\mathrm{d}E/\mathrm{d}x$ values from the fitted $\mathrm{d}E/\mathrm{d}x$ parametrisation for pions from exclusive ρ^0 production in DIS. The upper plots show the distribution of the pions in the $(\mathrm{d}E/\mathrm{d}x, p)$ plane, separately for positive and negative tracks; the lower histograms show the difference between the measured and the expected $\mathrm{d}E/\mathrm{d}x$ values for this sample in terms of the fitted resolution. If the measured $\mathrm{d}E/\mathrm{d}x$ were described perfectly by the parametrisation, these distributions would peak at zero and had a width of one.

the contamination from noise hits and Landau fluctuations leads to additional smearing. From a fit to this distribution, the variances have been measured to be

$$[\sigma^{\mathrm{neg}}_{\mathrm{d}E/\mathrm{d}x}(n_{\mathrm{trunc}})]^2 = 0.1558/\sqrt{n_{\mathrm{trunc}}} \oplus 0.0023 \,,$$

$$[\sigma^{\mathrm{pos}}_{\mathrm{d}E/\mathrm{d}x}(n_{\mathrm{trunc}})]^2 = 0.1488/\sqrt{n_{\mathrm{trunc}}} \oplus 0.0018 \,,$$

for negative and positive tracks, respectively. Thus the $\mathrm{d}E/\mathrm{d}x$ resolution for tracks having the maximum number of hits is 8% (design value: 6%). Figure 4.24 shows the result of a test of the parametrisations for the centre and width of the $\mathrm{d}E/\mathrm{d}x$ band for a single particle species. For this purpose, pions from exclusive ρ(700) production in DIS have been used. The deviations of the single $\mathrm{d}E/\mathrm{d}x$ measurements from the value expected for pions with the measured momentum has been according to the σ value expected for particles

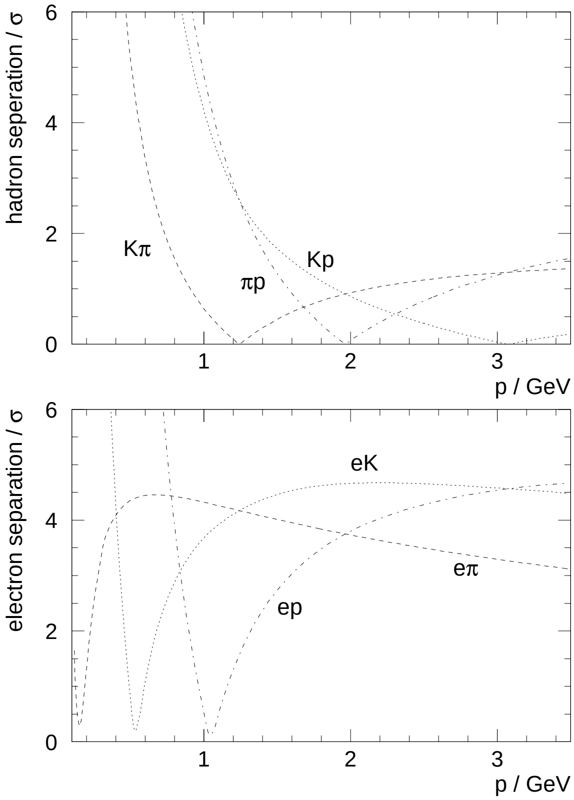

Fig. 4.25
Potential of the CTD to separate different hadron species from each other and from electrons, for tracks with $n_{\text{trunc}} = 32$

with the same number n_{trunc} of used hits. A shift of the mean by about 0.08σ towards larger values and a spread by $\sim 20\%$ can be seen. This discrepancy may be due to

- an underestimation of the pion $\mathrm{d}E/\mathrm{d}x$ below 300 MeV (cf. Sect. 7.3),
- the admixture of background particles (some points in the top plots Fig. 4.24 suggest that the sample contains traces of kaons and electrons),
- residual Landau tails in the distribution from tracks with low n_{trunc},
- a possible slight variation of $\mathrm{d}E/\mathrm{d}x$ as a function of n_{trunc}, the origin of which is still unknown [192]. This can lead to a systematic shift, because the band centres have been determined using only tracks with large n_{trunc}.

Knowing the band positions and widths, the particle separation power of the CTD can be estimated from $(\mathrm{d}E/\mathrm{d}x)_{\text{fit}}$. In the field of charm analysis, the kaon–pion separation is important for the study of hadronic D meson decays and the electron–hadron separation is relevant to studies of semileptonic decays. Figure 4.25 shows the particle separation power for long tracks with $n_{\text{trunc}} = 32$. The kaon–pion separation for these tracks is better than 2σ for particle momenta below 0.7 GeV. For the separation of electrons from hadrons there are two small windows around 0.3 GeV and 0.8 GeV and a large region beginning at 1.5 GeV with a separation of more than 3σ. Note, due to the small rate of electrons as compared to hadrons, they appear merely as a tail of the hadron peak when looking at the $\mathrm{d}E/\mathrm{d}x$ distribution above 1.2 GeV.

4.10 d*E*/d*x* Likelihood

How can one go about using $\mathrm{d}E/\mathrm{d}x$ in a physics analysis? The answer depends on the aim of the study. The measurement of charm cross-sections from semileptonic decays, for instance, relies on counting the absolute number of electrons produced; this number can be obtained by statistically subtracting the contribution from particles other than electrons from the measured $\mathrm{d}E/\mathrm{d}x$ distributions of the candidate tracks within a given momentum bin. For that purpose it is not necessary to know explicitly for every track in the candidate sample whether it did originate from an electron or not; however, clean reference $\mathrm{d}E/\mathrm{d}x$ distributions for signal and background are needed for the statistical subtraction and must be obtained using tagging methods other than $\mathrm{d}E/\mathrm{d}x$.

When studying hadronic decays of charmed mesons, particle identification through $\mathrm{d}E/\mathrm{d}x$ can help in purifying the sample by reducing the background from candidates with a wrong mass assignment. Here the total number of tracks attributed to a certain particle species is of no interest; instead one wants to know for each single track whether it possibly was produced by a particle of a certain species. This question is not the same as asking how large the probability is that the track belongs to a certain particle species: that likelihood depends not only on the positions and widths of the $\mathrm{d}E/\mathrm{d}x$ bands but also on the relative abundances of the species as a function of the track momentum. The abundances depend strongly on the track sample: compare, for example, the $\mathrm{d}E/\mathrm{d}x$ distribution near 350 MeV of all tracks from a sample run (Fig. 4.12) with that for the preselected 1995 DIS $\mathrm{D}^{*\pm}$ events with large n_{used} (Fig. 4.17).

The fits discussed above provide us with the mean and the standard deviation of the $\mathrm{d}E/\mathrm{d}x$ values measured for particles of fixed mass, momentum. They also show that for sufficiently large n_{trunc}, $\log \mathrm{d}E/\mathrm{d}x$ follows a Gaussian distribution. For a particle of known species i and momentum p we therefore can describe the deviation of a single $\mathrm{d}E/\mathrm{d}x$ measurement from the ideal $\mathrm{d}E/\mathrm{d}x$ values in terms of the random variable

$$\chi_i^2 = \frac{[\ln \langle \mathrm{d}E/\mathrm{d}x \rangle_{\mathrm{CTD}} - \ln (\mathrm{d}E/\mathrm{d}x)_{\mathrm{fit}}(p/m_i)]^2}{\sigma^2_{\mathrm{d}E/\mathrm{d}x}(n_{\mathrm{trunc}})} \, ,$$

of which the probability density is given by

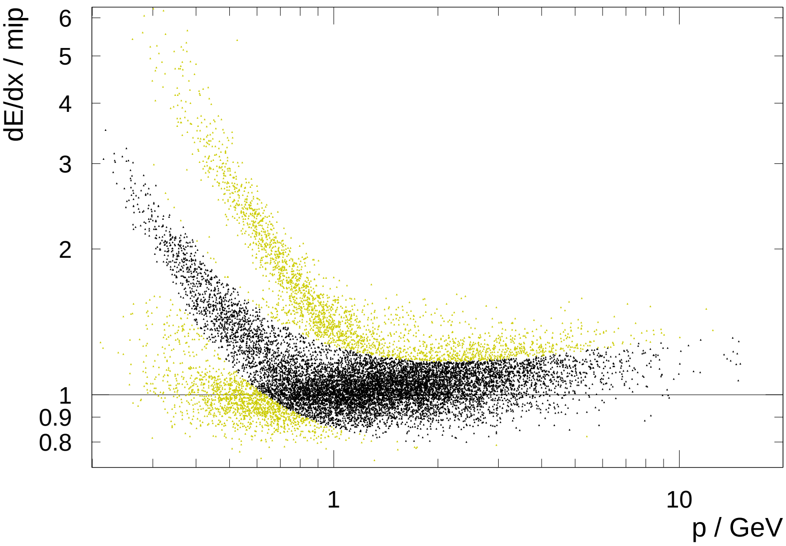

Fig. 4.26 Kaon tag using $\mathrm{d}E/\mathrm{d}x$ likelihood. The dark dots in the $(\mathrm{d}E/\mathrm{d}x, p)$ distribution mark tracks with $\ell_\mathrm{K} \geqslant 1.4\%$ (i.e. $\chi^2_\mathrm{K} < 6$); light dots mark tracks that fall below this level. Only tracks with $n_\mathrm{trunc} > 8$ are plotted.

$$f(\chi_i^2) = \frac{1}{\sqrt{2\pi\chi_i^2}}\,\mathrm{e}^{-\frac{1}{2}\chi_i^2}\ .$$

We define the *likelihood* ℓ_i to be the probability of measuring the observed or a larger value of χ_i^2,

$$\ell_i(\langle \mathrm{d}E/\mathrm{d}x\rangle_\mathrm{CTD}, p, n_\mathrm{trunc}) \equiv P(\chi_i^2 \geqslant \chi^2_{i\,\mathrm{obs}}) = \int_{\chi^2_{i\,\mathrm{obs}}}^{\infty} \mathrm{d}u\ \frac{1}{\sqrt{2\pi u}}\,\mathrm{e}^{-\frac{1}{2}u}\ , \tag{4.15}$$

provided that the track under study belongs to species i. This likelihood can be thought of as the significance of a statistical test. It is used for the removal of tracks with low significance for mass hypothesis i from a sample, as illustrated in Fig. 4.26. Being a significance level, the likelihood limit directly provides an estimate of the amount of type I errors produced by this kind of selection—for the sample presented in Fig. 4.26, for instance, we can expect to lose ≈1.4% of the true kaons through the likelihood cut $\ell_\mathrm{K} \geqslant 1.4\%$. The integral (4.15) does not need to be evaluated for each track and hypothesis; since ℓ_i is a monotonic function of $\chi^2_{i\,\mathrm{obs}}$, an identical selection is obtained by applying a corresponding cut in χ^2.

The exclusive production of $\phi(1020)$ mesons in the decay mode $\phi \to \mathrm{K}^+\mathrm{K}^-$ serves as an impressive example of a successful application of $\mathrm{d}E/\mathrm{d}x$ likelihood tagging at ZEUS [134, 111]. Since the sample contains only events with

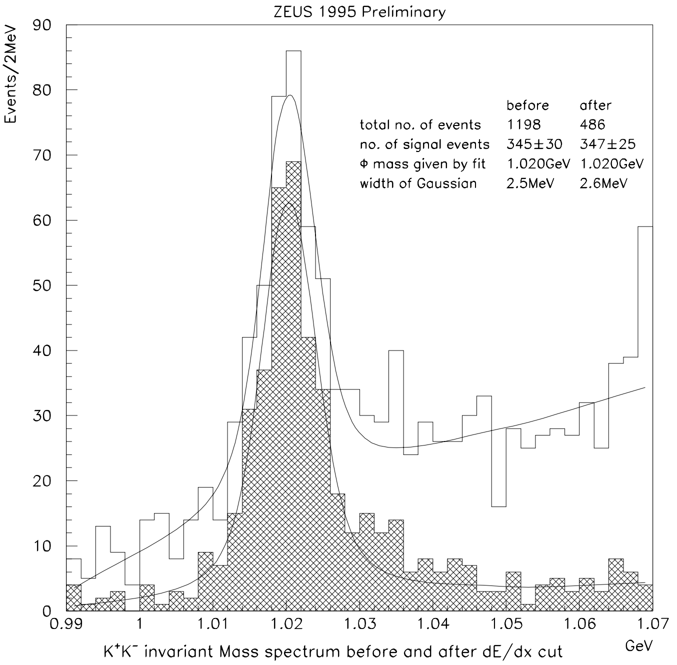

Fig. 4.27
Mass distribution of candidates for exclusive $\phi(1020)$ production in diffractive deep inelastic scattering. The open histogram shows the distribution for the full sample, requiring a positive and a negative track and assuming them to be kaons; the shaded histogram shows the distribution after removing all tracks with $\ell_{\mathrm{K}} < 0.1\%$. While the background is dramatically reduced, the signal remains virtually unchanged.

exactly two hadron tracks, and the momentum of at least one of the kaons is in a region where the kaon and pion bands are well separated, the background of pions from ρ^0 production can be suppressed efficiently without reducing the signal, as demonstrated in Fig. 4.27. For samples with not so clean conditions as for the ϕ sample, it is often desirable to use tighter constrains on ℓ_i in order to make the background rejection more powerful. However, this leads to unnecessary losses of events in $(\mathrm{d}E/\mathrm{d}x, p)$ regions where the particle bands are well separated. These losses can be prevented by accepting also candidates outside the likelihood limit if the $\mathrm{d}E/\mathrm{d}x$ likelihood assuming the track to belong to desired particle species is still large compared to the likelihoods for other mass assumptions. For this purpose, a *normalised likelihood* can be defined,

$$\ell_i^{\mathrm{norm}} = \ell_i \,/\, \textstyle\sum_j \ell_j \ ,$$

where the sum extends over all particle species considered. It should be noted that the quantity ℓ_i^{norm} is just a measure of how close a measured $\mathrm{d}E/\mathrm{d}x$ value is to the ideal value for species i as compared to other species. It is by no means the likelihood of a track to belong to species i rather than to one of the other species. A value of, say, $\ell_{\pi}^{\mathrm{norm}} = \ell_{\mathrm{K}}^{\mathrm{norm}} = 0.5$ does not mean that a track is equally likely to be a pion or kaon—it just means that the measured $\mathrm{d}E/\mathrm{d}x$ for this track is equally distant from the ideal values for kaons and pions of the same momentum.

4.11 Simulation of the dE/ dx Measurement

The amount of ionisation produced by a charged particle traversing the CTD is calculated in the simulation as follows: first the restricted mean energy loss is looked up for the particle species and energy under consideration. This value is then allowed to fluctuate according to the Landau theory. Look-up tables are provided for electrons, positrons, muons and protons; the proton table is used for other hadrons (e.g.kaons) after scaling the energy accordingly. These values are accumulated for each sense wire over all GEANT steps of the particle traversing its drift volume. The GEANT hits are converted to pulse heights by per-wire conversion and smearing factors. Finally the pulse heights are corrected for the wire gain, for geometric effects depending on the track and field angles (θ, λ, ψ') and on the z-position, according to the attenuation along the wire.

Figure 4.28 shows the reconstructed $\langle \mathrm{d}E/\mathrm{d}x \rangle_{\mathrm{norm}}$ values from MC tracks (MOZART 14.3, GEANT 3.13) in comparison with the parametrisations fitted to the data. The spread of the MC distribution is similar to that of the data (see Fig. 4.20), but the rise of the hadron bands at low velocities is much steeper in the MC simulation than in data; furthermore, the electron band lies at a $\approx$15% larger value. In addition, the difference between negative and positive tracks is exaggerated in the simulation as compared to the data.

The discrepancy between data and detector simulation makes it difficult to calculate efficiency and purity of selection cuts that are based on $\mathrm{d}E/\mathrm{d}x$, because both quantities depend on the sample under study. For low-multiplicity samples like the exclusive ϕ production (see Sect. 4.10), the efficiencies can in principle be obtained from the data by applying tight cuts to either of the two decay particles and studying the acceptance of the other. Yet the quantities thus obtained are not universally applicable. At larger multiplicities like those we typically find in open charm production, more than one or two particle species contribute to the $(\mathrm{d}E/\mathrm{d}x, p)$ distribution and the $\mathrm{d}E/\mathrm{d}x$ measurement deteriorates in a busy chamber, where wrong assignments of hits to tracks, track crossings, local showering, etc., are more likely to happen.

Changing the MC code such that $\mathrm{d}E/\mathrm{d}x$ features of the CTD are better reproduced is a demanding task. It does not suffice to replace the values in the $\mathrm{d}E/\mathrm{d}x$ look-up tables of GEANT with values obtained from the fitted parametrisation—this would solve the problem for either positive or negative tracks; but in order to simulate also the values for the other charge correctly, it is necessary to change via the ψ' angle correction how the ionisation-to-pulse-height transformation depends on the charge of the particle. Such a modification, however, affects also the charge dependences of other quantities (see Sect. 4.3), which already have been adjusted carefully in order to make data and MC predictions agree.

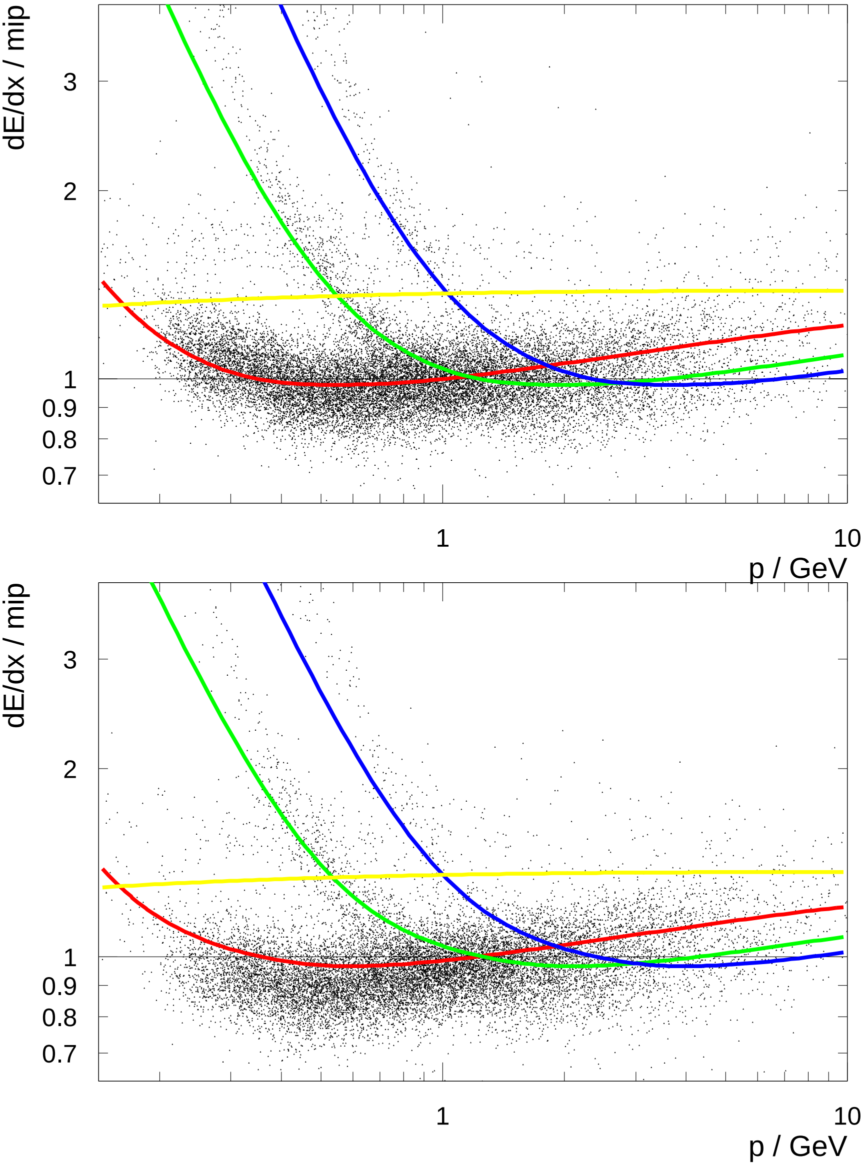

Fig. 4.28 Energy loss $\langle \mathrm{d}E/\mathrm{d}x \rangle_{\mathrm{CTD}}$ of positive (top) and negative (bottom) tracks as assumed by the detector simulation. The lines represent the values of the parametrisations fitted to the data for electrons, pions, kaons and protons.

5 Physics Simulation

For the calculation of acceptances, Monte Carlo (MC) simulations of the particle interactions and of the detector response were employed. A full event simulation consists of two steps: First an *event generator* calculates the primary scattering process at the parton level. Using a hadronisation model, the final state particles are obtained. Particle decays at the primary vertex (i.e., strong and electromagnetic decays) are simulated at this stage.† The list of 4-vectors is handed over to the *detector simulation,* which calculates the decays of long-lived particles and the detector response to the event. The ZEUS detector is modelled by the MOZART program (cf. Sect. 3.4). Based on the GEANT package [105], MOZART simulates for every particle its interaction with the detector material, possible decays, the signals produced in the sensitive components like tracking devices and calorimeters, and the digitisation of the signals, including the various sources of noise.

Event generators divide the simulation of the scattering process, which is illustrated in Fig. 5.1, into several phases.‡ Before generating events, the matrix

---

† The HERWIG generator restarts its hadronisation algorithm for the daughter particles of strong decays.

‡ The discussion concentrates on the hadronic side of the ep interaction; the phenomenology of the leptonic side is comparatively simple and well described by QED.

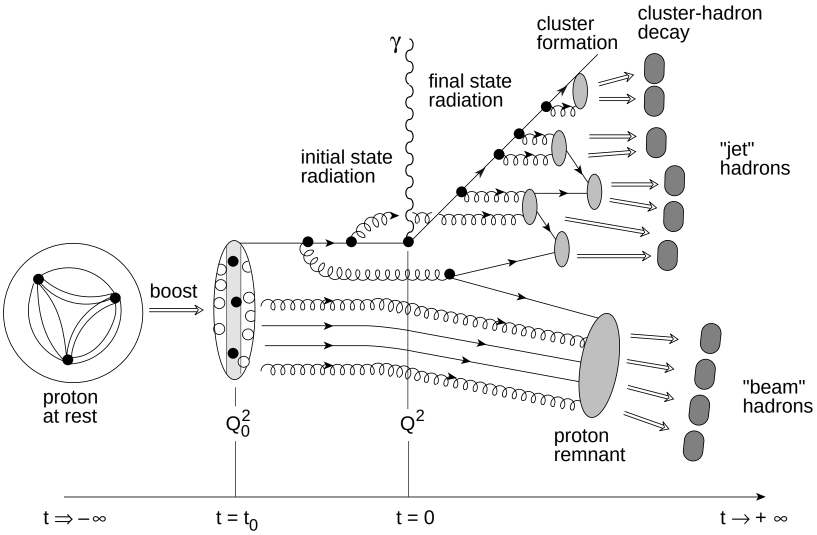

Fig. 5.1 General scheme for the γ^*p scattering process [89]

elements for the processes under study are calculated up to a certain order in α_s. For the simulation of a single event the generator chooses the flavour and momentum of the incoming partons, according to the parton density distributions, and the details of the hard subprocess, calculated from QCD matrix elements. For events that fall into the phase space region of interest, some terms of higher order in QCD can be added by evolving cascades of softer subprocesses, including gluon emission and gluon splitting. While at large time-scales the Lorentz-boosted proton resembles a flat pancake of independent partons (see figure, $t = t_0$), the short time-scale of the interaction with the boson exchanged makes the fluctuations inside the proton visible—not only the struck parton is affected, but the recombination of the whole evolution is disturbed by the impact. Most generators distinguish between the QCD cascade originating from initial fluctuations (initial state parton shower) and that which emerges from the hard subprocess (final state parton shower). These shower processes are described by the DGLAP formalism (see Sect. 2.2), considering only the leading terms in $\ln Q^2$. While the calculations up to this point are done on the parton level, in the last phase hadrons are formed from the partons, which tend to be clustered in jets. The scattered electron plus the produced hadrons define the final state that is handed over to the detector simulation.

From the variety of event generators and parameter sets available, those are chosen which give a reasonable description of the process under study. For D^* production in DIS, the process can be factorised into a QED subprocess deflecting the incoming electron, and a QCD subprocess giving rise to heavy flavour production; accordingly, the event selection and acceptance studies can be done separately for the reconstruction of DIS, where details of charm production and decay play a minor rôle, and the reconstruction of the outgoing D^* meson, where the MC generator does not need to include QED radiative corrections to the hard subprocess. The RAPGAP generator (Version 2.05 [136, 137]) currently is the only program that provides a good overall simulation of charm production *and* includes QED radiative corrections. Alternatively other programs were used in order to estimate systematic effects for the reconstruction of the event kinematics (LEPTO 6.3 [129]) and for charm production and decay (HERWIG 5.8 [147]). In order to save computing time and disk space, all generators were setup such that only events with at least on D^* meson in the central region of the detector were fully processed ($|\eta| < 2$). All MC programs were run with their default parameters.

The RAPGAP generator was originally designed for the simulation of diffractive events (which are marked by a rapidity gap, hence its name). It now simulates a large spectrum of processes, including heavy flavour production in leading order PGF. RAPGAP calls HERACLES 4.4 [140, 180] for including the simulation of QED radiation from the lepton line; it thereafter calculates the massive LO matrix element for the hard PGF subprocess $\gamma^* g \rightarrow c\bar{c}$

(cf. Fig. 2.8). For this analysis, the proton parton density functions were taken from the GRV 94 HO set [108]. In RAPGAP the ARIADNE 4 program [145] was called for adding the contribution from higher order QCD processes in the coherent parton shower approach of the colour dipole model [13]. This model does not distinguish between initial and final state cascades, but calculates a coherent sum of them, including interference terms. ARIADNE 4 provides the best description of the observed hadronic final state in inclusive DIS [80].

For the charm quarks a mass of $m_{\mathrm{c}} = 1.5\,\mathrm{GeV}$ was assumed. They were fragmented using the Peterson model (see Sect. 2.4) with the hardness parameter set to $\varepsilon_{\mathrm{P}} = 0.035$; the other partons were hadronised following the phenomenological approach of the Lund string model [12] as implemented in JETSET 7.4 [177].

The LEPTO generator was interfaced with HERACLES in the framework of the DJANGO 6.2 [66] program. It computes the zeroth and first order matrix elements for inclusive DIS, complemented by parton shower calculations (ME+PS), and also uses Lund fragmentation. The HERWIG program is another omni-purpose generator, but it does not include QED radiative corrections. For this analysis, HERWIG was used to calculate the matrix element for PGF charm production in LO, supplemented by LLA parton showers. The hadronisation was simulated by the HERWIG-specific cluster fragmentation model, which by construction takes the mass of the charm quark into account.

For the extrapolation of the measurements from the experimentally accessible kinematic range to the full phase space, the program HVQDIS 1.1 [118] was used, which calculates differential charm production cross-sections for any region of phase space and the heavy quark contributions to the structure functions F_2 and F_{L}. It computes the LO and NLO QCD matrix elements for PGF, where the latter includes the radiation of a third parton in addition to the two outgoing charm quarks. The calculations are done in the fixed flavour number $n_f = 3$ scheme (FFN 3), where the three light flavours (and the gluon) are considered massless and active, whereas charm is produced perturbatively (cf. Sect. 2.4). Peterson fragmentation was assumed with $\varepsilon_{\mathrm{P}} = 0.035$.

For the acceptance studies, 60000 events with $Q^2 > 0.6\,\mathrm{GeV}$ were generated with RAPGAP; 30000 events each were generated with LEPTO and HERWIG. RAPGAP has calculated the charm production cross-section to be $\sigma_{\mathrm{c\bar{c}}} = 88.3\,\mathrm{nb}$. Since all $\mathrm{c\bar{c}}$ events were forced to contain $\mathrm{D}^* \rightarrow \mathrm{K}\pi\pi_{\mathrm{s}}$ decays, the effective cross-section has to be scaled down by the production fraction for this decay mode (2.7), yielding a corresponding luminosity of $\int \mathrm{d}t\,\mathscr{L} \approx 58\,\mathrm{pb}^{-1}$ for the MC sample, which is about 10 times the luminosity of the data sample.

6 Reconstruction of DIS Events

6.1 Electron Reconstruction

Neutral current deep inelastic scattering events in this analysis are characterised by photon virtualities $Q^2 \gtrsim 1\,\mathrm{GeV}$, which are large enough to deflect the scattered electron into the main calorimeter (CAL). The energy deposits from electrons can be identified by their topology via software routines called *electron finders.* Four different routines were used:

LOCAL uses local maximum clustering and defines a likelihood from the energy weighted radius of the cluster and the EMC contribution to the total electron energy.

ELEC 5 investigates the radius of the electromagnetic cluster, the energy sharing between EMC and HAC, and the energy share inside and outside various cones around the impact position.

EEXOTIC is based on a precursor of ELEC 5, with fine-tuning for special topologies.

SINISTRA identifies electromagnetic clusters with a neural network, as will be elaborated below.

During the 1995 data taking customised versions of the fast LOCAL and ELEC 5 electron finders were run on the TLT for tagging DIS events. An event was accepted if at least one of the finders detected an electron candidate outside a box around the rear beam pipe. The size of the box varied during the data taking period with increasing luminosity from $(x \times y) = \pm 12\,\mathrm{cm} \times \pm 6\,\mathrm{cm}$ (thus exploiting the full range that became accessible by an inward shift of the central RCAL modules) up to $\pm 14\,\mathrm{cm} \times \pm 14\,\mathrm{cm}$.

In the off-line reconstruction all four electron finders were run. For the present analysis, the 1995 version of the SINISTRA [1, 176] electron finder was chosen, which in general provides the largest efficiency and purity (see Fig. 6.1). The electron acceptance decision of SINISTRA is based on the topology of calorimeter *islands.* Islands are formed by comparing the energy deposit of each calorimeter tower with that of its eight neighbours: if all neighbours have lower energy, the tower becomes an island *seed;* otherwise the tower is linked to its neighbour with the largest energy. In this way, the calorimeter is divided into contiguous clusters around the local maxima of the energy distribution (see Fig. 6.2). Islands are called *electromagnetic* if they have at least 90% of their energy deposited inside a window of 3×3 towers around the seed

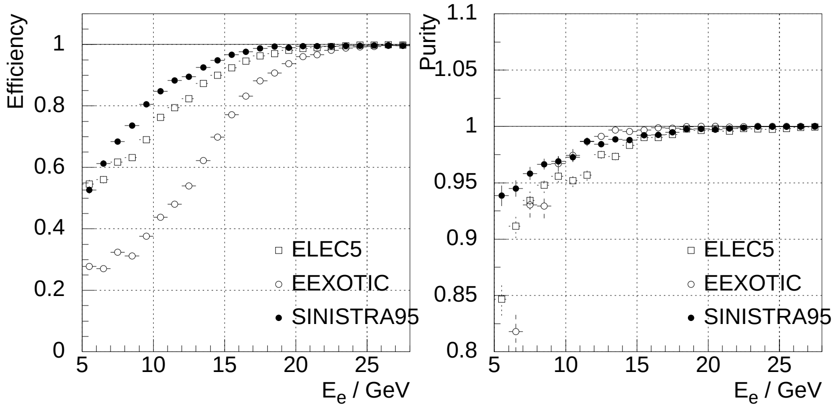

Fig. 6.1 Efficiency and purity of different electron finders as a function of the electron energy [158]. The LOCAL electron finder, which is not included in these diagrams always has a lower efficiency and purity than SINISTRA.

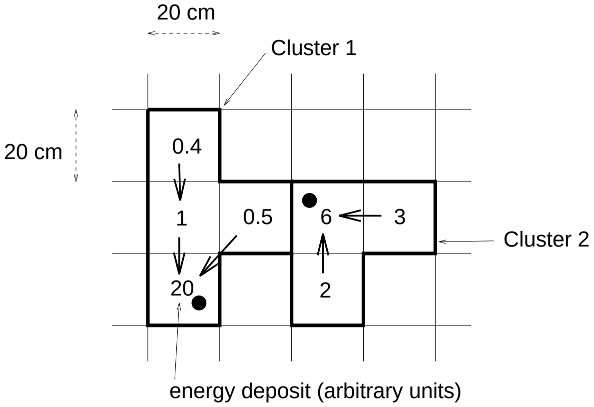

Fig. 6.2
Example of the island clustering used by SINISTRA [1]. The numbers show the energy deposits in arbitrary units; the arrows indicate how individual calorimeters towers are linked together, forming islands around the seed cells (marked with dots). A distinctive feature of this clustering algorithm is its power to split adjacent energy deposits into separate clusters if they are separated by a valley of low energy towers.

and less than 1 GeV outside the window, and if more than 80% of the window energy falls into in the EMC section. For each electromagnetic island, SINISTRA feeds the energy of all calorimeter cells in the 3×3 tower window into a neural network, together with the angle of incidence, which is obtained from the position of the island and the reconstructed vertex. By summing adjacent PMTs in the FCAL and BCAL towers, a similar granularity as for the RCAL is obtained, so that for all calorimeter sections the same number of 55 input variables characterise the candidate. The neural network determines a single output variable P_{SINI}, which is a measure of the probability that the candidate under study is the scattered electron. For the present analysis a value $P_{\mathrm{SINI}} > 0.9$ was required.

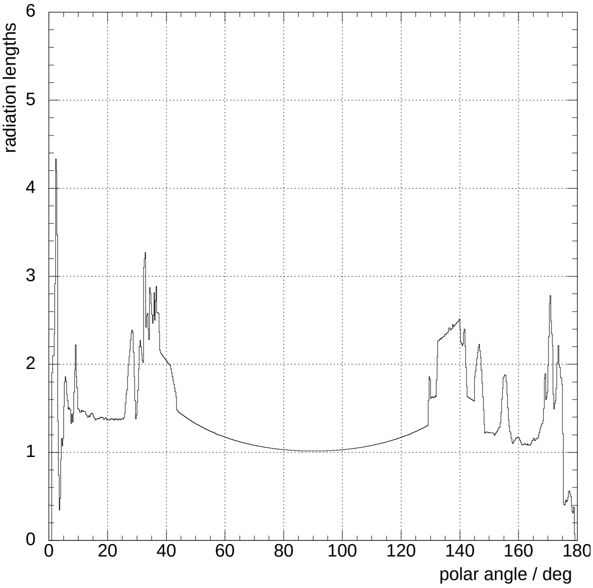

Fig. 6.3
Distribution of inactive material in front of the calorimeter as a function of the polar angle [127]

In general, electrons deposit a substantial amount of energy in the inactive material ahead of the calorimeter (cf. Fig. 6.3). The passive material constitutes about 1–1.5 radiation lengths, except near the beampipe and in the area of the support structure for the solenoid ($\theta \approx 35°,\ 135°$), where it amounts up to $3\,X_0$. For electrons emitted in the direction of the RCAL, the energy lost in inactive material can be corrected for using the information from the rear presampler, RSAM, and the SRTD. The correction constants were obtained from the neutral current DIS event sample in the kinematic peak, from quasi-elastic ρ^0 production and from *QED Compton* events. Kinematic peak events are constrained to the very low y region, where the scattered electron energy is close to the electron beam energy and can be determined with an accuracy of $\sim 0.5\%$ from the scattering angle; in quasi-elastic ρ^0 production ($\mathrm{ep} \rightarrow \mathrm{ep}\rho^0$, $\rho^0 \rightarrow \pi^+\pi^-$), the electron energy is calculated from its scattering angle and the pion momenta; QED Compton events ($\mathrm{ep} \rightarrow \mathrm{ep}\gamma$), where the electron and the photon are contained in the calorimeter, are fully determined by the measured scattering angles, because the transverse momentum of the scattered proton is small. The energy loss in the inactive material in front of the calorimeter is correlated with the energy deposited in the SRTD, yielding corrected energies

$$E_{\mathrm{corr}} = 1.037\,(E_{\mathrm{CAL}} + 0.028 E_{\mathrm{SRTD}})$$

for real data, and a similar relation for MC generated events [73]. Outside the acceptance of the SRTD a similar correction [41] was applied using the rear presampler,

$$E_{\text{corr}} = E_{\text{CAL}} + 0.072 E_{\text{RSAM}} \ .$$

After applying these corrections, there remains an absolute scale uncertainty of 2% at 10 GeV, gradually decreasing to 1% at 27.5 GeV.

The impact position of the electron is determined with a resolution of about 1 cm from the signal difference between the two PMTs of the hit cell and the energy share of neighbouring cells. By making use of the position data from the SRTD, the resolution is further improved to about 0.3 cm in the region of its coverage.

6.2 Event Kinematics

In order to assign a recorded event to a certain kinematic regime, the Lorentz-invariant variables characterising the inclusive DIS process must be accurately known. The fact that both the hadronic final state and the scattered electron of the events under study are registered in the detector, permits use of several methods for the determination of the kinematics from observed quantities. Figure 6.4 displays how the quantities used in the following are correlated with certain regions of phase space.

The kinematics can be calculated from the energy E'_{e} and polar angle θ of the scattered electron ('electron method'),

$$x_{\text{e}} = \frac{E_{\text{e}}}{E_{\text{p}}} \frac{E'_{\text{e}}(1+\cos\theta)}{2E_{\text{e}} - E'_{\text{e}}(1-\cos\theta)} \ , \tag{6.1a}$$

$$y_{\text{e}} = 1 - \frac{E'_{\text{e}}}{2E_{\text{e}}}(1-\cos\theta) \ , \tag{6.1b}$$

$$Q^2_{\text{e}} = 2E_{\text{e}}E'_{\text{e}}(1+\cos\theta) \ . \tag{6.1c}$$

For the majority of the events in this analysis, which is characterised by small electron scattering angles (i.e. large θ), the resolution of Q^2_{e} is governed by the resolution of the angle measurement. The resolution of y_{e} is best where E'_{e} is substantially smaller than the beam energy E_{e}.

The event kinematics can also be determined from the hadronic system, which balances the transverse momentum of the scattered electron. Jacquet and Blondel (JB) have shown [132] that it is not necessary to consider solely hadrons of the current jet: the event kinematics can be reconstructed directly from the transverse momentum and the difference $(E - p_z)$ of *all* hadrons found in the calorimeter, independently from the reconstruction of jets (viz. the current jet),

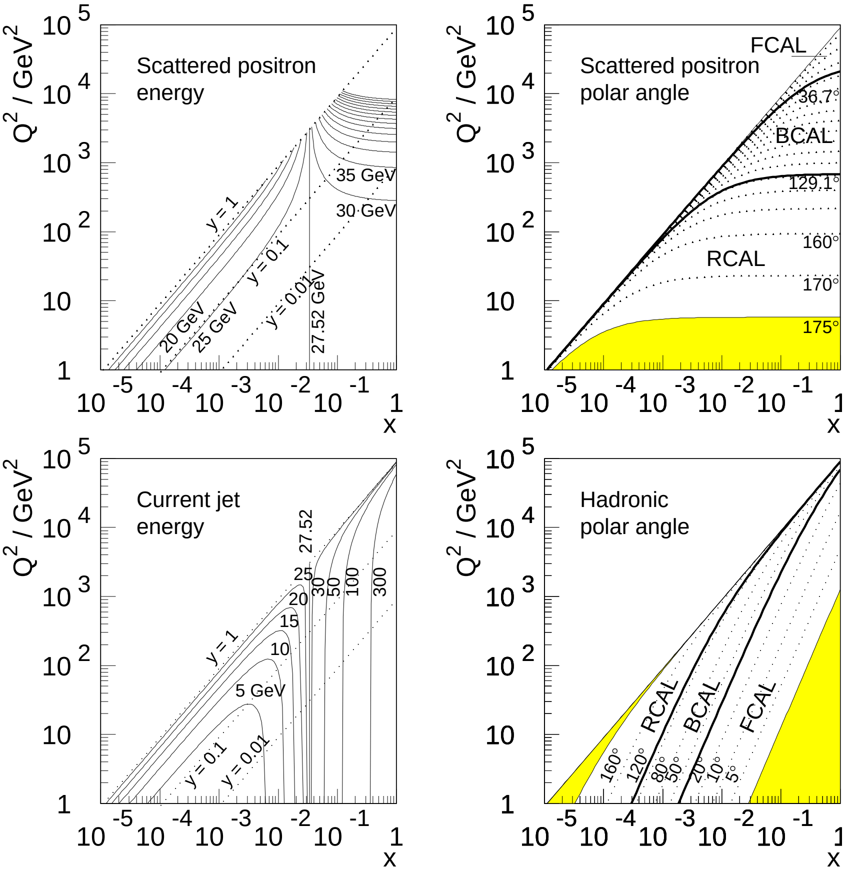

Fig. 6.4 Iso-lines of electron and hadronic energies and polar angles in (x, Q^2) phase space (adapted from Ref. 163)

$$y_{\mathrm{JB}} = \frac{\sum_{\mathrm{h}}(E_{\mathrm{h}} - p_{z\mathrm{h}})}{2E_{\mathrm{e}}}\,, \tag{6.2a}$$

$$Q^2_{\mathrm{JB}} = \frac{(\sum_{\mathrm{h}} p_{x\mathrm{h}})^2 + (\sum_{\mathrm{h}} p_{y\mathrm{h}})^2}{1 - y_{\mathrm{JB}}}\,, \tag{6.2b}$$

$$x_{\mathrm{JB}} = \frac{Q^2_{\mathrm{JB}}}{s\,y_{\mathrm{JB}}}\,. \tag{6.2c}$$

The JB method is based on the assumption that the net transverse momentum of particles lost through the beam hole is small and can be neglected. For low values of $y_{\mathrm{JB}} \lesssim 0.03$ the resolution is much better than with the electron method; however, the Q^2_{JB} resolution is always worse than Q^2_{e}.

The so-called *hadronic angle,* γ, under which hypothetically (in the framework of the QPM) a struck massless parton of the proton with no primordial transverse momentum would emerge, can be calculated from the JB variables [25, 125],

$$\begin{aligned}\cos\gamma &\equiv \frac{(\sum_{\mathrm{h}} p_{x\mathrm{h}})^2 + (\sum_{\mathrm{h}} p_{y\mathrm{h}})^2 - [\sum_{\mathrm{h}}(E_{\mathrm{h}} - p_{z\mathrm{h}})]^2}{(\sum_{\mathrm{h}} p_{x\mathrm{h}})^2 + (\sum_{\mathrm{h}} p_{y\mathrm{h}})^2 + [\sum_{\mathrm{h}}(E_{\mathrm{h}} - p_{z\mathrm{h}})]^2} \\ &= \frac{Q^2_{\mathrm{JB}}(1 - y_{\mathrm{JB}}) - 4E^2_{\mathrm{e}} y^2_{\mathrm{JB}}}{Q^2_{\mathrm{JB}}(1 - y_{\mathrm{JB}}) + 4E^2_{\mathrm{e}} y^2_{\mathrm{JB}}} \; .\end{aligned}$$

The event kinematics can also be determined from γ and θ alone (‘double angle method’, DA)—a method which is insensitive to the energy scales,

$$\begin{aligned}x_{\mathrm{DA}} &= \frac{E_{\mathrm{e}}}{E_{\mathrm{p}}} \, \frac{\sin\gamma + \sin\theta + \sin(\theta + \gamma)}{\sin\gamma + \sin\theta - \sin(\theta + \gamma)} \; , \\ y_{\mathrm{DA}} &= \frac{\sin\theta \, (1 - \cos\gamma)}{\sin\gamma + \sin\theta - \sin(\theta + \gamma)} \; , \\ Q^2_{\mathrm{DA}} &= 4E^2_{\mathrm{e}} \, \frac{\sin\gamma \, (1 + \cos\theta)}{\sin\gamma + \sin\theta - \sin(\theta + \gamma)} \; .\end{aligned}$$

The variable y_{DA} is independent of the energies of the incoming particles and hence resistent against initial state QED radiation.

The criteria for the choice of the reconstruction method are optimum resolution and minimisation of systematic shifts, in order to avoid migrations, i.e., shifts of the reconstructed values to a kinematic regions different from that of the true kinematics. Figure 6.5 demonstrates the reconstruction quality of the different methods. The electron method and the Jacquet–Blondel method provide the best resolution at high and low values of y, respectively, but they both fall behind in the opposite y regime. In addition, y_{JB} shows a systematic shift towards lower values for medium y and higher values for low y. The double angle method, on the other hand, does not provide the best resolution, but the resolution always remains acceptable; systematic shifts induced by the uranium noise only appear at very low y, where the current jet emerges at shallow angles. The energy deposits from noise in the BCAL cause the reconstructed hadronic angle γ to become too large. Since we want to reconstruct D* mesons in the CTD, sufficient genuine hadronic energy is guaranteed to be found in the BCAL, so that this noise effect can be neglected. In comparison with the data from 1992–94, the accuracy of the electron method has gained substantially through the presampler and SRTD corrections. At low Q^2 it now provides a Q^2 resolution better than that of Q^2_{DA}.

In Monte Carlo studies the smallest migrations for the binning of this analysis were found when using the electron method for the reconstruction of Q^2 and a combination of the electron with the double angle method for the reconstruction of y and x. For this purpose, y is obtained from the mixture of y_{e} and y_{DA}, weighted such that

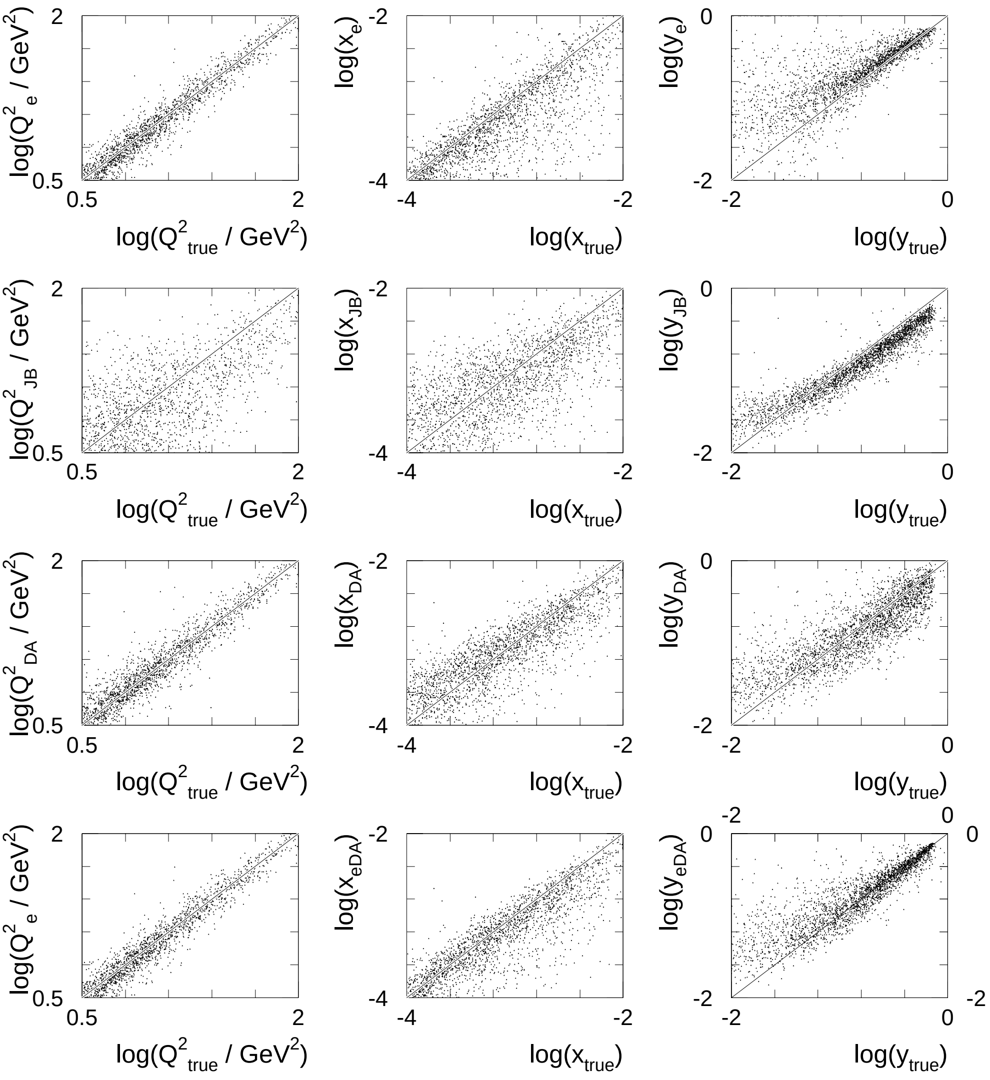

Fig. 6.5 Comparison of the true values of the kinematic variables with the values reconstructed using different methods (MC simulated events). In addition to the electron, Jacquet–Blondel and double angle methods, the ‘eDA’ method is also shown, which uses a weighted mean of y_e and y_DA (see text).

$$y_\mathrm{eDA} \equiv y_\mathrm{e}^2 + y_\mathrm{DA}(1 - y_\mathrm{DA})$$

basically equals y_e at high y, where the electron method has the best resolution; yet, at low y, were y_e becomes poor, y_DA becomes dominating.† The variable x is calculated from Q^2 and y by

---

† A similar method was used by H1 for measuring diffractive deep inelastic scattering [5].

$$x_{\mathrm{eDA}} \equiv \frac{Q_{\mathrm{e}}^2}{s\, y_{\mathrm{eDA}}} \, .$$

It should be noted that the number of charm events is low and therefore the kinematic bin size so large that the kinematic resolution and migrations have negligible effects on the final results of this analysis.

6.3 Background Suppression

Of the quantities used for suppression of background from non-DIS events in this analysis, the two most important ones will be discussed below in more detail.

The excellent time resolution of the calorimeter of $\Delta t \sim 1\,\mathrm{ns}$ for energy deposits $E > 4\,\mathrm{GeV}$ is used for the suppression of beam–gas and cosmic ray events by requiring the arrival times of the energy deposits in the calorimeter to be consistent with a collision of the beams within the nominal vertex region. For this purpose, energy-weighted sums of the time information from all cells are calculated separately for the FCAL and RCAL and for the upper and lower half of the BCAL. For each cell, the time is calibrated to be zero for energy deposits produced by relativistic particles that originate from the interaction point.

Figure 6.6 shows the distribution of the FCAL and RCAL arrival times, and of the time differences between FCAL and RCAL and between the two halves of the BCAL. Beam–gas events that are produced outside the inner volume of the ZEUS detector reach first the RCAL (p–gas events) or the FCAL (e–gas events) and only about 10 ns later the opposite calorimeter segment. The GSLT removes most of such events by requiring the absolute values of the RCAL and FCAL arrival times and their difference to be less than 9 ns [70]. This cut is tightened off-line in the DIS DST selection to 8 ns. The energy deposits in the upper half of the BCAL must not arrive more than 10 ns earlier than those of the lower half, so that cosmic ray events are removed where a muon traverses the BCAL in top-down direction.

For further suppression of these kinds of background and for the removal of hard initial state radiative and photoproduction events, the difference δ between the scalar and the longitudinal sum of all energy entries in the main and the LUMI photon calorimeter is used,

$$\delta = \sum_{i \in \mathrm{CAL}} (E_i - p_{zi}) + 2\, E_\gamma \, , \tag{6.3}$$

where $E_i - p_{zi} = E_i(1 - \cos\theta_i)$ and θ_i is the polar angle under which the cell centre is seen from the primary vertex. For contained events, energy-momentum conservation demands this quantity to equal its value for the initial

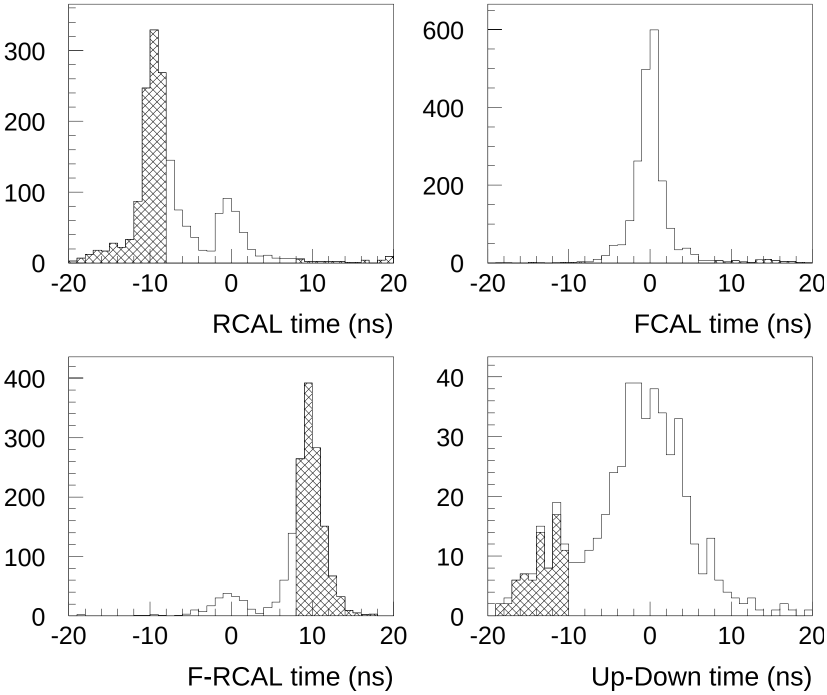

Fig. 6.6 Calorimeter timing cuts on the GSLT in 1995. The histograms show the time and time-difference distributions; their hashed areas indicate which events have been removed by the GSLT.

state, $\delta = 2E_\mathrm{e} = 55\,\mathrm{GeV}$. For photoproduction events, where the scattered electron escapes through the rear beam hole, as well as for proton beam–gas events a much smaller value of δ is expected. Electron beam–gas events, on the other hand, have $\delta \approx 2E$, while muons from cosmic rays in the RCAL can lead to a value of δ that is substantially larger than $55\,\mathrm{GeV}$.

The loss of particles that escape through the the forward beam hole has little impact on the value of δ, because for them $E \approx p_z$; however, losses through the rear beam hole diminish δ, but for the process under study little hadronic energy is expected in this region.

6.4 Trigger Selection

For this analysis only those runs of the 1995 data were considered where all major components used in this study (CAL, CTD, RSAM, SRTD) were fully operational and the interaction point was close to its nominal position. This period comprises 568 runs with an integrated luminosity of $6.08\,\mathrm{pb}^{-1}$. The events were selected using inclusive trigger slots for DIS, which rely on finding the scattered electron (positron) in the detector and do not take any specific quantities of charm hadron production into account.

The first selection step in the off-line analysis was performed by the DST selection bits, which are set by the event reconstruction program as the quasi 'fourth level trigger'. These bits provide a preselection based on the combination of various trigger bits—which in turn are determined from partially reconstructed objects or precandidates (tracks, jets, electrons, etc.)—with requirements on the objects of the full reconstruction. Since several FLT and SLT slots contribute to the inclusive DIS selection bits, not only the cuts on the variables from the full reconstruction must be refined for the final selection: also the exact trigger configuration must be specified. For this analysis the selection was done at the trigger level as follows:

1. *First level trigger.* Since the main feature of a DIS event is the detection of a scattered electron in the calorimeter, CAL FLT slots [178] were used for this study. One of the following slots had to have fired:

   FLT 30 In one of the RCAL trigger towers (calorimeter quadrants) an isolated EMC energy deposit of more than 2.5 GeV was found as a precandidate for the scattered lepton (so-called RCAL-IsoE trigger). Any accompanying entry in the HAC was lower than 0.95 GeV or less than $1/3$ of the EMC energy. In addition, the total energy deposited in the electromagnetic section of the RCAL was larger than 3.75 GeV ('REMCth' trigger); furthermore, none of the veto bits were allowed to be set by veto wall, the C5 beam monitor or the SRTD.

   FLT 40 The EMC energy sums were larger than 4.776 GeV in the BCAL or 3.404 GeV in the RCAL ('REMC' and 'BEMC' triggers). The same vetoes apply as above.

2. *Second level trigger.*

   DIS 1 One of the DIS FLT slots (e.g. 30 or 44) fired, or the transverse energy was larger than 25 GeV. Furthermore, $\delta > 29\,\mathrm{GeV}$ was required and the EMC energy in FCAL, BCAL or RCAL or the FCAL HAC energy had to be larger than 2.5 GeV.

   The SLT rejects events [69] where the calorimeter times are incompatible with an ep collision close to the nominal vertex, or where the trigger resulted from a photomultiplier spark.

3. *Third level trigger.* Either of the following conditions must be met [38, 101]:

   DIS 01 'Low Q^2 NC'. One of the DIS FLT slots fired (e.g. 30 or 44) and the difference between energy and longitudinal momentum sums was $30 < \delta < 100\,\mathrm{GeV}$. An electron candidate was found outside a box of $|x| < 12\,\mathrm{cm}$ and $|y| < 6\,\mathrm{cm}$ around the backward beampipe hole. This slot was prescaled by a fraction of 1/100 for high luminosity runs.

   DIS 03 'Medium Q^2 NC'. The same requirements as DIS 01, but without prescaling; instead, when the luminosity increased, the box cut was raised to $\pm 12\,\mathrm{cm} \times \pm 12\,\mathrm{cm}$ up to run 12130, then $\pm 13\,\mathrm{cm} \times \pm 13\,\mathrm{cm}$ up to run 12186, and finally $\pm 14\,\mathrm{cm} \times \pm 14\,\mathrm{cm}$ from run 12187 onward.

   In order to reduce the number of trigger configurations to be considered for this analysis, the sample was split into a low-luminosity subsample (runs 11539–12568 and 12613–12761; $2.408\,\mathrm{pb}^{-1}$) and a high-luminosity subsample (runs 12570–12576 and 12788–14056; $3.674\,\mathrm{pb}^{-1}$). For the low-luminosity sample, slot DIS 01 includes DIS 03; events from the high-luminosity sample were taken if DIS 03 fired (i.e., the small number of prescaled events was excluded from this analysis). For the DIS 03 slot a constant box cut of $\pm 14\,\mathrm{cm} \times \pm 14\,\mathrm{cm}$ was applied to the candidates from the TLT electron finders, leading to a uniform acceptance for the events from this trigger slot.

4. *DST selection bits.* All of the following bits must be set:

   DST 09 At least one of the electron finders SINISTRA, ELEC 5, LOCAL, or EEXOTIC found an electron with an energy $E_\mathrm{e} > 4\,\mathrm{GeV}$.

   DST 10 The track reconstruction succeeded in finding an event vertex.

   DST 11 This is the main neutral current DIS bit. One of the DIS slots of the TLT fired and the differences in the calorimeter arrival times were less than 8 ns. The difference between the total and the longitudinal momentum sums of the event must be $\delta > 30\,\mathrm{GeV}$.

   Events classified by their topology as being induced by cosmic rays or beam halo muons were rejected.

Of the 16.6 million events that were recorded during the run period considered, 2.4 million events survived the trigger-based preselection. The efficiency of the trigger with respect to the off-line selection described in the next section was found in the MC simulation to be rising from 65% for $Q^2 < 5\,\mathrm{GeV}^2$ to 92% for $Q^2 \approx 7\,\mathrm{GeV}^2$ and to be larger than 95% for $Q^2 > 10\,\mathrm{GeV}^2$ (for $y < 0.2$ larger than 99%).

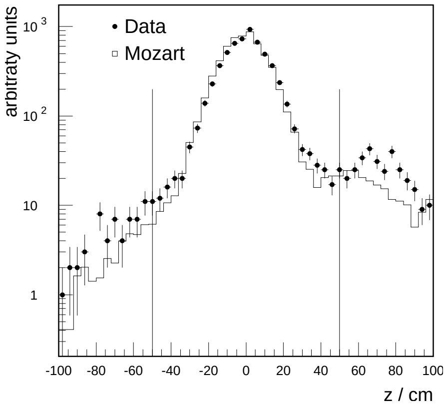

Fig. 6.7
Distribution of the vertex z-position in data (points) and in MOZART (histogram). The vertical lines indicate the cut at $z = \pm 50\,\mathrm{cm}$.

6.5 Off-Line Selection

In the off-line analysis, the electron finders were rerun and the following selection cuts were applied:

- The event vertex was required to lie within $|z| < 50\,\mathrm{cm}$. The event vertex z-position is important for the calculation of polar angles in the event. Figure 6.7 shows the vertex distribution for data and MC simulation after the preselection. The width of the main peak is governed by the proton bunch length (cf. Table 3.1). There is a small secondary peak at $z \approx +70\,\mathrm{cm}$ (and a tiny one at $z \approx -70\,\mathrm{cm}$), called the *proton satellite,* which originates from protons that were trapped in a neighbouring RF bucket and meet the electrons about 2.5 ns later. Since the secondary peak is not properly reproduced by MOZART, the vertex distribution is restricted to the interaction region of the nominal proton bunch.
- An electron was found by the SINISTRA finder with a probability value of $P_{\mathrm{SINI}} > 0.9$. This requirement suppresses most of the photoproduction background from misidentified electrons [175].
- The electron box cut eventually was set to $\pm 13\,\mathrm{cm} \times \pm 7\,\mathrm{cm}$ for the low-luminosity period and $\pm 14\,\mathrm{cm} \times \pm 14\,\mathrm{cm}$ for the high-luminosity period. While the larger box size follows the limit set by the TLT, the size of the smaller box takes the electron shower spread into account, which affects the energy and position measurement for electrons too close to the beam-hole.
- The corrected energy of the scattered electron must be $E'_{\mathrm{e}} > 8\,\mathrm{GeV}$. This cut ensures a good efficiency ($\varepsilon_{\mathrm{SINI}} > 80\%$) of the electron finder and suppresses photoproduction background.
- The difference between the scalar and the longitudinal momentum sums of the calorimeter energy entries, Eq. (6.3) must be within $35 < \delta < 60\,\mathrm{GeV}$. For the summation, the energy entries belonging to the scattered

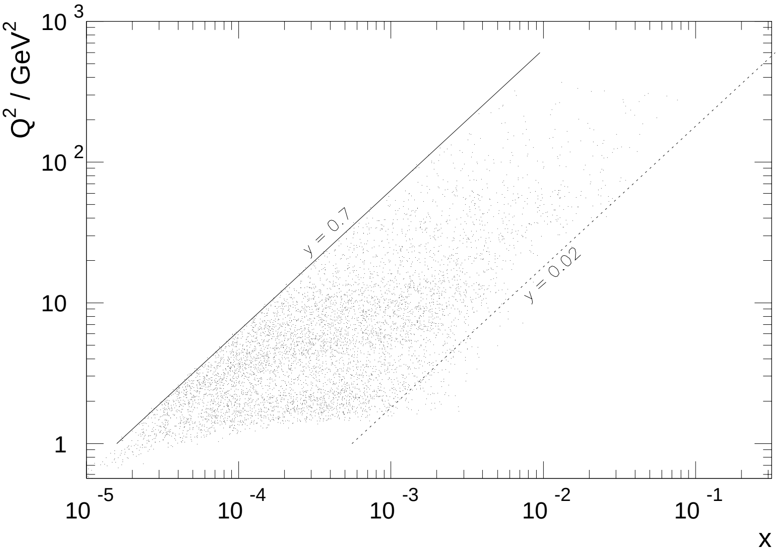

Fig. 6.8 (x, Q^2) distribution of the selected DIS events in run 11548.

electron were replaced by the energy-corrected momentum vector of the electron.

- The kinematic region was restricted to $y_e < 0.7$. As can be seen from (6.1b) and Fig. 6.4, the lower limit in the electron energy imposes an upper limit on the kinematic variable y (for not-too-high Q^2). Most events with larger values of y are due to photoproduction background, where another object was misidentified as the scattered electron. The y value obtained with the electron method was used, because it provides the best resolution in this regime. In many inclusive DIS analyses also a lower cut on y is applied; such a cut is implicitly contained in this analysis by the demand of a D* candidate to be registered in the central region of the detector (see next section).

Figure 6.8 shows for a sample run from the low-luminosity period the distribution of the selected DIS events in the (x, Q^2) plane. Towards low values of Q^2 the distribution is limited by the geometric acceptance of the RCAL. Besides the absolute limit at $Q^2 \sim 1\,\mathrm{GeV}^2$, corresponding to the boundaries of the innermost RCAL modules above and below the beampipe, a second edge can be discerned at $Q^2 \sim 4\,\mathrm{GeV}^2$, which corresponds to the side boundaries of the beampipe hole. For runs of the high-luminosity period, the absolute limit lies slightly above this second edge, on account of the quadratic box cut at ±14 cm × ±14 cm. Towards high values of Q^2 the final limit is $Q^2 = s = 90\,200\,\mathrm{GeV}^2$, but the event density becomes small much earlier, owing to the steep decrease of the cross-section with Q^2.

A total of 1.04 million events remained after the final DIS selection.

7 $D^{*\pm}$ Reconstruction

7.1 Tracking Quality and $D^{*\pm}$ Phase Space

As discussed in Sect. 2.3, the 3-prong decay channel $D^{*+} \rightarrow [D^0 \rightarrow K^-\pi^+]\pi_s$ (or charge-conjugated) was chosen for this analysis of D^* electroproduction. Only those decays were considered where candidate tracks for all daughter particles had been detected in the CTD, so that the 4-momenta of the D^*'s were fully reconstructed. When searching for track combinations that might result from a D^* decay, it is important to use only tracks that can be expected to have a high measuring precision and to restrict the analysis to a kinematic regime where the reconstruction efficiency is sufficient for all decay products, so that the acceptance corrections do not become large. In the present analysis, the tracks must meet the following requirements:

- In 1995 the track reconstruction allowed only for a single vertex per event, the *primary vertex.* The D^0 decay length, in general, is smaller than the vertex resolution of the CTD, so that the efficiency for tracks from D^* decays to be associated with the vertex is approximately the same as for the other tracks. All candidate tracks were therefore required to be associated with the reconstructed primary vertex. This removes in particular the background of low-momentum tracks ($p_\perp \lesssim 0.2\,\mathrm{GeV}$) from secondary interactions (see Fig. 7.1).
- Only tracks that reach superlayer 3 of the CTD were considered, in order to take advantage of the considerable resolution enhancement provided through the algorithms of the full stereo reconstruction. The implicit cuts thus imposed on transverse momentum and pseudorapidity of the tracks were raised off-line to $p_\perp > 120\,\mathrm{MeV}$ and $|\eta| < 1.75$, in order to stay away from the edge of acceptance.

Since the D^* and π_s momenta are closely correlated, the transverse momentum threshold for the slow-pion track candidate limits the acceptance for low-$p_\perp$ D^* mesons. For D^*'s emerging perpendicular to the beam direction ($\eta = 0$), the acceptance starts to drop at $p_{\perp D^*} \approx 2.5\,\mathrm{GeV}$ and is zero for $p_{\perp D^*} < 1.1\,\mathrm{GeV}$. For $p_{\perp D^*} \approx 1.5\,\mathrm{GeV}$, half of the outgoing π_s's fulfil the requirement $p_{\perp D^*} > 120\,\mathrm{MeV}$.† The D^* phase space is restricted to the region of high detector acceptance, which is

---

† These numbers follow directly from the relativistic kinematics of two-body decays.

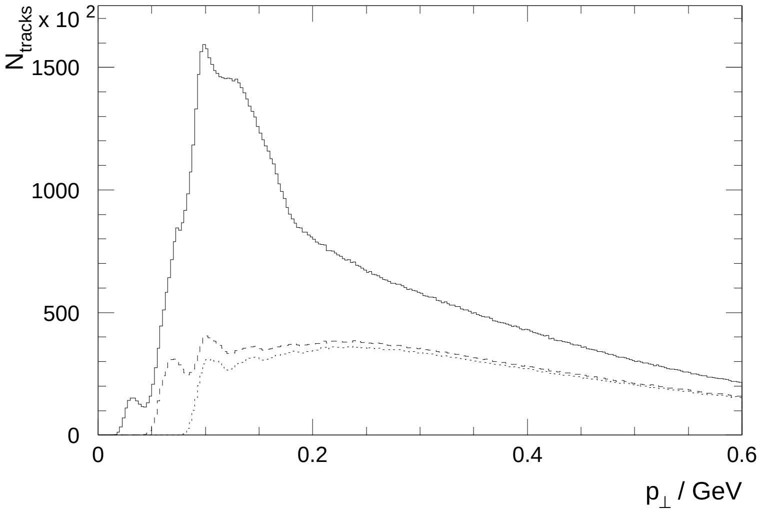

Fig. 7.1 Transverse momentum spectra of all CTD tracks (solid), of the vertex-associated subsample (dashed) and of the vertex-associated tracks that reach at least superlayer 3 (dotted). Tracks with low transverse momenta, $p_\perp < 173\,\text{MeV}$, curl up within the active volume of the CTD, giving rise to maxima related to the axial-superlayer boundaries (cf. Table 3.3).

$$1.5 < p_{\perp \mathrm{D}^*} < 10\,\text{GeV} \qquad \text{and} \qquad |\eta_{\mathrm{D}^*}| < 1.5\ .$$

The upper bound on the D* transverse momentum was chosen, because after all other cuts only 1.6% of the D*'s in the MC simulation have $p_{\perp \mathrm{D}^*} > 10\,\text{GeV}$. The lower bound is not only suggested by the slow pion acceptance; it is also desirable from the theoretical point of view, because for low transverse momenta, fragmentation effects become large.

After defining the D* phase space, additional cuts were introduced, which reduce the backgrounds from light quark processes and wrong particle combinations. Figure 7.2 shows the $p_\perp$ distributions of kaon tracks from D* decays in the RAPGAP MC simulation, after the tracking and D* cuts have been applied. The distribution is limited at the low $p_\perp$ end, predominantly by the cuts that have been imposed before. From Fig. 7.1 it can be seen that the efficiency and purity of the candidate tracks rises towards higher transverse momenta; for instance, the fraction of vertex-associated tracks is 45% at $p_\perp = 200\,\text{MeV}$, but 66% at $p_\perp = 400\,\text{MeV}$. Above $p_\perp \sim 350\,\text{MeV}$ almost all tracks fulfil the superlayer-3 requirement and the shape of the $p_\perp$ distribution is no more influenced by acceptance effects.

- For a further improvement of purity and resolution, a larger minimum transverse momentum of $p_\perp > 450\,\text{MeV}$ is imposed on the candidate tracks from D^0 decays. This removes the low-$p_\perp$ region where the acceptance is steeply falling (see Fig. 7.2).

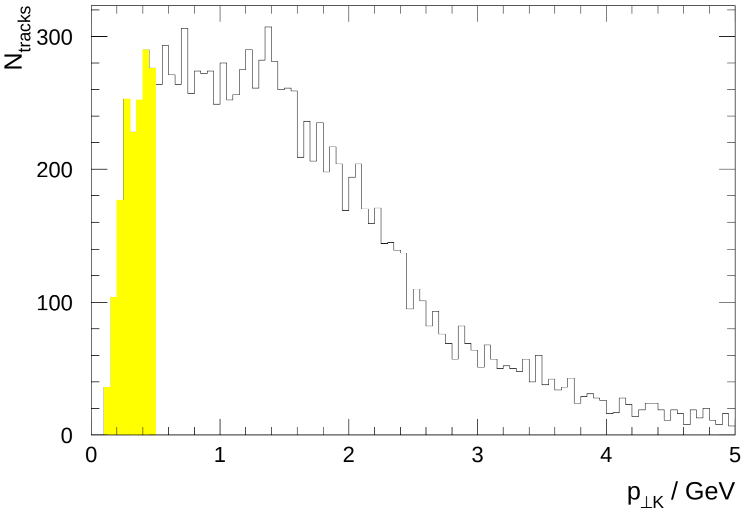

Fig. 7.2 Transverse momentum distribution of kaon tracks from D^0 decays in the MC simulation after tracking and D^* phase space cuts (the distribution is similar for the decay pions). The shaded area indicates the tracks with transverse momenta below 450 MeV. They account for 10.2% of the sample.

The suppression of random track combinations by a cut in the D^0 decay angle θ^*_K, which is common in e^+e^- physics (see, for example, Ref. 42), cannot be applied at HERA, because the D^* transverse momenta are generally lower, so that the detector acceptance suppresses the collinear decays with highly asymmetric momentum sharing as well as those background events which mimick such decays; in the resulting $\cos\theta^*_K$ distributions, signal and background thus have similar shape.

7.2 The $D^{*\pm}$ Signal

The procedure applied for finding the D^* mesons was as follows: In a first step, pairs of oppositely charged CTD tracks that fulfil the requirements above are combined to D^0 candidates. Each of the two tracks is alternatingly assumed to be a kaon or a pion, i.e., particle identification is not applied. Only those $K\pi$ combinations are kept, whose mass is near the nominal mass of the D^0 meson, $1.4 < M(K\pi) < 2.3$ GeV. Then a third track with charge opposite to that of the kaon candidate is assumed to be the slow pion and is combined with the two tracks of the D^0 candidate, provided that the mass difference to the plain $K\pi$ combination is not much larger than the pion mass, $\Delta M \equiv M(K\pi\pi_s) - M(K\pi) < 180$ MeV. Only those candidates are kept which fall into the D^* signal region, $1.8 < M(K\pi) < 1.91$ GeV and $143 < \Delta M < 148$ MeV.

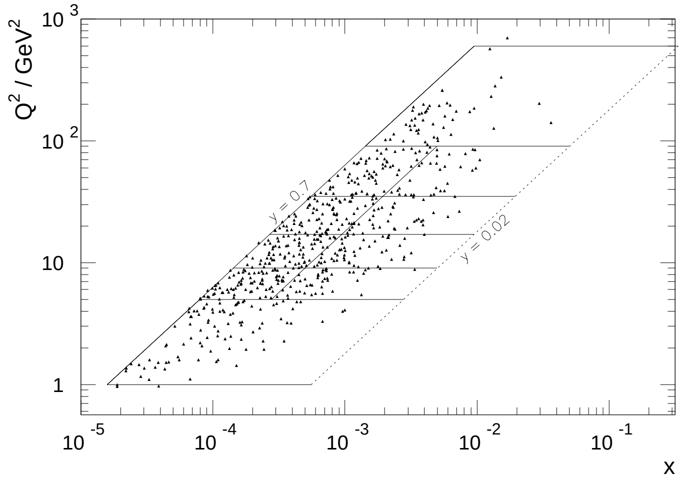

Fig. 7.3
Distribution in (x, Q^2) of the D* candidates in the signal region. The diagonal and horizontal lines indicate the binning chosen for further analysis.

Figure 7.3 shows the distribution of the events from the signal region in the (x, Q^2) plane. The kinematic region for the present analysis was chosen to be

$$1 < Q^2 < 600\,\mathrm{GeV}^2 \qquad \text{and} \qquad y < 0.7\ ,$$

A lower limit on y does not need to be set explicitly, because it follows from (6.2a) that for $|\eta_{\mathrm{D}^*}| < 1.5$, $p_{\perp\mathrm{D}^*} > 1.5\,\mathrm{GeV}$,

$$y \gtrsim \frac{p_{\mathrm{D}^*}(1-\cos\theta_{\mathrm{D}^*})}{2E_\mathrm{e}} \gtrsim 0.02\ .$$

For the statistical subtraction of the combinatorial background, also those combinations were kept where the D^0 candidate is composed of like-charge tracks (*wrong-charge combinations*). Maintaining the requirement on the sign of the slow pion's charge ensures that fake D* candidates have charge ±1 and thus almost the same phase space as the right-charge background.† However, in order to increase the statistics of the background estimate by about 70% and thereby reducing the statistical error of the signal by 17%, also combinations with charge ±3 were kept. These combinations are stochastically disfavoured against the charge ±1 combinations, but Figure 7.4 demonstrates that this induces no bias in the sample under study: no systematic shifts are visible in the ΔM spectrum as well as in the $M(\mathrm{K}\pi)$ spectrum and the normalisation factors with respect to the right-charge random combinations are within errors the same for the ΔM and $M(\mathrm{K}\pi)$ spectra. It also was checked that the η_{D^*} and $p_{\perp\mathrm{D}^*}$ distributions have the same shape for combinations with

---

† In fact, the combinatorial phase space for wrong-charge combinations is slightly smaller than for right-charge combinations, because the candidate tracks for right-charge combinations are taken from two independent samples (positive and negative tracks), while for wrong-charge combinations both tracks are taken from the same sample, so that the number of choices is reduced after the first track has been taken.

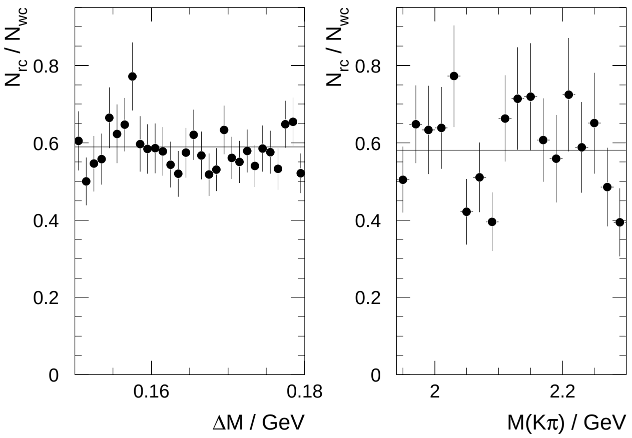

Fig. 7.4
Ratio of right-charge over wrong-charge combinations in the phase space outside the signal region, shown both for the ΔM and the $M(\mathrm{K}\pi)$ spectrum. The horizontal lines indicate the average values of the distributions.

charge ±1 and charge ±3. By scaling the wrong-charge combinations found in the signal region with the normalisation factors found in the region above the signal, the number of right-charge random combinations under the signal can be estimated.

Figure 7.5 shows the D^* candidate distribution after application of all selection cuts. A clear signal can be seen around the nominal values for $\mathrm{D}^0 \to \mathrm{K}^-\pi^+$ and $\mathrm{D}^*(2010)^+ \to \mathrm{D}^0\pi^+$ decays. By subtracting the background estimated from the wrong-charge combinations, the number of D^* mesons reconstructed in the signal region of both distributions was measured to be 355 ± 24 candidates over a background of 298 ± 23 candidates. Due to the low Q value of the $\mathrm{D}^{*+} \to \mathrm{D}^0\pi^+$ decay, the width of the ΔM peak can be attributed completely to the experimental resolution; therefore a Gaussian distribution of the signal superimposed on a background of the form

$$\mathrm{d}N \,/\, \mathrm{d}(\Delta M) = a(\Delta M - m_\pi)^b$$

was assumed in fitting the ΔM distribution. An unbinned maximum-likelihood fit results in 352 ± 32 candidates, in close agreement with the number stated above and the yield of 351 ± 34 candidates obtained from a least-squares integral fit. The fitted peak position of $\Delta M = 145.42 \pm 0.08\,\mathrm{MeV}$ is close to the PDG value for the mass difference between D^* and D^0 (2.6); the experimental resolution was measured to be $\sigma = 0.93 \pm 0.10\,\mathrm{MeV}$.

In addition to the background from random combinations, the $M(\mathrm{K}\pi)$ distribution contains signals from several decay modes other than $\mathrm{D}^0 \to \mathrm{K}\pi$. These modes have higher particle multiplicity and were reconstructed only partially; hence their $\mathrm{K}\pi$ masses are lower by at least the π^0 mass (which is much larger than the experimental resolution, so that their contribution to the $\mathrm{K}\pi$ signal is negligible). The wide bump seen at $M(\mathrm{K}\pi) \lesssim 1.75\,\mathrm{GeV}$ can be attributed to D^0 decays into $\mathrm{K}\rho^0$ or $\mathrm{K}^*\pi$; the additional excess over the wrong-charge combinations in this region originates from nonresonant

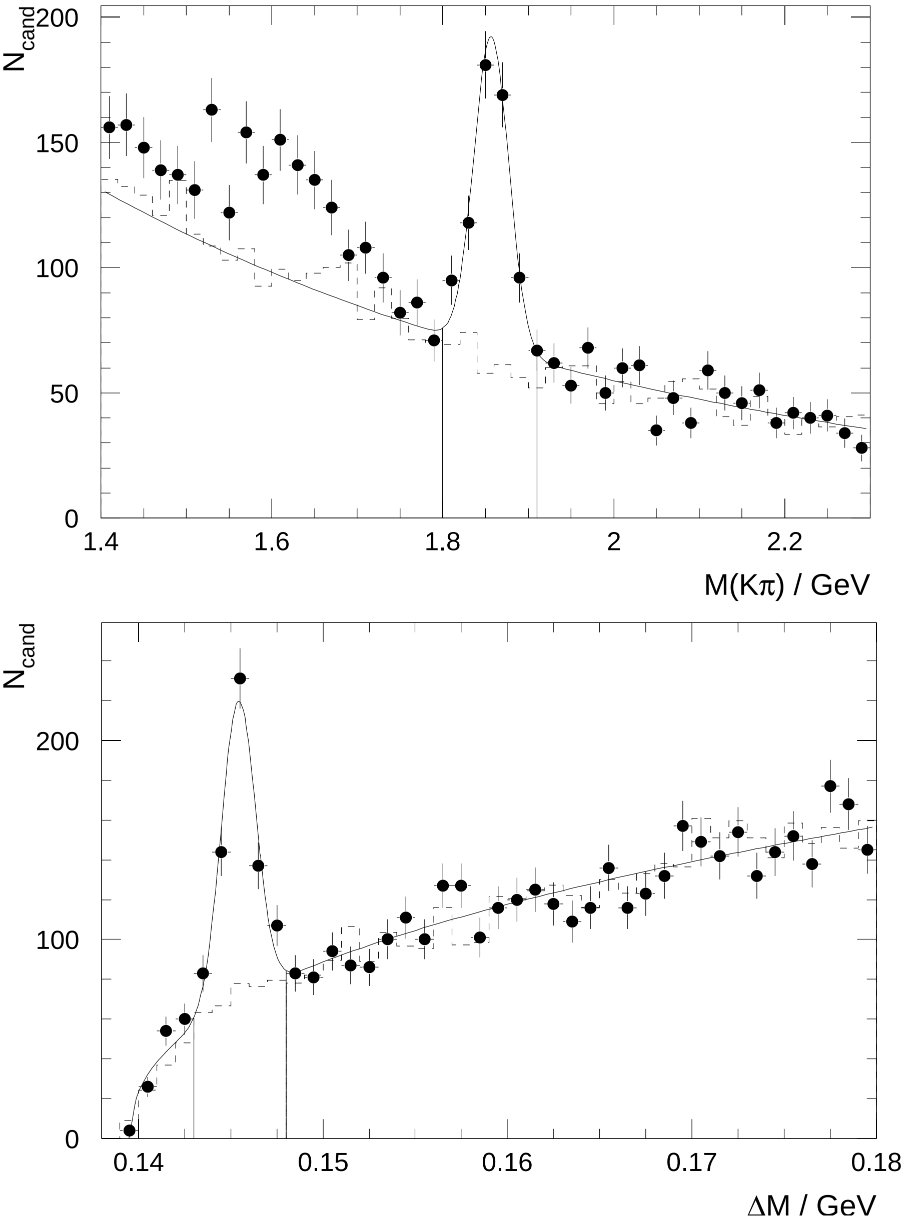

Fig. 7.5 $M(\mathrm{K}\pi)$ (top) and $\Delta M = M(\mathrm{K}\pi\pi_\mathrm{s}) - M(\mathrm{K}\pi)$ (bottom) distributions of the measured D^* candidates after application of all selection cuts. Each histogram contains the events that fall into the signal region of the distribution shown in the other histogram; the signal regions around the peaks ($1.80 < M(\mathrm{K}\pi) < 1.91\,\mathrm{GeV}$ and $143 < \Delta M < 148\,\mathrm{MeV}$) are marked with vertical lines. The distribution of the right-charge combinations (dots) are compared with a parametrisation resulting from an unbinned likelihood fit to this distribution (solid line) and with the background estimate from wrong-charge combinations (dashed line).

decays $D^0 \rightarrow K\pi\pi$. Since a fit to the ΔM distribution already provides sufficiently precise results, a fit to the $M(K\pi)$ resolution serves merely as a cross-check. The fit region considered extends only over the upper mass range, $1.775 < M(K\pi) < 2.3\,\mathrm{GeV}$. The signal is assumed to be Gaussian and the background to fall exponentially. Since this fit is less constrained than the ΔM fit, which is tightly bound by the phase space edge at $\Delta M = m_\pi$, it is less precise. The fit yielded 327 ± 34 D^* mesons contained in the $M(K\pi)$ peak; this agrees within errors with the result from the ΔM fit. The experimental resolution is $\sigma_{M(K\pi)} = 20.3 \pm 2.3\,\mathrm{MeV}$. The peak position, $M(K\pi) = 1857.8 \pm 2.0\,\mathrm{MeV}$, is 0.36% lower than the PDG value [62] for the D^0 mass, $M(D^0) = 1864.6 \pm 0.5\,\mathrm{MeV}$. A possible explanation for the shift towards lower masses is the underestimation of the CTD momentum scale by about 0.3%, which is within the uncertainty range of the absolute value for the strength of the solenoidal magnetic field [153].

Alternatively to the background estimate from wrong-charge combinations and from fitting the ΔM signal, the signal under the background was estimated by taking candidates from a control region above the nominal mass range, $2.0 < M(K\pi) < 2.5\,\mathrm{GeV}$, and normalising it to the number of events observed in the region $155 < \Delta M < 180\,\mathrm{GeV}$. The number of signal candidates obtained is 364 ± 35. This method is somewhat problematic, as the candidates for the background estimate come from another region of phase space with higher particle momenta; therefore the control region cannot be taken too large. Using side bands instead of a control region suffers similar problems. Hence the preferred method for subtracting the background is the use of wrong-charge combinations; the unbinned fitting of the ΔM distribution is used as a systematic check.

A sample event from the signal region is displayed in Fig. 7.6. It belongs to a region of phase space, where the hadronic activity is low ($W = 70\,\mathrm{GeV}$), so that the tracks from the D^{*-} candidate ($p_{\perp D^*} = 3.1\,\mathrm{GeV}$, $\eta_{D^*} = 1.1$) are well separated from other hadrons. The tracks from the D^0 decay hit the BCAL; the π_s candidate ($p_{\perp \pi_s} = 257\,\mathrm{MeV}$) reaches only to superlayer 7 and leaves the CTD through the forward endplate.

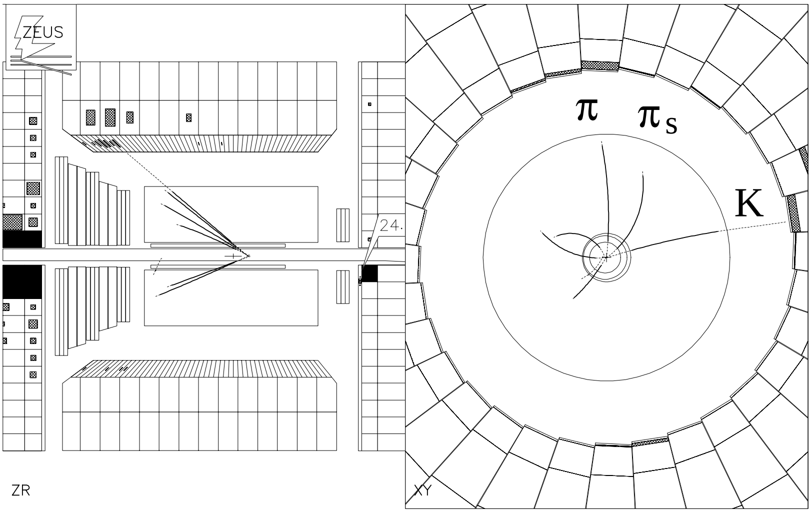

Fig. 7.6 A sample event from the signal region as visualised by the ZEUS event display, LAZE. Projections of the CAL and of the tracking chambers are shown in the (z, r) plane (left) and in the (x, y) plane (right). The size of the energy entries in the calorimeter is indicated by the area of the shaded rectangles. One entry in the RCAL is labelled '24.'; it marks the electron found by SINISTRA ($E'_{\mathrm{e}} = 24.9\,\mathrm{GeV}$) The reconstructed CTD tracks are shown as well; those belonging to the D^{*-} candidate are labelled in the (x, y) view.

7.3 Enhancement of the Signal Using dE/ dx

We will now check whether the D^* signal can be improved by application of the $\mathrm{d}E/\mathrm{d}x$ tagging method introduced in Sect. 4.10. The potential background reduction depends on the composition of the unrefined sample. Figure 7.7 shows the $(\mathrm{d}E/\mathrm{d}x, p)$ distribution of tracks from right-charge combinations in the signal region ($1.8 < M(\mathrm{K}\pi) < 1.91\,\mathrm{GeV}$, $143 < \Delta M < 148\,\mathrm{MeV}$), separately for tracks satisfying / not satisfying the following requirements:

- the number of non-saturated hits used for calculating the truncated $\mathrm{d}E/\mathrm{d}x$ mean must be sufficiently large, $n_{\mathrm{trunc}} > 8$ (tracks that have lower values of n_{trunc} are not included in Fig. 7.7);
- the probability (likelihood) that the observed value of $\mathrm{d}E/\mathrm{d}x$ is measured for a particle of mass m_i that produced n_{trunc} non-saturated hits must be $\ell_i > 1.4\%$, and
- the value of ℓ_i normalised by the sum over the likelihoods for the mass assumptions $j = \mathrm{K}, \pi, \mathrm{p}, \mathrm{e}$ must be $\ell_i^{\mathrm{norm}} > 12\%$.

The last criterion has the purpose of increasing the efficiency of the selection in those $(\mathrm{d}E/\mathrm{d}x, p)$ regions where the hadron bands are well separated. This

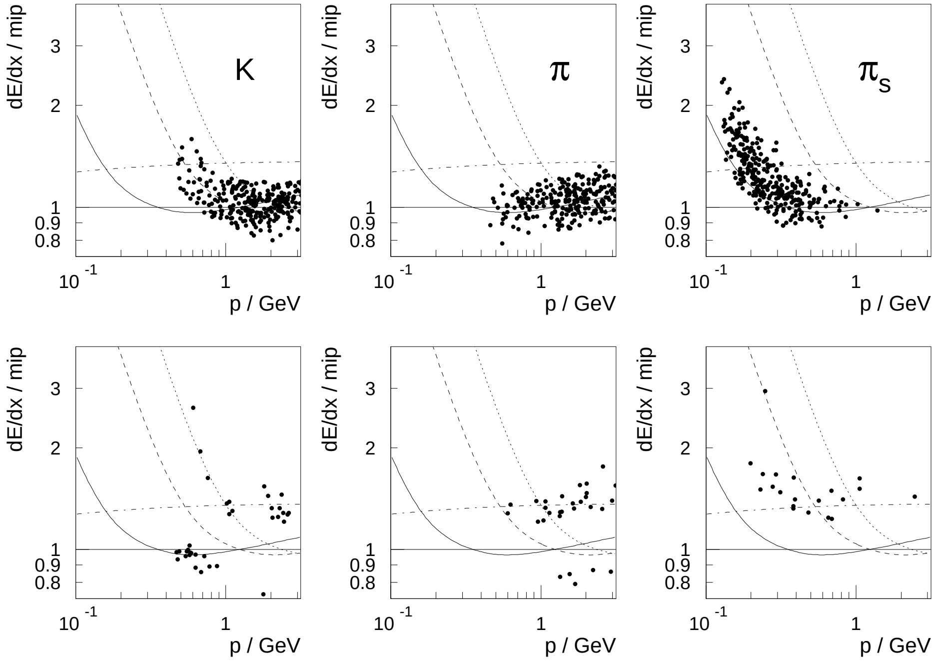

Fig. 7.7 $(\mathrm{d}E/\mathrm{d}x, p)$ distribution of D^* candidate tracks from the signal region, separately for the tracks assumed to be the K, π or π_s. The upper distributions show the tracks accepted by the likelihood cuts, while the tracks that have been rejected are shown below. Only tracks with $n_\mathrm{trunc} > 9$ have been considered. Positive and negative tracks are shown together. The lines indicate the central $\mathrm{d}E/\mathrm{d}x$ values expected for e, π, K and p (cf. Sect. 4.8)

is especially important for the slow-pion candidates where we see the measured band deviating from the expected position for momenta $p \lesssim 0.3\,\mathrm{GeV}$ (see Fig. 7.7, bottom right). This cannot be attributed solely to the admixture of electrons to this sample.[†]

Comparing the resulting distributions with the inclusive sample used for the parametrisation fit (cf. Fig. 4.20), one finds that the D^* candidate sample already has a higher purity. The selection cuts applied to the tracks of the

---

[†] The $\mathrm{d}E/\mathrm{d}x$ of slow pions rises more steeply towards low momenta than it does for other hadrons of the same initial velocity. The effect was not seen when fitting the parametrisation, because for the purpose of obtaining high resolution only long tracks were used for the fit, whereas a large fraction of the slow pions curl-up inside the chamber and do not reach the outermost layers. The steeper slope means that the additional contribution to $\mathrm{d}E/\mathrm{d}x$ becomes larger with decreasing momentum; it therefore cannot be just a pathlength effect, which would level off when approaching momenta at which the tracks curl. A possible explanation is that the pions loose speed on their way through the CTD, so that the velocity is on average lower than at the vertex. Particles heavier than pions but of the same speed suffer the same absolute amount of ionisation loss as the pions; however, owing to their larger inertia they loose much less speed. Therefore, at very low momentum ($p \sim 0.1\,\mathrm{GeV}$) the *registered* ionisation loss of pions must be systematically larger than that of heavier hadrons.

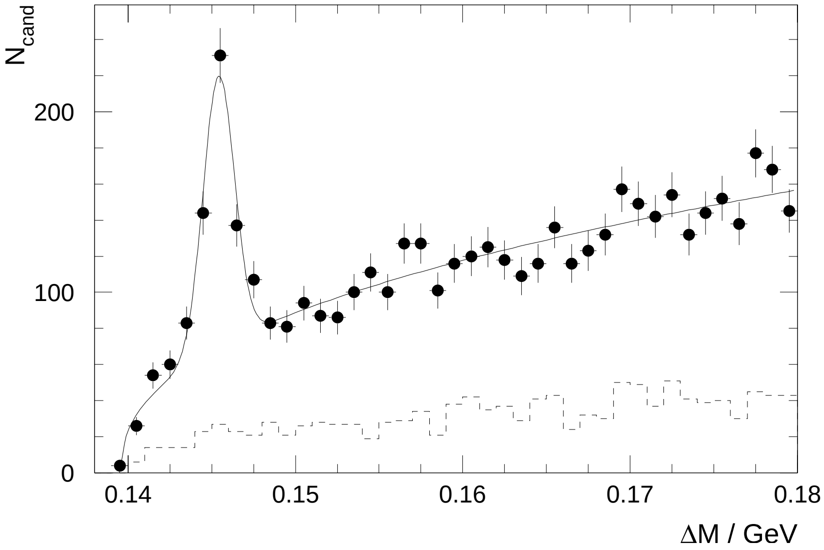

Fig. 7.8 Application of dE/dx likelihood cuts on the D* data sample. The dots show the ΔM distributions of the D* candidates inside the M(Kπ) signal window after all selection cuts. The histogram shows the candidates of this sample which are rejected by dE/dx cuts.

D* decay particles were chosen so that regions of low acceptance are excluded. Since the background concentrates in these regions (low $p_\perp$, high η), the cuts are also quite selective. The strongest background suppression originates from the low Q value of the decay, placing the signal peak close to the edge of the phase space. Of the remaining combinatorial background, most particles are pions or kaons; however, for the major part of the momentum region under study, they are hardly distinguishable. Nevertheless, the signal can slightly be improved by employing dE/dx information, since there is some background left from tracks that have a low likelihood of belonging to the desired species. Figure 7.7 suggests that electrons account for most of the identifiable background; some proton and (supposedly) deuteron candidates can also be seen in the sample of rejected tracks (Fig. 7.7, bottom left).

The background reduction that can be achieved when applying the likelihood cuts listed above to all three candidate tracks is demonstrated in Fig. 7.8; it amounts to about 25% of the total background. Although these cuts are rather loose, we must consider the loss through type I errors, i.e., the erroneous rejection of good candidates. From the likelihood requirements it can be estimated that the loss is of the order of 4%. A least-squares integral fit yields a number of 351 ± 34 signal candidates before and 345 ± 32 candidates after application of the dE/dx cuts. In the sample of candidates rejected by the dE/dx cuts the fit finds a residual signal of 20 ± 9 events. These are consistent with the naïve expectation of 15 ± 4 events lost. The use of dE/dx likelihood

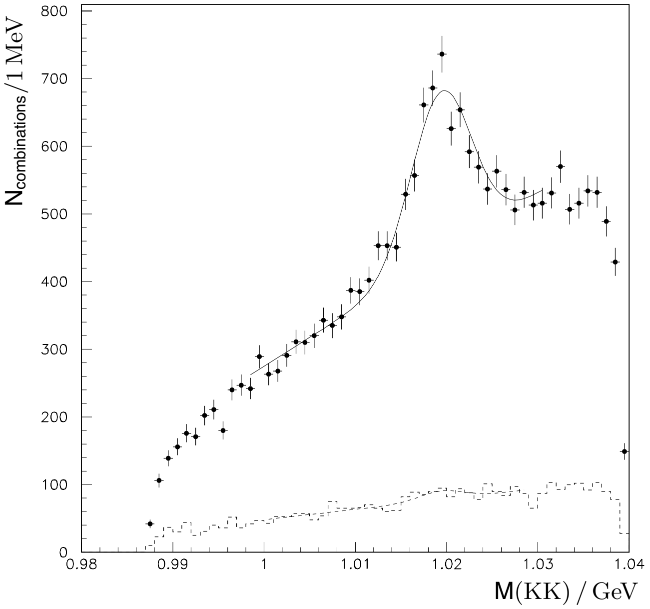

Fig. 7.9
Mass distribution of ɸ candidates after D_s preselection (dots) and the subset of candidates that are rejected by dE/dx likelihood cuts (histogram)

cuts remains a future option for this decay channel, when high statistics data samples of other channels (e.g., exclusive $K^*(892)$ production) exist, which allow an independent determination of the cut efficiencies.

The applicability of dE/dx likelihood cuts was also tested in a study of D_s photoproduction [205] in the decay channel $D_s^{\pm} \rightarrow (\phi \rightarrow K^+K^-)\,\pi^{\pm}$, using data of the 1996/97 running period. While the leading signature for the D^* is the slow pion, it is the resonant decay via the ɸ(1020) that helps in identifying the D_s. The kinetic energy of the ɸ decay is rather low, $Q \approx 24\,\text{MeV}$; this —and the Zweig-suppression of the decay into pions—makes the ɸ relatively narrow for a vector meson, but does not provide as tight a constraint as we find it for the D^* decay. The vector nature of the ɸ leads to a $\cos^2\theta^*_K$ distribution of the decay angle of the K^+ in the ɸ rest frame. This property can be used to further reduce the background from random combinations, which is isotropic. Figure 7.9 shows the mass distribution of ɸ(1020) candidates after a D_s preselection, where all cuts of the final selection except explicit D_s phase space cuts have been applied; for the ɸ candidates two oppositely charged tracks where required with $p_\perp > 0.75\,\text{GeV}$, $20° < \theta < 160°$ and $\left|\cos^3\theta^*_K\right| > 0.15$; they were combined with a third track ($p_\perp > 0.5\,\text{GeV}$, $20° < \theta < 160°$) to form a D_s candidate in the mass range $1.94 < m_{D_s} < 2.00\,\text{GeV}$. From an unbinned fit to the mass signal around the nominal ɸ(1020) mass over a linear background, the number of D_s candidates was determined to be 1990 ± 133. The figure also shows the background rejected when applying the same likelihood cuts as above to the two kaons and the pion that emerge from the D_s decay. Also here the loss of good candidates is expected to be of the order of 4%. Fitting the rejected background, which is about 17% of the total background,

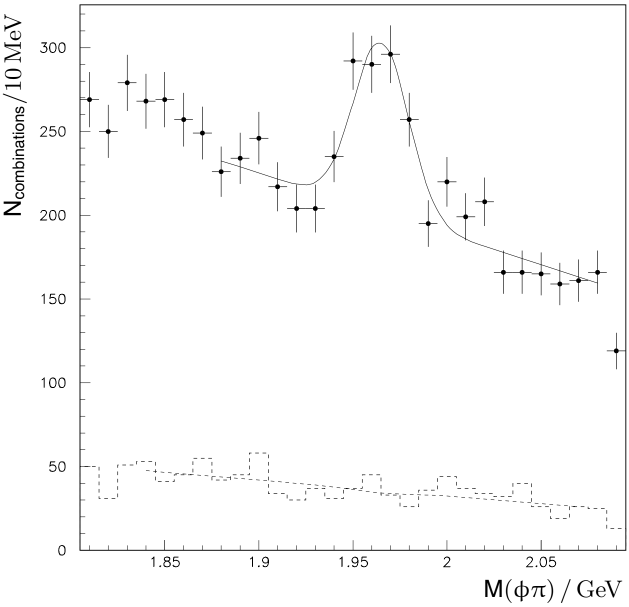

Fig. 7.10
Mass distribution of the $\mathrm{D_s}$ candidates after all cuts except for $\mathrm{d}E/\mathrm{d}x$ likelihood requirements (dots), and of the subsample rejected by $\mathrm{d}E/\mathrm{d}x$ cuts (dashed histogram)

yields a residual signal of 75 ± 37 events, thus a loss of $3.8 \pm 1.9\%$ of the good candidates.

The mass distribution of the $\mathrm{D_s}$ candidates after applying the remaining phase space cuts ($115 < W_{\mathrm{JB}} < 250\,\mathrm{GeV}$, $3 < p_{\perp\mathrm{D_s}} < 12\,\mathrm{GeV}$, $-1.5 < \eta_{\mathrm{D_s}} < 1.0$) is shown in Fig. 7.10. The background reduction through the $\mathrm{d}E/\mathrm{d}x$ cuts is again about 17%. There is no visible signal loss —the signal is as high after the cuts and no signal is observed in the background. Thus, although the amount of background suppression through the $\mathrm{d}E/\mathrm{d}x$ cuts is low, the signal is notably enhanced, because the background after the cuts is better behaved. In addition, this channel allows (in principle) for the cuts on the kaon tracks to determine the true efficiency of the cuts from the data, since they provide two independent tags of the same kind.

7.4 DIS Acceptance for $\mathrm{D}^{*\pm}$ Events

Due to the small statistics of the D^* sample, the kinematic bins are larger than the experimental resolution and migrations between the bins can be neglected; it is therefore sufficient to apply bin-by-bin correction factors, which are the inverse of the binwise acceptances, provided that the MC sample has large statistics (see Ref. 36). The DIS acceptance for bin i is defined as the fraction $\varepsilon_i^{\mathrm{ep}} = k_i^{\mathrm{ep}}/n_i^{\mathrm{ep}}$, where

- k_i^{ep} is the number of reconstructed events that fulfil the trigger conditions of Sect. 6.4 and the off-line selection criteria of Sect. 6.5 and of which the reconstructed kinematics belong to bin i, and

- $n_i^{\rm ep}$ is the number of events that were generated in the kinematic region $1 < Q^2 < 600\,{\rm GeV}^2$ and $y < 0.7$ and of which the true kinematics fall into bin i.

In both cases it was required that an outgoing D^* meson was generated in the restricted D^* phase space region, $p_{\perp D^*} > 1.5\,{\rm GeV}$ and $|\eta_{D^*}| < 1.5$. It must now be clarified how the number of events was determined, since a small fraction of the signal events ($1.0 \pm 0.4\%$ in data and $0.9 \pm 0.1\%$ in the MC simulation) had more than one right-charge candidate in the signal region. Although this can partly be attributed to true *double tags,* where both charm quarks fragmented as D*'s and decayed through the 3-prong channel and were registered in the central region of the detector (0.2% of the MC signal events, i.e., $\lesssim 1$ event in the data), most of the double tags originate from random combinations, where one of the tracks of a reconstructed D^* was randomly interchanged with another track in the event. In order not to introduce any bias by a best-candidate selection, events with a second candidate are counted doubly; the resulting excess will automatically be removed by the acceptance correction.

Before using the MC simulation for correcting the data it must be tested whether the simulation gives a good description of the observable quantities. Figure 7.11 shows for data and for events generated with RAPGAP, after all DIS and D^* selection cuts, the distribution of the reconstructed detector-level quantities that are basic for the determination of the event kinematics: energy and polar angle of the scattered electron, hadronic angle and $\delta = \sum(E - p_z)$, and the z-position of the primary vertex. The MC distributions have been normalised such that the total number of signal events is the same in data and simulation.† In all histograms the combinatorial background has been removed by subtracting the distributions obtained from wrong-charge combinations. Good agreement between data and MC-generated events is observed. In the MC simulation random combinations contribute at the level of a few percent only; in the data, however, the background is substantial and its subtraction is crucial, because it biases the distributions.‡ Note that the signal-to-background ratio in the data is in the order of unity; therefore the errors on the distributions are not Poissonian. The generally good agreement between data and MC distributions indicates that the background subtraction method applied does not bias the result.

The binwise DIS acceptances as obtained from RAPGAP are displayed in Fig. 7.12 as a function of the kinematic variables. The change between the

---

† Note that the LO MC simulation is only used for acceptance correction; hence the overall normalisation (i.e., the actual cross section) is of less importance than the shape of the distributions.

‡ Unsubtracted background biases, for example, the $E_{\rm e}$ distribution towards low electron energies (high y), because the multiplicity of the hadronic final state is large and therefore the rate of random combinations is high. This motivated the choice of the y binning (Fig. 7.3): the high-y bins have larger signals than the low-y bins, but the combinatorial background is also larger.

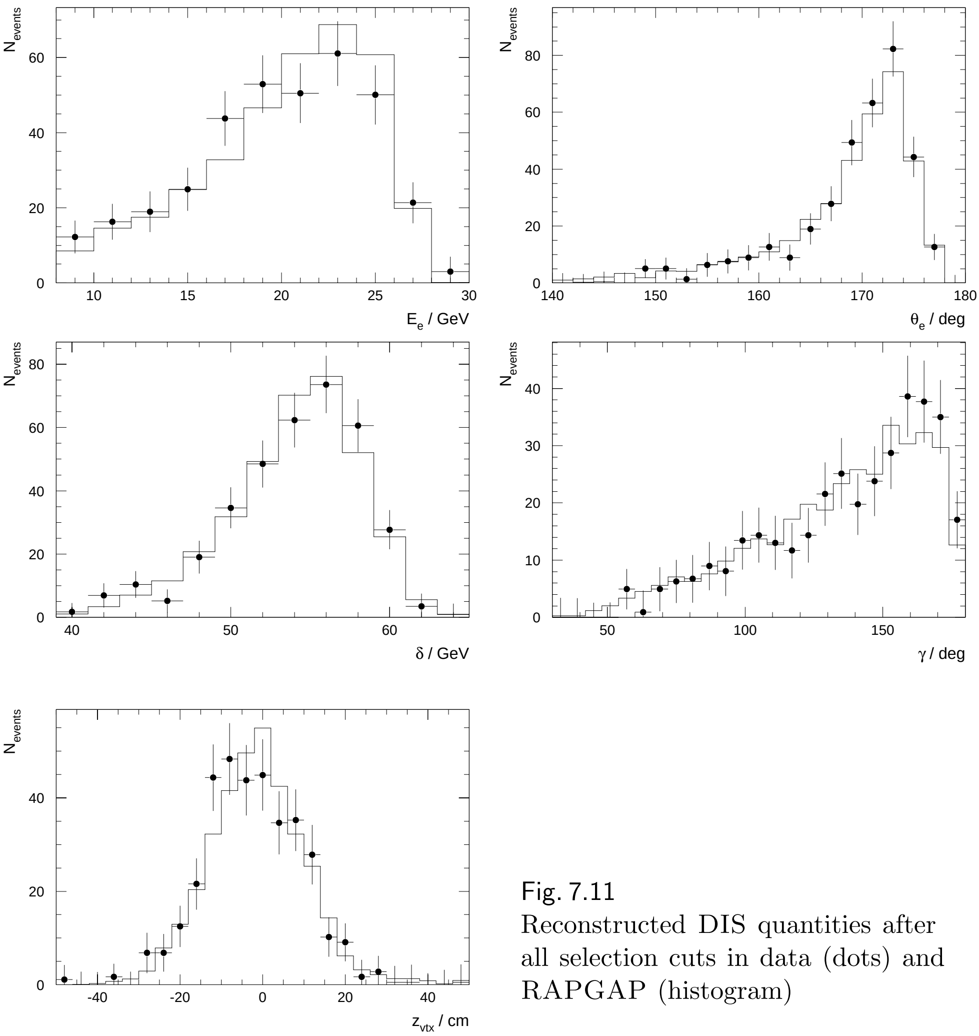

Fig. 7.11
Reconstructed DIS quantities after all selection cuts in data (dots) and RAPGAP (histogram)

trigger configurations for the low-luminosity and high-luminosity periods was taken into account by accepting all events that fired DIS 01 and reweighting the events that did not fire DIS 03 simultaneously by the fraction by which the low-luminosity periods contributed to the integrated luminosity (39.6%). Averaged over the whole kinematic range, the DIS acceptance for events with a D* generated in the restricted $(p_\perp, \eta)$ region is $\varepsilon^{\mathrm{ep}} = 63.0\%$; for the range $5 < Q^2 < 100\,\mathrm{GeV}$ the acceptance is $\varepsilon^{\mathrm{ep}}_{5<Q^2<100\,\mathrm{GeV}} = 78.9\%$. The acceptances calculated with DJANGO closely agree with those from RAPGAP except for $Q^2 \lesssim 15\,\mathrm{GeV}^2$, where DJANGO yields acceptances that exceed the RAPGAP values by up to 10%.

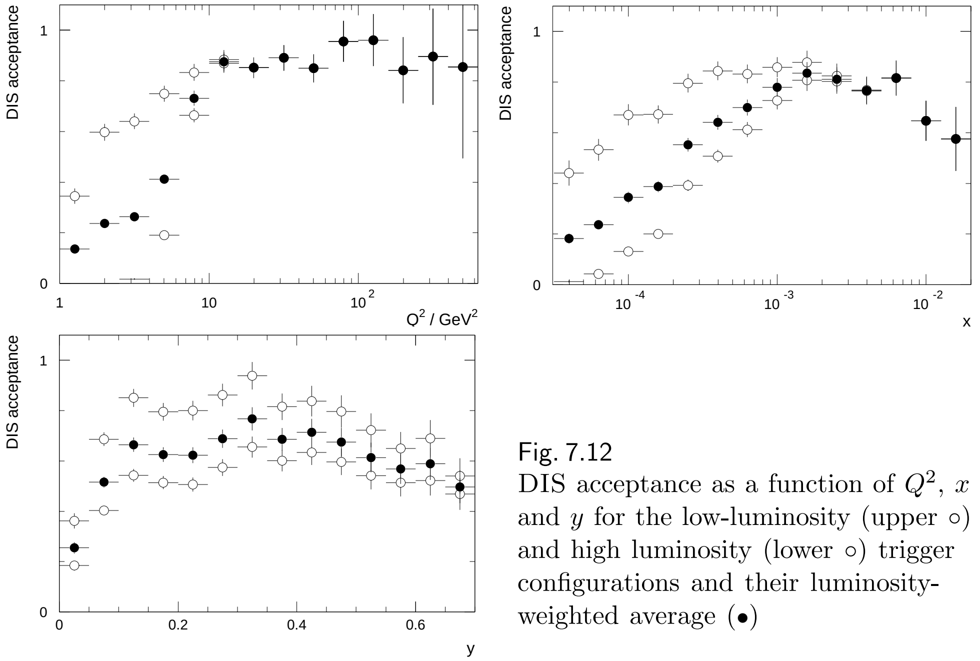

Fig. 7.12
DIS acceptance as a function of Q^2, x and y for the low-luminosity (upper ○) and high luminosity (lower ○) trigger configurations and their luminosity-weighted average (●)

7.5 $D^{*\pm}$ Acceptance

In principle, the acceptance of D* mesons is determined by the acceptance of their daughter particles; however, for the D* daughter particles only the acceptance folded with the matching efficiency can be determined. A global comparison of the generated D* mesons with the reconstructed candidates does not suffer from that difficulty and, in addition, handles the combinatorial effect of multiple candidates within single events, which cannot be inferred from the individual particles. The D* acceptance for bin i is defined as the fraction $\varepsilon_i^{\mathrm{D}^*} = k_i^{\mathrm{D}^*}/n_i^{\mathrm{D}^*}$, where

– $k_i^{\mathrm{D}^*}$ is the number of D* candidates that fulfil the selection criteria of Sect. 7.1 and were reconstructed in bin i, and

– $n_i^{\mathrm{D}^*}$ is the number of generated D* mesons that had true momenta $p_{\perp\mathrm{D}^*} > 1.5\,\mathrm{GeV}$ and $|\eta_{\mathrm{D}^*}| < 1.5$ and were generated in bin i.

Figures 7.13 and 7.14 show the uncorrected $p_\perp$ and η distributions for data and for the RAPGAP simulation. Within the statistical errors, there is reasonably good agreement between the distributions, although the η distributions in the simulation seem to be shifted towards lower values of η. This effect is slightly less pronounced in the HERWIG simulation (see Fig. 7.15), which otherwise achieves a similar performance.

The D* acceptance as determined by the two MC simulations is shown in Fig. 7.16 as a function of $p_\perp$ and of η. Averaged over the accessible phase space,

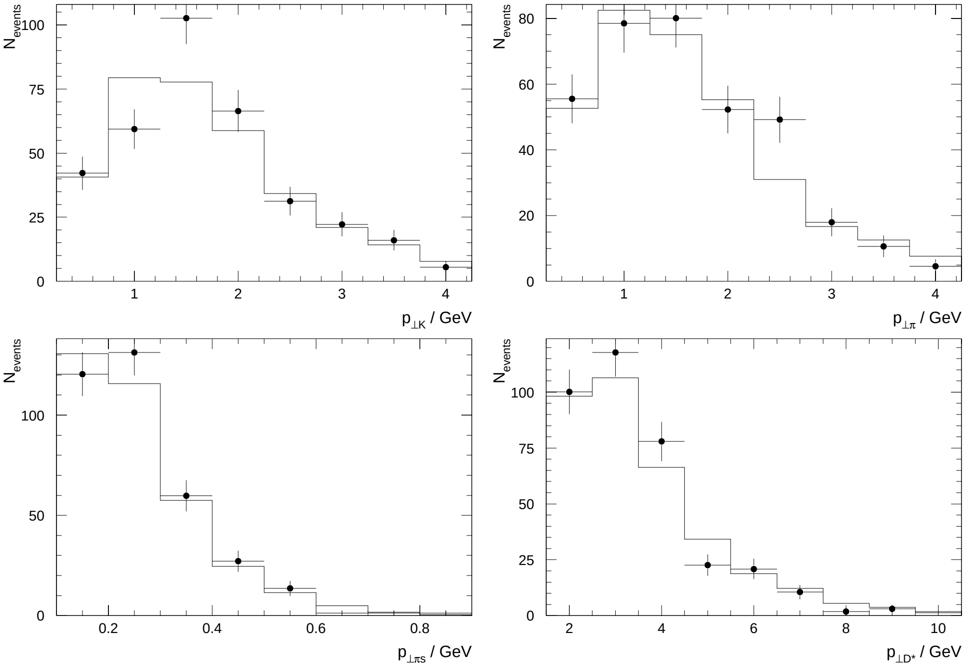

Fig. 7.13 Distributions of transverse momenta of D* mesons and their daughter particles in data (dots) and in the RAPGAP simulation (histogram)

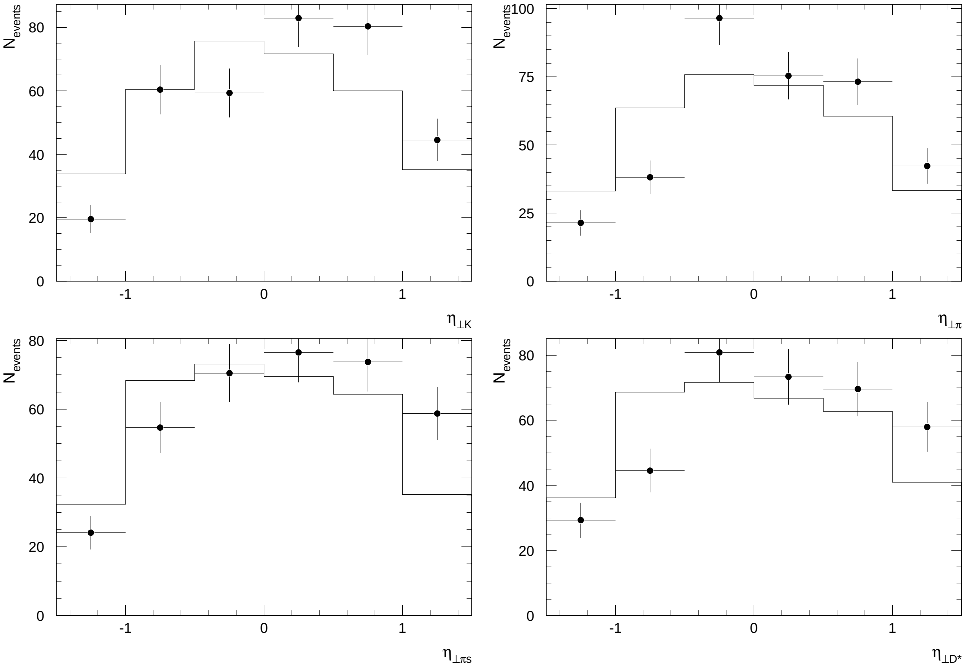

Fig. 7.14 Distributions of pseudorapidities of D* mesons and their daughter particles in data (dots) and in the RAPGAP simulation (histogram)

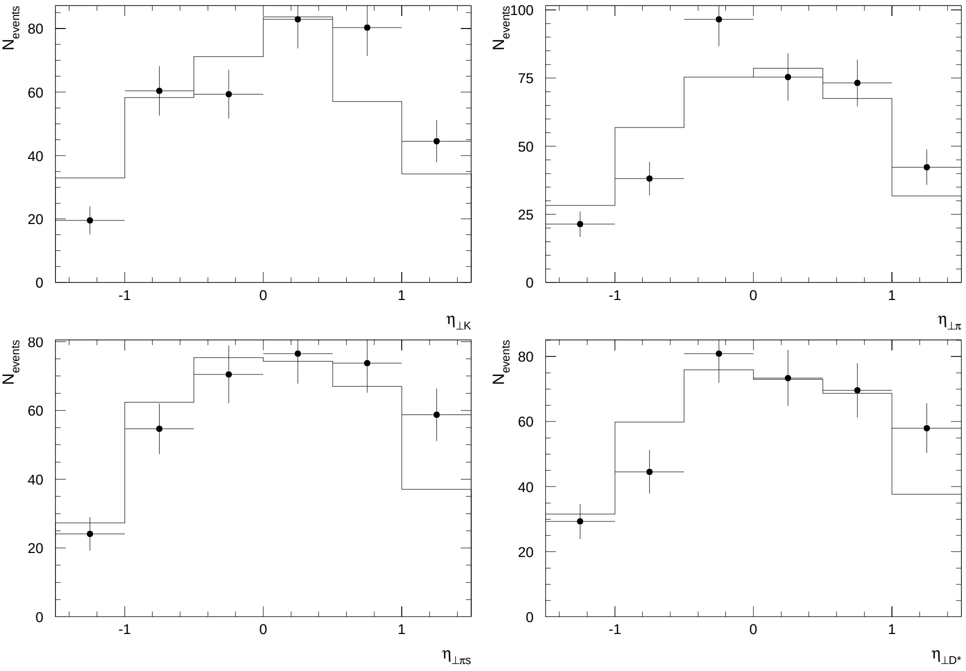

Fig. 7.15 Distributions of pseudorapidities of D^* mesons and their daughter particles in data (dots) and in the HERWIG simulation (histogram)

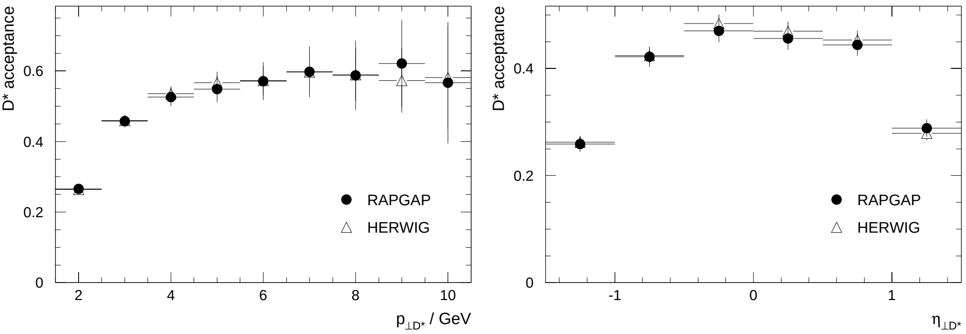

Fig. 7.16 D^* acceptance as a function of $p_\perp$ (left) and η (right)

the acceptance for $D^*(2010)^\pm$ mesons is 39.0% as determined with RAPGAP and 39.7% as determined with HERWIG, where the small difference results from the different η distributions of the two simulations.

7.6 Positive and Negative D*± Candidates

From the charge dependence of the track reconstruction, especially for low momentum tracks (see Sect. 4.3), we expect slow positive pions to be favoured against the negative ones and thus the ΔM resolution as well as the D* acceptance to be larger for D^{*+} than for D^{*-} Mesons. Figure 7.17 shows, for data and for the MC simulation, the ΔM distributions separately for the D^{*+} and the D^{*-} candidates. Data and simulation agree well on the charge dependence of the signal width, which widens from 0.7 ± 0.1 MeV (MC: 0.6 MeV) for positive tracks to 1.2 ± 0.2 MeV (MC: 1.0 MeV) for negative tracks. It can therefore be assumed that also the acceptance difference between D^{*+} and D^{*-} is correctly modelled, esp. since all charge effects known from single track distributions are well reproduced by the MOZART simulation (from version 95v2 onwards; see, for instance, Ref. 72). From the RAPGAP simulation 40.3% acceptance was obtained for positive tracks and 37.9% for negative tracks. In the data 168.3 ± 16.8 D^{*+}'s and 187.1 ± 17.7 D^{*-}'s were found. This 11% difference rises to 18% after acceptance correction. Considering the statistical error of the event numbers ($\sim 10\%$), this difference is statistically not significant, but may suggest some charge dependence of the cross-section for D* production—even more so as also in photoproduction some indication of

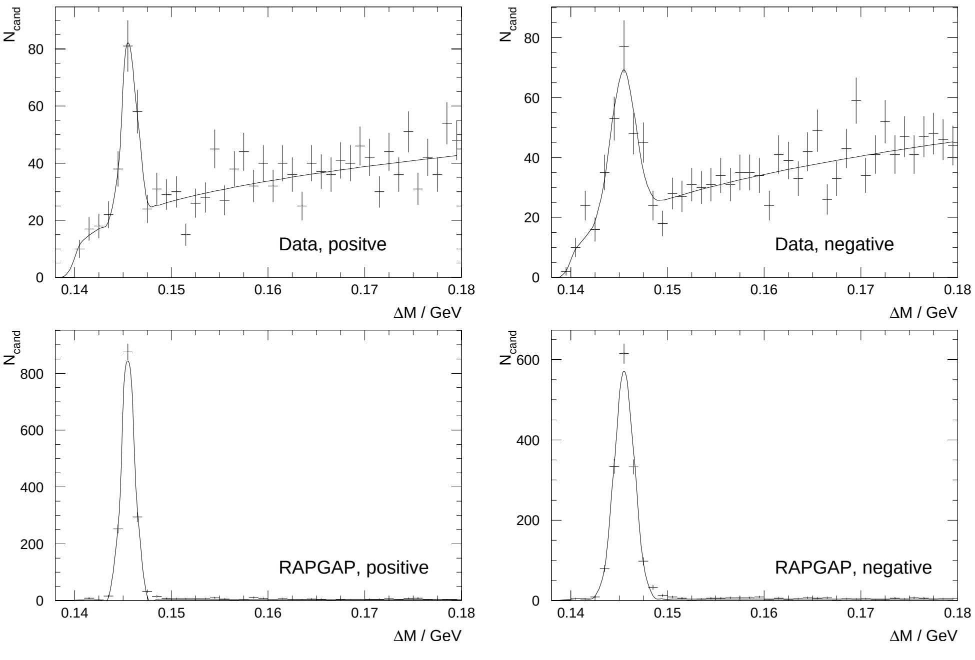

Fig. 7.17 ΔM distributions for positive (left) and negative tracks (right) in data (top) and MC simulation (bottom)

a charge dependence has been seen [157, 57]. Whether a possible asymmetry could be attributed to fragmentation effects (cf. Sect. 2.4) or to yet unknown detector effects needs further study with more statistics.[†]

[†] Similar observations were made at FermiLab for $W \sim 20\,\mathrm{GeV}$ [98].

8 $\mathrm{D}^{*\pm}$ Cross-Sections and F_2^{c}

8.1 Cross-Sections for $\mathrm{D}^{*\pm}$ Production

The D^* electroproduction cross-section in the restricted phase region ($1.5 < p_{\perp\mathrm{D}^*} < 10\,\mathrm{GeV}, |\eta_{\mathrm{D}^*}| < 1.5$) can be calculated from the number of D^* candidates observed, according to

$$\sigma^{(p_\perp,\eta)}_{\mathrm{ep}\to\mathrm{eD}^{*\pm}X} = \frac{N_{\mathrm{D}^*}}{\varepsilon_{\mathrm{DIS}}\,\varepsilon_{\mathrm{D}^*}\,\mathscr{B}(\mathrm{D}^{*\pm}\to\mathrm{K}\pi\pi_{\mathrm{s}})\,L}\ , \tag{8.1}$$

where N_{D^*} is the number of D^* candidates in the signal region after background subtraction, $\varepsilon_{\mathrm{DIS}}$ is the DIS acceptance (see Sect. 7.4), $\varepsilon_{\mathrm{D}^*}$ the D^* acceptance (see Sect. 7.5), $\mathscr{B}(\mathrm{D}^{*\pm}\to\mathrm{K}\pi\pi_{\mathrm{s}}) = \mathscr{B}(\mathrm{D}^{*\pm}\to\mathrm{D}^0\pi^+)\times\mathscr{B}(\mathrm{D}^0\to\mathrm{K}^-\pi^+) = 2.63 \pm 0.08\%$ is the combined branching fraction for the decay chain studied (see Sect. 2.3) and $L \equiv \int \mathrm{d}t\,\mathscr{L} = 6.03\,\mathrm{pb}^{-1}$ the integrated luminosity of the data sample. Table 8.1 presents the cross-sections as determined for two different Q^2 ranges. The smaller Q^2 interval corresponds to that of the published 1994 analysis; the earlier cross-section data agree well with the new measurement.

The measured cross-sections are compared with the result of the NLO QCD calculation by Harris and Smith [117] as obtained with the HVQDIS [118] program. For this calculation, the GRV 94 HO (NLO) set [108] from the parton distribution function library [162] provided the input gluon and light quark momentum densities.† The charm quark mass was set to $m_{\mathrm{c}} = 1.5\,\mathrm{GeV}$; the factorisation and renormalisation scales were $\mu_{\mathrm{F}}^2 = \mu_{\mathrm{R}}^2 = Q^2 + 4m_{\mathrm{c}}^2$, and for the charm branching the value measured by OPAL [3] was taken, $f(\mathrm{c}\to\mathrm{D}^{*+}) = 0.222 \pm 0.014 \pm 0.014$; Peterson fragmentation was applied with $\varepsilon_{\mathrm{P}} = 0.035$ (see Sect. 2.4). The prediction agrees reasonably well with the measured cross-section, considering that a change of the charm quark mass in the theoretical calculation by $\pm 0.2\,\mathrm{GeV}$ varies the predicted cross-section by $\pm$15–20%, making it the dominant uncertainty of the calculation.

The following systematic checks were performed (with the resulting fractional change of the D^* cross-section listed in brackets):

– The electron method instead of the double angle method was used for the reconstruction of the event kinematics (−1.4%).

---

† The choice of the parton distribution set is conceptually limited by the fact that the NLO calculation by Harris and Smith treats charm quarks as massive particles, which are produced in the hard subprocess, solely. The GRV 94 approach fits well into this framework as it does not entail heavy quarks among the (massless) intrinsic partons. It uses the same renormalisation scheme as HVQDIS ($\overline{\mathrm{MS}}$), which is required for a consistent calculation.

Table 8.1 Integrated cross-section in the restricted ($p_{\perp\mathrm{D}^*}, \eta_{\mathrm{D}^*}$) region for $y < 0.7$ and three different Q^2 ranges. The first error given is statistical, the second systematic.

Q^2	1–5 GeV^2	5–100 GeV^2	1–600 GeV^2
N_{D^*}	52 ± 11	256 ± 20	355 ± 24
$\varepsilon_{\mathrm{DIS}}$	21.8%	78.9%	63.0%
$\varepsilon_{\mathrm{D}^*}$	39.0%	39.0%	39.0%
$\sigma^{(p_\perp,\eta)}_{\mathrm{ep}\to\mathrm{eD}^{*\pm}X}$	$3.8 \pm 0.8 \pm 0.7\,\mathrm{nb}$	$5.24 \pm 0.42\,^{+0.45}_{-0.40}\,\mathrm{nb}$	$9.11 \pm 0.63\,^{+0.55}_{-0.50}\,\mathrm{nb}$
$\sigma\,(\mathrm{ZEUS\,94})$ [a]		$5.3 \pm 1.0 \pm 0.8\,\mathrm{nb}$	
$\sigma\,(\mathrm{NLO}, m_c = 1.5\,\mathrm{GeV})$	3.6 nb	4.3 nb	8.2 nb

[a] The D* phase space region of the 1994 analysis was $1.3 < p_{\perp\mathrm{D}^*} < 9\,\mathrm{GeV}$, $|\eta_{\mathrm{D}^*}| < 1.5$.

- The electron box cuts around the rear beampipe were loosened/tightened by 0.5 cm ($^{+1.5}_{-1.2}\%$).
- An additional cut $y_{\mathrm{JB}} > 0.02$ was introduced (+0.4%).
- The cut on the event vertex was removed (+1.4%).
- N_{D^*} was determined by an unbinned likelihood fit and not from background subtraction using wrong charge combinations (−1%).
- The D^0 mass window was widened/narrowed by ±20 MeV (+2.8/2.4%).
- The ΔM signal region was widened/narrowed by ±1 MeV ($^{+1.2}_{-0.8}\%$).
- The transverse momentum cut on the slow pion was varied by ±10 MeV ($^{+3.2}_{-4.1}\%$).
- The transverse momentum cut on the kaon and pion from the D^0 decay was varied by ±50 MeV ($^{+1.5}_{-2.3}\%$).
- HERWIG was used instead of RAPGAP for calculating $\varepsilon_{\mathrm{D}^*}$ (−1.7%).
- DJANGO was used instead of RAPGAP for calculating $\varepsilon_{\mathrm{DIS}}$ (+1.4%).

The overall systematic error is obtained by separately summing positive and negative contributions in quadrature. Additional systematic uncertainties, which are not included in the above errors, arise from

- the luminosity measurement (1.4%),
- the uncertainties of the D* and D^0 branching fractions [62] (3.1%),
- contamination from photoproduction ($\sim 1\%$ as estimated from running the event selection on simulated photoproduction events),
- the subsample of diffractively produced D* mesons ($\lesssim 1\%$), which contribute about 6% of the cross-section [74] and might have selection efficiencies

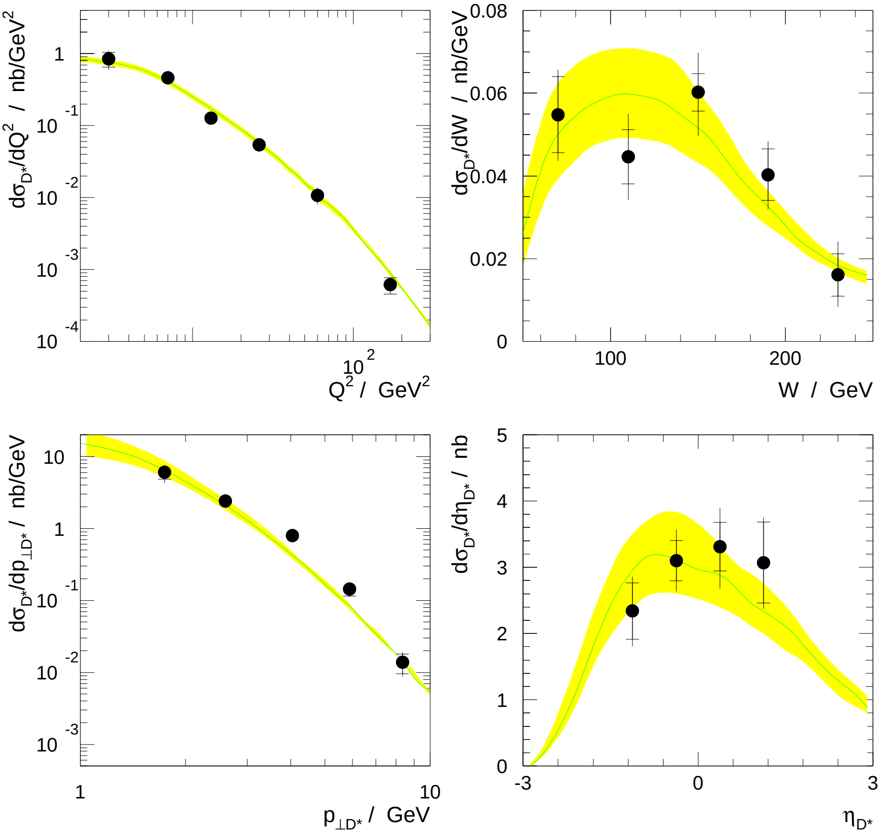

Fig. 8.1 Differential cross-sections for the production of $D^{*\pm}$ Mesons in the restricted phase space region (see text) as functions of Q^2, W, $p_{\perp D^*}$ and η_{D^*} for data (dots) and the NLO QCD prediction of HVQDIS (band). The inner and outer error bars denote the statistical errors and the statistical and systematic errors added in quadrature, respectively. There are additional systematic uncertainties of $\lesssim 11\%$, which have not been included in the error bars (see text). The shaded band for the calculation corresponds to a variation of the charm quark mass between $m_c = 1.3\,\mathrm{GeV}$ (upper limit of the band) and $1.7\,\mathrm{GeV}$ (lower limit).

slightly different from the rest of the sample, which is not accounted for in the MC simulation,

- the charge dependence of the D^* cross-section (see Sect. 7.6), which could be due to an unknown detector effect ($\lesssim 10\%$).

The total expected uncertainty from these sources is $\lesssim 11\%$. Differential cross-sections were obtained by replacing the total N_{D^*} and acceptances in (8.1) with their bin-wise values and dividing by the bin width. Figure 8.1 shows the differential cross-sections in bins of Q^2, W, $p_{\perp D^*}$ and η_{D^*}. The fall-offs observed in the Q^2 and η_{D^*} distributions mainly result from the decreasing photon flux factor in (2.1). The $p_{\perp \mathrm{D}^*}$ distribution is exponentially falling, while the η_{D^*} distribution is peaked in the central–forward region. Within the uncertainty band for the charm quark mass, the NLO predictions from HVQDIS are generally in good agreement with the data, except for a possible shift in the η_{D^*} distribution.

8.2 Determination of the Charm Structure Function F_2^{c}

From the measured D* production cross-section, the cross-section for open charm production can be determined by extrapolating from the restricted to the full $(p_\perp, \eta)$ phase space using the NLO calculation and scaling the result with the probability that a charm quark fragments into a D* meson, $f(\mathrm{c}{\to}\mathrm{D}^{*+})$,

$$\sigma^{\mathrm{meas}}_{\mathrm{ep}\to\mathrm{e\,c\bar{c}}\,X} = \frac{C^{(p_\perp,\eta)}\,\sigma^{(p_\perp,\eta)\,\mathrm{meas}}_{\mathrm{ep}\to\mathrm{e\,D}^{*\pm}X}}{2f(\mathrm{c}\to\mathrm{D}^{*+})(1+\delta_{\mathrm{b}}+\delta_{\mathrm{g}\to\mathrm{c\bar{c}}})}\,,$$

$$C^{(p_\perp,\eta)} \equiv \frac{\sigma^{\mathrm{theo}}_{\mathrm{ep}\to\mathrm{e\,c\bar{c}}\,X}}{\sigma^{(p_\perp,\eta)\,\mathrm{theo}}_{\mathrm{ep}\to\mathrm{e\,c\bar{c}}\,X}}\,,$$

where the factor 2 in the denominator allows for the charge-conjugated process $\bar{\mathrm{c}}{\to}\mathrm{D}^{*-}$, which is assumed to have the same probability. The corrections $\delta_{\mathrm{b,g}\to\mathrm{c\bar{c}}}$ account for the fraction of D* mesons that do not originate from charm quarks produced in the hard subprocess, but from beauty decays or from charm produced through gluon splitting in the fragmentation. The beauty contribution δ_{b} is suppressed by the large mass of the beauty quark and is expected to be of the order of 2% [76], integrated over the whole accessible phase space. First preliminary measurements of open beauty photoproduction at ZEUS [200] indicate that the beauty *fraction*—yet not the overall magnitude—is well described by contemporary LO MC simulations. The fraction of events containing a $\mathrm{c\bar{c}}$ pair produced in fragmentation has been measured at OPAL to be $\langle n_{\mathrm{g}\to\mathrm{c\bar{c}}}\rangle = 2.38 \pm 0.48\%$ [7]; H1 extrapolated this to HERA energies, obtaining $\delta_{\mathrm{g}\to\mathrm{c\bar{c}}} = 2 \pm 2\%$ for their restricted phase space region [4]. Since δ_{b} and $\delta_{\mathrm{g}\to\mathrm{c\bar{c}}}$ can only roughly be estimated, but are expected to be much smaller than the uncertainty of $f(\mathrm{c}{\to}\mathrm{D}^{*+})$ of 9%, they are neglected in the cross-section calculation.

HVQDIS was run with the same parameter setting as for the previous section ($m_{\mathrm{c}} = 1.5\,\mathrm{GeV}$). For $f(\mathrm{c}{\to}\mathrm{D}^{*+})$ again the value obtained by OPAL was taken, thus neglecting the fragmentation differences between charm quarks produced in photon–gluon fusion (PGF) at HERA and those produced in hadronic Z decays at LEP.† The extrapolation factors obtained are listed in

---

† An example for a difference of this type is the hadronisation of a $\mathrm{c\bar{c}}$ pair as a bound $\mathrm{c\bar{c}}$ state if the quark pair has been produced in a hard process: this is suppressed at LEP, while at

Table 8.2 The factors $C^{(p_\perp,\eta)}$ used for the extrapolation from the restricted $(p_{\perp\mathrm{D}^*}, \eta_{\mathrm{D}^*})$ range to the full phase space as obtained with HVQDIS in NLO [116]

Q^2 range	$y < 0.2$	$y < 0.7$	$0.2 < y < 0.7$
$90 < Q^2 < 600\,\mathrm{GeV}^2$		1.80	
$35 < Q^2 < 90\,\mathrm{GeV}^2$	2.32		1.79
$17 < Q^2 < 35\,\mathrm{GeV}^2$	2.55		2.21
$39 < Q^2 < 17\,\mathrm{GeV}^2$	3.02		2.73
$5 < Q^2 < 9\,\mathrm{GeV}^2$	3.73		3.28
$1 < Q^2 < 5\,\mathrm{GeV}^2$		4.81	

Table 8.2. The extrapolation factors become large for low values of Q^2, because in that regime the transverse momenta of the D* mesons are small and often fall below the limit of the restricted phase space region.

The double differential open charm cross-section can be expressed in terms of the charm structure function F_2^c, analogously to (2.3),

$$\frac{\mathrm{d}^2\sigma_{\mathrm{ep}\to\mathrm{e\,c\bar{c}}\,X}}{\mathrm{d}x\,\mathrm{d}Q^2} \approx \frac{2\pi\alpha^2}{xQ^4}[1 + (1-y)^2]F_2^c(x, Q^2)\,. \tag{8.2}$$

The correction terms in (2.3) are small and can be neglected (see below). Inclusive calculations by Laenen *et al.* [141] infer the structure function F_2^c from the PGF matrix elements in NLO QCD, folded with the parton densities of the proton. From the measured cross-sections, the values of F_2^c can be extracted. Since F_2^c varies only weakly within the kinematic bins, the simple technique of correcting the calculation to the measurement by binwise factors can be applied and we assume

$$F^c_{2\,\mathrm{meas}}(\hat{x}_i, \hat{Q}_i^2) = \frac{(\sigma_{\mathrm{ep}\to\mathrm{e\,c\bar{c}}\,X})_{i,\mathrm{meas}}}{(\sigma_{\mathrm{ep}\to\mathrm{e\,c\bar{c}}\,X})_{i,\mathrm{theo}}} F^c_{2\,\mathrm{theo}}(\hat{x}_i, \hat{Q}_i^2)\,, \tag{8.3}$$

where $\hat{x}_i$ and $\hat{Q}_i^2$ are the averages of x and Q^2 in bin i. Provided that the calculation describes the data shapewise well, we can use it also to shift the phase space position to another point (x, Q^2), so that (8.3) holds in any point not-too-far from the bin average,

$$F^c_{2\,\mathrm{meas}}(x, Q^2) = \frac{(\sigma_{\mathrm{ep}\to\mathrm{e\,c\bar{c}}\,X})_{i,\mathrm{meas}}}{(\sigma_{\mathrm{ep}\to\mathrm{e\,c\bar{c}}\,X})_{i,\mathrm{theo}}} F^c_{2\,\mathrm{theo}}(x, Q^2)\,.$$

The theoretical cross-sections were obtained with HVQDIS, while for the F_2^c calculation the parametrisation by Riemersma *et al.* [165] was used. The same

---

HERA the cross section for this process could be as large as 200–400 pb for $Q^2 > 4\,\mathrm{GeV}^2$ [95], which is a few percent of the D* cross section. Since the NLO calculation only considers charm quarks produced dynamically from the gluon content of the proton, contributions from other production mechanisms, e.g., from an intrinsic charm component in the proton, are neglected, too.

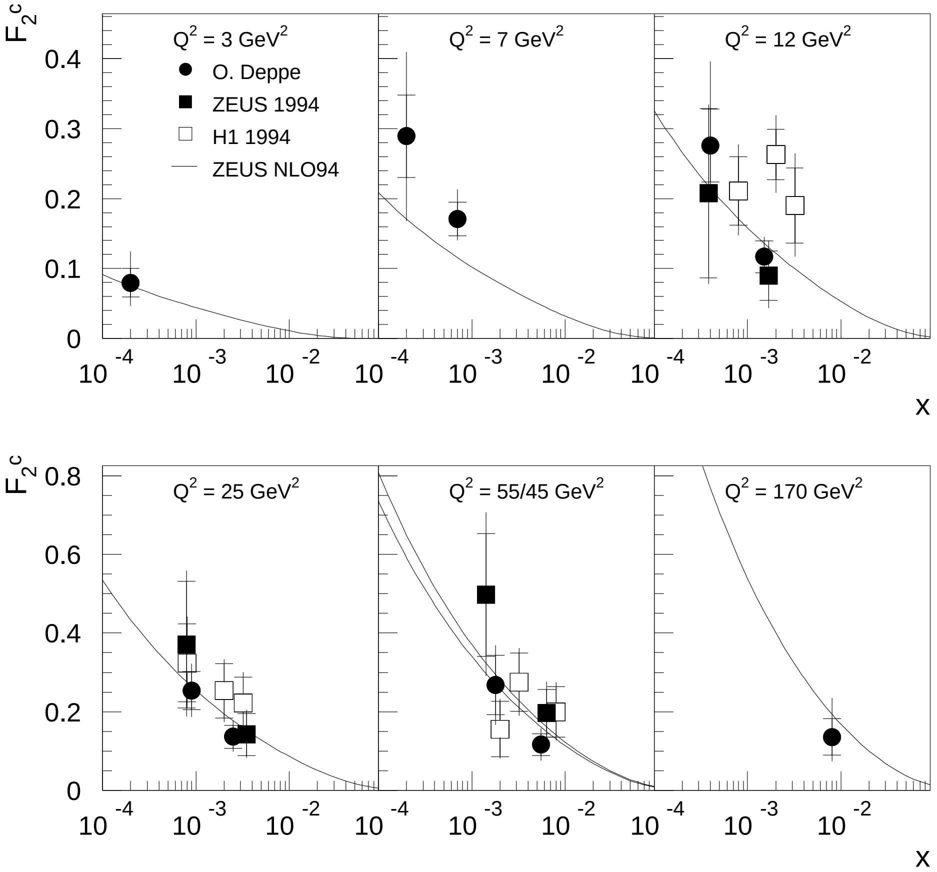

Fig. 8.2 The $F_2^c(x, Q^2)$ results of this analysis (1995) in comparison with HERA results from the 1994 data taking. In the fifth bin, the 1994 values lie at $Q^2 = 45\,\mathrm{GeV}$. An additional uncertainty of $\sim 25\%$ is not included in the error bars (see text). The curves show the NLO prediction for $m_c = 1.5\,\mathrm{GeV}$ using the gluon density extracted by ZEUS [81].

parameter settings were used as above and the GRV 94 HO set provided the input parton distributions.

Figure 8.2 shows the extracted structure function F_2^c for the 10 kinematic bins of Table 8.2. The unfolded F_2^c values suffer additional uncertainties with respect to the D* cross-section measurement, not included in the error bars:

- contributions from a charm component in the proton which is not produced through PGF (H1 set an upper limit of 5% on the size of this contribution [4]),
- a possible admixture of charm production from beauty or through gluon splitting in the fragmentation (both $\sim 2\%$, see above),

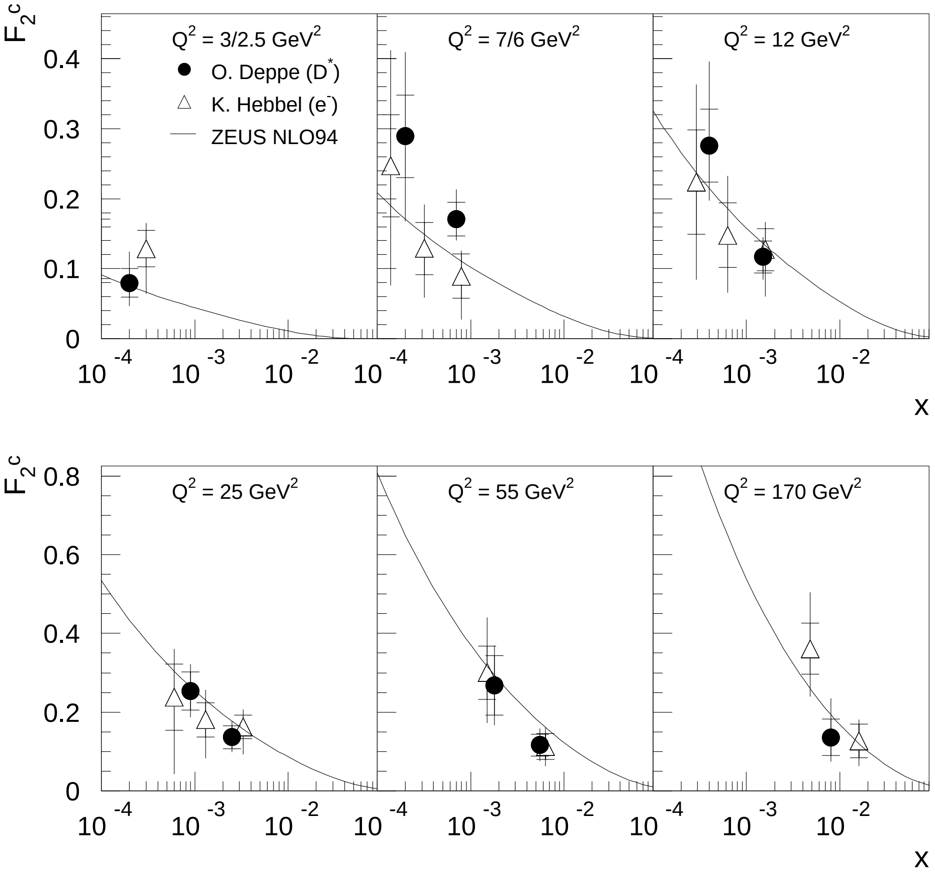

Fig. 8.3 $F_2^c(x, Q^2)$ as determined from D^* production, in comparison with the results from a study of semileptonic charm decays [121] from the same year of data taking (1995). The curves show the NLO prediction for $m_c = 1.5\,\mathrm{GeV}$ using the ZEUS 94.

- the influence of the choice of the input gluon distribution, which can be seen from Fig. 8.4 to be less than 5–10%,
- the uncertainty of the charm quark mass, which adds an error of 15–20%,
- the contribution from the F_L term, which has been estimated using the program by Riemersma *et al.* [165] to be well below 1% for $y < 0.2$, but to reach up to 7% for $y = 0.6$ at high Q^2,
- QED radiative corrections of less than 4% (at high Q^2) as estimated using RAPGAP,
- the 9% uncertainty of the branching fraction $f(c \rightarrow D^{*+})$. By taking the OPAL value at $\mu = m_Z$, we neglected the scale dependence of this branching fraction, which is expected to grow by $\sim 8\%$ if $\mu \rightarrow 2m_c$ [30].

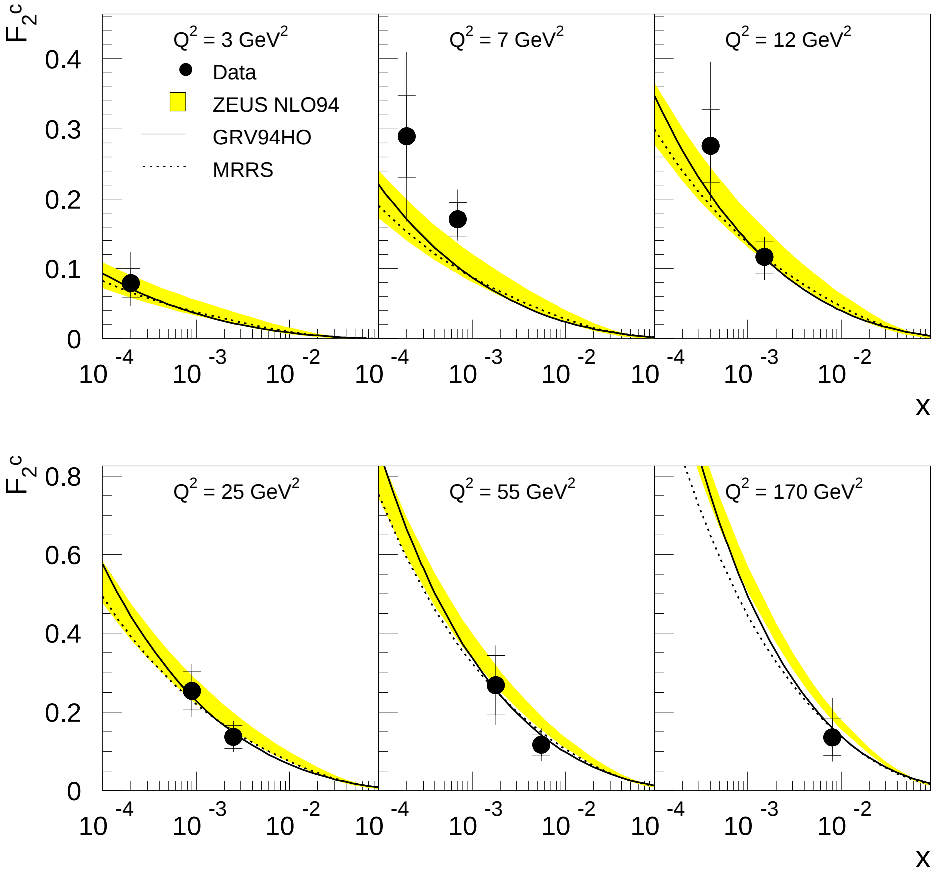

Fig. 8.4 $F_2^c(x, Q^2)$ from the 1995 data in comparison with predictions for different structure functions. The band demonstrates the dependence on the choice of the charm quark mass, which was varied between $m_c = 1.3\,\text{GeV}$ (upper edge) and $m_c = 1.7\,\text{GeV}$ (lower edge of the band).

Added in quadrature, these uncertainties amount to an additional systematic error of $\sim 25\%$.

A rise of F_2^c with decreasing x is observed, which becomes steeper with rising Q^2. This behaviour can be understood as the result of the steeply rising density of gluons in the proton as $x \to 0$ [48, 81]. The results of this analysis are in agreement with previous findings at HERA shown in the same figure.

Charm production can also be measured via the detection of the outgoing charged lepton from semileptonic decays of charmed mesons. This approach benefits from the much larger branching fraction $f(c \to \ell^+) \sim 10\%$, but suffers from a large background of leptons produced in other processes and from the fact that the presence of a neutrino in the final state makes it impossible to fully reconstruct the D meson and its momentum. The results of such a study [121] are compared with this analysis in Fig. 8.3 (note that the higher statistics of the semileptonic decays allow a finer binning), showing a good agreement between the results of the two experimentally very different analyses.

In Fig. 8.4 the extracted structure function values are compared with F_2^{c} predictions obtained using different parton distribution sets: GRV 94 HO [108], MRRS [148] and the distributions obtained from a NLO QCD analysis performed by the ZEUS collaboration with its 1994 data, ZEUS NLO 94 [81]. The impact of the charm quark mass uncertainty is shown as well. Within the experimental error and the theoretical uncertainties, the measured F_2^{c} values and the theoretical predictions agree well.

9 Summary and Conclusions

An analysis of the production of $D^*(2010)^\pm$ mesons in deep inelastic scattering at HERA has been presented. It is based on data taken with ZEUS in 1995. The integrated luminosity of $6\,\mathrm{pb}^{-1}$ is about twice as large as what had been used for the 1994 analysis published by ZEUS [47].

In the course of this study a new analysis shell program, $\mathcal{EZ}$ [77], has been developed, which provides the user with a uniform interface to the generated and reconstructed objects and in particular makes the study of single particles and their decays straightforward. It has since become a central part of the ZEUS event display program, LAZE.

A detailed study of particle identification by means of the ionisation energy loss, $\mathrm{d}E/\mathrm{d}x$, in the CTD has been performed. A hadron identification method using the likelihood of the $\mathrm{d}E/\mathrm{d}x$ measurement has been developed and tested. While this method has been found to allow a substantial background reduction in other studies of processes involving charm and strange particles, it has yielded only a limited gain in the study of D^* production presented here and has not been used for the final results.

The integrated cross-section for D^* production and differential cross-sections in Q^2, W, $p_{\perp D^*}$ and η_{D^*} have been measured in the kinematic range $1 < Q^2 < 600\,\mathrm{GeV}^2$ and $y < 0.7$ for a restricted region of the D^* phase space, $1.5 < p_{\perp D^*} < 10\,\mathrm{GeV}$ and $|\eta_{D^*}| < 1.5$. In this region, the integrated cross-section has been determined as $9.11 \pm 0.63\,^{+0.55}_{-0.50}\,\mathrm{nb}$; in the phase space region of the 1994 ZEUS analysis, $5 < Q^2 < 100\,\mathrm{GeV}$, the result is $5.24 \pm 0.42\,^{+0.45}_{-0.40}\,\mathrm{nb}$, in good agreement with the earlier measurement. The differential D^* cross-sections fall exponentially in Q^2 and $p_{\perp D^*}$. With respect to the η_{D^*} distribution a maximum is observed around $\eta_{D^*} \approx 0.5$. As a function of W, the D^* cross-section shows a slow fall-off with increasing W. Within the experimental and theoretical uncertainties, the integrated and differential cross-sections are well reproduced by NLO calculations [117] of perturbative QCD.

Using the NLO calculations, the measurements have been extrapolated to the full D^* phase space and the charm contribution F_2^c to the proton structure function F_2 has been determined. The unfolded F_2^c values are in good agreement with the 1994 ZEUS results and with results from an analysis of semileptonic charm decays also using 1995 data [121]. F_2^c has been found to rise steeply towards low values of Bjorken-x; the rise becomes steeper with increasing Q^2. With photon–gluon fusion being the leading process, the observed rise of F_2^c is directly related to an increase of the gluon momentum density of the proton, $xg(x)$, as $x \to 0$. The NLO QCD calculations [165] performed for F_2^c using $xg(g)$, as determined from the scaling violations of F_2 observed in the 1994 ZEUS data [81], show good agreement with the data. Therefore, the data presented in this analysis provide an important consistency test of perturbative quantum chromo-dynamics.

* * *

I am deeply grateful to my adviser G. Wolf for the kind and heartening support I received from him. I am indebted to him and to E. Lohrmann, N. A. McCubbin and N. Pavel for their valuable advice and comments on parts of the manuscript. I would also like to express my gratitude to Y. Eisenberg, D. Hochman, U. Karshon, R. Klanner, L. M. Shcheglova and A. M. Solomin for their support and encouragements. Many thanks go to C. D. Caterall, G. F. Hartner and J. B. Lane, who helped my understanding of the CTD. Many thanks go also to B. W. Harris and S. Riemersma for supplying me with cross-section calculations and their program code. I warmly thank J. P. Fernandez and L. K. Gladilin for helpful discussions, and the students of the Hamburg group for their care and friendship.

References

1. Abramowicz H., A. Caldwell, R. Sinkus. Neural network based electron identification in the ZEUS calorimeter. *Nucl. Instrum. Methods* A 365 (1995) 508–17, hep-ex/9505004.
2. Abt I. *et al.* (H1 Collab.). The H1 detector at HERA. *Nucl. Instrum. Methods* A 386 (1997) 310–47.
3. Ackerstaff K. *et al.* (OPAL Collab.). Measurement of $f(\mathrm{c} \rightarrow \mathrm{D}^{*+}X)$, $f(\mathrm{b} \rightarrow \mathrm{D}^{*+}X)$ and $\Gamma_{\mathrm{c\bar{c}}}/\Gamma_{\mathrm{had}}$ using $\mathrm{D}^{*\pm}$ mesons. *Eur. Phys. J.* C 1 (1998) 439–59, hep-ex/9708021.
4. Adloff C. *et al.* (H1 Collab.). Inclusive D^0 and $\mathrm{D}^{*\pm}$ production in deep inelastic ep scattering at HERA. *Z. Phys.* C 72 (1996) 593–605, hep-ex/9607012.
5. Adloff C. *et al.* (H1 Collab.). Inclusive measurement of diffractive deep inelastic ep scattering. *Z. Phys.* C 76 (1997) 613–29, hep-ex/9708016.
6. Ahlen S. P. Theoretical and experimental aspects of the energy loss of relativistic heavily ionizing particles. *Rev. Mod. Phys.* 52 (1980) 121–73.
7. Akers R. *et al.* (OPAL Collab.). A measurement of the production of $\mathrm{D}^{*\pm}$ mesons on the Z^0 resonance. *Z. Phys.* C 67 (1995) 27–44, CERN-PPE-94-217.
8. Akers R. *et al.* (OPAL Collab.). Measurement of the multiplicity of charm quark pairs from gluons in hadronic Z^0 decays. *Phys. Lett.* B 353 (1995) 595–605, CERN-PPE-95-058.
9. Albrecht H., E. Blucher, J. Boucrot. ALPHA user's guide. ALEPH-94-092, CERN, 1994.
10. Allison W. W. M. and J. H. Cobb. Relativistic charged particle identification by energy loss. *Annu. Rev. Nucl. Part. Sci.* 30 (1980) 253–98.
11. Altarelli G. and G. Parisi. Asymptotic freedom in parton language. *Nucl. Phys.* B 126 (1977) 298–318.
12. Andersson B., G. Gustafson, G. Ingelman, T. Sjöstrand. Parton fragmentation and string dynamics. *Phys. Rep.* 97 (1983) 31–145.
13. Andersson B., G. Gustavson, L. Lönnblad, U. Petterson. Coherence effects in deep inelastic scattering. *Z. Phys.* C 43 (1989) 625–32.
14. Andresen A. *et al.* (ZEUS Calorimeter Group). Construction and beam test of the ZEUS forward and rear calorimeter. *Nucl. Instrum. Methods* A 309 (1991) 101–42.
15. Andruszkòw J. *et al.* (ZEUS Luminosity Monitor Group). First measurement of HERA luminosity by ZEUS lumi monitor. DESY-92-066, Hamburg, 1992.
16. Anjos J. C. *et al.* (E691 Collab.). Charm photoproduction. *Phys. Rev. Lett.* 62 (1989) 513–17.
17. Aubert J. J., U. Becker, P. J. Biggs, *et al.* Experimental observation of a heavy particle J. *Phys. Rev. Lett.* 33 (1974) 1404–6.
18. Augustin J. E., A. Boyarski, M. Breidenbach, *et al.* Discovery of a narrow resonance in $\mathrm{e}^+\mathrm{e}^-$ annihilation. *Phys. Rev. Lett.* 33 (1974) 1406–8.
19. Bailey D. S., B. Foster, G. P. Heath, *et al.* The design and performance of the ZEUS central tracking detector z-by-timing system. *Nucl. Instrum. Methods* A 396 (1997) 320–49, hep-ex/9707032.
20. Bamberger A. *et al.* (ZEUS Presampler Group). The presampler for the forward and rear calorimeter in the ZEUS detector. *Nucl. Instrum. Methods* A 382 (1996) 419–29, hep-ex/9609006.
21. Bamberger A. *et al.* (ZEUS SRTD Group). The small angle rear tracking detector of ZEUS. *Nucl. Instrum. Methods* A 401 (1997) 63–80.

22. Barkas W. H. and M. J. Berger. Tables of energy losses and ranges of heavy charged particles. In *Studies in Penetration of Charged Particles in Matter* (Nuclear Science Series 39, 1964), NAS-NRC Publication № 1133, National Academy of Sciences–National Research Council, pp. 103–72, NASA-SP-3013.
23. Bauerdick L. A. T., O. Derugin, D. Gilkinson, *et al.* ZARAH—The central computing facility for the ZEUS experiment. In *Computing in High Energy Physics '95,* Proceedings of the international conference (Rio de Janeiro, 1995), R. Shellard and T. D. Nguyen (Eds.), LAFEX/CBPF and FermiLab, World Scientific, Singapore 1996, pp. 288–93.
24. Behnke T. Heavy Flavour Physik. Presentation at the DPG meeting, Hamburg, Mar. 1996.
25. Bentvelsen S., J. Engelen, P. Kooijman. Reconstruction of (x, Q^2) and extraction of structure functions in neutral current scattering at HERA. In Ref. 56, *Phys. HERA Proc.*, Vol. 1, pp. 23–41.
26. Bethe H. Zur Theorie des Durchgangs schneller Korpuskularstrahlen durch Materie. *Ann. Physik 5.* 5 (1930) 325–400.
27. Bethe H. and J. Ashkin. In Vol. 1 of *Experimental Nuclear Physics*, E. Segrè (Ed.). John Wiley & Sons, New York, 1953. Part II: Passage of Radiations through Matter, pp. 166–357.
28. Bethe H. and W. Heitler. On the stopping of fast particles and on the creation of positive electrons. *Proc. R. Soc. London* A 146 (1934) 83–112.
29. Bhabha H. J. On the penetrating component of cosmic radiation. *Proc. R. Soc. London* A 164 (1938) 257–94.
30. Binnewies J., B. A. Kniehl, G. Kramer. Predictions for $\mathrm{D}^{*\pm}$ photoproduction at HERA with new fragmentation functions from LEP 1. *Phys. Rev.* D 58 (1998) 014014, hep-ph/9712482.
31. Bjorken J. D. and E. A. Paschos. Inelastic electron–proton and γ–proton scattering and the structure of the nucleon. *Phys. Rev.* 185 (1969) 1975–82.
32. Bjørken B. J. and S. L. Glashow. Elementary particles and SU(4). *Phys. Lett.* 11 (1964) 255–57.
33. Blietschau J., K. Böckmann, P. Bosetti, *et al.* Production of charmed mesons in neutrino interactions in hydrogen. *Phys. Lett.* 86B (1979) 108–14.
34. Blissett J. A., D. K. Hasell, A. G. Parham, *et al.* Development of a tapered cell drift chamber II : Operation of high magnetic fields and different gas pressures. *Nucl. Instrum. Methods* A 245 (1986) 291–98.
35. Blümlein J. and M. Klein. Structure functions and QCD tests. In Ref. 56, *Phys. HERA Proc.*, Vol. 1, pp. 23–41, DESY-92-038.
36. Blobel V. Unfolding methods in high-energy physics experiments. In *CERN School of Computing* (Aiguablava, 1984), C. Verkerk (Ed.), pp. 88–127, CERN-85-09.
37. Bloch F. Zur Bremsung rasch bewegter Teilchen beim Durchgang durch Materie. *Ann. Physik 5.* 16 (1933) 285–320.
38. Bénard F., R. S. Orr, S. Polenz, D. Simmons. The 1995 TLT filter software. Internal ZEUS-Note 95-164, DESY, Hamburg, 1995.
39. Bohr N. On the theory of the decrease of velocity of moving electrified particles on passing through matter. *Philos. Mag.* 25 (1913) 10–31.
40. Bohr N. On the decrease of velocity of swiftly moving particles in passing through electrified matter. *Philos. Mag.* 30 (1915) 581–612.
41. Bornheim A. Kalibration des Presamplers für die Elektron-Energiemessung im ZEUS-Detektor. Diplom thesis, University of Bonn, July 1995, BONN-IB-95-24.
42. Bortoletto D. *et al.* (CLEO Collab.). Charm production in nonresonant $\mathrm{e}^+\mathrm{e}^-$ annihilations at $\sqrt{s} = 10.55\,\mathrm{GeV}$. *Phys. Rev.* D 37 (1988) 1719–43.

43. Botje M. A. J. (for the ZEUS Collab.). QCD fits to ZEUS and fixed target structure function data. NIKHEF/97-028, Amsterdam, 1997. Presented at the 5th International Workshop on Deep Inelastic Scattering and QCD (DIS 97), Chicago, Apr. 1997.
44. Bragg W. H. and R. Kleeman. On the α particles of radium, and their loss of range in passing through various atoms and molecules. *Philos. Mag.* 10 (1905) 318–40.
45. Brandelik R. *et al.* (TASSO Collab.). Evidence for planar events in e^+e^- annihilation at high energies. *Phys. Lett.* 86B (1979) 243–61.
46. Breidenbach M., E. D. Bloom, *et al.* Observed behavior of highly inelastic electron–proton scattering. *Phys. Rev. Lett.* 23 (1969) 935–39.
47. Breitweg J. *et al.* (ZEUS Collab.). D^* production in deep inelastic scattering at HERA. *Phys. Lett.* B 407 (1997) 402–18, hep-ex/9706009.
48. Breitweg J. *et al.* (ZEUS Collab.). ZEUS results on the measurement and phenomenology of F_2 at low x and low Q^2. *Eur. Phys. J.* C 7 (1999) 609–30, hep-ex/9809005.
49. Breitweg J. *et al.* (ZEUS Collab.). Measurement of inclusive $D^{*\pm}$ and associated dijet cross sections in photoproduction at HERA. *Eur. Phys. J.* C 6 (1999) 67–83, hep-ex/9807008.
50. Brodsky S. J., P. Hoyer, A. H. Mueller, W. K. Tang. New QCD production mechanisms for hard processes at large x. *Nucl. Phys.* B 369 (1992) 519–42.
51. Brodsky S. J., P. Hoyer, C. Peterson, N. Sakai. The intrinsic charm of the proton. *Phys. Lett.* 93B (1980) 451–55.
52. Brook N. H. (for the H1 Collab. and the ZEUS Collab.). QCD at HERA. GLAS-PPE/98-02, Glasgow, May 1998. Presented at the 2nd Latin America Symposium on High-Energy Physics, San Juan, Puerto Rico, Apr. 1998.
53. Brooks C. B. *et al.* (ZEUS-UK Collab.). Development of the ZEUS central tracking detector. *Nucl. Instrum. Methods* A 283 (1989) 477–83.
54. Brun R., M. Goosens, H. Meinhard, *et al.* *The ZEBRA System.* CERN Program Library Long Writeups Q100/Q101, Geneva, 1995.
55. Bruni P., G. Ingelman, A. Solano. Diffractively produced hadronic final states and the pomeron structure. In Ref. 56, *Phys. HERA Proc.*, Vol. 1, pp. 363–75.
56. Buchmüller W. and G. Ingelman (Eds.). *Physics at HERA,* Proceedings of the workshop (Hamburg, 1991), DESY, Hamburg 1992.
57. Butterworth J., C. Coldewey, O. Deppe, *et al.* D^* and associated dijet photoproduction at HERA. Internal ZEUS-Note 98-047, DESY, Hamburg, 1998.
58. Caldwell A., I. Gialas, S. Mishra, *et al.* Design and implementation of a high precision readout system for the ZEUS calorimeter. *Nucl. Instrum. Methods* A 321 (1992) 356–64.
59. Callan, Jr. G. and D. J. Gross. High-energy electroproduction and the constitution of the electric current. *Phys. Rev. Lett.* 22 (1969) 156–59.
60. *HERA : A Proposal for a Large Electron Proton Colliding Beam Facility at DESY* (Hamburg, 1981), DESY-HERA-81/10.
61. Cashmore R., S. Dagan, O. Deppe, *et al.* Measurement of weak neutral current couplings of quarks at HERA. In Ref. 128, *Fut. Phys. HERA Proc.*, Vol. 1, pp. 161–89, DESY-96-235.
62. Caso C. *et al.* (Particle Data Group). Review of particle physics. *Eur. Phys. J.* C 3 (1998) 1–794 and 1999 off-year partial update for the 2000 edition available on the PDG WWW pages ⟨http://pdg.lbl.gov/⟩.
63. Cassidy A. S. *Optimising the Central Tracking Detector Readout at ZEUS & Measuring the Longitudinal Structure Function at HERA.* PhD thesis, H. H. Wills Physics Laboratory, University of Bristol, Feb. 1997.
64. Caterall C. *Measurement of Charged Particles from the Hadronic Final State of Electron–Proton Deep Inelastic Scattering at a Centre of Mass Energy of 296 GeV.* PhD thesis, University College, London, Sept. 1995.

65. Chang C., L. N. Hand, S. C. Loken, *et al.* Observed deviation from scale invariance in high-energy muon scattering. *Phys. Rev. Lett.* 35 (1975) 901–4.
66. Charchula K., G. A. Schuler, H. Spiesberger. Combined QED and QCD radiative effects in deep inelastic lepton–proton scattering : The Monte Carlo generator DJANGO 6. *Comput. Phys. Commun.* 81 (1994) 381–402, CERN-TH-7133-94.
67. Charpak G., R. Bouclier, T. Bressani, *et al.* The use of multiwire proportional counters to select and localize charged particles. *Nucl. Instrum. Methods* 62 (1968) 262–68.
68. Chechin V. A. and V. C. Ermilova. The ionization-loss distribution at very small absorber thickness. *Nucl. Instrum. Methods* 136 (1976) 551–58.
69. Chlebana F. Description of the ZEUS global second level trigger in 1994. Internal ZEUS-Note 94-102, DESY, Hamburg, 1995.
70. Chlebana F. Description of the ZEUS global second level trigger in 1995. Internal ZEUS-Note draft, NIKHEF, Amsterdam, Feb. 1996.
- ▷ CLEO Collaboration, see Refs. 42, 112.
71. Cohen E. R., P. Giacomo, *et al.* (SUNAMCO Commission). Symbols, units, nomenclature and fundamental constants in physics. *Physica* 146A (1987) 1–68, IUPAP-25.
72. Coldewey C. Comparison of positive and negative tracks using D^* data and MC samples. Presentation at the ZEUS tracking meeting, Oct. 1997.
73. Cole J. E. A study of positron energy correction in 1995 DIS data using the SRTD. Internal ZEUS-Note 98-022, DESY, Hamburg, 1998.
74. Cole J.E. *Open Charm Production in Deep Inelastic Diffractive* ep *Scattering at HERA*. PhD thesis, Imperial College, London, Jan. 1999.
75. Crispin A. and G. N. Fowler. Density effect in the ionization energy loss of fast charged particles in matter. *Rev. Mod. Phys.* 42 (1970) 291–316.
76. Daum K., S. Riemersma, B. W. Harris, *et al.* The heavy-flavour contribution to proton structure. In Ref. 128, *Fut. Phys. HERA Proc.*, Vol. 1, pp. 89–101, hep-ph/9609478.
77. Deppe O. and L. A. T. Bauerdick. User's guide to $\mathcal{EZ}$: Version 3.07/03. Internal ZEUS-Note 97-012, DESY, Hamburg, 1997.
78. Derman E. Tests for a weak neutral current in $l^{\pm} + \mathrm{N} \to l^{\pm} +$ anything at high energy. *Phys. Rev.* D 7 (1973) 2755–75.
79. Derrick M., D. Gacek, N. Hill, *et al.* Design and construction of the ZEUS barrel calorimeter. *Nucl. Instrum. Methods* A 309 (1991) 77–100.
80. Derrick M. *et al.* (ZEUS Collab.). Comparison of energy flows in deep inelastic scattering events with and without a large rapidity gap. *Phys. Lett.* B 338 (1994) 483–96.
81. Derrick M. *et al.* (ZEUS Collab.). Extraction of the gluon density of the proton at small x. *Phys. Lett.* B 345 (1995) 576–88.
82. Derrick M. *et al.* (ZEUS Collab.). Study of $D^*(2010)^{\pm}$ production in ep collisions at HERA. *Phys. Lett.* B 349 (1995) 225–37, hep-ex/9502002.
83. DESY Machine Division. In *Wissenschaftlicher Jahresbericht 1994*, DESY (Ed.). Hamburg, 1995. Chap. 'Speicherringanlage HERA'.
84. DESY-PR. Research at DESY. Brochure, Hamburg, Sept. 1996.
85. DESY-PR. DESY : Fotos und Grafiken. Web page ⟨http://www.desy.de/pr-info/foto-grafik-sammlung/foto_grafik_idx_d.html⟩, accessed Jan. 1997.
86. Dokshitser Yu. Calculation of structure functions of deep-inelastic scattering and e^+e^- annihilation by perturbation theory in quantum chromodynamics. *Sov. Phys. JETP* 46 (1977) 641–53 [*Zh. Eksp. Teor. Fiz.* 73 (1977) 1216–40].
87. Dulinski Z. Luminosity 1995. Presentation at the ZEUS weekly meeting, DESY, Hamburg, Jan. 1997.
- ▷ E687 Collaboration, see Ref. 98.
88. Eichten T. *et al.* (Gargamelle Collab.). Measurement of the neutrino–nucleon and antineutrino–nucleon total cross sections. *Phys. Lett.* 46B (1973) 243–61.

89. Ellis J., K. Geiger, H. Kowalski. Deep-inelastic final states in a space-time description of shower development and hadronization. *Phys. Rev.* D 54 (1996) 5443–62, hep-ph/9605425.
90. Fano U. Penetration of protons, alpha particles and mesons. *Annu. Rev. Nucl. Sci.* 13 (1963) 1–66.
91. Feldman G. J., F. Bulos, D. Luke, *et al.* Observation of the decay $D^{*+} \to D^0\pi^+$. *Phys. Rev. Lett.* 38 (1977) 1313–15.
92. Fermi E. The ionization loss of energy in gases and in condensed materials. *Phys. Rev.* 57 (1940) 485–93.
93. Fesefeldt H. C. Simulation of hadronic showers : Physics and applications. PITHA 85-02, RWTH Aachen, 1985.
94. Fisher S. M. *et al.* (Programming Techniques Group, ECP Division, CERN). *ADAMO Entity-Relationship Programming System : Version 3.3 : User's Guide.* CERN, Oct. 1993.
95. Fleming S. and T. Mehen. Leptoproduction of J/ψ. *Phys. Rev.* D 57 (1998) 1846–57, hep-ph/9707365.
96. Foster B., J. Malos, D. H. Saxon, *et al.* The design and construction of the ZEUS central tracking detector. *Nucl. Instrum. Methods* A 338 (1994) 254–83.
97. Fox D. J., L. N. Hand, W. Vernon, *et al.* Early test of scale invariance in high-energy muon scattering. *Phys. Rev. Lett.* 33 (1974) 1504–7.
98. Frabetti P. L. *et al.* (E687 Collab.). Charm–anticharm asymmetries in high energy photoproduction. *Phys. Lett.* B 370 (1996) 222–32.
99. Fritzsch H. and M. Gell-Mann. Current algebra : Quarks and what else? In *High energy physics,* Proceedings of the XVIth international conference (Chicago, 1972), J. D. Jackson, A. Roberts and R. Donaldson (Eds.), Vol. 2, NAL, Batavia 1995, pp. 131–65.
100. Gaillard M. K., B. W. Lee, J. L. Rosner. Search for charm. *Rev. Mod. Phys.* 47 (1975) 277–310.
101. Gallo E. The TLT and DST filters for the DIS group in 1995. Internal ZEUS-Note 96-001, DESY, Hamburg, 1996.
102. Gather K. and D. H. Saxon. Axes, units, conventions. Internal ZEUS-Note 88-012, DESY, Hamburg, 1988.
103. Gell-Mann M. A schematic model of baryons and mesons. *Phys. Lett.* 8 (1964) 214 f.
104. Georgi H. D–$\overline{D}$ mixing in heavy quark effective field theory. *Phys. Lett.* B 297 (1992) 353–57, hep-ph/9209291.
105. Giani S. *et al.* (CERN Application Software Group). *GEANT : Detector Description and Simulation Tool.* CERN Program Library Long Writeup W5013, Geneva, Oct. 1994.
106. Glashow S. L., J. Iliopoulos, L. Maiani. Weak interactions with lepton-hadron symmetry. *Phys. Rev.* D 2 (1970) 1285–92.
107. Glück M., E. Reya, A. Vogt. Parton distributions for high-energy collisions. *Z. Phys.* C 53 (1992) 127–34.
108. Glück M., E. Reya, A. Vogt. Dynamical parton distributions of the proton and small x physics. *Z. Phys.* C 67 (1995) 433–48.
109. Gribov V. N. and L. N. Lipatov. Deep inelastic ep scattering in perturbation theory. *Sov. J. Nucl. Phys.* 15 (1972) 438–50 [*Yad. Fiz.* 15 (1972) 781–807].
110. Gribov V. N. and L. N. Lipatov. e^+e^--pair annihilation and deep inelastic ep scattering in perturbation theory. *Sov. J. Nucl. Phys.* 15 (1972) 675–84 [*Yad. Fiz.* 15 (1972) 1218–37].
111. Groll M. Electroproduction of ϕ-mesons at $0.25 < Q^2 < 0.85\,\mathrm{GeV}^2$ at HERA (in German). Diplom thesis, University of Hamburg, May 1998, DESY-THESIS-1998-008.

112. Gronberg J. (for the CLEO Collab.). D^0 mixing at CLEO-II. Presented at the meeting of the American Physical Society, Division of Particles and Fields (DPF 99), Los Angeles, Jan. 1999, hep-ph/9903368.

▷ H1 Collaboration, see Refs. 2, 4, 5, 52, 113, 139.

113. H1 Collaboration. First H1 observation of open b production at HERA. Contributed paper to the 29th International Conference on High Energy Physics, ICHEP 98, Vancouver, Canada, July 1998.

114. Hall-Wilton R. CTD aging effects. Presented by D. Bailey at the ZEUS tracking meeting, Bristol, Apr. 1997.

115. Hall-Wilton R., N. McCubbin, P. Nylander, *et al.* The CTD tracking resolution. Internal ZEUS-Note 99-027, DESY, Hamburg, 1999.

116. Harris B. W. Private communication, 1997.

117. Harris B. W. and J. Smith. Heavy-quark correlations in deep-inelastic electroproduction. *Nucl. Phys.* B 452 (1995) 109–60, hep-ph/9503484.

118. Harris B. W. and J. Smith. Charm quark and $D^{*\pm}$ cross-sections in deeply inelastic scattering at HERA. *Phys. Rev.* D 57 (1998) 2806–12, hep-ph/9706334.

119. Hartner G. F. VCTRAK briefing : Program and math. Internal ZEUS-Note 98-058, DESY, Hamburg, 1998.

120. Hartner G. F., Y. Iga, J. B. Lane, N. A. McCubbin. VCTRAK (3.06/20) : Offline output information. Internal ZEUS-Note 96-013, DESY, Hamburg, 1996.

121. Hebbel K. $F_2^{c\bar{c}}$ from semileptonic charm decays. Internal ZEUS-Note 99-036, DESY, Hamburg, 1999.

122. Hendricks R. W. Space charge effects in proportional counters. *Rev. Sci. Instrum.* 40 (1969) 1216–23.

▷ HERA-B Collaboration, see Ref. 170.

123. HERMES Collaboration. *Technical Design Report.* DESY, July 1993.

124. Hilger E. ZEUS coordinate system. Internal ZEUS-Note 86-017, DESY, Hamburg, 1986.

125. Hoeger K. C. Measurement of x, y, Q^2 in neutral current events at HERA. In Ref. 56, *Phys. HERA Proc.*, Vol. 1, pp. 43–55.

126. Holm U. (Ed.) (ZEUS Collab.). *The ZEUS Detector : Status Report 1993.* DESY, Hamburg, Feb. 1993.

127. Iga Y. Private communication, 1995.

128. Ingelman G., A. de Roeck, R. Klanner (Eds.). *Future Physics at HERA,* Proceedings of the workshop (Hamburg, 1996), DESY-96-235.

129. Ingelman G., A. Edin, J. Rathsman. LEPTO 6.5 : A Monte Carlo generator for deep inelastic lepton–nucleon scattering. *Comput. Phys. Commun.* 101 (1997) 108–34, hep-ph/9605286.

130. Jackson J. D. *Classical Electrodynamics.* John Wiley & Sons, New York, 2nd edn, 1976.

131. Jakubowski Z. and M. Kobel. A verified upgrade of the GHEISHA 6/7 simulation of particle interactions. *Nucl. Instrum. Methods* A 297 (1990) 60–86.

132. Jaquet F. and A. Blondel. As discussed in R. Turlay: Report from the study group on detectors for charged current events. In *Proceedings of the Study on an* ep *Facility for Europe* (Hamburg, 1979), U. Amaldi (Ed.), DESY, ECFA, pp. 377–414, DESY-79/48.

133. Jeanne D., P. Lazeyras, I. Lehraus, *et al.* High energy particle identification using multilayer proportional counters. *Nucl. Instrum. Methods* 111 (1973) 287–300.

134. Jing Z. Private communication, 1997.

135. Jones L. M. and H. W. Wyld. Charmed-particle production by photon–gluon fusion. *Phys. Rev.* D 17 (1977) 759–63.

136. Jung H. Hard diffractive scattering in high energy ep collisions and the Monte Carlo generator RAPGAP. *Comput. Phys. Commun.* 86 (1995) 147–61, DESY-93-182.

137. Jung H. *The RAPGAP Monte Carlo for Deep Inelastic Scattering : Version 2.06/26.* Physics Dept, University of Lund, Mar. 1998.
138. Klein M. and T. Riemann. Electroweak interactions probing the nucleon structure. *Z. Phys.* C 24 (1984) 151–55.
139. Kleinwort C. (for the H1 Collab.). Studies of charm production with the H1 detector at HERA and observation of elastic vector meson photoproduction at HERA. In *High Energy Physics,* Proceedings of the XXVII$^{\text{th}}$ international conference (Glasgow, 1994), P. J. Bussey and I. G. Knowles (Eds.), Vol. 2, IOK, Bristol 1995, pp. 1007–9.
140. Kwiatkowski A., H. Spiesberger, H. J. Möhring. HERACLES : An event generator for ep interactions at HERA including radiative processes. *Comput. Phys. Commun.* 69 (1992) 155–72.
141. Laenen E., S. Riemersma, J. Smith, W. L. van Nerven. Complete $\mathcal{O}(\alpha_s)$ corrections to heavy-flavour structure functions in electroproduction. *Nucl. Phys.* B 392 (1993) 162–228.
142. Lai H. L., J. Huston, S. Kuhlmann, *et al.* Improved parton distributions from global analysis of recent deep inelastic scattering and inclusive jet data. *Phys. Rev.* C 74 (1997) 1280–96, hep-ph/9701256.
143. Landau L. On the energy loss of fast particles by ionization. *J. Phys. (Moscow)* 8 (1944) 201–5.
144. Leo W. R. *Techniques for Nuclear and Particle Physics Experiments : A How-to Approach.* Springer-Verlag, Berlin, 2$^{\text{nd}}$ edn, 1992.
145. Lönnblad L. Ariadne version 4 : A program for simulation of QCD cascades implementing the colour dipole model. *Comput. Phys. Commun.* 71 (1992) 15–31.
146. Maccabee H. D. and D. G. Papworth. Correction to Landau's energy loss formula. *Phys. Lett.* 30A (1969) 241 f.
147. Marchesini G., B. R. Webber, G. Abbiendi, *et al.* HERWIG : A Monte Carlo event generator for simulating hadron emission reactions with interfering gluons : Version 5.1 —April 1991. *Comput. Phys. Commun.* 67 (1992) 465–508.
148. Martin A. D., R. G. Roberts, M. G. Ryskin, W. J. Stirling. Consistent treatment of charm evolution in deep inelastic scattering. *Eur. Phys. J.* C 2 (1998) 287–300, hep-ph/9612449.
149. Martin A. D., R. G. Roberts, W. J. Stirling. Parton distributions : A study of the new HERA data, α_s, the gluon and $p\bar{p}$ jet production. *Phys. Lett.* B 387 (1996) 419–26, hep-ph/9606345.
150. Martin A. D., W. J. Stirling, R. G. Roberts. Parton distributions updated. *Phys. Lett.* B 306 (1993) 145–50; B 309 (1993) 492 (E).
151. Martin A. D., W. J. Stirling, R. G. Roberts. Parton distributions of the proton. *Phys. Rev.* D 50 (1994) 6734–52, hep-ph/9406315.
152. McCubbin N. Private communication, 1996.
153. Mengel S., J. Lane, F. Corriveau. The magnetic field in the ZEUS central tracking region. Internal ZEUS-Note 92-098, DESY, Hamburg, 1992.
154. Nason P. and C. Oleari. A fixed order calculation of the heavy-quark fragmentation function in e^+e^- collisions. *Phys. Lett.* B 447 (1999) 327–30, hep-ph/9811206.
155. Ne'eman Y. Derivation of strong interactions from a gauge invariance. *Nucl. Phys.* 26 (1961) 222–29.
156. Nussinov S. On possible effects of decays of charmed particle resonances. *Phys. Rev. Lett.* 35 (1975) 1672–84.
157. Nylander P. Questions regarding D^{*+} vs D^{*-} in 1996 photoproduction events. Presentation at the ZEUS tracking meeting, Sept. 1997.
158. Ohrenberg K. *Measurement of the Proton Structure Function F_2 Using the Hadron Electron Separator of the ZEUS Detector at HERA.* Doctoral thesis, Physics Dept, University of Hamburg, Nov. 1996, DESY-F35D-96-17.

▷ OPAL Collaboration, see Refs. 3, 7, 8.

▷ Particle Data Group, see Ref. 62.

159. Peterson C., D. Schlatter, I. Schmitt, P. M. Zerwas. Scaling violations in inclusive e^+e^- annihilation spectra. *Phys. Rev.* 27 (1983) 105–11.
160. Piotrzkowski K. and M. Zachara. Determination of the ZEUS luminosity in 1993. Internal ZEUS-Note 94-167, DESY, Hamburg, 1995.
161. Piotrzkowski K. and M. Zachara. Determination of the ZEUS luminosity in 1994. Internal ZEUS-Note 95-138, DESY, Hamburg, 1995.
162. Plothow-Besch H. The parton distribution function library. *Int. J. Mod. Phys.* A 10 (1995) 2901–20.
163. Quadt A. *Measurement and QCD Analysis of the Proton Structure Function F_2 from the 1994 HERA Data Using the ZEUS detector.* PhD thesis, Christ Church, University of Oxford, Michaelmas Term 1996, DESY-THESIS-1998-007.
164. Ramana Murthy P. V. and G. D. Demeeter. The use of gas proportional counters to distinguish protons from pions in the cosmic radiation at energies of near or greater than 100 GeV. *Nucl. Instrum. Methods* 56 (1967) 93–165.
165. Riemersma S., J. Smith, W. L. van Nerven. Rates for inclusive deep-inelastic electroproduction of charm quarks at HERA. *Phys. Lett.* B 347 (1995) 143–51, hep-ph/9411431.
166. Roberts J. H. C. Cell design and electrostatic optimisation for the ZEUS central tracking detector. RAL-87-095, Chilton, 1987.
167. Rothwell P. Fluctuations in the energy-loss of fast electrons in a proportional counter. *Proc. Phys. Soc. London* B 64 (1951) 911–15.
168. Sampson S. Charm tagging at the SLT with a microvertex detector. Internal ZEUS-Note 97-077, DESY, Hamburg, 1997.
169. Schlenstedt S. S. Schlenstedt's ZEUS lumi page. Web page ⟨http://www-zeus.desy.de/~schlenst/lumi.html⟩, accessed July 1996.
170. Schmidt-Parzefall W. (for the HERA-B Collab.). HERA-B : An experiment to study CP violation at the HERA proton ring using an internal target. *Nucl. Instrum. Methods* A 368 (1995) 124–32.
171. Schneekloth U. (Ed.). *The HERA Luminosity Upgrade.* Hamburg, July 1998, DESY-HERA-98-05.
172. Schroeder W. von. Private communication, 1996.
173. Seymour M. H. Heavy quark production in jets. *Z. Phys.* C 63 (1994) 99–109.
174. Sideris D. G. Simulation of the avalanche region of an anode wire in the ZEUS CTD. Internal ZEUS-Note 95-076, DESY, Hamburg, 1995.
175. Sinkus R. *Measurement of the Proton Structure Function F_2 from the 1994 HERA Data Using a Neural Network for the Identification of the Scattered Lepton.* Doctoral thesis, Physics Dept, University of Hamburg, Apr. 1996, DESY-F35D-96-10.
176. Sinkus R. and T. Voss. Particle identification with neural networks using a rotational invariant moment representation. *Nucl. Instrum. Methods* A 391 (1997) 360–68, DESY-96-264.
177. Sjöstrand T. High-energy physics event generation with PYTHIA 5.7 and JETSET 7.4. *Comput. Phys. Commun.* 82 (1994) 74–90.
178. Smith W. H., I. Ali, B. Behrens, *et al.* The ZEUS calorimeter first level trigger. *Nucl. Instrum. Methods* A 355 (1995) 278–94.
179. Sokolov A. A. and I. M. Ternov. On polarization and spin effects in the theory of synchrotron radiation. *Sov. Phys. Dokl.* 8 (1964) 1203–5 [*Dokl. Akad. Nauk SSSR* 53 (1963) 1052–54].
180. Spiesberger H. *HERACLES : An Event Generator for* ep *Interactions at HERA Including Radiative Processes : Version 4.6.* DESY, Hamburg, Jan. 1996.
181. Stange T. and F. Zetsche. Monitoring the reconstruction of ZEUS data 1993. Internal ZEUS-Note 94-028, DESY, Hamburg, 1994.
182. Sternheimer R. M. The density effect for the ionization loss in various materials. *Phys. Rev.* 88 (1952) 851–59.

183. Sternheimer R. M. In Vol. 5 of *Methods of Experimental Physics*, L. Marton (Ed.). Academic Press, New York, 1961. Chap. 1.1: Interaction of radiation with matter, pp. 1–88.

184. Sternheimer R. M., M. J. Berger, S. M. Seltzer. Density effect for the ionization loss of charged particles in various substances. *At. Data Nucl. Data Tables* 30 (1984) 261–71.

185. Sternheimer R. M. and R. F. Peierls. General expression for the density effect for the ionization loss of charged particles. *Phys. Rev.* B 3 (1971) 3681–92.

186. Suszycki L. *et al.* (ZEUS Luminosity Monitor Group). Luminosity monitor pictures. Web page ⟨http://zaxp05.desy.de/pictures.html⟩, Dec. 1995.

187. Sutton M. R. *Charm in Dijet Photoproduction at HERA.* PhD thesis, University College, London, 1998.

▷ Tagged Photon Spectrometer Collaboration—E691, see Ref. 16.

▷ TASSO Collaboration, see Ref. 45.

188. Uehling E. A. Penetration of heavy charged particles in matter. *Annu. Rev. Nucl. Sci.* 4 (1954) 315–50.

189. Vavilov P. V. Ionization loss of high-energy heavy particles. *Sov. Phys. JETP* 5 (1957) 749–51 [*Zh. Eksp. Teor. Fiz.* 32 (1957) 920–23].

190. Va'Vra J. Review of wire chamber aging. In *Radiation Damage to Wire Chambers,* Proceedings of the workshop (Berkeley, 1986), J. Kadyk (Ed.), LBL-21170.

191. Verkerke W. dE/dx studies. Presentation at the ZEUS tracking meeting, May 1996.

192. Verkerke W. Private communication, 1996.

193. Verkerke W. Private communication, 1997.

194. Verkerke W. *Measurement of Charm Production in Deep Inelastic Scattering.* Doctoral thesis, Faculty of Science, University of Amsterdam, May 1998.

195. Waloschek P. HERA-Bulletin. № 4, DESY, Hamburg, 1985.

196. Wiik B. H. HERA status. In Ref. 56, *Phys. HERA Proc.*, Vol. 1, pp. 1–16.

197. Wing M. Particle identification using dE/dx in the CTD at ZEUS. First-year transfer report, University College, London, Sept. 1996.

198. Wing M. Status of 1996 dE/dx corrections. Presentation at the ZEUS tracking meeting, Bristol, Apr. 1997.

199. Wing M. dE/dx help page. Web page ⟨http://www-zeus.desy.de/~wing/dedx/dedx.html⟩, accessed July 1998.

200. Wing M. (for the ZEUS Collab.). Semi-leptonic decays of heavy quarks in dijet photoproduction at HERA. To appear in the proceedings of the DIS 99 conference, Berlin, Apr. 1999, hep-ex/9905051.

201. Wolf G. HERA physics. In *High Energy Phenomenology,* Proceedings of the 42nd Scottish Universities Summer School in Physics (St. Andrews, 1993), K. J. Peach and L. L. J. Vick (Eds.), Institute of Physics, Philadelphia 1994, pp. 135–224, DESY-94-022.

202. Youngman C. The ZEUS data acquisition system. In *Computing in High Energy Physics '92,* Proceedings of the international conference (Annecy, 1992), C. Verkerk and W. Wojcik (Eds.), pp. 145–50, CERN-92-07.

▷ ZEUS Collaboration, see Refs. 43, 47–49, 52, 80–82, 126, 200, 203–205.

203. ZEUS Collaboration. A microvertex detector for ZEUS. DESY-PRC-97/01, Hamburg, Jan. 1997. Internal ZEUS-Note 97-006.

204. ZEUS Collaboration. A forward plug calorimeter for the ZEUS detector. DESY-PRC-97/02, Hamburg, Jan. 1997. Internal ZEUS-Note 97-007.

205. ZEUS Collaboration. Measurement of inclusive $\mathrm{D}_s^\pm$ and $\mathrm{D}^{*\pm}$ cross-sections in photoproduction at HERA. Contributed paper to the International Europhysics Conference on High Energy Physics, HEP 99, Tampere, July 1999.

▷ ZEUS Groups, see Refs. 14, 15, 20, 21, 53, 186.

206. Zweig G. An SU(3) model for strong interaction symmetry and its breaking (II). CERN-TH-412, Geneva, Feb. 1994.

D* Electroproduction

CROP PAGE